UNIVERSITY OF CALIFORNIA, SAN DIEGO

Characterization and Constitutive Modeling of Polyurea and Polyurea-Based Composites and Their Acoustic Applications

A Dissertation submitted in partial satisfaction of the
requirements for the degree
Doctor of Philosophy

in

Engineering Sciences (Mechanical Engineering)

by

Wiroj Nantasetphong

Committee in charge:

Professor Sia Nemat-Nasser, Chair
Professor Alireza Vakil Amirkhizi
Professor Gaurav Arya
Professor Yuri Bazilevs
Professor Renkun Chen
Professor Vlado Lubarda

2016

The Dissertation of Wiroj Nantasetphong is approved, and it is acceptable in quality and form for publication on microfilm and electronically:

_____

_____

_____

_____

_____

_____

Chair

University of California, San Diego

2016

DEDICATION

To my mom, dad, brothers, and sister whose love transcends distance and time.

EPIGRAPH

Ever tried. Ever failed. No matter. Try again. Fail again. Fail better.

—Samuel Beckett

TABLE OF CONTENTS

LIST OF FIGURES

LIST OF TABLES

ACKNOWLEDGEMENTS

First and foremost, I would like to sincerely thank Professor Sia Nemat-Nasser for constant guidance and support throughout my graduate studies. My research work, many technical papers, and this dissertation would not have been possible without his feedback and contribution.

In addition to my advisor, I would like to thank Professor Alireza Vakil Amirkhizi for his collaboration, support and guidance on my work. Aside from being great colleague, he is like my big brother here in the united state. I also extend my thanks to Mr. Jon Isaacs for his advices on the measurement equipments, methods, and comments on my experimental work and Mrs. Lauri Jacobs-Cohantz for handling all of the administrative details for my research and her kind help on whatever issues I had during my graduate study, as well as Professor Gaurav Arya, Professor Yuri Bazilevs, Professor Renkun Chen and Professor Vlado Lubarda for being part of my dissertation committees.

I was very fortunate to be able to work with many wonderful people. I would like to particularly thank Mrs. Zhanzhan Jia, Dr. Christian Eric Nielsen, and Dr. M. Arif Hasan, whom I directly collaborated with on many projects. Much of the work presented in this dissertation was greatly enhanced by their contributions. I am also grateful to fellow labmates and other CEAM members: Dr. Kristin Holzworth, Dr Ankit Srivastava, Dr. Yan Gao, Dr. Sara Wheeland, Dr. Hossein Sadeghi, Mr. Yesuk Song, and Mr. Shailendra Singh for the wonderful conversations, friendships, and all the great times.

I am grateful to meet many great friends and to be a part of the Thai community here in San Diego. In particular, I would like to thank Ms. Nidarat Urailert-

prasert, Dr. Poochit Nonejuie, Dr. Vorrapon Chaikeeratisak, Mr. Karu Chongsiripinyo, Mr. Teerapong Pirojsirikul, Dr. Oraphin Chantarasriwong, Mr. Edward Dechaumphai, and Dr. Tissana Kijsanayotin. My life in San Diego would not have been as colorful without all of them.

My deepest gratitude goes to my parents, Mrs. Wilawan and Mr. Vorathep Nantasetphong, for their unconditional love and support. I also thank my brothers and sister, Mr. Noppol, Mr. Chayanin, and Miss. Sirinapa Nantasetphong, who are always with me when I feel lost. I also thank my girl friend, Miss. Tritip Tachkaewkorapin who is always there for me. All the experiences and memories that we shared and difficult moments that we overcame together are the testament of our unbreakable bonds.

Subchapter 3.4 in chapter 3, is a reprint of the material, entitled "Dynamic Properties of Polyurea-Milled Glass Composites Part I: Experimental Characterization", as it appears in Mechanics of Materials, 2016, Nantasetphong, Wiroj; Jia, Zhanzhan; Amirkizhi, Alireza V.; Nemat-Nasser, Sia, Elsevier, 2016. The dissertation author was the primary investigator and author of this paper, and co-authors have approved the use of the material for this dissertation.

Subchapter 3.5 in chapter 3, is currently being prepared for submission for publication of the material that may be entitled as "A Novel Technique for Characterization of Elastomeric Polyurea at kHz Frequencies". Nantasetphong, Wiroj; Jia, Zhanzhan; Amirkizhi, Alireza V.; Nemat-Nasser, Sia. The dissertation author was the primary investigator and author of this paper, and co-authors have approved the use of the material for this dissertation.

Subchapter 4.2 in chapter 4, has been submitted for publication of the mate-

rial, entitled "Constitutive Modeling and Experimental Calibration of Pressure Effect for Polyurea Based on Free Volume Concept", as it may appear in Polymer, 2016, Nantasetphong, Wiroj; Amirkizhi, Alireza V.; Nemat-Nasser, Sia, Elsevier, 2016. The dissertation author was the primary investigator and author of this paper, and co-authors have approved the use of the material for this dissertation.

Subchapter 5.4 in chapter 5, is a reprint of the material, entitled "Dynamic Properties of Polyurea-Milled Glass Composites Part II: Micromechanical Modeling", as it appears in Mechanics of Materials, 2016, Nantasetphong, Wiroj; Amirkizhi, Alireza V.; Jia, Zhanzhan; Nemat-Nasser, Sia, Elsevier, 2016. The dissertation author was the primary investigator and author of this paper, and co-authors have approved the use of the material for this dissertation.

VITA

2008	Bachelor of Science in Mechanical Engineering (with High Distinction, Summa Cum Laude), Chulalongkorn University, Thailand
2011	Master of Science in Engineering Sciences (Applied Mechanics), University of California, San Diego, USA
2016	Doctor of Philosophy in Engineering Sciences (Applied Mechanics), University of California, San Diego, USA

PUBLICATIONS

Nantasetphong, W., Jia, Z., Amirkhizi, A.V., Hasan, M. A., and Nemat-Nasser, S. A Novel Technique for Characterization of Elastomeric Polyurea at kHz Frequencies, *in preparation* .

Nantasetphong, W., Amirkhizi, A.V., and Nemat-Nasser, S. Constitutive Modeling and Experimental Calibration of Pressure Effect for Polyurea Based on Free Volume Concept, *in preparation* .

Nantasetphong, W., Jia, Z., Amirkhizi, A.V., and Nemat-Nasser, S. Dynamic Properties of Polyurea-Milled Glass Composites Part I: Experimental Characterization, *Mechanics of Materials*, 2016.

Nantasetphong, W., Amirkhizi, A.V., Jia, Z., and Nemat-Nasser, S. Dynamic Properties of Polyurea-Milled Glass Composites Part II: Micromechanical Modeling, *Mechanics of Materials*, 2016.

Agrawal, V., Holzworth, K., Nantasetphong, W., Amirkhizi, A. V., Oswald, J., and Nemat-Nasser, S. Prediction of viscoelastic properties with coarse-grained molecular dynamics and experimental validation for a benchmark polyurea system, *Journal of Polymer Science Part B: Polymer Physics*, 2016.

Jia, Z., Amirkhizi, A. V., Nantasetphong, W., and Nemat-Nasser, S. Experimentally-based relaxation modulus of polyurea and its composites, *Mechanics of Time - Dependent Materials*, 1-20, 2016.

Qiao, J., Nantasetphong, W., Amirkhizi, A. V., and Nemat-Nasser, S. Ultrasonic properties of fly ash/polyurea composites, *Materials & Design*, 89: 264-272, 2016.

Jia, Z, Amirkhizi, A.V., Nantasetphong, W, and Nemat-Nasser, S. Determining the Shear Relaxation Modulus and Constitutive Models for Polyurea and Polyurea-Based Composite Materials from Dynamic Mechanical Testing Data, *In Mechanics of Composite and Multi-functional Materials*, Volume 7, pp. 363-367. Springer International Publishing, 2016.

Nemat-Nasser, S., Amirkhizi, A., Holzworth, K., Jia, Z., Nantasetphong, W., and Song, Y. Block Copolymer-Based Multi-scale Composites for Shock Mitigation, Book chapter in Elastomeric Polymers with High Rate Sensitivity: Applications in Blast, Shockwave, and Penetration Mechanics, (R. Barsoum, R.G.S., ed.), *William Andrew*, 2015

Nantasetphong, W., Amirkhizi, A. V., Jia, Z., and Nemat-Nasser, S. Low-Density, Polyurea-Based Composites: Dynamic Mechanical Properties and Pressure Effect, *In Challenges In Mechanics of Time-Dependent Materials and Processes in Conventional and Multifunctional Materials*, 2:145-150, 2014

Nantasetphong, W., Amirkhizi, A. V., Jia, Z., and Nemat-Nasser, S. Modifying the acoustic impedance of polyurea-based composites, *In SPIE Smart Structures and Materials+ Nondestructive Evaluation and Health Monitoring*, 86891B-86891B, 2013

Nantasetphong, W., Amirkhizi, A. V., Jia, Z., and Nemat-Nasser, S. Polyurea-Based Composites: Ultrasonic Testing and Dynamic Mechanical Properties Modeling. *In Composite Materials and Joining Technologies for Composites*, 7:235-243, 2013

Amirkhizi, A. V., Qiao, J., Nantasetphong, W., Schaaf, K., and Nemat-Nasser, S. Experimental Investigation of Dynamic Mechanical Properties of Polyurea-Fly Ash Composites. *In Mechanics of Time-Dependent Materials and Processes in Conventional and Multifunctional Materials*, 3:149-150, 2011

ABSTRACT OF THE DISSERTATION

Characterization and Constitutive Modeling of Polyurea and Polyurea-Based Composites and Their Acoustic Applications

by

Wiroj Nantasetphong

Doctor of Philosophy in Engineering Sciences (Mechanical Engineering)

University of California, San Diego, 2016

Professor Sia Nemat-Nasser, Chair

Nowadays polymer has become one of the most used engineering materials. Polymers have pervaded our life to such an extent that we cannot avoid using them on any given day. Polymers have special characteristics and offer some advantages over the traditional materials such as metals, ceramics, glasses, etc. Such advantages are, for example, corrosion resistance, low density, high ductility and toughness. Their mechanical properties can be easily modified and improved when combined with other materials to form polymeric composites. In this research, polyurea is studied due to its promising advantages for blast-and-shock protection and acoustic appli-

cations. Polyurea-based composites are also created in order to improve properties of polyurea and expand its usages. Fabrication procedures for polyurea, phenolics-microballoon filled polyurea, glass-microballoon embedded polyurea and milled-glass reinforced polyurea are discussed. In order to fully understand their mechanical behaviors which depend strongly on frequency (or time), temperature, and pressure, various characterization techniques spanning from quasi-static to high frequency dynamic ranges are conducted on these materials. Some new techniques; for example, ultrasonic wave measurement under low and high pressures and acoustic ball impact test, are developed for specific test conditions that cannot be accessed by other traditional testing techniques. The ultrasonic wave measurement under low and high pressures allows us to measure wave speed and attenuation of acoustic wave in viscoelastic materials in the pressure range of 0 to 1 GPa. The acoustic ball impact test allows us to measure the wave speed and attenuation in kHz frequency range and the temperature range of -50 to 50 °C, which is not practical for ultrasonic wave measurement using regular acoustic transducers. To reduce the time for experimental characterization, mathematical models based on micromechnics are also created in order to accurately estimate mechanical properties of polymeric composites. The models can be used for both elastic and viscoelastic composites with various shapes of inclusions. Moreover, experiment-based constitutive model for polymeric materials, which is implementable by finite element software, is presented. Lastly, a design of a novel periodic layered composite is demonstrated. The designed composite can be potentially used for acoustic sensing, transmitting, and silencing applications.

Chapter 1

Introduction

A polymer is a material that is composed of long-chain molecules, where each molecule is made up of repeating monomers connected together through a chemical reaction process called polymerization. During polymerization, a monomer is covalently bonded with other monomers within its vicinity to produce long chain molecules or polymer chains. Typically, most polymers are either hydrocarbon or silicone based since carbon and silicon in group 4 of periodic table have the ability to form long chains of atoms that include bonds with other elements [1]. The other heavier elements in group 4 are, however, too big to form long chains and compounds for which silicon and carbon are noted. There are many ways to characterize polymers, for example, (1) by types of reaction by which these monomers are joined together to make polymers, i.e. addition, condensation, and ring-opening polymerizations, (2) by number of kinds of monomers existing in a polymer chain, i.e. homopolymers or heteropolymers (co-polymers), (3) by polymer network structure, i.e. thermoplastics (no crosslinking), thermosets (closely-meshed crosslinking), and rubbers or elastomers (wide-meshed or loose crosslinking), and (4) degree of alignment of polymer chains

which can be divided into amorphous, crystalline, and semi-crystalline polymers.

Polymers have special characteristics and offer some advantages over the traditional materials such as metals, ceramics, glasses and etc. Such advantages are, for example, corrosion resistance, low density, high ductility and toughness. To design application or usage of a polymer, its mechanical behavior is one of the the key required informations. Generally, mechanical properties of polymers depend on many factors; e.g., their structures, operating temperature, pressure, frequency, time, UV light exposure, humidity, and strain rate of induced deformation, etc. In this research, polyurea which is a polymer with promising advantages for blast-and-shock protection and acoustic applications is studied. Polyurea-based composites are also created and studied in order to improve properties of polyurea and expand its usages. Their mechanical properties are studied, and characterized with respect to temperature, pressure, and frequency (or time). Characterization techniques for different ranges of frequency, pressure, and temperature are discussed. Constitutive model for polyurea under extreme environmental conditions is developed. It is implementable by finite element software. Micromechanics-based models are developed to estimate mechanical properties of polyurea-based composites. Dynamic homogenization model for one-dimensional periodic layered composites is developed to aid composite design for acoustic applications. Each model developed in this research is not limited to polyurea. It could be applied to other polymers with behaviors similar to that of polyurea.

1.1 Polyurea and Polyurea-Based Composites

Polyurea (PU) is a segmented block copolymer derived by the reaction of a diisocyanate component and a diamine component. The rapid reaction of an isocyanate group and an amine group yields a urea linkage and microphase-separated morphology [2–4]. The microstructure of polyurea has nano-scale hard domains dispersed in the soft domain due to the thermodynamic incompatibility of the segmented chain blocks of polyurea [5]. The hard segments has a high glass transition temperature (T_g) while the soft segments has a low T_g. The soft phase is primarily constituted of long chain diamine, which confers flexibility to the material, and the hard phase consists of diisocyanate typically in a semi-crystalline ordered state created by hydrogen bonding, which gives an enhanced initial stiffness and high mechanical toughness [3, 5]. The mechanical properties of polyurea may be tuned by using different isocyanates and amines [5]. The reaction ratio or stoichiometric ratio between the diisocyanate and diamine components controls the microstructure and mechanical behavior of the resulting polyurea. Fragiadakis et al. have studied the effect of stoichiometry variations on local segmental relaxation dynamics of polyurea. It was shown that increased hard segment content is associated with a greater sensitivity to pressure and volume changes [3]. Holzworth et al. also showed that the stoichiometric ratio affects the dynamic mechanical properties of polyurea through Dynamic Mechanical Analysis (DMA) [4]. Theoretically, the isocyanate component and amine component must be mixed in a stoichiometric ratio of 1:1, i.e., the total number of isocyanate functional ends must equal the total number of amine functional sites. However, as specified by the manufacturer, a stoichiometric ratio of 1.05:1 is used, i.e., a five percent excess of the isocyanate component is used beyond the stoichiometric ratio required for a

complete reaction [6]. This excess isocyanate helps account for that which is lost upon reaction with residual moisture during storage or application [4, 7]. Furthermore, the slight excess aids in producing a lightly cross-linked polymer through the development of biuret structures [4, 8, 9]. The research study discussed herein is focused on 1.05:1 molar ratio of of isocyanate to amine groups.

Mechanical behavior of polyurea is characterized as viscoelastic, deformable and incompressible. It depends strongly on the strain rate, temperature and pressure [9, 10]. Polyurea with crystalline well-dispersed hard segment morphology also shows strong hysteresis and cyclic softening [11]. It is also capable of resisting large strain and shape change due to small forces, without losing its original properties. The elongation at tearing can be as high as 800% [9]. Polyurea is both chemically and mechanically strong. It can be used for chemical resistance (chemical protection for lab and factory floors) and truck bed abrasion protection [12]. It is non-flammable. It shows excellent characteristics, including, but not limited to, environmental and safety compliance, long-term stability and appearance, and high mechanical performance [13]. A recent application of elastomeric polyurea is to improve the resistance of hard sturcture to failure [14] and ballistic penetration [15–17]. Various experiments show that this improvement can change the response from full penetration of a projectile to fully eliminating failure [17, 18]. Recent researches show that coating a layer of polyurea to the back of a steel plates significantly improves the impact and blast resistance of the composite structure. Amini et al. also showed that the location of the coating polyurea layer can have a significant effect on the response of the steel plate to dynamic impulsive loads, both in terms of failure mitigation and energy absorption, if it is coated on the back face of the plate. And, remarkably, when polyurea is applied

on the front face of the plate, it may actually enhance the destructive effect of the blast, promoting (rather than mitigating) the failure of the steel plate, depending on the interface bonding strength between the polyurea and steel layers [16]. The real mechanism underlying this effect is not yet fully understood, but an important contribution to the coatings' effectiveness is their ability to transition to the stiff glassy state during the deformation [19]. The viscoelastic rubber-to-glass transition is accompanied by large energy absorption, which thus toughens the coating.

Due to that polyurea is promising for many civilian and military applications, many researches have been conducted to create polyurea-based composites in order to improve its properties and expand its usages. Qiao et al studied polyurea with fly ash composites [20, 21]. They showed that by mixing polyurea with fly ash, the strength and stiffness of polyurea could be increased along with decrease in density. Carey investigated mechanical properties and blast mitigation performance of different discrete fiber-reinforced polyurea systems through experimental and analytical work. She found that the addition of glass fiber provides improved stiffness and strength to the composite system while the polyurea base material provides ductility [22]. Mihut et al. mixed hematite hybrid nanoparticles into polyurea and studied its mechanical and thermo-mechanical properties for small and large deformations as a function of the particle weight fraction. Their results indicate that significant reinforcement of the polyurea-based hybrid nanocomposite is achieved even at very low nanoparticle content with respect to the pure elastomeric matrix [23]. Qian et al. created graphite-oxide/polyurea and graphene/polyurea nanocomposites and studied their mechanical behaviors. They found that the two nanocomposites show different trend with respect to the weight percentage of the filler materials. They re-

ported that the graphene/polyurea nanocomposites has better tensile strength as the graphene content increase while the graphite-oxide/polyurea nanocomposite shows the drop in the tensile strength as the graphite oxide content increases. They reasoned that the graphite-oxide particles tend to aggregate in polyurea matrix, leading to poor dispersion and weakening the hydrogen bonds among polyurea molecules, resulting in the deduced mechanical properties of polyurea, while the graphene sheets have good dispersion and the larger mechanical strength compared to graphite-oxide, therefore improving the mechanical properties and the glass-transition temperature of the graphene/polyurea composite [24]. Cai et al. studied the effect of integrating C20 organoclay into highly and lowly crosslinked polyurea matrices. They found that the significant reinforcement was acheived in highly crosslinked polyurea with C20 nanocomposite, in which the Young's modulus, stress and elongation at break was improved by 40%, 110% and 50%, respectively at 5 wt% of C20. They also noted that the reinforcement is not equally significant in the lowly crosslinked polyurea matrix, indicating that macromolecular structure of the polyurea matrix is important for optimizing the nano-effect in the nanocomposites [25].

In this research, three polyurea-based composites; milled glass/polyurea, phenolic microballon/polyurea, and glass microballoon/polyurea composites as well as pristine polyurea are created for acoustic applications. The milled glass reinforced polyurea composite is created in order to improve the stiffness of polyurea, while the phenolic microballon filled polyurea and the glass microballoon embedded polyurea composites are created in order to reduce the mass density and stiffness of polyurea. These two microballoons are made of two different materials. The glass microballoon is stiff and brittle, while the phenolic microballoon is softer and more ductile. The

mechanical properties of the composites and pure polyurea are characterized with respect to frequency, temperature, and pressure. The characterization techniques for various experimental conditions are presented. Moreover, a constitutive model is developed for polyurea in order to understand and predict its behavior under various environmental conditions. The model can also be applied to polyurea-based composites and other polymeric materials with similar behavior.

1.2 Motivation and Objective of Research

Polyurea has a unique microphase-separated structure which consists of nanoscale semi-crystalline hard domains dispersed in the amorphous soft domain. The soft phase confers flexibility to the material, and the hard phase semi-crystalline state created by hydrogen bonding gives an enhanced initial stiffness with high mechanical toughness, leading to excellent overall mechanical properties, especially for blast-and-shock protection and acoustic applications. However, its mechanical behaviors which depend strongly on frequency, temperature, and pressure are not fully understood, and it is even more unclear for polyurea-based composites, leading to poor performance in the designed applications. Thus, the objectives of this research are (1) to study and understand the behaviors of polyurea and polyurea-based composites using commonly-used and in-house developed characterization techniques (2) to reduce the dependence of experimental characterization through mathematical models which are created in oder to accurately estimate mechanical properties and behaviors of polyurea-based composites (3) to design and use polyurea and polyurea-based composites for novel acoustic applications.

1.3 Organization of Chapters

Background materials, motivation, and objective of this research have been mentioned in this first chapter. Chapter 2 discuss fabrication procedures of polyurea and polyurea-based composites: polyurea with milled glasses, polyurea with phenolic microballons, and polyurea with glass microballoons. Various material characterization techniques are described in Chapter 3, i.e., quasi-static compression test, dynamic mechanical analysis (DMA), ultrasonic wave measurement at ambient, low, and high pressures, and acoustic ball impact test (ABI). In Chapter 4, the backgrounds of viscoelastic behaviors of polymeric materials are explained in detail. Time-temperature superposition for constructing viscoelastic modulus master curve is discussed. Experiment-based constitutive model that includes effect of temperature and pressure is demonstrated for polyurea. Numerical model for finite element analysis is also provided in this chapter. Micromechanical models for estimating mechanical properties of polymeric composites with various types of inclusion are presented in Chapter 5. In Chapter 6, the analysis of acoustic wave propagation in a one-dimensional periodic layered composite is discussed. A design of a novel polymeric periodic layered composite is demonstrated. The designed composite can potentially used for acoustic sensing, transmitting, and silencing applications.

Chapter 2

Material Fabrications

2.1 Polyurea

Polyurea is synthesized from the reaction of an aromatic isocyanate component and an amine-terminated resin blend component. In this research, the aromatic isocyanate component is Isonate 143L modified MDI from Dow Chemicals. It has 144.5 g/equivalent weight. It is a polycarbodiimide-modified diphenylmethane diisocyanate. Isonate 143L is in liquid form at room temperature and has a low viscosity and good storage stability down to 24 °C (see Figure 2.1a). In this diisocyanate, the carbodiimide linkage aids the stabilization of the polymer against hydrolytic degradation [26]. The amine-terminated resin blend component is Versalink P-1000 oligomeric diamine from Air Products. It has 600 g/equivalent weight. It is a polytetramethyleneoxide-di-p-aminobenzoate. Versalink P-1000 is a liquid at ambient temperature (see Figure 2.1b). Thus, it can be mixed, cast, and cured at room temperature. This oligomeric diamine is often used as a curative for both methylene diphenyl diisocyanates (MDI) and toluene diisocyanates (TDI) [6].

Figure 2.1: (a) Isonate 143L (b) Versalink P-1000

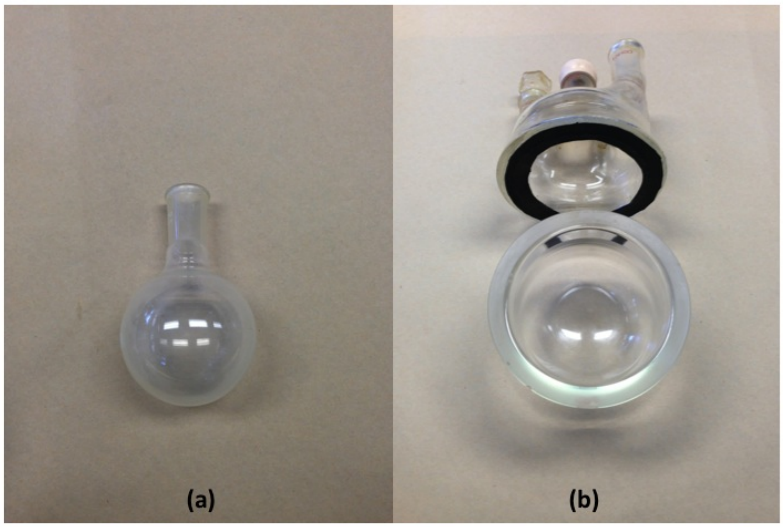

Figure 2.2: (a) Single-neck round-bottom flask for Isonate 143L (b) Three-neck round-bottom flask for Versalink P-1000

The recommended stoichiometric ratio between Versalink P-1000 oligomeric diamine and Isonate 143L is 1.05:1 [6,27]. While 1:1 stoichiometry provides the exact balance of isocyanate to amine functional sites, a five percent excess of Isonate 143L is

typically recommended to ensure that a lightly cross-linked polyurea is formed, and it also helps to account for the amount that is lost upon reacting with residual moisture during storage or application [4, 9]. The exact amount of excess Isonate 143L was estimated through weight measurements of containers before and after processing

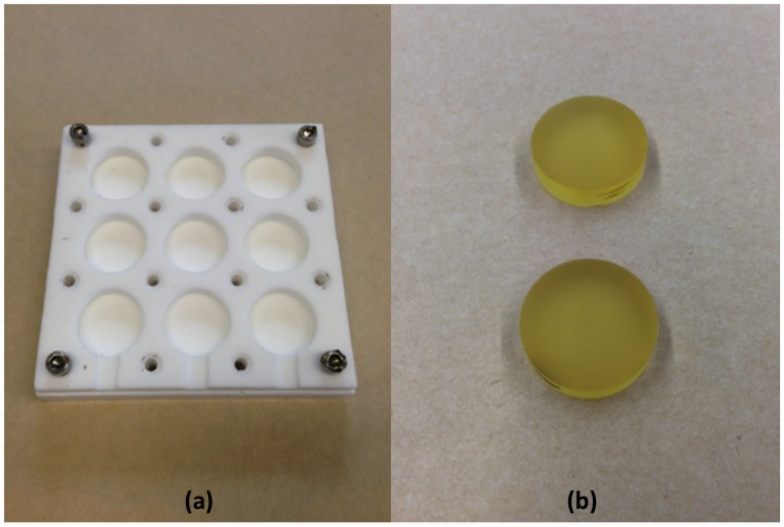

Figure 2.3: (a) Teflon molds for ultrasonic longitudinal wave measurement (b) Button-shaped polyurea samples for ultrasonic longitudinal wave measurement

Insonate 143L is degassed in a single-neck round-bottom flask (see Figure 2.2a) for 1 h at a vacuum pressure level of approximately 133.32 Pa. At the same time, Versalink P-1000 is degassed separately in a 500 ml round-bottom reaction vessel with a three-neck flat flange cover (see Figure 2.2b) for 1 h at the same vacuum pressure level as Isonate 143L. At room temperature, polyurea fabrication is conducted in the round-bottom reaction vessel of Versalink P-1000. After degassing for 1 hr, the precise mass of the Isonate 143L weighted with a digital scale is added to the Versalink P-1000. The mixture is then stirred using an egg-shaped magnetic stirrer and degassed for 5 min at the vacuum pressure level of 133.32 Pa. Viscosity of Versalink P-1000

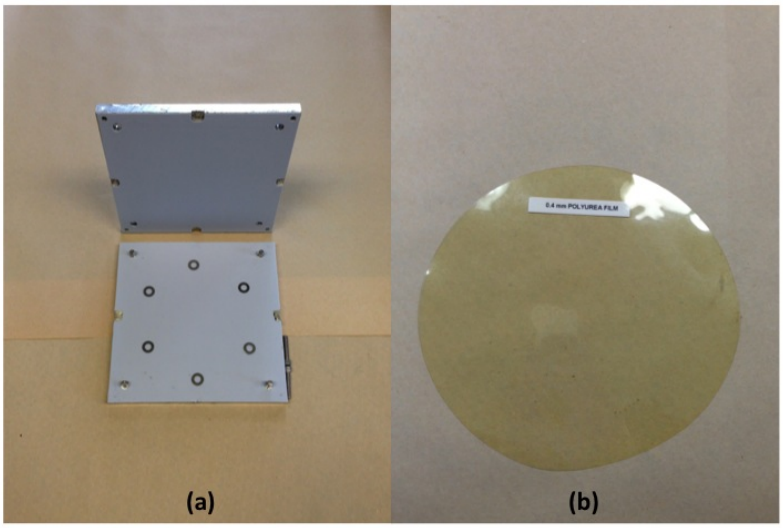

Figure 2.4: (a) Teflon molds for ultrasonic shear wave measurement (b) Polyurea film for ultrasonic shear wave measurement

oligomeric diamine is relatively high at room temperature, however when mixing, the diluent effect from the lower-viscosity isocyanate decreases the viscosity of the mixture and allows easy mixing and complete degassing prior to casting [4, 6]. The polyurea working time, inclusive of mixing time, is approximately 20 mins at ambient conditions [20].

After stirring and degassing for 5 min, the mixture is transferred from the reaction flask to molds via syringe. Specimens for ultrasonic longitudinal wave measurement are casted in Teflon molds to form button shape (see Figure 2.3). Due to high dissipative nature of ultrasonic shear wave in polymer, the specimens for ultrasonic shear wave measurement need to be very thin. Teflon coated aluminum plates and spacers with a specific thickness are used as a mold to cast polyurea sheet with desired thickness (see Figure 2.4). The liquid mixture is compressed between the two plates in order to create a thin polyurea film with uniform thickness. Specimens for

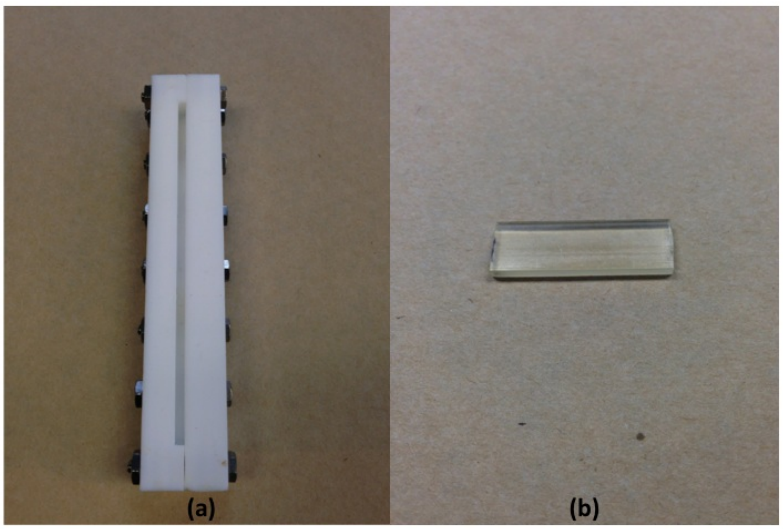

Figure 2.5: (a) Teflon molds for DMA (b) Retangular polyurea sample for DMA

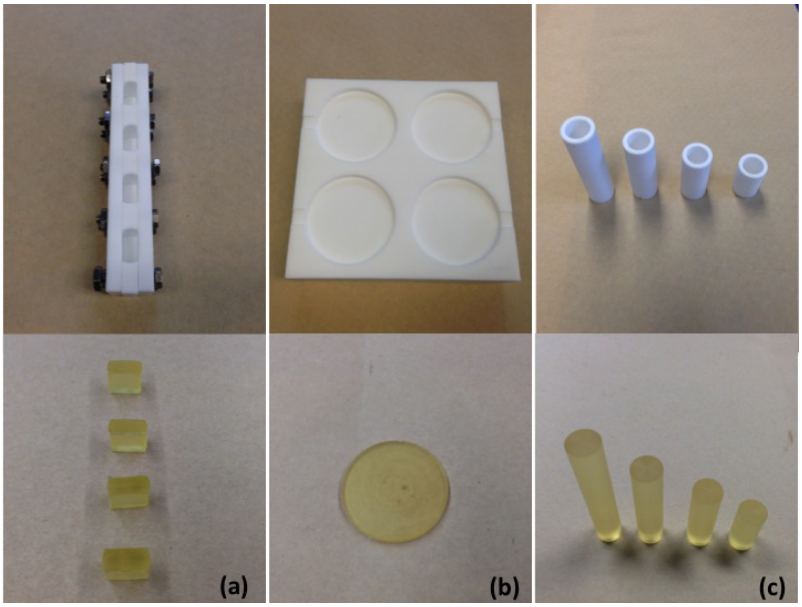

Figure 2.6: (a) Teflon molds and polyurea samples for high pressure ultrasonic wave measurement (b) Teflon molds and polyurea sample for low pressure ultrasonic wave measurement (c) Teflon molds and polyurea samples for acoustic ball impact measurement

DMA are casted in long-rectangular-bar-shaped molds (see Figure 2.5). Teflon molds and samples for high pressure ultrasonic wave measurement, low pressure ultrasonic

wave measurement, and acoustic ball impact measurement are shown in Figure 2.6. All polyurea specimens are cured at room temperature in a moisture controlled environmental chamber that maintains the relative humidity level at 10%. Two weeks are required to achieve complete cure at ambient conditions, with 75% of the ultimate physical properties being realized within 24 hrs [6]. All polyurea test specimens are stored in the environmental chamber prior to testing.

2.2 Phenolic Microballoon Filled Polyurea Composite

Phenolic resin or phenol formaldehyde (PF) is synthetic polymer obtained by the reaction of a phenol or substituted phenol with formaldehyde. It is very well known due to its excellent Fire Smoke Toxicity (FST) properties, retention of properties after long-term exposure to high temperatures, and excellent electrical and chemical resistance [28]. Its bulk density is $1.28\,\mathrm{g\,cm^{-3}}$ [29]. In this study, it is used in the shape of thin-shelled microballoon with 37 µm average diameter and 1 µm shell thickness. Its apparent density is $0.227\,\mathrm{g\,cm^{-3}}$. The phenolic microballoon filler was purchased from Fiberglass Supply. Figure 2.7a shows a bag of phenolic microballoons. This thermosetting plastic serves as a filler material in the fabrication process of phenolic-microballoon filled polyurea composite.

Due to the short gel time of polyurea at room temperature, pheonolic microballoons are first added to Versalink P-1000 in a predetermined volume fraction. The mixture is mixed by hand to prevent the vacuum blowing out the microballoons, and then mixed for 1 hour using a mechanical stirrer under vacuum (133.32 Pa

absolute pressure) until most of the trapped air bubbles are gone. The second component, Isonate 143L, is also degassed for 1 h separately. After the degassing process, the Isonate 143L is added into the mixture of Versalink P-1000 and phenolic microballoons, and all of the components are thoroughly mixed together under vacuum for 5 min. The resultant mixture is then transferred into a Teflon mold (depend on which measurement the samples are made for) and allowed to cure at room temperature for 24 h in an environmental chamber at 10% relative humidity. The samples are then removed from the mold and allowed to cure unrestrained for two weeks in the chamber before testing. They are unrestrained to prevent the formation of residual stresses. A similar procedure was also used for the fabrication of polyurea with glass microballoons

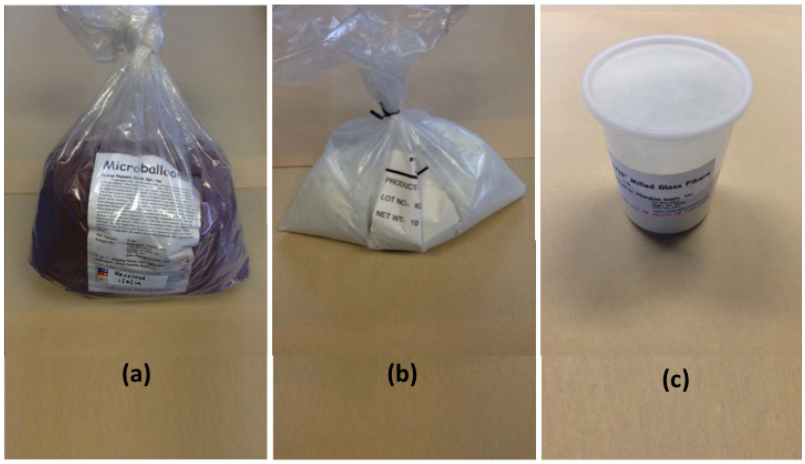

Figure 2.7: (a) A bag of phenolic microballoons (b) A bag of glass microballoons (a) A box of milled glasses

2.3 Glass Microballoon Filled Polyurea Composite

K1 glass microballoons (from 3M) are soda-lime-borosilicate engineered hollow glass microspheres. They have a high strength-to-weight ratio, low alkalinity and high

water resistance. They are useful for increasing strength and stiffness, while reducing weight. The bulk density of glass is around 2.23 - 2.53 $\mathrm{g\,cm^{-3}}$. The apparent density of microballoons is around 0.1 - 0.14 $\mathrm{g\,cm^{-3}}$ [30]. They have 65 µm average diameter with 0.6 µm average shell thickness. Figure 2.7b shows a bag of glass microballoons. Due to the chemical stability of glass microballoon, The fabrication procedure is similar to that of polyurea with phenolic microballoons

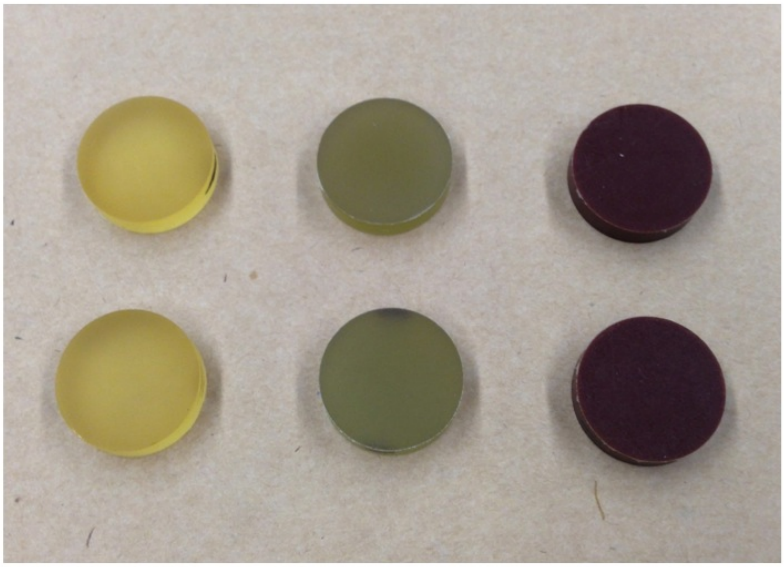

Figure 2.8: Samples for ultrasonic longitudinal wave measurements (left to right: polyurea, milled glass reinforced polyurea, and phenolic microballoon filled polyurea composites)

2.4 Milled Glass Reinforced Polyurea Composite

The milled glass fiber is purchased from Fibertec, Inc. (product number 3032). Figure 2.7c shows a box of milled glasses. Milled glass 3032 is made of E glass fiber. This cylindrical shaped micro glass has average diameter of 16 m and average length of 200 m. Polyurea with milled glasses of volume fractions of 5%, 10%, and 20% are

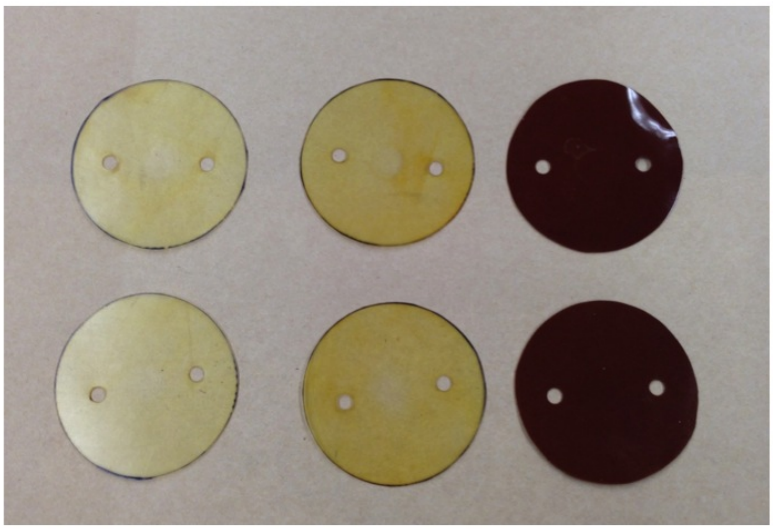

Figure 2.9: Samples for ultrasonic shear wave measurements (left to right: polyurea, milled glass reinforced polyurea, and phenolic microballoon filled polyurea composites)

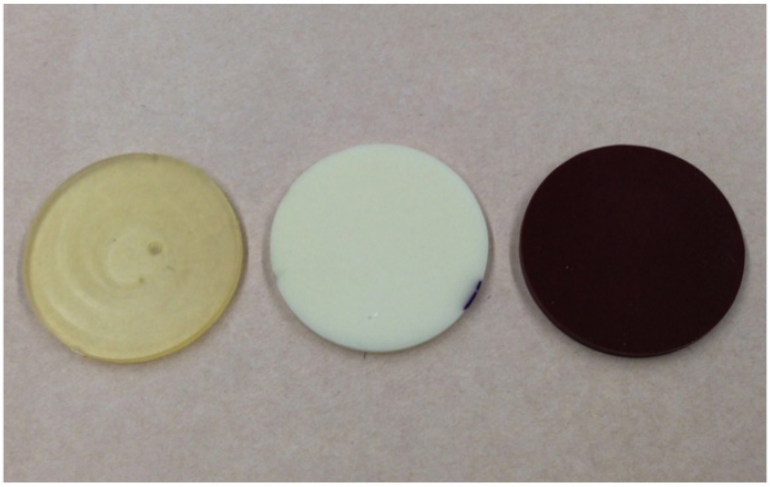

Figure 2.10: Samples for low pressure ultrasonic longitudinal wave measurements (left to right: polyurea, glass microballoon filled polyurea, and phenolic microballoon filled polyurea composites)

fabricated.

To clean the glass surface, piranha solution, which is a mixture of H_2SO_4 and 30% H_2O_2 solution in the ratio of 3:1 (by volume), is used. Mixing the piranha

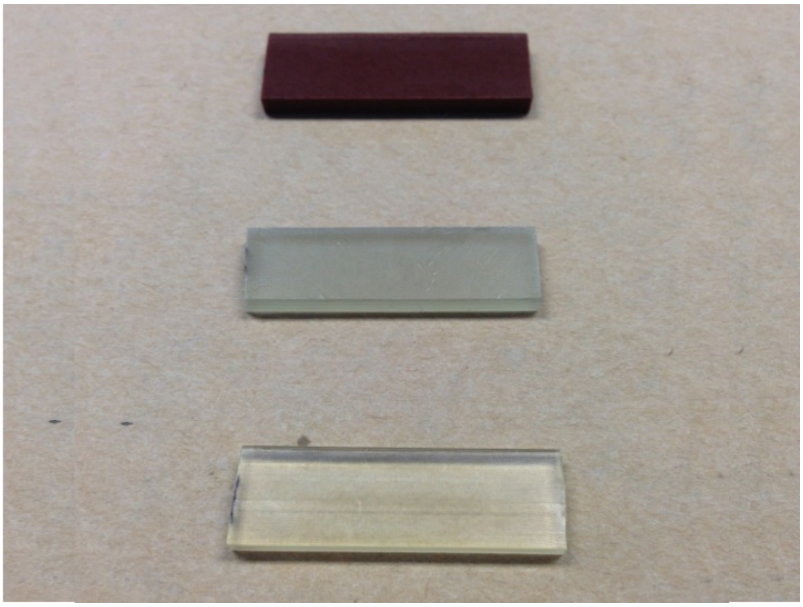

Figure 2.11: Samples for DMA (top to bottom: phenolic microballoon filled polyurea composite, milled glass reinforced polyurea composite, and polyurea)

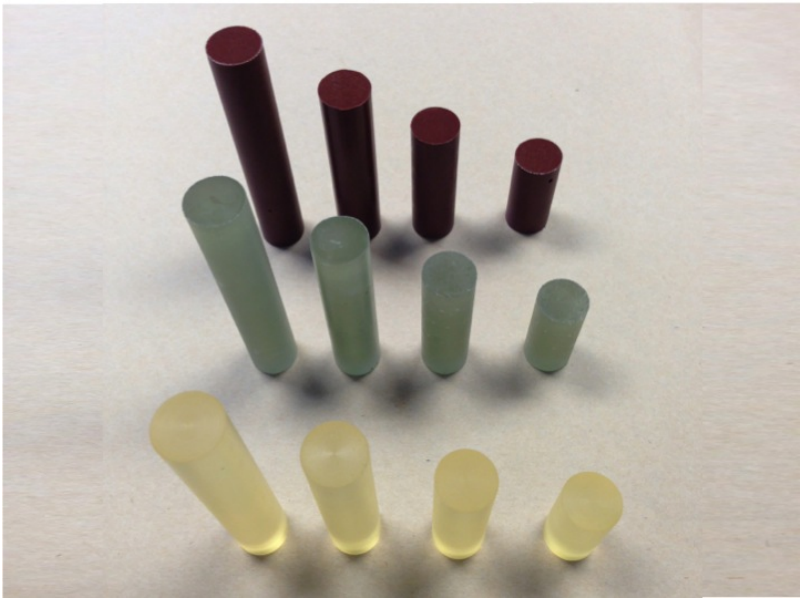

Figure 2.12: Samples for acoustic ball impact measurement (top to bottom: phenolic microballoon filled polyurea composite, milled glass reinforced polyurea composite, and polyurea)

solution is exothermic. The resultant heat can cause solution temperatures exceeding 100°C. The milled glass is washed in the boiling solution for 10 min. Then the milled

glass is neutralized in deionized water and dried in a vacuum oven overnight at 110°C. The milled glass is first mixed with the more viscous component Versalink P-1000 using the magnetic stir bar to prevent the milled glass from being blown away by the vacuum in the following degassing step. Then the Isonate 143L and Versalink P-1000 with milled glass are degassed separately under vacuum (133.32 Pa) while stirred using magnetic stirrers. The degassing process lasts 2 hours until most of the air bubbles are removed. Then the two parts are mixed together with the stoichiometric ratio of 1.05:1 (isocyanate: amine). After adding Isonate 143L into Versalink P-1000 (with the pre-mixed milled glasses), the mixture is mixed and degassed for 5 min before transferring, using disposable syringes, into a Teflon mold (depend on which measurement the samples are made for). The samples are cured in the environmental chamber, in which relative humidity is controlled at 10%, for two weeks before testing.

Figures 2.8, 2.9, 2.10, 2.11,and 2.12 show shapes and colors of the samples for ultrasonic longitudinal and shear wave measurements, low pressure ultrasonic longitudinal wave measurement, DMA, and acoustic ball impact measurement, respectively.

Acknowledgments

This work has been conducted at the Center of Excellence for Advanced Materials (CEAM) at the University of California, San Diego, and has been supported through ONR Grant N00014-09-1-1126 and DARPA Grant RDECOM W91CRB-10-1-0006. I would like to thank Mrs. Zhanzhan Jia for her help and guidance on sample fabrication

Chapter 3

Material Characterization Techniques

Mechanical properties of polymers depend on many variables. Three major variables affecting the properties are temperature, pressure and frequency (or time). Mechanical properties of polymers can change significantly over a narrow range of temperature. Some polymers are very sensitive to pressure. For example, stiffness of polyurea under confined compression can increase 10 to 20 folds with increasing pressure [9]. Also, the stiffness at very high frequency is several orders of magnitude higher than that at low frequency [31]. In this chapter, quasi-static and dynamic testing methods for measuring mechanical properties of polyurea and polyurea-based composites under various conditions will be discussed in detail.

3.1 Quasi-Static Testing

Quasi-static material testing is necessary for characterization of mechanical properties at low strain rate or slow loading rate and for the development of constitutive model for quasi-static deformation. Materials under quasi-static load will go

through a sequence of infinitesimal and slow deformation that remains close to equilibrium such that inertial effects are negligible. In other words time and inertial mass are irrelevant. In this research, we are interested in quasi-static confined compression mode. In general, compressible materials under this compression mode undergo uniaxial deformation while there is no lateral deformation. Longitudinal modulus can be measured using the confined compression mode. However, this mode can also create hydrostatic pressure condition on materials which are nearly incompressible. Polyurea is an example of nearly incompressible polymers. Under hydrostatic pressure condition, it allows to measure bulk modulus of the tested material. In this case, bulk modulus is very close to longitudinal modulus.

3.1.1 Experimental Setup

The experimental setup consists of force-displacement and temperature control units (see Figure. 3.1). Instron servo-hydraulic machine model 1332 is used as loading test machine. It has capability to generate force up to 100 kN (22 klbf). MTS controller model 407 is used to control the Instron load cell. Either displacement or force control can be selected. The loading rate is adjustable depending on the test condition. In this research, the slow loading rate of 15 lbf/s ($67\,\mathrm{N\,s^{-1}}$) is used to load sample. With this slow loading rate it ensures that sample is under quasi-static condition. In order to control testing temperature, an MTS environmental chamber model 651 is equipped with Instron load cell. The chamber can provide cooling range from ambient to $-129\,^{\circ}\mathrm{C}$ ($-200\,^{\circ}\mathrm{F}$) when equipped with liquid nitrogen. The heating range can go up to $315\,^{\circ}\mathrm{C}$ ($600\,^{\circ}\mathrm{F}$). Testing temperature is controlled by MTS temperature controller model 409.80.

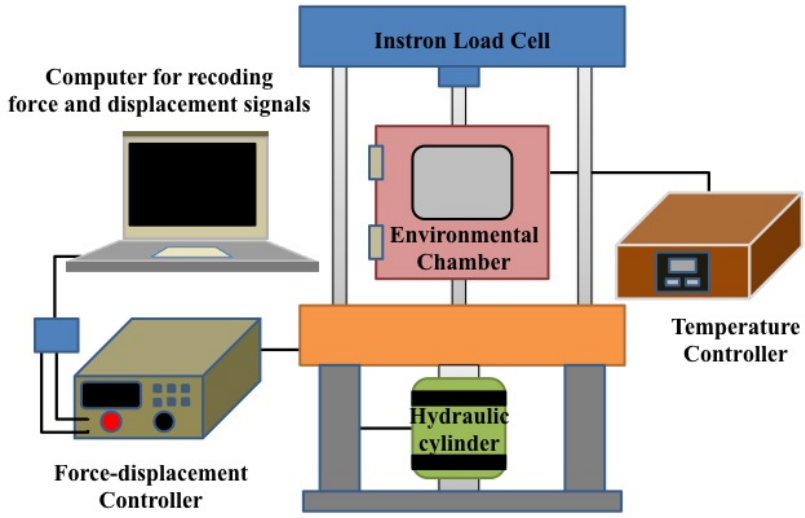

Figure 3.1: Schematic diagram shows force-displacement and temperature control units

In this research, pressure or compressive stress is divided into two ranges: low and high pressures. Low pressure is considered from 0 to 20 MPa, while high pressure is from 50 MPa to 1 GPa. Low-pressure range is used for characterizing material behaviors under moderate pressure environment such as several-kilometer-depth under water, whereas high-pressure range can be used for characterizing material behaviors under extreme pressure conditions such as in blast or explosion. Specially designed test fixtures for low and high pressure ranges are developed. The low-pressure test fixture is made of aluminum. It consists of two cylindrical pistons for compressing the sample, one collar to confine the sample, and potentiometer for measuring displacement or contraction of the sample (see Figure. 3.2). Sample for the fixture is designed to have 63.5 mm diameter so that at the maximum load of 100 kN, the sample will be compressed with around 31.6 MPa pressure which is enough to cover our low-pressure

range. The high-pressure test fixture is made of maraging steel. It consists of two pistons for compressing the sample, a cell to confine the sample (see Figure. 3.3). The compression area of high-pressure sample is around 33 time smaller than low-pressure sample. At the maximum load, the sample will be, approximately, under 1000 MPa. Figures 3.4, 3.5, and 3.6 show the dimensions of the confinement cell, piston, and sample for high-pressure test, respectively.

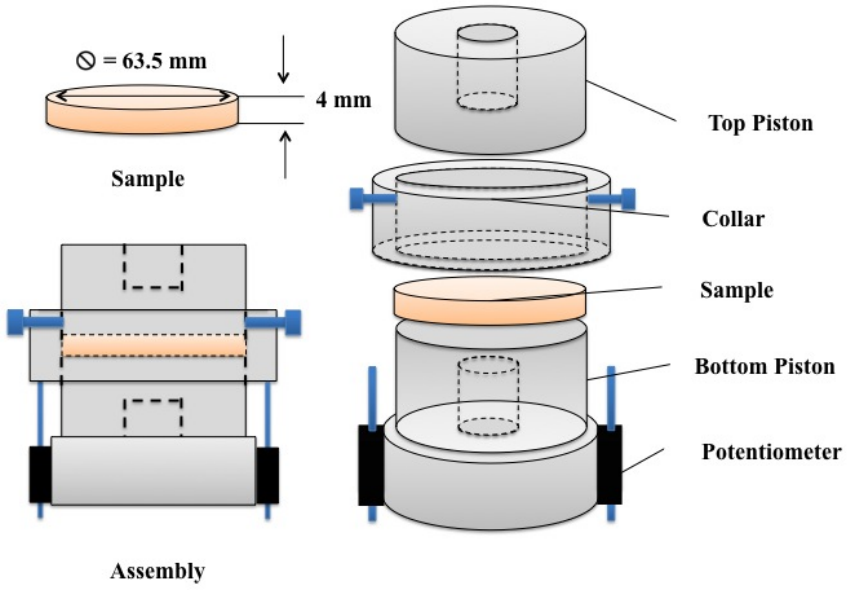

Figure 3.2: Schematic diagram shows the low-pressure test fixture

3.1.2 Measurement Procedure

Polymeric samples that are completely cured and have no defect are chosen for testing (see Chapter 2 for sample fabrication). The samples are prepared such that they have required shapes (see Figure. 3.2 for low-pressure test sample and Figures 3.3 and 3.6 for high-pressure test sample). Surfaces of the sample that will be in contact

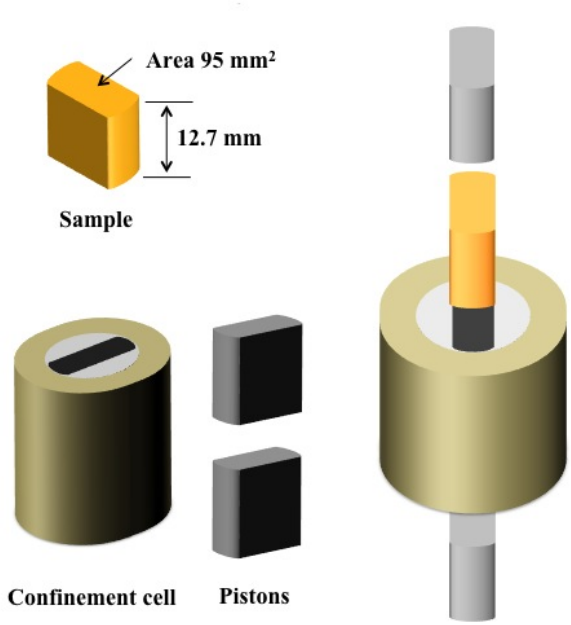

Figure 3.3: Schematic diagram shows the high-pressure test fixture

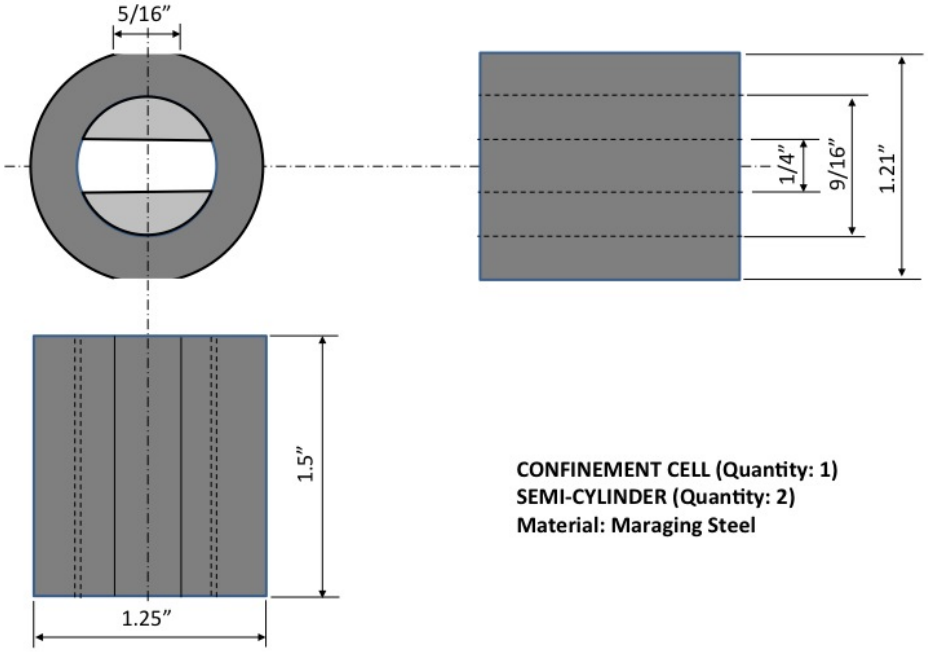

Figure 3.4: Drawing shows dimensions of the high-pressure confinement cell

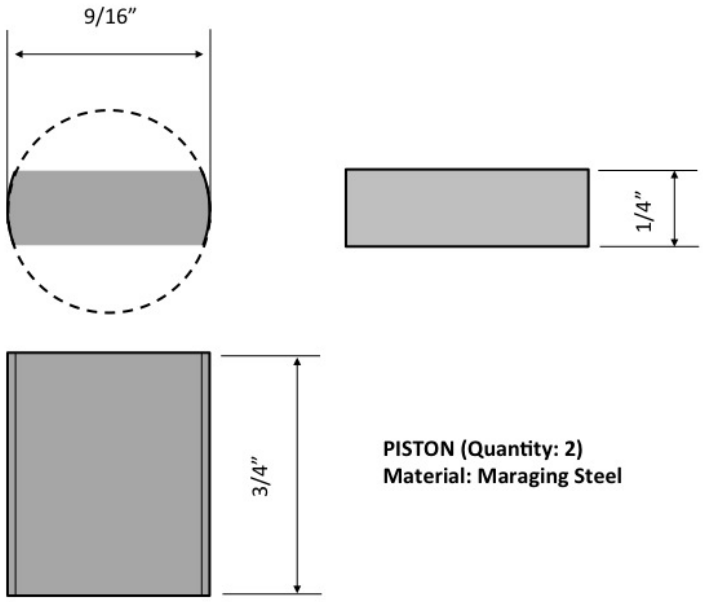

Figure 3.5: Drawing shows dimensions of the high-pressure piston

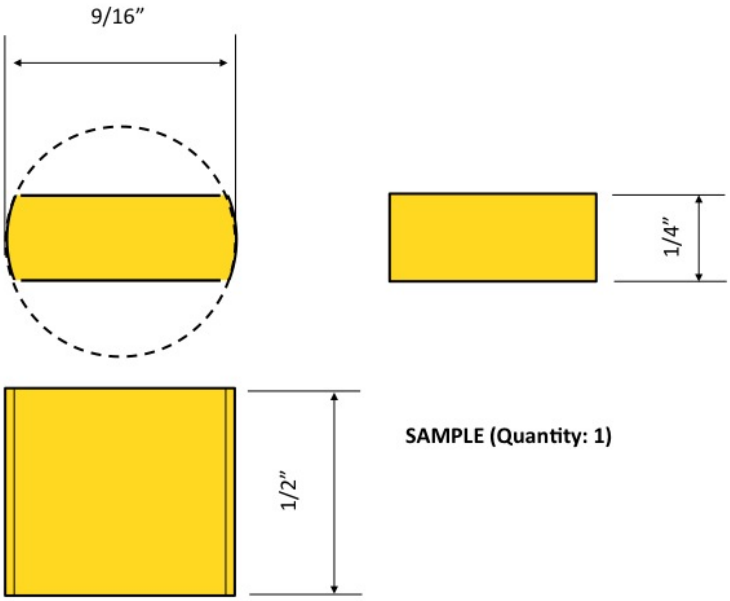

Figure 3.6: Drawing shows dimensions of the high-pressure test sample

with the surface of the piston are sanded to eliminate all invisible defects and to make sure that they are parallel. The macro-grit sandpaper (320 CAMI Grit designation) is, first, used to get rid of big defects and followed by the super-fine-grit-size sandpaper (600 CAMI Grit designation) at the end of sanding process. All dimensions of the ready-to-test samples are measured. The sample is then put into the test fixture, sitting between the loading pistons. The test fixture is then placed in environmental chamber and uniaxially aligned with the loading bar of the compression machine. A testing temperature is chosen. Then, the testing system is equilibrated under the testing temperature for an hour. After that the compressive load is applied normal to the surface of the sample at the loading rate of 15 lbf/s ($67\,\mathrm{N\,s^{-1}}$). Compressive force-time history is measured by loading cell. Axial displacement-time history is measured by two potentiometers in the low-pressure test (see Figure 3.2), while it is measured by the linear variable differential transformer (LVDT) of the Instron machine in the high-pressure test. The potentiometer has higher sensitivity than the LVDT so it is better for measuring small sample displacement in the low-pressure test. During test, both force and displacement are recorded in a text file for analysis. The stiffness of the machine is also measured through the same test procedure but without sample. At the same pressure, the measured strain from test with sample is subtracted by the strain of the machine from the test without sample. The resulting strain is the pure sample strains. The sample strain and coefficient of thermal expansion are later used to calculate the density of the sample at each pressure. After testing is finished. Stress and strain are calculated with equations 3.1 and 3.2 using force and displacement histories from tests with sample and without sample, thermal expansion coefficient, C_{TE} and initial dimensions of the sample measured before the test starts:

$$\sigma = P = \frac{F(t)}{A_o}, \tag{3.1}$$

$$\epsilon(T,P) = \frac{[d(P) - d(P=0)] - [d_m(P) - d_m(P=0)]}{h_o(1 + C_{TE}(T - T_o))}, \tag{3.2}$$

where σ and ϵ are engineering confined compressive stress and strain, $F(t)$ is the compressive force history, $d(P)$ and $d_m(P)$ are displacements from the tests with sample and without sample at pressure P, respectively, T and T_o are the testing and ambient temperatures, respectively, h_o and A_o are initial length and compression area, respectively. The compression area of the sample is constant because the sample is confined laterally. Due to the incompressible nature of polyurea and polyurea-based composites in this research, the confined compressive stress is referred to as pressure, P. Density of the sample can be calculated using:

$$\widetilde{\rho}(T,P) = \frac{\rho_o}{(1 + 3C_{TE}(T - T_o) + \epsilon(T,P))}, \tag{3.3}$$

where $\widetilde{\rho}$ and ρ_o are the measured and initial densities of the sample.

3.1.3 Results and Discussions

In this research, one of our goals is to create a low-density polyurea-based composite with pressure-invariant and low acoustic impedance (density times wave speed). The operating pressure range is from 0 to 10 MPa. The composite should be able to maintain its integrity with in this range. This composite will be used later as a component in a periodic layered composite which is designed for a submarine skin. In order to reduce the mass density, polyurea was mixed with two candidate filler

materials; (1) glass microballoon and (2) phenolic microballoon. The resulting composites are glass microballoon filled polyurea (PUGMB) and phenolic microballoon filled polyurea (PUPMB) composites. The dimensions and apparent densities of the filler materials are provide in Chapter 2.

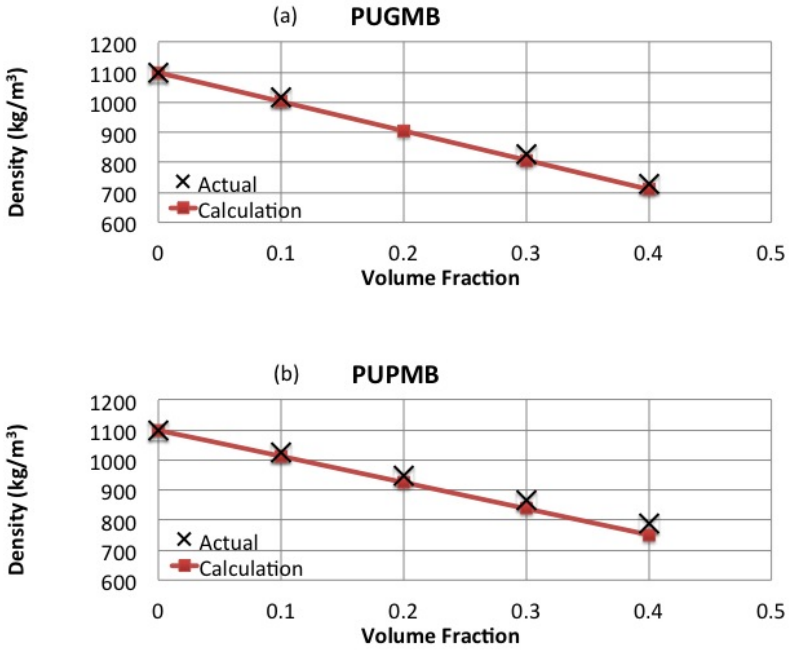

Figure 3.7: (a) Densities of PUGMB composites (b) Densities of PUPMB composites

The glass microballoon filled polyurea composite was first studied. The composites with 10%, 20%, 30%, and 40% volume fractions of glass microballoon were created. The densities of the composites are shown in Figure 3.7a. As we can see, the actual densities match very well with the calculated densities of the composites. As volume fraction increases, the density of the composite linearly decreases. At the maximum 40% volume fraction of glass microballoon, the density of the composite can be as low as $730\,\mathrm{kg\,m^{-3}}$. There is no data for 20% volume fraction due to that the sample has defect. PUGMB composites were then preliminarily tested under pressure

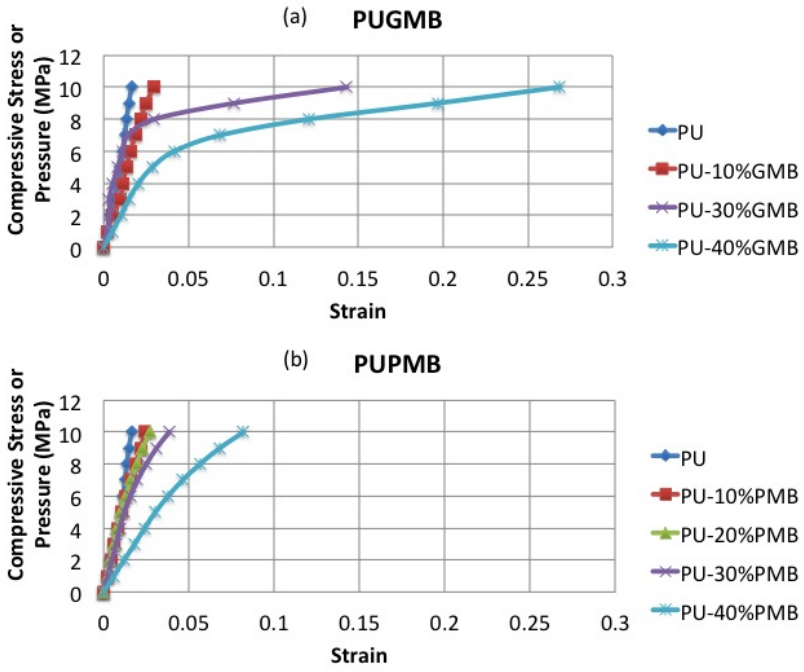

Figure 3.8: (a) Stress-strain curves of PUGMB composites (b) Stress-strain curves of PUPMB composites

from 0 to 10 MPa. The loading rate is very slow (67 N s^{-1} or 0.21 MPa s^{-1}) to make sure that the effect of strain rate is negligible. The stress-strain curves are shown in Figure 3.8a. To be noted, for this preliminary study, the contraction of samples is measured with LVDT of the Instron machine which is not quite accurate for small displacement. Later on, we improved our measurement by using potentiometer (see Figure 3.2). This is why the nonlinearity is observed at low pressure. However, these curve are good enough to reveal distinct behaviors of PU-30%GMB and PU-40%GMB composites. The PU-30%GMB is softening at around 8 MPa while the PU-40%GMB becomes softening around 6 MPa. This is due to that some of the glass microballoons are crushed. This is also confirmed by the plot between densities of the composites versus pressure (see Figure 3.9a). Similar to the stress-strain curves, the densities of PU-30%GMB and PU-40%GMB have sudden increases at around 8 and 6 MPa,

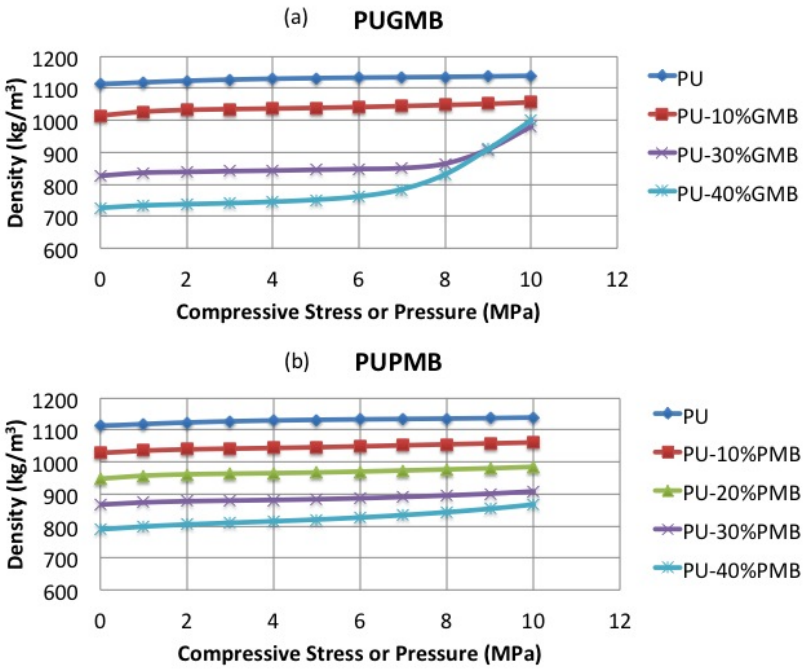

Figure 3.9: (a) Densities of PUGMB composites versus pressure (b) Densities of PUPMB composites versus pressure

respectively. It is worth noting that the type of the glass microballoon that we used has the lowest apparent density among all glass microballoon from 3M [32]. If we choose to try with thicker shell and higher strength microballoon, the density of the composite will be higher at the same volume fraction. After we found that the glass microballoon was crushed below 10 MPa, the phenolic microballoon filled polyurea composites were then studied.

The phenolic microballoon filled polyurea composites with 10%, 20%, 30%, and 40% volume fractions of phenolic microballoon were created. The reasons that we chose to try phenolic microballoon are that (1) it has density as low as the glass microballoon, (2) It is more flexible than the glass microballoon and it could possibly recover when the pressure is released, and (3) its price is cheaper than the glass microballoon. Figure 3.7b shows the density of the PUPMB compsites as a function

of volume fraction. Consider at the same volume fraction, the density of PUPMB is as low as that of PUGMB. Low pressure quasi-static test was preliminarily conducted on the PUPMB composites. As mentioned earlier, the contractions of samples in this preliminary studies were measured with LVDT of the Instron machine which is not accurate for small displacement. Later on, we improved our measurement by using two potentiometers (see Figure 3.2). Figure 3.8b shows the stress-strain curves of PUPMB composites. At high pressures (7-10 MPa), PUPMB composites tend to maintain their shapes better than PUGMB composite. Figure 3.9b shows densities of PUPMB composties versus pressure. It is apparent that densities of PU-10%PMB, PU-20%PMB, and PU-30%PMB do not change much within 0 to 10 MPa, while density of PU-40%PMB has significant increase between 4 and 10 MPa. This suggests that some phenolic microballons in PU-40%PMB might deform. However, the its deformation is less than that of glass microballoon.

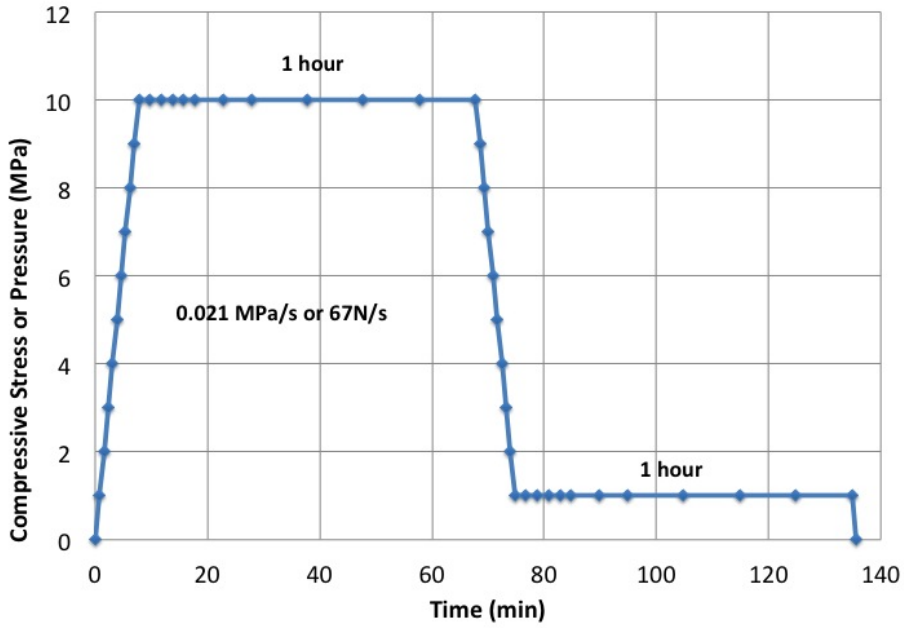

Figure 3.10: Load profile for low pressure test

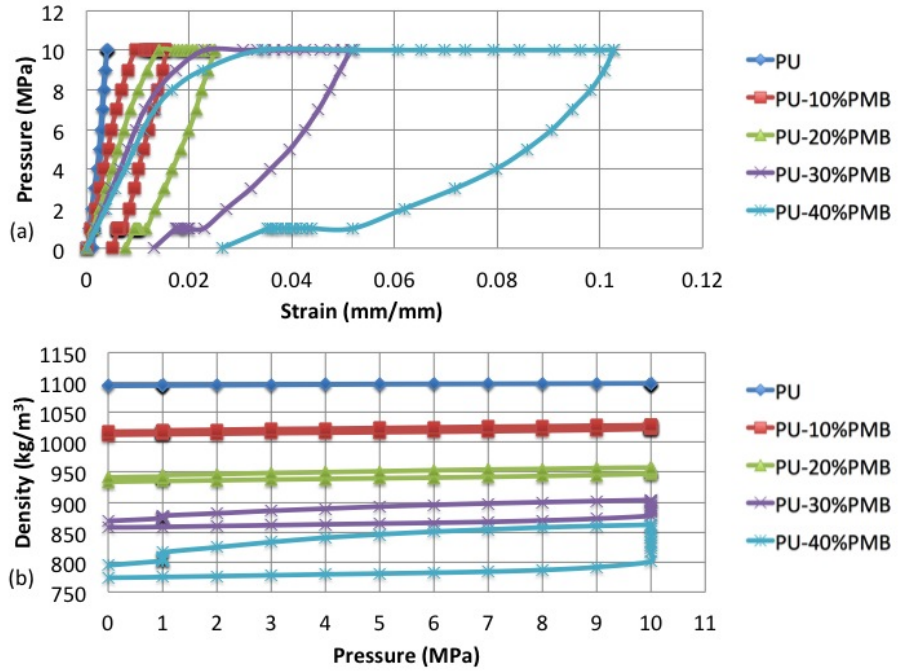

Figure 3.11: (a) Stress-strain curves of PUPMB composites (b) Densities of PUPMB composites versus pressure

From our observation, PUPMB composite has better ability to maintain its shape, compared to PUGMB. So we decided to perform thorough characterization on PUPMB composites. We fabricated new PUPMB samples with the same volume fractions as previous discussed. The low pressure quasi-static test was performed on the composites with the load profile shown in Figure 3.10. Pressure was increased from 0 to 10 MPa with the rate of 0.021 MPa s^{-1}. At 10 MPa, the pressure was kept constant for an hour to observe material's creep. Then pressure was decreased with the same rate. At 1 MPa, we kept pressure constant for another hour to observe material's recovery. All the dots on the curve are points where we performed ultrasonic wave measurement. The result of the ultrasonic measurement will be discussed in Section 3.3.4. In this test, the potentiometers were used, instead of LVDT, leading to the much higher accuracy of the measured strains of the samples. The stress-strain

curves of the PUPMB composites are shown in Figure 3.11a. With the pressure profile in Figure 3.10, it shows that while the pressure is kept constant at 10 MPa, all PUPMB composites have creeps. The higher the volume fraction, the larger the creep the composite has. This is also true for the recovery at 1 MPa. Both the creep and recovery are due to the deformation of the phenolic microballoon since there is no creep or recovery obsreved in the pure polyurea sample. When looking at density, it appears that only PU-40%PMB has significant change in density 10 MPa. Interestingly, after the recovery, all composites almost gain their initial densities.

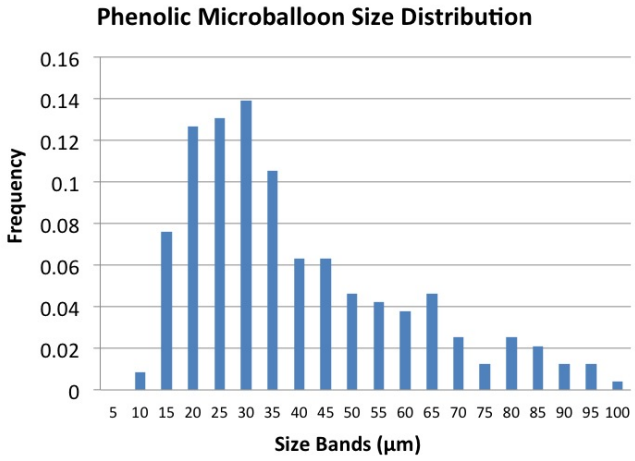

Figure 3.12: Size distribution of phenolic microballoon

From the creep and recovery that we observed, we wanted to know what is the crush pressure of the phenolic microballoon. The sizes of 237 phenolic microballoons were measured under a microscope. The size distribution is shown in Figure 3.12. The smallest diameter is 10 µm and the biggest is 100 µm. Mostly, the microballoon population (around 71%) falls in the range of 15 to 45 µm where the highest count frequency is at the diameter of 30 µm. It is found that the average diameter of the phenolic microballoon is 37 µm. From this observation, it implies that the nonlinearity

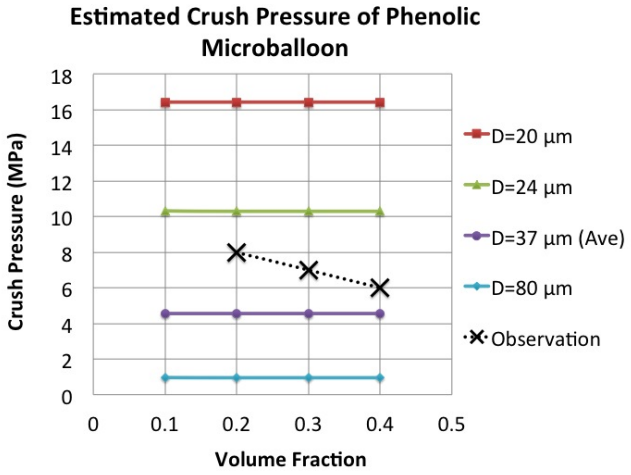

Figure 3.13: Crush pressure of phenolic microballoons

that we observed in the stress-strain curves of the PUPMB composites is due to the microballoons collaspe in succession from larger down to smaller sizes. The the crush pressures of various size of the microballoons were estimated and are shown in Figure 3.13. The estimated crush pressure were calculated based on the elastic buckling strength of spherical glass shells [33]. For calculation detail, please see appendix 3.A. As we can see, the crush pressure of the 37-μm-diameter microballoon is around 4.56 MPa which is below the observed crush pressures of 6,7 and 8 MPa for 0.2, 0.3, and 0.4 volume fractions, respectively. This underestimation might due to that in our estimation, we assume that he crush pressure is applied directly to the shell of microballoon (in other words, there is no polyurea matrix around the microballoon), while in reality the pressure is applied on to the polyurea matrix phase and some pressure might be supported by the matrix phase, thereby less pressure is transmitted to the microballoon. If we include the effect of the matrix phase that surrounds the microballoon, the estimated crush pressure of the microballoon would be higher and would not be flat as volume fraction of the microballoon changes. Importantly,

from this calculation, it suggests that If we can sieve out the microballoons that are larger than 25 µm and use only the smaller ones to fabricate PUPMB composites, the composites would be able to resist the pressure up to 10 MPa without damage of the microballoons. This will be our future work.

3.2 Dynamic Mechanical Analysis

Dynamic mechanical analysis (DMA) is a technique that is used to study the response of a material subjected to a harmonic force. In this research, it is restricted to the range of small-strain amplitude deformations. This technique can also be called as forced oscillatory measurement or dynamic mechanical thermal analysis (DMTA). Viscoelastic properties, such as modulus (stiffness) and damping (energy dissipation) of solid and soft solid materials can be measured using this technique. Moreover, it can be used to locate the glass transition temperature of polymeric materials, as well as to identify transitions corresponding to other molecular motions. Figure 3.14 shows transitions in polymeric materials, which can be seen as changes in the storage modulus E' [34].

3.2.1 Background

DMA is used to measure complex stiffness and damping of polymers. They are reported as storage and loss moduli for complex stiffness and $\tan\delta$ for damping. A sinusoidal force (or displacement) is applied to a sample with specific dimensions. The machine measures displacement (or force) of the sample and calculates stress, strain, and the phase shift between the measured stress and strain, using the input force (or displacement) and dimensions of the sample. The measured sinusoidal stress

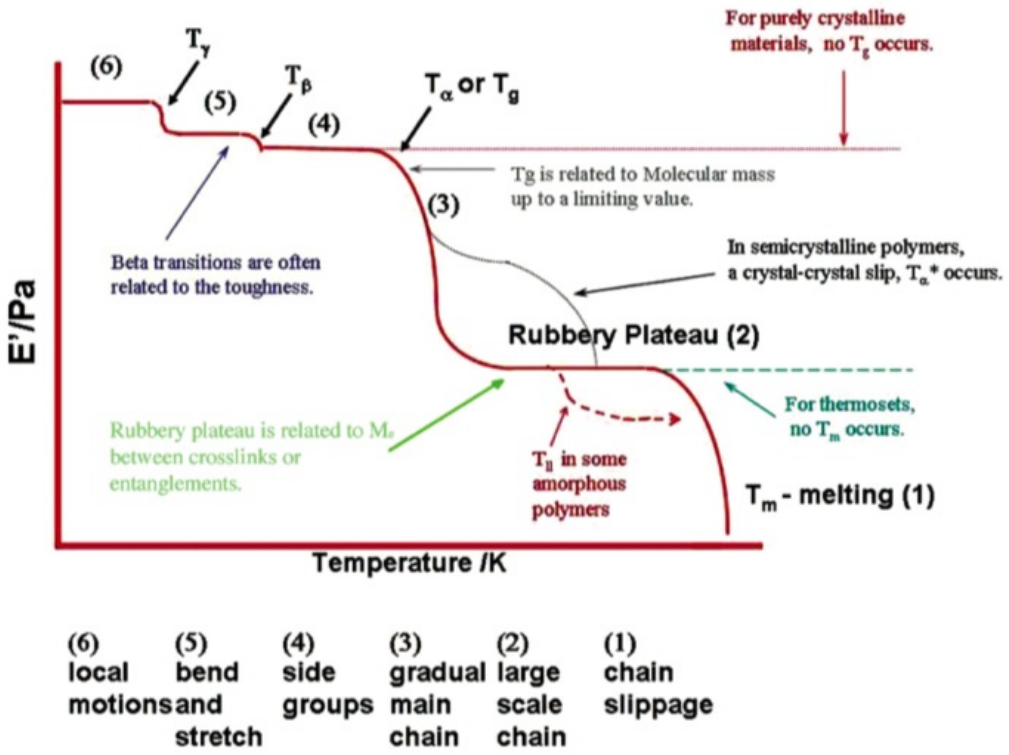

Figure 3.14: Storage modulus E' versus temperature and transitions in polymeric materials [34]

variation in time is usually described as a rate specified by the frequency f or angular frequency ω. The measured strain of a polymer is generally out of phase with the stress, by the phase shift angle, δ. This phase lag is due to the excess time necessary for molecular motions and relaxations to occur. The dynamic stress, σ, and strain, ϵ, can be written as:

$$\sigma(t) = \sigma_o e^{i(\omega t+\delta)}, \tag{3.4}$$

$$\epsilon(t) = \epsilon_o e^{i(\omega t)}, \tag{3.5}$$

where σ_o and ϵ_o are the measured stress and strain amplitudes. To be noted, complex form is used to simplify calculation. In general, only real parts of the stress and strain

have physical meaning. The complex modulus, E^* can be calculated as:

$$E^* = \frac{\sigma}{\epsilon} = \frac{\sigma_o}{\epsilon_o} e^{i\delta} = \frac{\sigma_o}{\epsilon_o} \left(\cos\delta + i \sin\delta\right). \tag{3.6}$$

The real and imaginary parts of the complex modulus are refered to as storage and loss moduli, respectively. They are given as:

$$E^* = E' + iE'', \tag{3.7}$$

$$E' = \frac{\sigma_o}{\epsilon_o} \cos\delta, \tag{3.8}$$

$$E'' = \frac{\sigma_o}{\epsilon_o} \sin\delta, \tag{3.9}$$

where E' and E'' are storage and loss moduli, respectively. Equation 3.7 shows that the complex modulus obtained from DMA consists of storage and loss moduli. The storage modulus describes the ability of the material to store and release potential energy during deformation. The loss modulus is associated with energy dissipation in the form of heat upon deformation. The ratio of the loss to the storage is the $\tan\delta$ and is often called damping. It can be represented as:

$$\tan\delta = \frac{E''}{E'}. \tag{3.10}$$

It is a measure of the energy dissipation of a material. Figure 3.15 shows the DMA stress and strain for different types of materials. For ideal elastic solids, the stress

and strain will be in phase ($\delta = 0$). For ideal viscous liquids, the stress will lead the strain by $\pi/2$. For a viscoelastic materials, the phase angle will lie somewhere between 0 to $\pi/2$.

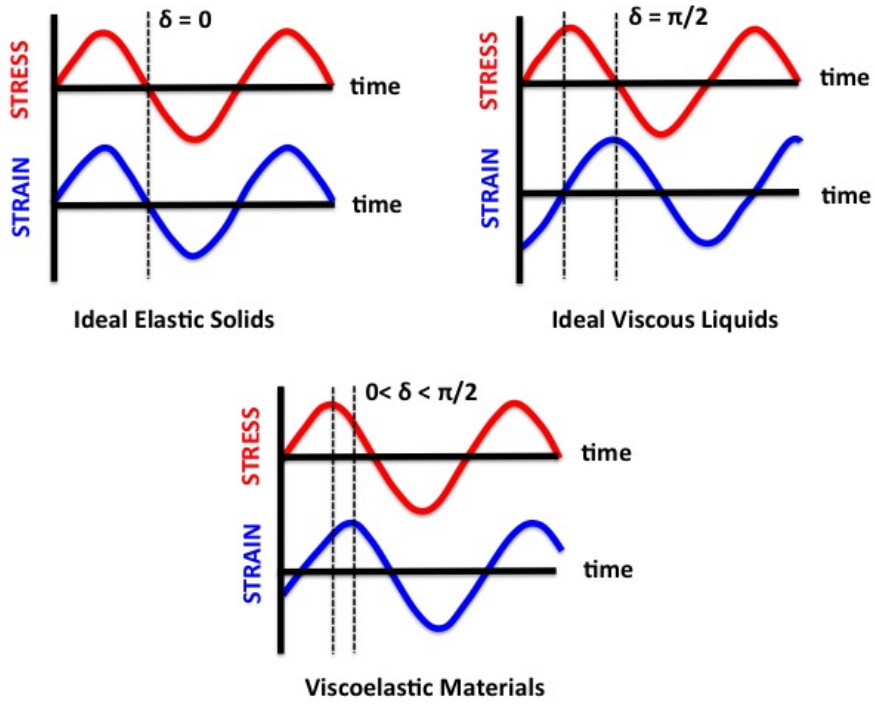

Figure 3.15: DMA stress and strain for different types of materials

3.2.2 Experimental Setup

Dynamic mechanical analysis is performed using the TA Instrument Dynamic Mechanical Analyzer 2980. Figure 3.16 shows DMA 2980 model. This model operates over a temperature range of $-145\,^{\circ}\mathrm{C}$ to $600\,^{\circ}\mathrm{C}$, using heating rates up to $50\,^{\circ}\mathrm{C}/\,\mathrm{min}$. It can determine changes in sample properties resulting from changes in temperature, time, frequency, force, and strain. Samples can be in bulk solid, film, fiber, gel, or viscous liquid form. For detail of components of the machine, please see [35].

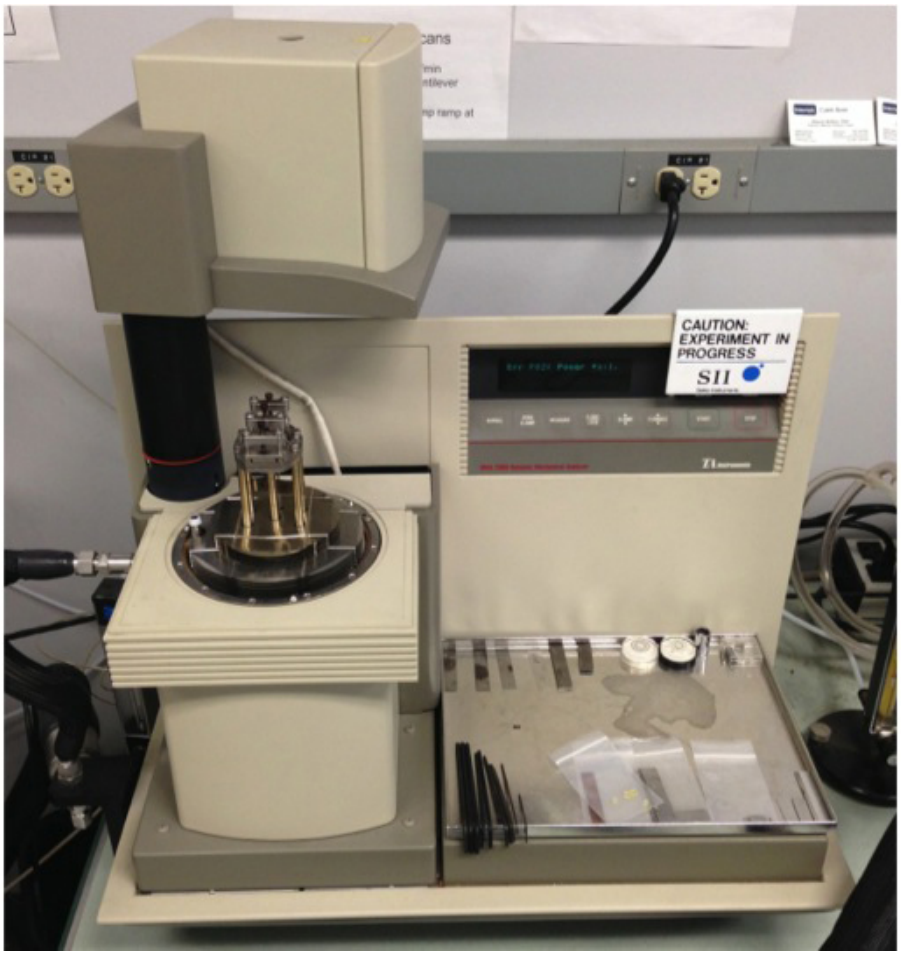

Figure 3.16: Dynamic Mechanical Analysis Model 2980 from TA instrument

This machine comes with interchangeable clamps for various dynamic tests. In this research, single-cantilever clamp is used (see Figure 3.17). The required dimension of the sample for this clamp can be calculated using the following equation and the chart in Figure 3.18 [35]:

$$GF = \frac{1}{F}\left[\frac{L^3}{12I} + 2S\left(1+\nu\right)\frac{L}{A}\right], \tag{3.11}$$

$$A = WT, \tag{3.12}$$

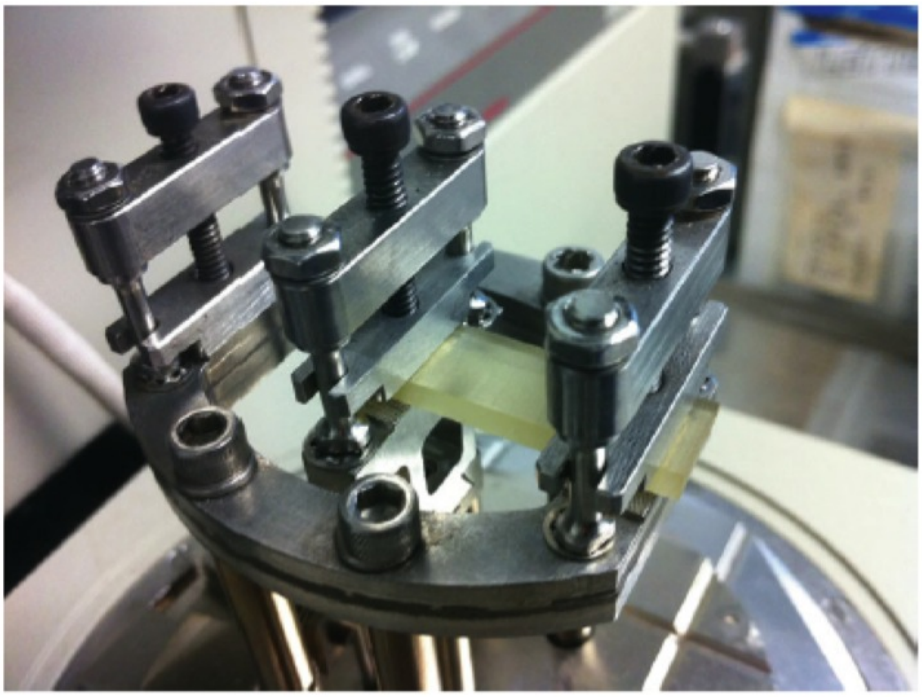

Figure 3.17: Single cantilever clamp for Dynamic Mechanical Analysis Model 2980

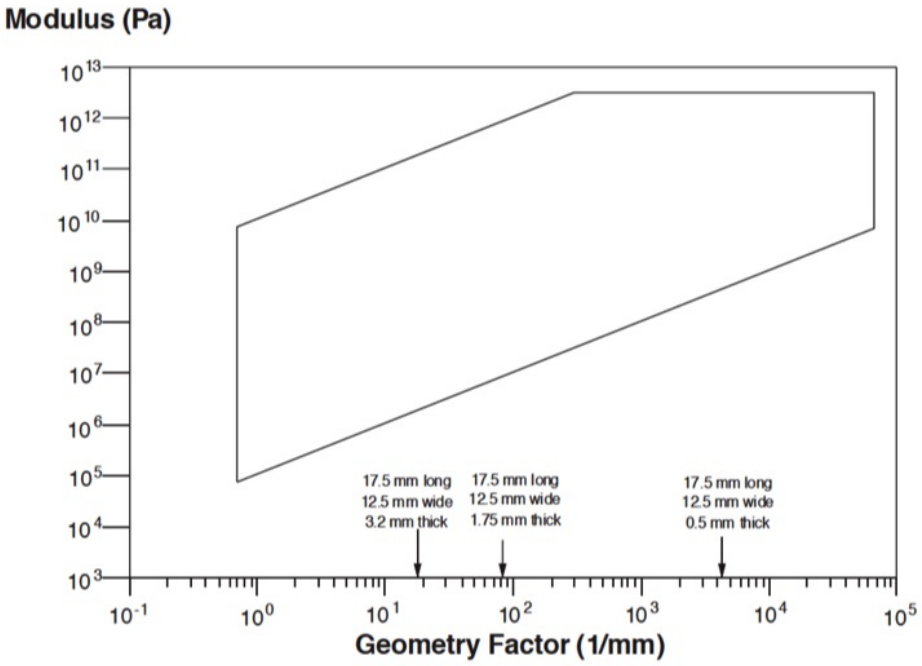

Figure 3.18: Modulus vs Geometry Factor Chart [35]

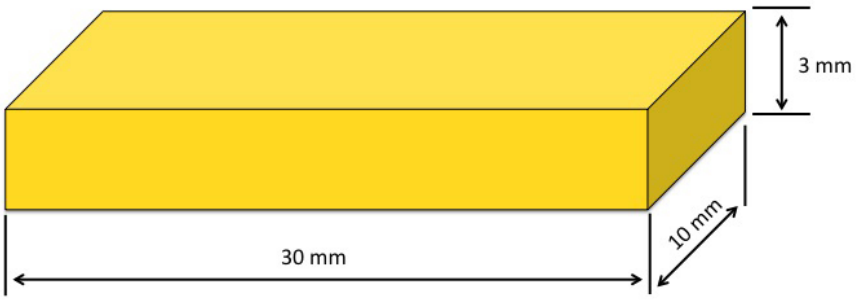

Figure 3.19: Dimension of the sample for single cantilever test

$$I = \frac{1}{12} W T^3, \tag{3.13}$$

where GF is geometry factor in Figure 3.18, L, W, and T are length, width, and thickness of the sample in mm, respectively, A is sample cross sectional area in mm^2, I is geometric moment in mm^4, F and S are clamping and shearing factors (nominally 0.9 and 1.5, respectively), ν is Poisson's ratio of the sample (nominally 0.44). For polyurea and polyurea-based composites in this research, the dimension of the test sample is 30 mm X 10 mm X 3 mm.

3.2.3 Measurement Procedure

Before testing, clamp, position, and instrument calibrations need to be done. Please see [35] for procedures. During the test, the sample is clamped at both ends with a free length of 17.5 mmin between the clamps. One end of the sample is fixed, and the other end is attached to the movable clamp (center clamp see Figure 3.17), which moves sinusoidally normal to the length of the sample with the chosen amplitude of 15 µm. The experiments are performed over the temperature range from −80 °C to 70 °C, with increments of 3 °C. Liquid nitrogen is used to cool the system

down to sub-ambient temperatures. At each temperature step, five frequencies of 20 Hz, 10 Hz, 5 Hz, 2 Hz, and 1 Hz are tested sequentially. The thermal soaking time is 3 minutes for each temperature point. One complete test with this protocol takes about 4.5 hours on TA 2980. After the test is finished, DMA data are collected using the corresponding TA data analysis software (see Figure 3.20).

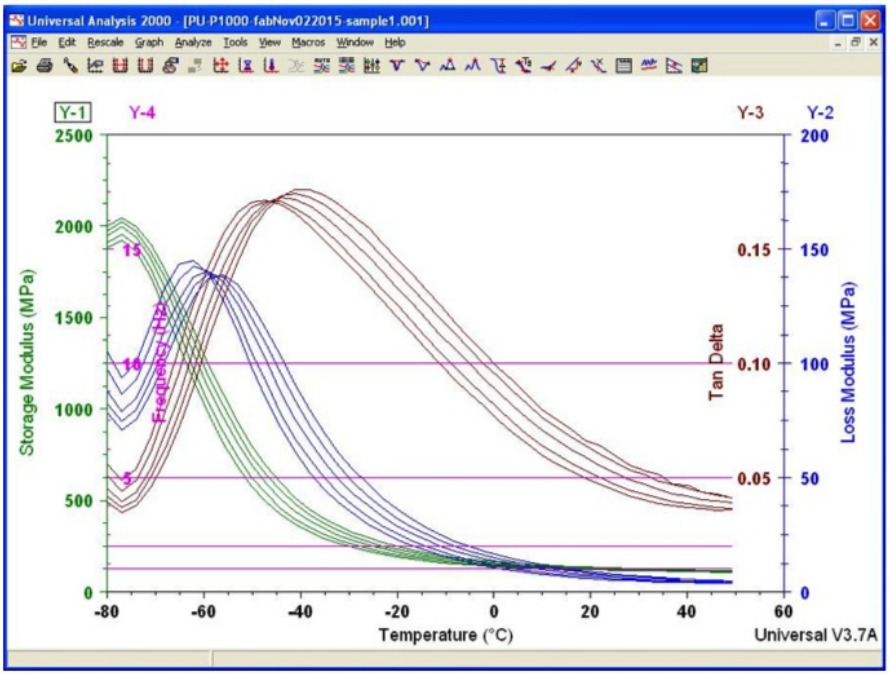

Figure 3.20: TA Universal Analysis Software

3.2.4 Results and Discussions

Please see section 3.4

3.3 Ultrasonic Wave Measurement

Ultrasonic wave or ultrasound is a sound pressure wave with the frequency higher than upper limit of human hearing capability (average 18 kHz). The use of

ultrasound covers large range of frequency, from 20 kHz up to several GHz. Ultrasonic wave measurement is used widely as a non-destructive testing technique for detection of defects, cracking, pores and etc. It is also well suited for determining the viscoelastic properties of polymeric materials [36]. When an acoustic wave propagates in the materials, the particles in the materials are forced to vibrate around their equilibrium positions. For crystalline materials, which are nearly elastic, their mechanical moduli are real numbers and proportional to the squares of speeds of sound in the materials. For the viscoelastic materials, the energy of the wave is dissipated during the propagation. Most of the dissipated energy is converted into heat. The amplitude of the wave becomes smaller as the wave propagates further in the viscoelastic materials. The mechanical moduli of such materials are no longer enough to be described with real number. The modulus of a viscoelastic material must be computed from the relation involving wave speed and attenuation [36, 37]. Similar to DMA, the viscoelastic modulus of a viscoelastic material can be expressed as a complex modulus where its real part is related to the elastic portion of the material and its imaginary part is associated with the viscous portion.

3.3.1 Background

Ultrasound uses mechanical wave, which requires a medium for the transfer of energy to occur, to make measurement. The particles in the medium will, in general, oscillate as the wave propagates through. For elastic materials, the motion of the particles can be imagined as the motion of a mass-spring system in which the mass is subjected to a linear elastic force governed by Hooke's law. The displacement of the particle can be found by solving, in this case, elastic wave equation [38]. The

simplest case is the one-dimensional wave equation. The displacement of the particle can be perpendicular or parallel to the propagation direction of the wave. The term “Longitudinal wave" is used to describe the wave in which the displacement of the medium is in the same direction as, or the opposite direction to, the direction of the traveling wave, while “shear wave" describes the wave in which the displace of the medium are at right angles to the direction of the propagation of the wave. The one-dimensional elastic wave propagation in x direction can be expressed as follows:

$$M\frac{\partial^2 u}{\partial x^2} = \rho\frac{\partial^2 u}{\partial t^2}, \tag{3.14}$$

where u is the displacement of particle, M is the elastic modulus of the medium, ρ is the mass density of the medium. The wave speed or phase velocity (c_o) in the medium can be calculated as:

$$c_o = \sqrt{\frac{M}{\rho}}. \tag{3.15}$$

The harmonic solution of equation 3.14 is:

$$u = u_o e^{i\omega\left(t-\frac{x}{c_o}\right)} = u_o e^{i(\omega t - kx)}, \tag{3.16}$$

where

$$k = \frac{2\pi}{\lambda}, \tag{3.17}$$

$$c_o = \frac{\omega}{k}, \tag{3.18}$$

u_o is displacement amplitude, f and ω are frequency and angular frequency, k is wave number, λ is wavelength. For elastic media, all parameters used in equations 3.14 -

3.18 are real numbers. In the case of viscoelastic media, the wave loses its energy during propagation. This results in the reduction in amplitude (attenuation). The motions of particles can, no longer, be modeled as the energy-conserved mass-spring system. Normally, the dashpot is added into the system to represent where the energy is converted into heat. The one-dimensional wave equation 3.14, and the wave speed equation 3.15 need to be modified for the case of wave propagation in a viscoelastic medium as follows [20, 37]:

$$M^* \frac{\partial^2 u}{\partial x^2} = \rho \frac{\partial^2 u}{\partial t^2}, \tag{3.19}$$

$$c^* = \sqrt{\frac{M^*}{\rho}}, \tag{3.20}$$

where M^* is the complex modulus of the viscoelastic medium, c^* is the complex wave speed. c^* and M^* can be expressed as:

$$c^* = c' + ic'', \tag{3.21}$$

$$M^* = M' + iM'', \tag{3.22}$$

where

$$M' = \rho \left(c'^2 - c''^2 \right), \tag{3.23}$$

$$M'' = 2\rho c' c'', \tag{3.24}$$

c' and c'' are real and imaginary parts of the complex wave speeds, M' and M'' are storage and loss moduli of the viscoelastic medium. The solution of equation 3.19 is in the following form:

$$\begin{aligned} u &= u_o e^{i\omega\left(t-\frac{x}{c^*}\right)} \\ &= u_o e^{i(\omega t)} e^{-i\left(\frac{\omega x}{c'+ic''}t\right)} \\ &= u_o e^{i(\omega t)} e^{-i\left(\frac{\omega c' x}{c'^2+c''^2}\right)} e^{-\left(\frac{\omega c'' x}{c'^2+c''^2}\right)}. \end{aligned} \tag{3.25}$$

An attenuated harmonic wave in a viscoelastic material can be represented with a mathematic equation as:

$$u = u_o e^{i(\omega t)} e^{-i\left(\frac{\omega x}{c}\right)} e^{-(\alpha x)}, \tag{3.26}$$

where c is the measured wave speed in the viscoelastic material, α is the measured attenuation. Equate equations 3.25 and 3.26, the real and imaginary parts of the complex wave speed are given by:

$$c' = \frac{c}{1+r^2}, \tag{3.27}$$

$$c'' = \frac{cr}{1+r^2}, \tag{3.28}$$

where

$$r = \frac{\alpha c}{\omega}, \tag{3.29}$$

r is the dimensionless parameter. Substitute equations 3.27, 3.28 into equations 3.23 and 3.24, we arrive at:

$$M' = \frac{\rho c^2 \left(1 - r^2\right)}{\left(1 + r^2\right)^2}, \tag{3.30}$$

$$M'' = \frac{2\rho c^2 r}{\left(1 + r^2\right)^2}. \tag{3.31}$$

The loss modulus, M'' measures how much energy would be dissipated as heat when the wave propagates through the material, while the storage modulus, M' measures how much energy would be stored. Another parameter commonly used to describe the energy damping of the material is:

$$\tan \delta = \frac{M''}{M'} = \frac{2r}{1 - r^2}. \tag{3.32}$$

It is defined the ratio of the energy dissipated per cycle to the potential energy stored during a cycle. For ultrasonic wave measurement, there are two wave modes; longitudinal and shear, which can be generated, using longitudinal and shear transducers, respectively. For longitudinal wave mode, the complex modulus M^* can be replaced by the complex longitudinal modulus, L^* or complex shear modulus, G^* for shear wave mode. The diameters of the specimens for both shear and longitudinal modes are much larger than its thickness to avoid the interferences from the reflected waves from the edges of the specimens. To make sure that all reflected waves in the specimen will not interfere the first transmitted wave, the thickness of the specimen should be at least one wavelength long at the frequency of interest.

Table 3.1: Relations of viscoelastic moduli

	K^*	E^*	G^*	ν^*	L^*
(K^*, E^*)	K^*	E^*	$\frac{3K^*E^*}{9K^*-E^*}$	$\frac{3K^*-E^*}{6K^*}$	$\frac{3K^*(3K^*+E^*)}{9K^*-E^*}$
(K^*, G^*)	K^*	$\frac{9K^*G^*}{3K^*+G^*}$	G^*	$\frac{3K^*-2G^*}{2(3K^*+G^*)}$	$K^* + \frac{4G^*}{3}$
(K^*, ν^*)	K^*	$3K^*(1-2\nu^*)$	$\frac{3K^*(1-2\nu^*)}{2(1+\nu^*)}$	ν^*	$\frac{3K^*(1-\nu^*)}{1+\nu^*}$
(K^*, L^*)	K^*	$\frac{9K^*(L^*-K^*)}{3K^*+L^*}$	$\frac{3(L^*-K^*)}{4}$	$\frac{3K^*-L^*}{3K^*+L^*}$	L^*
(E^*, G^*)	$\frac{E^*G^*}{3(3G^*-E^*)}$	E^*	G^*	$\frac{E^*}{2G^*} - 1$	$\frac{G^*(4G^*-E^*)}{3G^*-E^*}$
(E^*, ν^*)	$\frac{E^*}{3(1-2\nu^*)}$	E^*	$\frac{E^*}{2(1+\nu^*)}$	ν^*	$\frac{E^*(1-\nu^*)}{(1+\nu^*)(1-2\nu^*)}$
(G^*, ν^*)	$\frac{2G^*(1+\nu^*)}{3(1-2\nu^*)}$	$2G^*(1+\nu^*)$	G^*	ν^*	$\frac{2G^*(1-\nu^*)}{1-2\nu^*}$
(G^*, L^*)	$L^* - \frac{4G^*}{3}$	$\frac{G^*(3L^*-4G^*)}{L^*-G^*}$	G^*	$\frac{L^*-2G^*}{2L^*-2G^*}$	L^*
(ν^*, L^*)	$\frac{L^*(1+\nu^*)}{3(1-\nu^*)}$	$\frac{L^*(1+\nu^*)(1-2\nu^*)}{1-\nu^*}$	$\frac{L^*(1-2\nu^*)}{2(1-\nu^*)}$	ν^*	L^*

3.3.2 Experimental Setup

Acoustic wave in ultrasonic range is used to determine the dynamic response of materials in the frequency range of 0.5 to 1.5 MHz. To completely characterize mechanical properties of isotropic elastic (or viscoelastic) materials, at least two elastic (or viscoelastic) parameters are required. The other parameters, in general, can be calculated from the two known parameters (see Table 3.1). In this section, the longitudinal and shear moduli of materials are measured through ultrasonic-longitudinal- and ultrasonic-shear-wave measurements, respectively. For ultrasonic longitudinal wave measurement, the longitudinal transducers which create longitudinal vibration mode are required. In this longitudinal mode, the particles in a tested material are forced to vibrate parallel to the wave propagation direction. For ultrasonic shear wave measurement, the transducers which generate transverse vibration mode are required. In this mode, the particles in the tested material are forced to vibrate perpendicular to the wave propagation direction. In general, these two measurements have almost the same equipment and measurement procedure except for the types of transducers

as previous mentioned. However, due to the unique characteristic of shear wave, complexity of the ultrasonic shear wave measurement occurs and will be discussed later on.

Ultrasonic Longitudinal Wave Measurement

Direct contact measurement is used to measure the speed of longitudinal wave in the viscoelastic materials. The experimental setup consists of a desktop computer containing a Matec TB-1000 Toneburst Card, two Panametrics videoscan longitudinal transducers (V103 Panametrics-NDT OLYMPUS), an 100:1 attenuator box, and a digital Oscilloscope. As shown in Figure 3.21, a toneburst signal with a nominal frequency is sent from the card to the attenuator box where the signals in voltage form are attenuated so that the signals would be able to be shown on the oscilloscope's screen and to the generating transducer through BM-174-3 cable where the measurement is performed. The received signal is sent directly to the oscilloscope and displayed on the oscilloscope where the amplitude and travel time are measured.

The specially designed test fixture for ultrasonic longitudinal wave measurement is used to align and hold the sample and transducers together (see Figure 3.22). The samples for ultrasonic longitudinal wave measurement are made carefully. Their thicknesses are bigger than one wavelength at the testing frequency so that the transmitted and reflected longitudinal waves are separated apart and can be distinguished easily. The assembly of the test fixture and sample dimensions are shown in Figure 3.22.

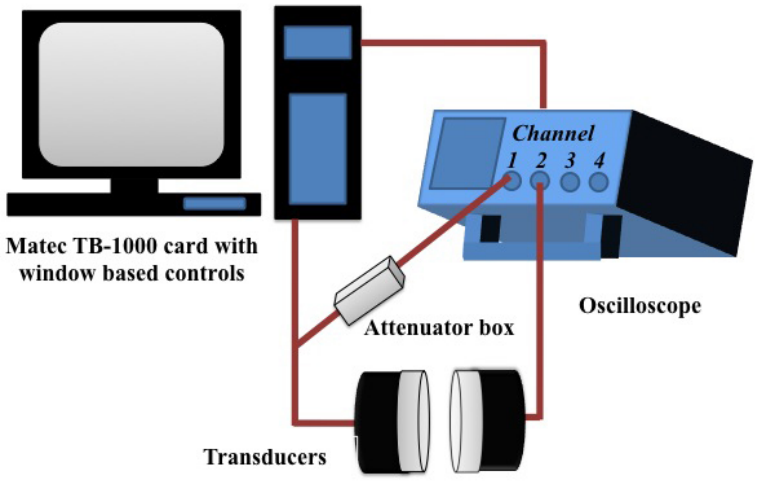

Figure 3.21: Schematic diagram shows ultrasonic wave measurement equipment

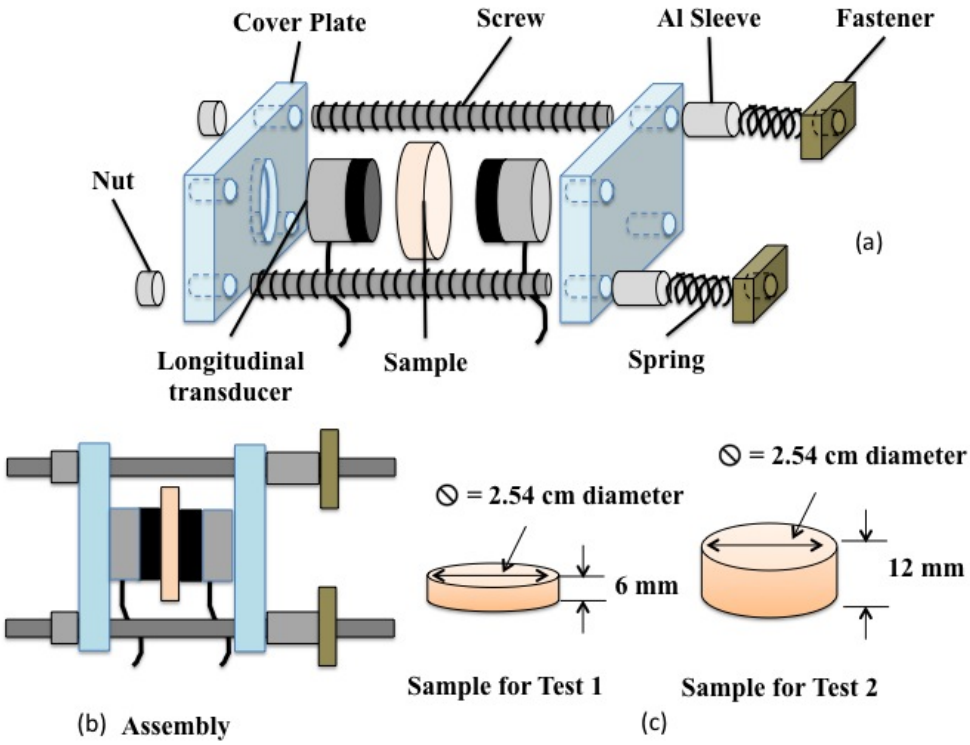

Figure 3.22: Schematic diagram shows (a) the components of the test fixture for ultrasonic longitudinal wave measurement (b) assembly of the test fixture (c) sample dimensions

Ultrasonic Shear Wave Measurement

The previously described setup for longitudinal wave measurement is used with shear transducers (V153 Panametrics-NDT OLYMPUS) instead of longitudinal transducers. Due to an unavoidable coupled longitudinal wave signal generated by the shear transducers, an aluminum rod is inserted between the generating transducer and the sample to delay the shear wave, separating it from the longitudinal wave (see Figure 3.23). Wave speed and attenuation of the shear wave are calculated after two tests (with samples of different thicknesses) are conducted. Shear wave couplant is applied to all interfaces to get better surface contact. Similar to longitudinal wave testing, shear wave tests are conducted at 1MHz and -50 to 50 °C with 10 °C increments. The speed of shear wave and its attenuation are used to calculate storage and loss shear moduli of the tested materials. The samples are made carefully. We have to ensure that their thicknesses are bigger than half of the wavelength so that the transmitted and reflected shear waves are separated apart and can be distinguished easily. However, the shear wave is very dissipative. Special care is needed when considering the thickness of the samples. In this test on polyurea, the assembly and sample dimensions are shown in Figure 3.23.

Low-Pressure Ultrasonic Longitudinal/Shear Wave Measurement

The low pressure test fixture discussed previously (see Figure 3.2) is integrated with the ultrasonic measurement apparatus shown in Figure 3.21 for conducting ultrasonic longitudinal/shear wave measurement at low pressure (0-20 MPa). Figure 3.24 shows the test fixture and samples for low-pressure ultrasonic longitudinal and shear wave measurements. The force-displacement and temperature control unit shown in

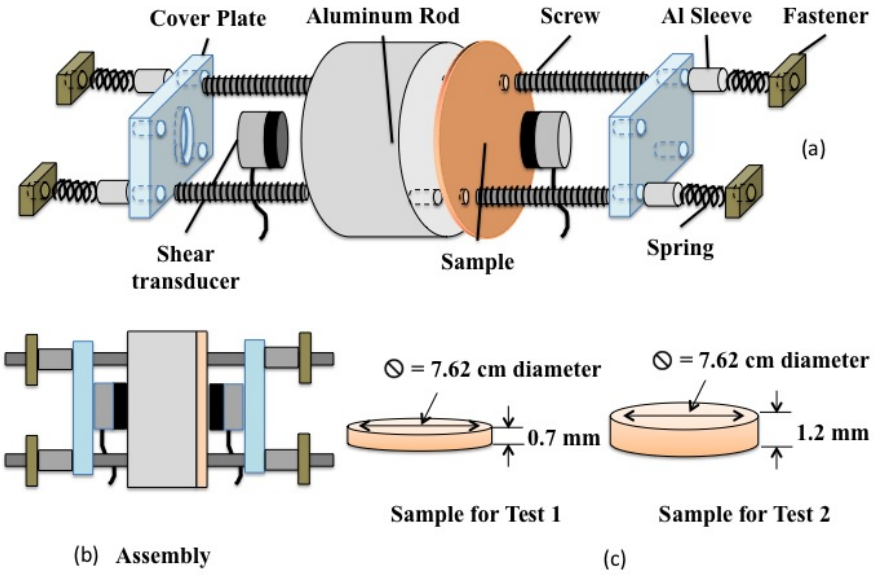

Figure 3.23: Schematic diagram shows (a) the components of the test fixture for ultrasonic shear wave measurement (b) assembly of the test fixture (c) sample dimensions

Figure 3.1 is used to equilibrate and compress the test sample to the desired testing temperature and pressure. The potentiometer attached on the test fixture (see Figure 3.24) measures the contraction of the sample during the test. The contraction will be used later to calculate density of the sample at the corresponding testing condition.

High-Pressure Ultrasonic Longitudinal Wave Measurement

The high pressure test fixture discussed previously (see Figure 3.3) is integrated with the ultrasonic measurement apparatus shown in Figure 3.21 for conducting ultrasonic longitudinal/shear wave measurement at high pressure (50-1000 MPa). Figure 3.25 shows the test fixture and samples for high-pressure ultrasonic longitudi-

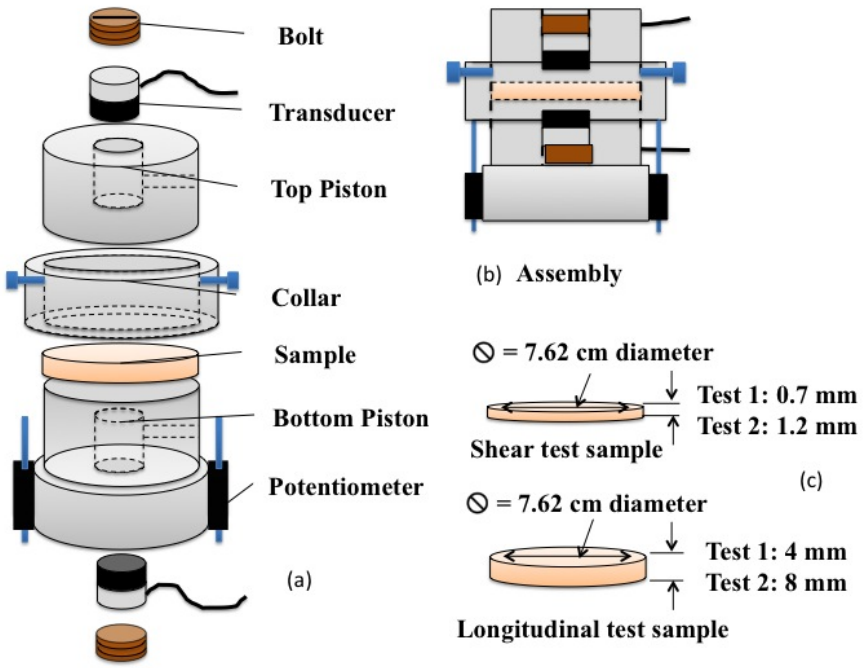

Figure 3.24: Schematic diagram shows (a) the components of the test fixture for low pressure ultrasonic longitudinal/shear wave measurement (b) assembly of the test fixture (c) sample dimensions

nal wave measurement. The force-displacement and temperature control unit shown in Figure 3.1 is used to equilibrate and compress the test sample to the desired testing temperature and pressure and also to measure the contraction of the sample during the test. The contraction will be used later to calculate density of the sample at the corresponding testing condition. For high pressure range, it is difficult to perform ultrasonic shear measurement using the same test fixture that is designed for longitudinal wave measurement since the thickness of the test sample is too thick such that the received shear wave signal becomes too small for measuring and observing with the oscilloscope. In this study, we will focus only on high pressure ultrasonic longitudinal wave measurement.

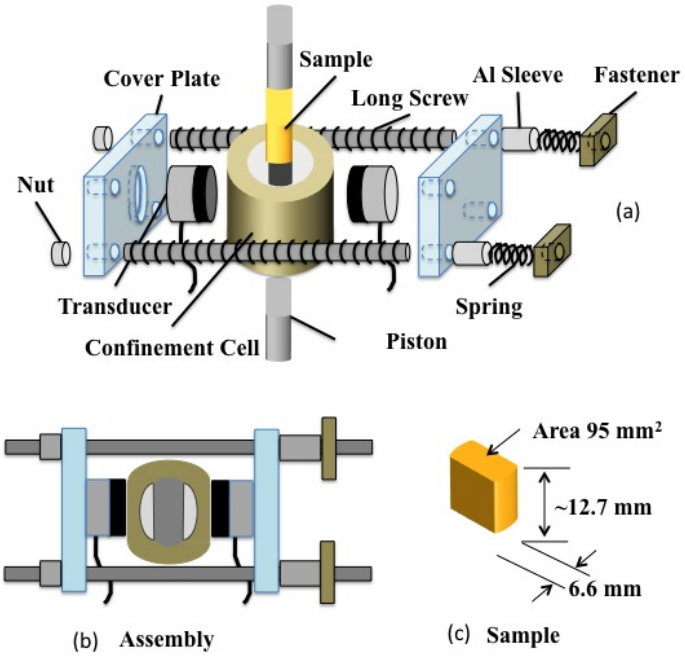

Figure 3.25: Schematic diagram shows (a) the components of the test fixture for high pressure ultrasonic longitudinal/shear wave measurement (b) assembly of the test fixture (c) sample dimensions

3.3.3 Measurement Procedure

To find wave speed and attenuation of longitudinal (or shear) wave at ambient pressure, two tests need to be performed using two different sample thicknesses. The specially designed test fixture is used to align and hold the sample and transducers together (see Figure 3.22 for longitudinal wave measurement and Figure 3.23 for shear wave measurement). The longitudinal wave (or shear wave) couplant is applied to all contact surfaces between the transducer and the sample. Tests are conducted at 0.5 to 1.5 MHz with 0.5 MHz increments and -50 to 50 °C with 10 °C increments. From observation, polyurea and polyurea-based composites in this research are quite insensitive to frequency within 0.5 to 1.5 MHz. So the result at 1 MHz is generally used as the representative for the frequency range. The speed of longitudinal wave (or

shear wave) is determined by measuring the difference between the times of travels through two samples of different thicknesses. By subtracting the results from the two tests, interfacial problems and time lags in the system are assumed to cancel out. Sample in each of the two tests is sandwiched between a pair of longitudinal transducers (or shear transducers) and is tested at the same environmental condition. The attenuation is measured using the transmitted wave amplitudes of these two tests. The mass densities of the samples are first measured and averaged before the test starts. The measured wave speed, attenuation, and average mass density at each temperature are used to calculate longitudinal (or shear) storage and loss moduli of the tested materials. With the known geometry of sample, the mass density, ρ of a sample can be calculated by:

$$\rho = \frac{m}{V}, \tag{3.33}$$

where m and V ave mass and volume of the sample. The wave speed, c in the equations 3.29, 3.30, and 3.31 is calculated by:

$$c = \frac{h_2 - h_1}{t_f}, \tag{3.34}$$

where h_1 and h_2 are thicknesses of the samples in test 1 and 2, respectively, t_f is the time of flight (see Figure 3.26). The attenuation, α in equation 3.29 can be calculated by:

$$\alpha = \frac{1}{h_2 - h_1} \ln \frac{A_1}{A_2}, \tag{3.35}$$

where A_1 and A_2 are amplitudes of the waves traveling through the samples in test 1 and 2, respectively (see Figure 3.26). If the wave speed, c and attenuation, α are calculated from the longitudinal wave measurement, the storage and loss moduli (M'

and M'') calculated from equations 3.30 and 3.31 represent the longitudinal storage and loss moduli (L' and L'') of the tested material. Similarly, if we conduct the shear wave measurement, M' and M'' will represent the shear storage and loss moduli (G' and G''). Once we obtain both longitudinal and shear moduli, we can calculated other moduli using relation in Table 3.1.

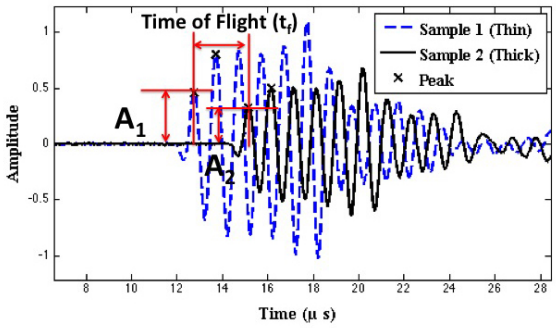

Figure 3.26: Longitudinal wave signals, amplitudes A_1 and A_2 from tests 1 and 2, and time of flight t_f (dashed line shows signal traveling through thin sample (test 1), solid line shows signal traveling through thick sample (test 2))

The test procedure for ultrasonic wave testing under low pressure is slightly modified from the testing at atmospheric pressure. Two tests under the same pressure are required, each using a different sample thickness. In each of the two tests, the sample is confined in the closed fixture (see Figure 3.24), placed in the environmental chamber (see Figure 3.1), uniaxially aligned with the loading post of the Instron load cell, and equilibrated at a chosen temperature for an hour. The compressive force is then gradually applied normal to the surface of the sample with the rate of 15 lbf/s ($67\,\mathrm{N\,s^{-1}}$). The compressive force is kept constant at every 1 MPa pressure to perform ultrasonic wave measurement while the temperature is kept unchanged for the whole test. The testing pressure ranges from 0 to 20 MPa with 1 MPa step. To be noted, due to the nearly incompressible nature of polyurea ($\nu \sim 0.5$), pressure can be calculated

by dividing compressive force with the compression area of the sample. Compressive force and displacement histories are measured by the load cell and the two potentiometers, respectively, and recorded for analysis. After the tests are completed, the stress and strain of the tested samples are calculated using the initial dimensions of the samples, the compressive force, and the contraction histories. The stiffness of the machine is also measured through the same test procedure but without sample. At the same pressure, the measured strains from the two tests with samples with different thicknesses are subtracted by the strain of the machine from the test without sample. The resulting strains are the pure sample strains. The sample strain and coefficient of thermal expansion are later used to calculate the density of the sample at each pressure. Ultrasonic wave signals of the two tests with samples are recorded separately at each pressure. The wave speed and attenuation, which take into account the contraction of the sample at each pressure and temperature, are calculated. Then, the moduli are calculated using the density, wave speed, and attenuation. The same procedure is repeated for other testing temperatures. Temperature range is from -50 to 50 °C, with 10 °C increment. The compressive stress or pressure can be calculated as:

$$\sigma_1 = P_1 = \frac{F_1(t)}{A_{o1}}, \tag{3.36}$$

$$\sigma_2 = P_2 = \frac{F_2(t)}{A_{o2}}, \tag{3.37}$$

$$\sigma_{ave} = P = \frac{\sigma_1 + \sigma_2}{2}, \tag{3.38}$$

where σ_1, σ_2, and σ_{ave} are engineering confined compressive stresses from test 1, test

2, and the average stress, respectively, t is time, A_{o1} and A_{o2} are the compression areas of samples in test 1 and 2, and they are constants since the sample in each test is confined in the closed volume. Due to the nearly incompressible nature of polyurea and polyurea-based composites in this research, the confined compressive stress is referred to as pressure. Generally, P_1, P_2, and P are almost the same since F_1 and F_2, and A_{o1} and A_{o2} are very close. The compressive strain can be calculated as:

$$\epsilon_1(T,P) = \frac{[d_1(P) - d_1(P=0)] - [d_m(P) - d_m(P=0)]}{h_1(1 + C_{TE}(T - T_o))}, \tag{3.39}$$

$$\epsilon_2(T,P) = \frac{[d_2(P) - d_2(P=0)] - [d_m(P) - d_m(P=0)]}{h_2(1 + C_{TE}(T - T_o))}, \tag{3.40}$$

$$\epsilon_{ave} = \frac{\epsilon_1 + \epsilon_2}{2}, \tag{3.41}$$

where ϵ_1, ϵ_2 and ϵ_{ave} are the engineering strains from test 1, test 2, and the average strain, respectively, $d_1(P)$, $d_2(P)$, and $d_m(P)$ are displacements from test 1 and test 2, and the displacement of the machine from the test without sample at pressure P, respectively, h_1 and h_2 are the initial thicknesses of sample in tests 1 and 2, T and T_o are the testing and room temperatures, respectively, C_{TE} is thermal expansion coefficient of the sample ($207\,\mu m\,m^{-1}\,K^{-1}$ for polyurea, $151\,\mu m\,m^{-1}\,K^{-1}$ for polyurea with 40% volume fraction of phenolic microballoon, and $103\,\mu m\,m^{-1}\,K^{-1}$ for polyurea with 20% volume fraction of milled glass). The average stress and strain in equations 3.38 and 3.41 are used to construct the stress-strain relation of the sample. The

thicknesses of the samples at each pressure and temperature can be written as:

$$\widetilde{h}_1(T,P) = h_1\left(1 + C_{TE}\left(T - T_o\right) + \epsilon_1(T,P)\right), \tag{3.42}$$

$$\widetilde{h}_2(T,P) = h_2\left(1 + C_{TE}\left(T - T_o\right) + \epsilon_2(T,P)\right), \tag{3.43}$$

where $\widetilde{h}_1$ and $\widetilde{h}_2$ are thicknesses of the samples in tests 1 and 2 that include effects of extensions from pressure and temperature. Densities of the samples can be calculated as:

$$\widetilde{\rho}_1(T,P) = \frac{\rho_1}{\left(1 + 3C_{TE}\left(T - T_o\right) + \epsilon_1(T,P)\right)}, \tag{3.44}$$

$$\widetilde{\rho}_2(T,P) = \frac{\rho_2}{\left(1 + 3C_{TE}\left(T - T_o\right) + \epsilon_2(T,P)\right)}, \tag{3.45}$$

$$\widetilde{\rho}_{ave} = \frac{\widetilde{\rho}_1 + \widetilde{\rho}_2}{2}, \tag{3.46}$$

where ρ_1 and ρ_1 are initial densities of the samples in test 1 and 2 at ambient condition, $\widetilde{\rho}_1$, $\widetilde{\rho}_2$, and $\widetilde{\rho}_{ave}$ are the densities of the samples in tests 1, 2, and the average density that include effects of extensions from pressure and temperature. In general, the effect of thermal contraction or expansion is very small compared to that from pressure. So we might neglect the thermal term for simplicity.

With the received ultrasonic wave signals recorded from the two tests at each pressure and temperature, the time of flight can be calculated (see Figure 3.26). Wave speed and attenuation can be calculated from equations 3.34 and 3.35 using the previously calculated time of flight, $\widetilde{h}_1$, and $\widetilde{h}_2$ defined in equations 3.42 and 3.43.

Then, the storage and loss moduli are calculated, using equations 3.30 and 3.31 with the average density, $\widetilde{\rho}_{ave}$ calculated using equation 3.46.

For high-pressure test, the test fixture is designed for inserting only one sample with smaller cross-sectional area to create higher pressure than low-pressure test at the same load (see Figure 3.25). Thus one test is performed at each pressure and temperature, and only the wave speed is measured. The high pressure ultrasonic wave measurement will be discussed in detail later in Section 4.2 of Chapter 4.

3.3.4 Results and Discussions

Ultrasonic Wave Measurement at Ambient Pressure

Polyurea (PU), phenolic microballoon filled polyurea (PUPMB), and milled glasses reinforced polyurea (PUMG) composites were tested with ultrasonic wave measurement at ambient pressure in order to study their viscoelastic responses in the frequency range of 0.5 to 1.5 MHz. In this section, PU and PUPMB are discussed first; while PUMG will be discussed later in Section 3.4. Figure 3.27 shows the results of ultrasonic longitudinal wave measurement on PU. The plot of longitudinal wave speed, c_L as a function of temperature (from -90 to 30 °C) is shown in Figure 3.27a. The testing frequencies are 0.5, 0.75, 1, 1.25, and 1.5 MHz. To be noted, 1 MHz is the central frequency of the longitudinal transducers that we used. It appears that 0.5 and 1.5 MHz are the minimum and maximum frequencies that the transducers can perform effectively. c_L decreases with increasing temperature. It has a flat reverse S shape, in which low negative slopes occur at low and high temperature regions. High negative slope occurs around -40 °C. The c_L curves of the five frequencies lie on top of each other, suggesting that c_L is frequency-insensitive within this frequency range.

Figure 3.27b shows attenuation of longitudinal wave per unit length of the sample, α_L as a function of temperature. Unlike c_L, it is apparent that α_L is frequency-sensitive. It increases with increasing frequency. α_L is a dome-shaped curve where the peak is around $-50\,^{\circ}\mathrm{C}$ for all the five frequencies. The dome shape becomes flatter at lower frequency. The longitudinal storage and loss moduli, L' and L'' as functions of temperature are shown in Figrues 3.27c and d, respectively. Similar to c_L, L' decreases with increasing temperature and it is frequency-insensitive within 0.5 to 1.5 MHz. Unlike L', L'' is frequency-dependent. L'' decreases with increasing frequency. This behavior is opposite to that of α_L. L'' reaches its peak around $-70\,^{\circ}\mathrm{C}$ while, as mentioned earlier, α_L peaks at around $-50\,^{\circ}\mathrm{C}$. It is worth noting that the behavior of L' is dominated by the behavior of c_L while the behavior of L'' is influenced by the combination of c_L and α_L.

The ratio of L'' to L', called $\tan\delta$ is shown in Figure 3.28. It gives a ratio of the viscous portion to the elastic portion. Mostly, the behavior of $\tan\delta$ is similar to that of L'', except that its peak is around $-60\,^{\circ}\mathrm{C}$. Generally the three peaks of α_L, L'', and $\tan\delta$ are used to locate the temperature of transition from rubbery to glassy behaviors (or glass transition temperature, T_g) of viscoelastic materials. However, they can be at different temperatures. Therefore, this glass transition is not a particular temperature but rather a range of temperature.

Figure 3.29 shows the results of ultrasonic shear wave measurement on polyurea. Due to lower performance of the shear transducers (compared to the longitudinal transducers) and higher dissipation of shear wave, we study only three frequencies (0.5, 1, and 1.5 MHz) and narrower temperature range (-50 to 30 °C). We found that the shear transducers work poorly below $-50\,^{\circ}\mathrm{C}$. Above 30 °C, shear wave in polyurea

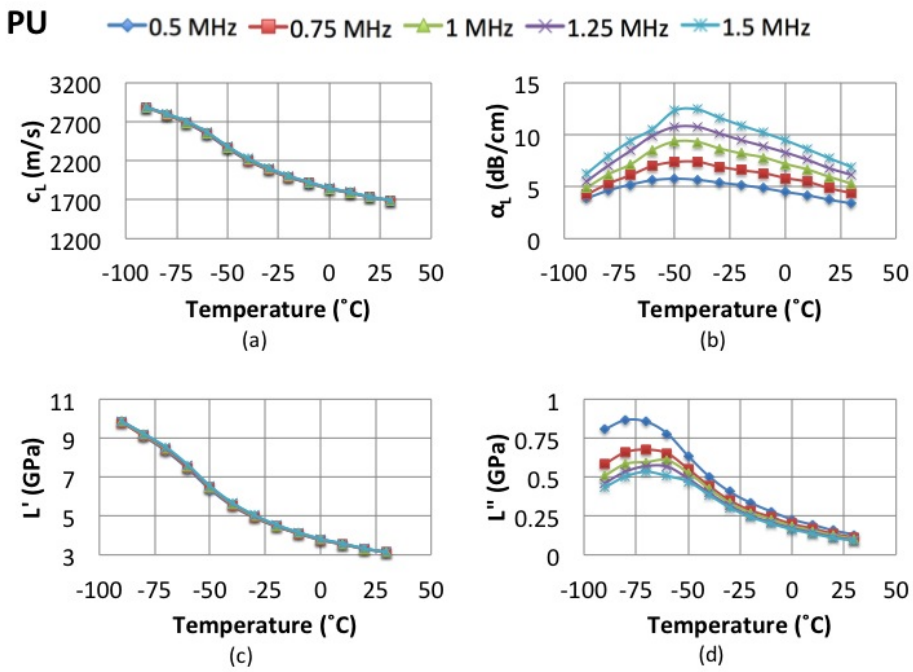

Figure 3.27: PU: (a) Longitudinal wave speed as a function of temperature (b) Attenuation of longitudinal wave per unit length of the sample as a function of temperature (c) Longitudinal storage modulus as a function of temperature (d) Longitudinal loss modulus as a function of temperature

become very attenuated, especially at high frequency. Samples for shear wave measurement need to be very thin to allow us to see the transmitted shear wave signal in polyurea at high temperature. To be noted, the accuracy of shear wave measurement is lower than that of longitudinal wave measurement. Figure 3.29a shows the plot of shear wave speed, c_G as a function of temperature (from -50 to 30 °C). Similar to c_L, c_G decreases with increasing temperature. Due to narrower testing temperature range of this measurement than that of the longitudinal wave measurement, we cannot see clearly the flat reverse S shape of shear wave speed. However, we did observe that c_G flattens out at around 20 °C. The c_G is quite frequency-insensitive within this frequency range. Figure 3.29b shows attenuation of shear wave per unit length

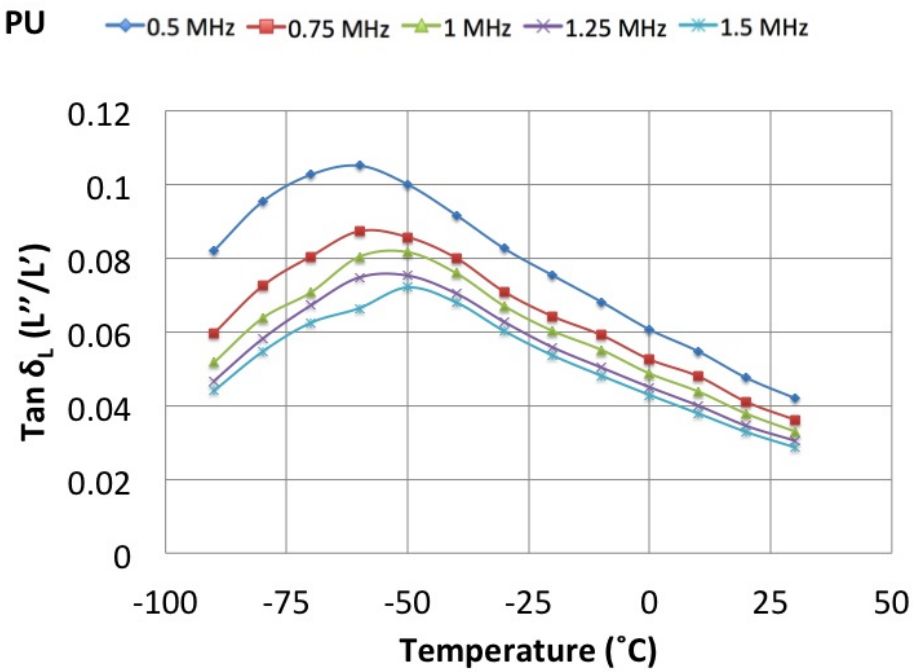

Figure 3.28: PU: $\tan\delta$ versus temperature

of the test sample, α_G as a function of temperature. Unlike c_G, we can see that α_G is frequency-sensitive. Similar to α_L, α_G also increases with increasing frequency. However α_G does not show the dome-shaped curve as in α_L. α_G increases with increasing temperature, instead. The shear storage and loss moduli, G' and G'' as functions of temperature are shown in Figrues 3.29c and d, respectively. Similar to c_G, both L' and L'' decreases with increasing temperature. From observation, they are quite frequency-insensitive within 0.5 to 1.5 MHz.

The results of ultrasonic longitudinal wave measurement on PUPMB composites with 10%, 20%, and 40% volume fractions are shown in Figure 3.30. In this study, the viscoelastic behaviors of the composites are characterized at 1 MHz (central frequency of the longitudinal transducers) and from -50 to 30 °C.

Figure 3.30a shows c_Ls of the PUPMB composites as functions of temperature. Apparently, c_L of each composite decreases as temperature increases. c_L also decreases

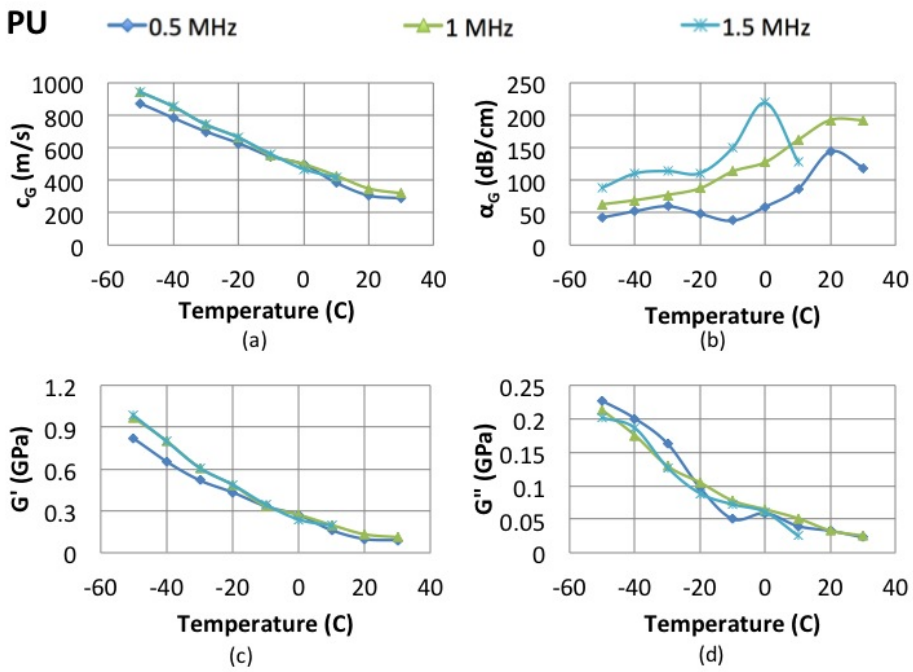

Figure 3.29: PU: (a) Shear wave speed as a function of temperature (b) Attenuation of shear wave per unit length of the sample as a function of temperature (c) Shear storage modulus as a function of temperature (d) Shear loss modulus as a function of temperature

with increasing volume fraction of the PMB filler. This is due to that the voids in the microballoon are obstacles of the propagating wave, thereby, slowing down the wave speed. Figure 3.30b shows the plots of α_Ls of the PUPMB composites as functions of temperature. α_Ls of the composites behave differently from that of pure polyurea. α_Ls of the composites increase with increasing temperature while α_L of polyurea decreases with increasing temperature. α_L increases with increasing volume fraction of the microballoon. A jump of α_L is observed, at low temperature, between 10% and 20% volume fraction while at higher temperature α_L spread out evenly. This complicate behavior may be caused by the difference in temperature-dependent viscoelastic behaviors of two polymeric materials, i.e., polyurea and phenolic microballoon. L' and L'' as functions of temperature are shown in Figrues 3.30c and d, respectively.

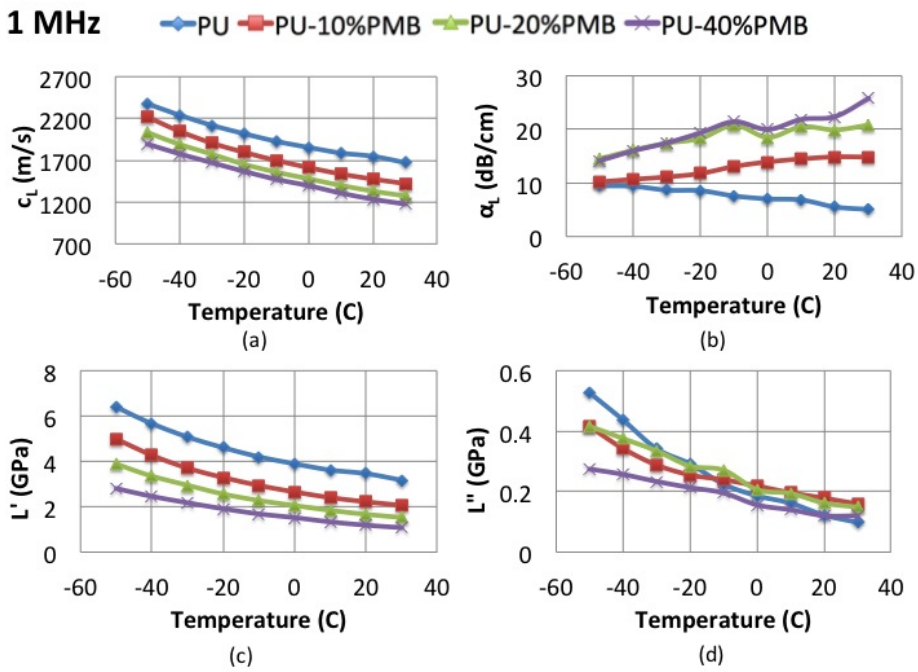

Figure 3.30: PUPMB: (a) Longitudinal wave speed as a function of temperature (b) Attenuation of longitudinal wave per unit length of the sample as a function of temperature (c) Longitudinal storage modulus as a function of temperature (d) Longitudinal loss modulus as a function of temperature

Similar to c_L, L' decreases as temperature and volume fraction of the microballoon increase. Unlike L', the behavior of L'' is more complicate. At low temperature L'' decreases with increasing volume fraction while at temperature above 0 °C it increases first, reaches a peak at around 10% volume fraction, and drops back down as volume fraction increases further. This behavior at 20 °C can also be predicted by micromechanical models that will be discussed in Chapter 5.

Figure 3.31a shows c_Gs of the PUPMB composites as functions of temperature. Unlike c_L, c_G does not vary much when volume fraction changes. With careful notice, we can see that at low temperature c_G slightly decreases with increasing volume fraction. However, the trend reverses as temperature increases. Apparently, c_G decreases

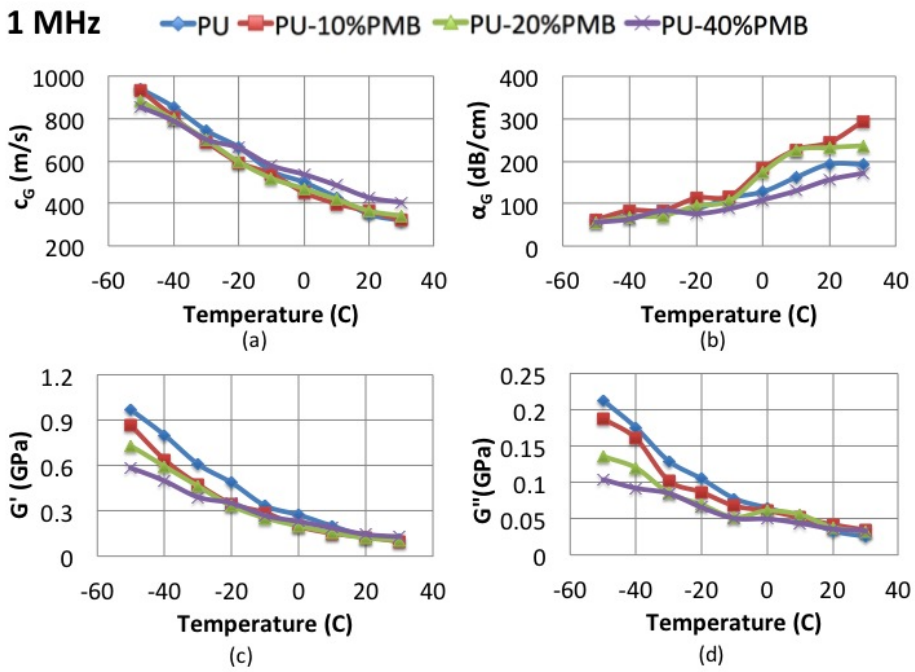

Figure 3.31: PUPMB: (a) Shear wave speed as a function of temperature (b) Attenuation of shear wave per unit length of the sample as a function of temperature (c) Shear storage modulus as a function of temperature (d) Shear loss modulus as a function of temperature

as temperature increases in the same way as c_L. α_Gs of the PUPMB composites as functions of temperature are shown in Figure 3.31b. α_Gs of the composites increase with increasing temperature. At low temperature α_Gs of the composites converge to c_G of pure polyurea, while at high temperature they spread out. Consider in term of volume fraction, it seems that α_G peaks out at 10% volume fraction and drops down as volume fraction increases further. Figrues 3.31c and d show G' and G'' as functions of temperature, respectively. Both G' and G'' decrease with increasing temperature. At low temperature, both G' and G'' decrease with increasing volume fraction, while at high temperature they converge to G' and G'' of polyurea.

Low Pressure Ultrasonic Wave Measurement

Previously in Section 3.1.3, we discussed the results of low pressure quasi-static tests on PUPMB composites. The stress-strain and density curves of the composites as functions of pressure from 0 to 10 MPa were explained in detail there. Here, we will discuss about the results of ultrasonic longitudinal wave measurement with respect to pressure. As a reminder, the objective of this test is that we want to study the acoustic impedances of the PUPMB composites and determine whether or not they are pressure invariant.

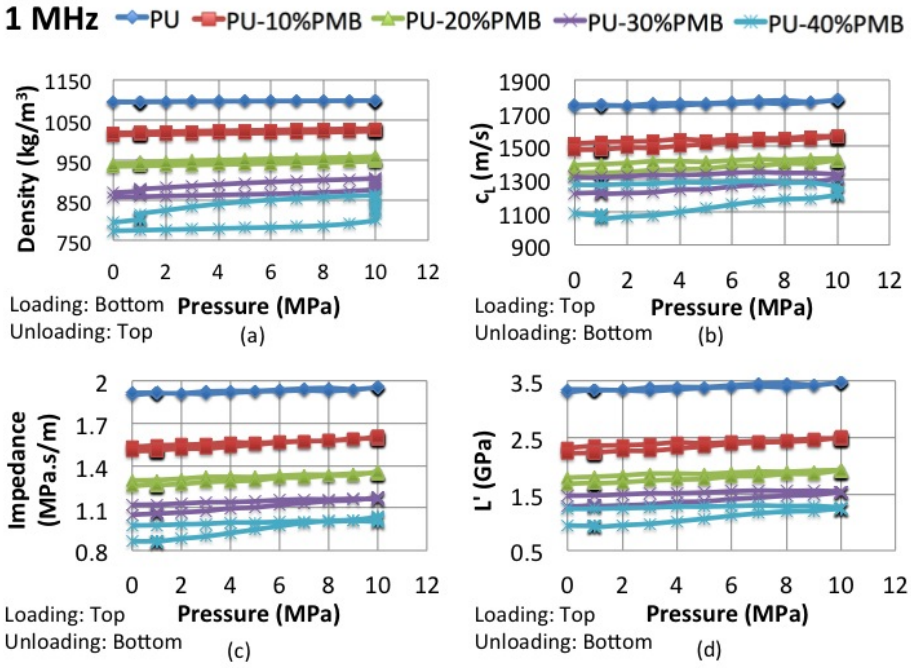

Figure 3.32: PUPMB: (a) Density as a function of pressure (b) Longitudinal wave speed as a function of pressure (c) Acoustic impedance as a function of pressure (d) Longitudinal storage modulus as a function of pressure

Similar to Figure 3.11b, densities of PUPMB composites as functions of pressure are also shown here in Figure 3.32a for the sake of discussion. To be noted, the load or pressure profile is shown in Figure 3.10. Figure 3.32b shows longitudinal

wave speeds, $c_L s$ of PUPMB composites as functions of loading and unloading pressures. For each composite, the top solid line refers to loading and bottom solid line is unloading. The knots in each plot observed at 10 and 1 MPa are at the creep and recovery steps where we kept the testing pressure fixed for 1 hour (see Figure 3.10). As we can see from Figure 3.32b, c_L decreases with increasing volume fraction of the PMB filler. During loading, c_L is constant over the pressure range of study; however, during the creep stage where we applied 10 MPa pressure for 1 hour, c_L drops as time passes. The drop of c_L is larger in the composite with higher volume fraction of microballoon. This is due to that higher amount of microballons were collapsed by pressure in the the composite with higher volume fraction of microballoon. During unloading, c_L slightly decreases and slightly recover at the recovery stage where we fixed the applied 1 MPa pressure for 1 hour. Acoustic impedance as a function of pressure for each composite is shown in Figure 3.32c. It is apparent that the impedance decreases with increasing volume fraction. At 40% volume fraction, the impedance is lowered by over 50%, compared to the impedance of the pure polyurea. More interesting, the impedance, which is the product of the multiplication between density and wave speed, seems to be pressure-invariant even though many micro balloons were collapsed by pressure during loading and unloading. At 0 MPa, a little drop of impedance (around 10%) is observed for PUPMB composite with 40% volume fraction. This is due to that drop of wave speed during unloading is compensated by the jump in density of the composite at the same stage. This behavior is also observed in L' since L' in this study was calculated by density times the square of the wave speed. In conclusion, this suggest that the PUPMB composites have the ability to maintain its acoustic impedance in this range of pressure. As discussed in Section 3.1.3, we

can improve the quality of PUPMB composites if we sieve out the microballoons that are larger than 25 µm and use only the smaller ones to fabricate PUPMB composites. The composites would be able to resist the pressure up to 10 MPa without damage of the microballoons. This will be our future work.

3.4 Dymamic Properties of Polyurea-Milled Glass Composites Part I: Experimental Characterization

Polyurea (PU) is an elastomer, which exhibits unique thermo-mechanical properties. It is synthesized from a di-functional amine, e.g. Versalink P-1000 and a diisocyanate, e.g. Isonate143L. In this study, various volume fractions milled glass (MG) was added to create polyuria-milled glass composites (PU-MG). Milled glass is a micro fiber with cylindrical shape. The distribution of the milled glass in the polyurea matrix was observed under the scanning electron microscope. The dynamic properties of pure polyurea and the PU-MG composites were measured by dynamic mechanical analysis (DMA) in the low frequency range (1-20 Hz) and by ultrasonic wave measurement in the high frequency range (0.5-1.5 MHz). Both experiments show that increasing the milled glass volume fraction drastically increases both the storage and loss moduli of the composites. DMA results show that dynamic Young's modulus increases with increasing frequency. However, longitudinal and shear moduli from ultrasonic wave measurement appears to be insensitive to frequency within the range of 0.5 to 1.5 MHz. The experimental dynamic moduli master curves of PU and PU-MG composites were constructed and compared. The relaxation function or creep com-

pliance are generally useful than dynamic moduli for modeling of material response under complex histories. It is of practical use to convert dynamic mechanical data from the frequency domain into the time domain. The discrete relaxation spectra of the composites were calculated by fitting Prony series to the master curves, using least square nonlinear regression. Retardation spectra were then calculated using the interrelation between relaxation modulus and creep compliance in Laplace domain. Finally, the time domain relaxation modulus and creep compliance for each composite were obtained from the two spectra. In order to extend our understanding of the dynamic behavior of the PU-MG composite, micromechanical models have been created and are discussed in the accompanying paper [39].

3.4.1 Introduction

Polyurea (PU) is a segmented block copolymer derived by the reaction of a diisocyanate component and a diamine component. Generally, polyurea is formulated to have hard segments with a high glass transition temperature (Tg) and soft segments with a low Tg. The soft phase is primarily constituted of long chain diamine, which confers flexibility to the material, and the hard phase consists of diisocyanate typically in a semi-crystalline ordered state created by hydrogen bonding, which gives an enhanced initial stiffness often followed by a yield-like event. The hard and soft domain phase separation is due to the thermodynamic incompatibility of the segmented chain blocks of polyurea [5]. Therefore, the microstructure of polyurea has nano-scale hard domains dispersed in the soft domain. The microstructure mechanical properties of polyurea may be tuned by using different isocyanates and amines [5]. Holzworth et al. also showed that even for the same chemistry, the stoichiometric ratio affects

the mechanical properties of polyurea [4]. In this study, molar ratio of isocyanate to amine groups is chosen to be 1.05 as recommended by the manufacturer [6].

Previous researches have shown that the mechanical properties of polyurea depend strongly on the strain rate, temperature and pressure [9, 20, 40, 41]. It also shows strong hysteresis and cyclic softening [11]. For the polyurea-based composites, not much data is available. Qiao et al studied polyurea with fly ash composites [42, 43]. They showed that by mixing polyurea with fly ash, the strength of polyurea increases along with decrease in density. Alternatively, glass fibers can be blended with a polymer to improve the strength of the polymer. Experiments on milled-glass-fiber-filled polyethylene terephthalate-co-isophthalate composites were conducted by Velasco et al. [44]. Their results showed a trend of increasing composite Young's modulus and tensile strength with increasing fiber volume fraction. Increasing wear and impact resistances is another advantage of polymeric composites containing milled glass fibers [45].

In this study, the micron-scale cylindrical glass fibers were introduced as the filler material into polyurea. Pure polyurea and polyurea with milled glass (PU-MG) composites with 5%, 10%, 15%, and 20% volume fractions of inclusions were created. The main contributions of this study are the following:

1. The effect of milled glass volume fraction, frequency, and temperature on dynamic mechanical properties of PU-MG composites was experimentally measured. The composites were studied using dynamic mechanical analysis (DMA) in the low frequency range of 1 to 20 Hz and -80 to 50 °C and through ultrasonic wave measurements in the high frequency range of 0.5 to 1.5 MHz and -50 to 30 °C.

2. The energy dissipation behavior of PU and PU-MG composites were stud-

ied, considering volume fraction, frequency, and temperature.

3. The master curves of PU and PU-MG composites were constructed with the assumption that PU and PU-MG composites are thermorheologically simple. These curves contain the material information over wider ranges of frequency than can be obtained from a single standard experimental technique. These master curves and their parameterization in selected ranges of strain rates/frequencies and temperatures may be used for robust computational modeling of complex structures that include these composites as layers, dampers, or high strain-rate stiffeners and stabilizers [46–48]. While the comparison of the master curves obtained from DMA with the ultrasonic results show that this assumption is justified for use in storage modulus, it was observed that the loss modulus at higher frequencies is consistently higher than what is predicted from DMA master curves. This indicates the presence of enhanced dynamic loss mechanisms at ultrasonic frequencies and underlines the need for further modeling that can capture these effects.

4. Discrete relaxation and retardation spectra, as well as uniaxial relaxation function and creep compliance of the composites were calculated. The discrete relaxation and retardation spectra can be used with finite element programs for designing and analysis of the composites, under dynamic and unsteady load histories. A small modification to the formulation previously presented in [49] was realized for the solid viscoelastic cases. The effect of volume fraction of milled glass on the profiles of the relaxation and compliance were studied.

Additionally, in our accompanying paper, micromechanical models will be discussed and used as a computational tool to estimate mechanical properties of the composite and to extend our understanding of their dynamic behavior [39]. These

models are not limited to PU-MG composite and can be directly used for other composites with similar particulate microstructure; see for example [21].

3.4.2 Material Fabrication

In this study, Isonate 143L [26], which is a polycarbodiimide modified diphenylmethane diisocyanate, was used with the diamine Versalink P-1000 [6], which is a poly(tetramethyleneoxide-di-p-aminobenzoate). The milled glass was purchased from Fibertec, Inc. (product number 3032). The fibers have an average diameter of 16 µm, average length of 200 µm, and average density of 2.5 g cm^{-3}. PU-MG composites of volume fractions of 5%, 10%, 15%, and 20% were fabricated, as well as PU with no MG (PU-0%MG). The composite fabrication procedure is shown elsewhere [31]. The nominal dimension of the DMA samples was 3 mm x 10 mm x 20 mm. Two DMA samples from the same batch were fabricated for each milled glass volume fraction. The nominal dimension of the ultrasonic test samples were 25.4 mm (1 inch) in diameter and 6 mm in thickness for longitudinal waves, and 76.2 mm in diameter (3 inch) and 0.7 mm (hereafter referred to as thin) or 1.2 mm (thick) in thickness for shear waves. Two longitudinal-, one thick and one thin shear-wave-test samples were fabricated for each volume fraction.

3.4.3 Characterization

Dynamic Mechanical Analysis

Dynamic mechanical analysis was conducted on a TA Instrument Dynamic Mechanical Analyzer 2980. The experimental data was collected and analyzed using the Universal Analysis software to obtain storage modulus E', loss modulus E'', and

$\tan\delta$. During the test, the sample was cantilevered at both ends with a free length of 17.5 mm between the clamps. One end of the sample was fixed, and the other end was attached to the movable clamp, which oscillated harmonically with amplitude of 15 µm. The temperature range of the test was -80 to 50 °C with 3 °C increments for each step. The sample was equilibrated at each temperature point for 3 minutes before the frequency sweep. The tested frequencies were 20 Hz, 10 Hz, 5 Hz, 2 Hz and 1 Hz, stepping down sequentially for each sweep. Liquid nitrogen was used to cool the system down to subambient temperatures.

Scanning Electron Microscopy

The fractured surfaces of polyurea with milled glass composites were observed using a Philips Environmental Scanning Electron Microscope XL30 scanning electron microscopy (SEM).

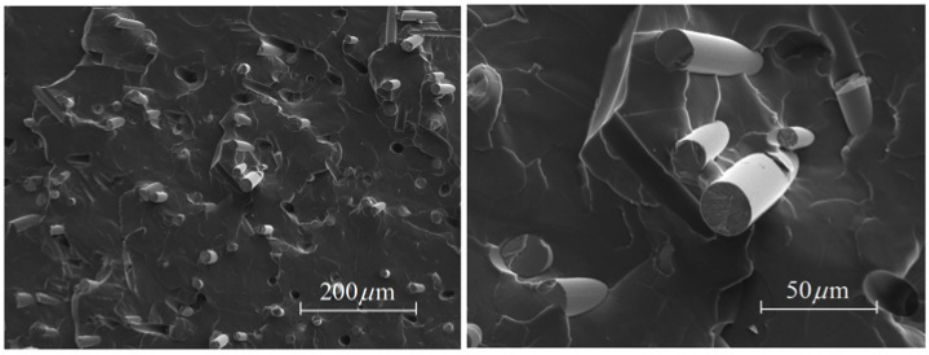

Figure 3.33: Fractured surface of PU-10%MG-DMA sample

The fractured surface was coated with 75 nm of iridium in an automatic sputter. DMA and longitudinal-wave-test samples were cross-sectioned, fractured, and observed under SEM. It shows that the milled glass fibers are randomly dispersed in the polyurea matrix as shown in Figure 3.33. The milled glass fibers in shear-wave-

test samples, as shown in Figure 3.34, tend to lie parallel to the surface of the samples due to fabrication process needed to achieve such thin samples. The mixture has to flow parallel to the surface of the top and bottom glass plate molds and this will naturally push the fibers to rearrange themselves parallel to the two plates as well.

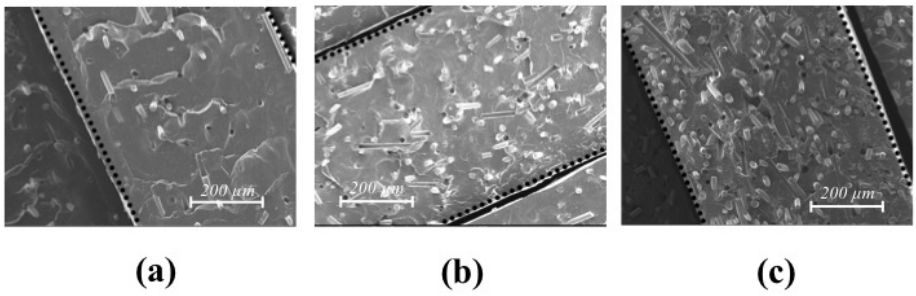

Figure 3.34: (a) Fractured surface of PU-5%MG-ultrasonic-shear-wave-test sample (b) Fractured surface of PU-10%MG-ultrasonic-shear-wave-test sample (c) Fractured surface of PU-20%MG-ultrasonic-shear-wave-test sample. (Dotted line shows surface of the sample)

Composite Density Measurement

The density of each composite was determined through the application of Archimedes' principle by measurement of the weight of the specimen in air and in water, respectively [42].

$$\rho_c = \frac{w_{air}}{w_{air} - w_{water}} \rho_{water}, \tag{3.47}$$

where ρ_c is the density of the composite, ρ_{water} is the density of water, w_{air} is the weight of the composite in air, and w_{water} is the weight of the composites in water. Five measurements were conducted for each volume fraction. The measured densities were compared with the calculated densities and are shown in Figure 3.35.

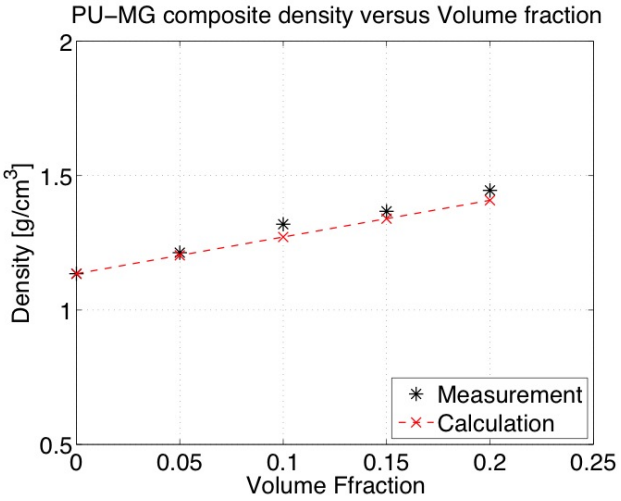

Figure 3.35: PU-MG composite density versus volume fraction

Longitudinal and Shear Ultrasonic Wave Measurements

The longitudinal wave speed in the composites was measured by direct contact measurement. The experimental setup is shown and discussed elsewhere [20, 50]. To determine the wave speed and attenuation of the longitudinal wave, two tests were performed using two different sample thicknesses (for longitudinal wave test, the thicker sample was made by stacking two thin ones). The samples were sandwiched between a pair of longitudinal transducers using a fixture to ensure relatively uniform pressure applied at all times, and longitudinal wave couplant was applied to all contact surfaces. Tests were conducted at 0.5, 1.0, and 1.5 MHz and from -50 to 30 °C with 10 degreeCelsius increments. The longitudinal wave speed was determined by measuring the difference between the travel times of the two tests with different sample thicknesses:

$$v_L = \frac{d}{t}, \tag{3.48}$$

where v_L is the longitudinal wave speed in the composite, d is the difference of sample thickness between the two tests, and t is the time shift observed between the two tests.

The longitudinal-wave attenuation coefficient per unit thickness was measured using the transmitted-wave amplitudes of these two tests:

$$\alpha_L = \frac{1}{d} \ln \left(\frac{A_1}{A_2} \right), \tag{3.49}$$

where α_L is the longitudinal-wave attenuation coefficient per unit thickness, A_1 is the amplitude of the longitudinal wave in single-sample test, and A_2 is the amplitude of the longitudinal wave in double-sample test. The wave speed and attenuation are used to calculate longitudinal storage and loss moduli of the composites as follows [20,50]:

$$L' = \frac{\rho_c v_L^2 \left[1 - r_L^2\right]}{\left[1 + r_L^2\right]^2}, \tag{3.50}$$

$$L'' = \frac{2\rho_c v_L^2 r_L}{\left[1 + r_L^2\right]^2}, \tag{3.51}$$

where

$$r_L = \frac{\alpha_L v_L}{\omega}, \tag{3.52}$$

r_L is a dimensionless parameter, ω is the angular frequency, L' is the longitudinal storage modulus, and L'' is the longitudinal loss modulus. The speed of shear wave (v_G) and shear attenuation (α_G) are also calculated using equations 3.48 and 3.52 for each material. Then the shear storage and loss moduli (G' and G'') are calculated in the same manner, using equations3.50 and 3.51 with dimensionless shear parameter (r_G), equation 3.52.

3.4.4 Results and Discussion

DMA

In the DMA single cantilever test, the general expression of the complex Young's modulus is defined as $E^* = E' + iE''$, where E' is the Young's storage modulus and E'' is the Young's loss modulus. E' reflects the elastic stiffness of the material and E'' is related to the energy loss. $\tan\delta$ is defined as $\frac{E''}{E'}$. The complex longitudinal and shear moduli can be used to calculate the complex Young's modulus as

$$E^* = \frac{G^*\left(3L^* - 4G^*\right)}{L^* - G^*}, \tag{3.53}$$

where E^*, L^*, and G^* are complex Young's, longitudinal, and shear moduli. Figures 3.36a-d show the average Young's storage and loss moduli of the two tests for PU-0%MG, PU-10%MG, PU-15%MG and PU-20%MG respectively. The average was taken between the two samples made from the same batch. Both storage and loss moduli increase drastically with the increase of the volume fraction of the milled glass, as shown in Figures 3.37a-b, which summarize the ratio of the modulus of each PU-MG composite with different volume fraction to that of pure polyurea at 1 and 20 Hz. This behavior can also be observed at other test frequencies. For higher temperatures above 5 °C, the storage and loss moduli increases to about 2, 2.6, and 4 times comparing to the pure polyurea for the 10%, 15% and 20% milled glass volume fraction, respectively. Note that for higher temperatures above 5 °C, $\tan\delta$ of each composite approaches that of pure PU (see Figure 3.38). This means that although as the milled glass volume fraction increases, and the PU-MG composite gets stiffer, the energy loss does not drop. This is opposite to our expectation that

the composites should have less energy dissipation due to the reduction of the volume of PU. In other words, one gets a stiff composite with the same dissipation potential as the flexible matrix. The peak of the loss modulus (E'') indicates the glass transition in the material. As can be seen in Figures 3.36a-d, the peaks of E'' are all around $-60\,^{\circ}\mathrm{C}$, which is consistent with the measurement by differential scanning calorimetry (DSC) for pure polyurea [4]. For higher milled glass volume fraction, the peaks shift slightly towards higher temperature. This implies that the existence of the milled glass hinders the movement of the polymer chains.

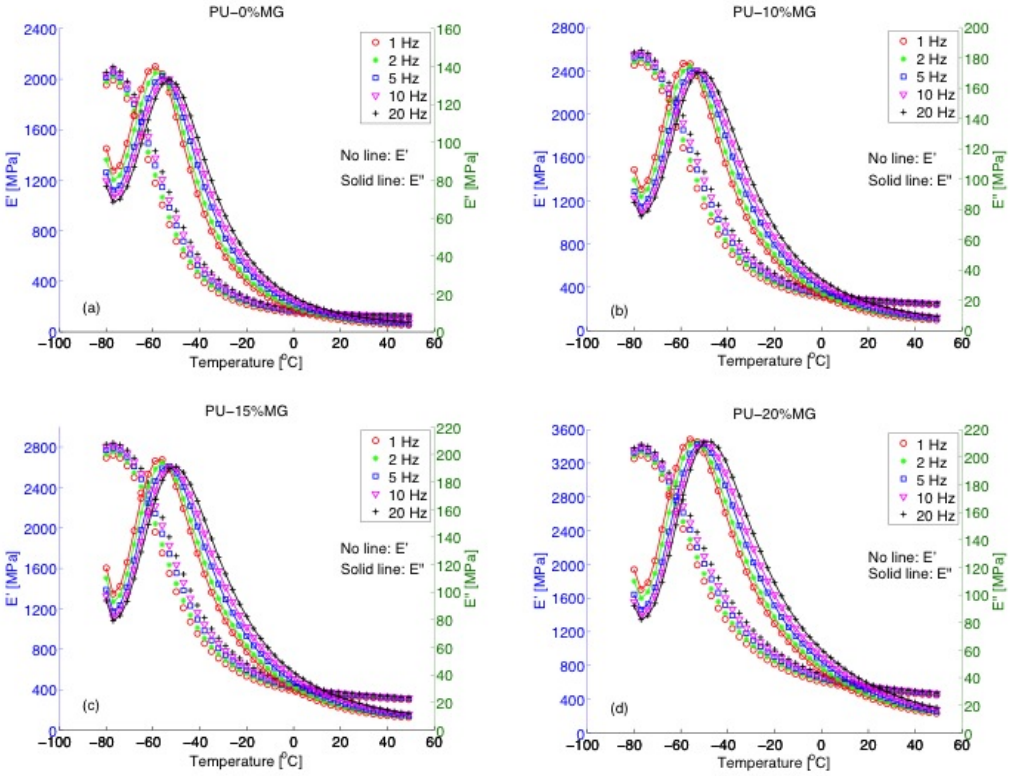

Figure 3.36: (a) E' and E'' of PU-0%MG. (b) E' and E'' of PU-10%MG. (c) E' and E'' of PU-15%MG. (d) E' and E'' of PU-20%MG

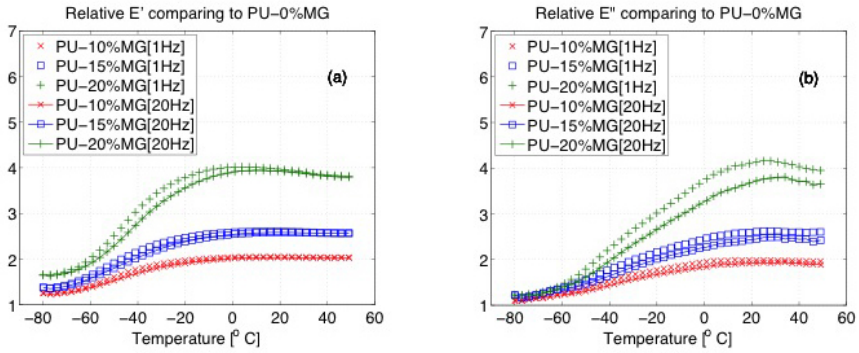

Figure 3.37: (a) Relative E' of PU-MG composites comparing with PU-0%MG. (b) Relative E'' of PU-MG composites comparing with PU-0%MG

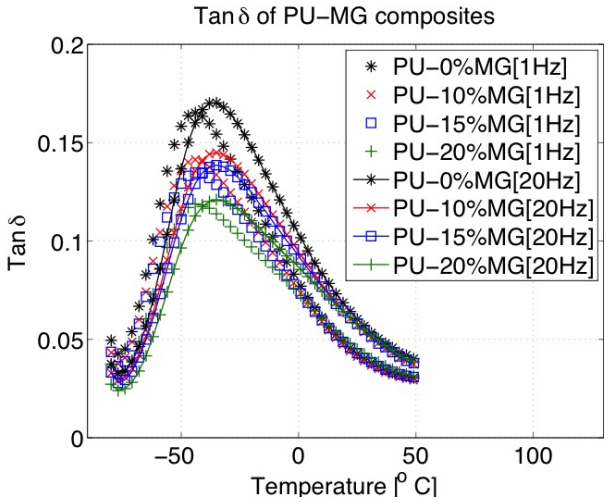

Figure 3.38: $\tan\delta$ of PU-MG composites versus temperature.

Ultrasonic Wave Measurement

It is observed that within 0.5 to 1.5 MHz interval (normal working range of the transducers used in this study) and -50 to 30 °C, the longitudinal and shear moduli may be considered nearly frequency insensitive. Thus, only the results at 1 MHz, which is the central frequency of both longitudinal and shear transducers, will be presented as representative. The longitudinal- and shear-wave speeds as functions of temperature at 1 MHz are shown in Figures 3.39a-b. It can be seen that both

longitudinal- and shear-wave speeds increase monotonically with decreasing temperature and increasing volume fraction of milled glass fiber. However, at low volume fraction 5% and 10%, the increases of both wave speeds compared to pure polyurea are not obvious. At 20% volume fraction, the two wave speeds increase significantly, especially at low temperature. At $-50\,^{\circ}\mathrm{C}$ the ratio of longitudinal wave speed (v_L) to shear wave speed (v_G) is at minimum around 2.5. As the temperature increases, this ratio increases remarkably and reaches its maximum around 5 at the highest measured temperature, $30\,^{\circ}\mathrm{C}$ (see Figure 3.39c). This monotonic increase in the ratio of v_L to v_G is due to shear softening at higher temperatures. This leads to the higher drop in shear wave speed, compared to longitudinal wave speed. The material with higher volume fraction of milled glass tends to have lower ratio of v_L to v_G due to the stiffening effect of the milled glass.

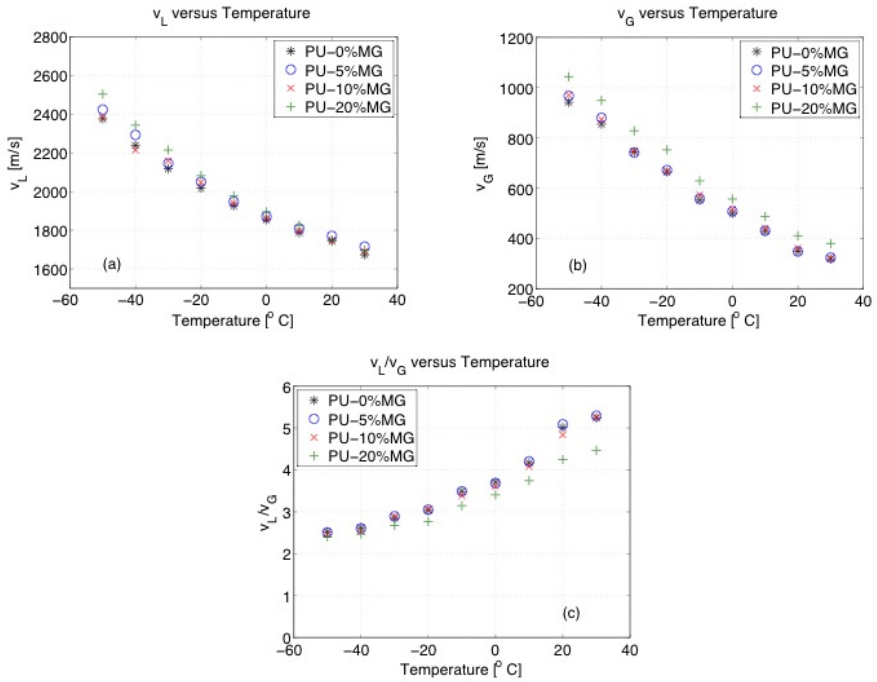

Figure 3.39: : (a) v_L versus temperature at 1 MHz, atmospheric pressure. (b) v_G versus temperature at 1 MHz, atmospheric pressure (c) $\frac{v_L}{v_G}$ versus temperature at 1 MHz, atmospheric pressure

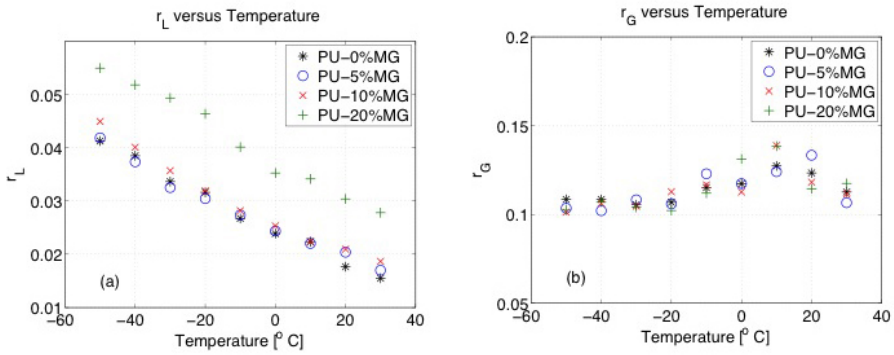

Figure 3.40: (a) r_L versus temperature at 1 MHz, atmospheric pressure (b) r_G versus temperature at 1 MHz, atmospheric pressure

The dimensionless parameters r_L and r_G, which are the attenuations per wavelength of the longitudinal and shear waves divided by 2π, are calculated, using equation 3.52 and shown in Figures 3.40a-b. r_L decreases as temperature increases; while r_G is relatively flat with a slight curved bump between 0 to 20 °C. As volume fraction increases, r_L shows increasing trend and a significant jump between 10% and 20% volume fraction. However, there is no perceptible increase for r_L at low volume fractions of 0% and 5%. Unlike r_L, there is no obvious trend observed for r_G with respect to the volume fraction. With v_L, v_G, r_L, and r_G, the longitudinal- and shear-storage moduli, L' and G', are calculated from equation 3.50 and shown in Figures 3.41a-b. The longitudinal- and shear-loss moduli, L'' and G'', are calculated using equation 3.51 and shown in Figures 3.41c-d. Overall, the longitudinal and shear moduli have the same trend. They all increase with decreasing temperature and increasing the volume fraction of milled glass particle. While the wave speeds and normalized attenuations appear to be independent of volume fraction at lower values the moduli show clearly increasing trend, indicating a rise proportional to the density. However, L', L'', G' and G'' increase as the volume fraction increases with an outstanding jump at 20%

with an effect well beyond that of densityUnlike the relative Young's storage and loss moduli from DMA, the ultrasonic longitudinal and shear moduli normalized to those of pure PU are flat over the range of testing temperatures. The longitudinal loss tangent $\frac{L''}{L'}$ decreases as temperature increases and significantly rises at 20% volume fraction, while shear loss tangent $\frac{G''}{G'}$ is flat with a bump between 0 to 20 °C and insensitive to volume fraction. These curves behave, as expected, similarly to those of r_L and r_G, and therefore are not graphed in this paper.

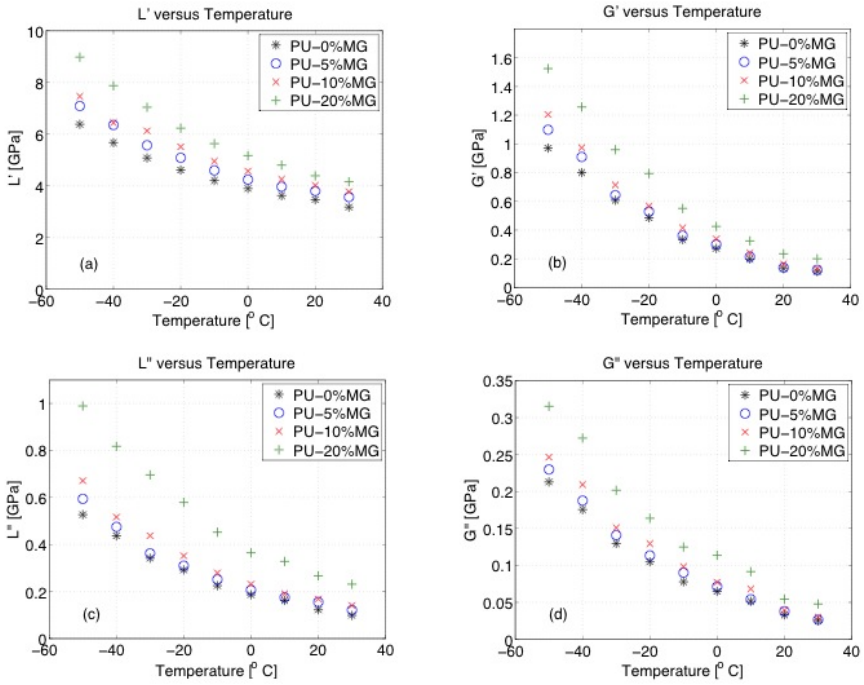

Figure 3.41: (a) L' versus temperature at 1 MHz, atmospheric pressure (b) G' versus temperature at 1 MHz, atmospheric pressure (c) L'' versus temperature at 1 MHz, atmospheric pressure. (d) G'' versus temperature at 1 MHz, atmospheric pressure

Frequency Dependent Master Curves

The time-temperature superposition was applied to DMA and ultrasonic wave testing data. With the assumption that all materials are thermorheological simple,

master curves were constructed. The process of how each master curve is constructed is discussed below, and this process will be used in the accompanying paper on micromechanical models for PU-MG composites [39]. The Young's storage and loss moduli for each material from DMA are shown in Figures 3.36a-d. Young's storage and loss moduli from ultrasonic wave testing are calculated, using equation 7.To construct Young's modulus master curve, both Young's storage and loss moduli of each material need to be normalized, by a factor that depends on density and temperature. This factor is suggested, based on the flexible chain theory (see equation 8) [36].

$$E_R^*(T,\omega) = E^*(T,\omega)\,\frac{\rho_{ref}T_{ref}}{\rho T}, \tag{3.54}$$

where $E_R^*(T,\omega)$ is the reduced complex Young's modulus at testing temperature, T and angular frequency, ω, and ρ_{ref} and ρ are densities of polyurea at reference temperature, T_{ref} and testing temperature, T respectively. We also use the density of pure polyurea in the factor for other PU-MG composites since the frequency-dependent behavior of the composites are essentially dominated by polyurea. The milled glass particles behave fully elastically and do not contribute to the frequency sensitivity of the composites (unless the wavelength is comparable with their length and spacing). T_{ref} and T are absolute temperatures. To construct the master curves, we only use the data above glass transition temperature ($-50\,^{\circ}$C for PU-0%MG and a little higher for other PU-MG composites), i.e. from -50 to 50 °C with 3 °C increments for DMA data and from -50 to 30 °C with 10 °C steps for ultrasonic wave testing. The reduced storage and loss moduli at each testing temperature are calculated, using equation 3.54 and plotted with respect to angular frequency in logarithmic scale. Each isothermal segment of the reduced storage and loss moduli is then shifted horizontally

and independently relative to the isothermal segment at a reference temperature, T_{ref}. We chose the reference temperature at around 1 °C that is the mid point of the considered testing temperature range. The shifted isothermal segments are assembled together; thereby creating a resultant master curve that covers a very wide range of angular frequency. The shift distance of each isothermal segment, a_T is plotted with respect to the testing temperature, T. Williams et al. proposed that the shift factor of a polymer is a function of a fractional free volume that is defined as a ratio of the free volume inside a polymer to the total volume (free volume plus occupied volume) of the polymer [51]. They also showed that the fractional free volume may be considered as a linear function of temperature.

$$\log a_T = \frac{B}{2.303}\left(\frac{1}{f\left(T\right)} - \frac{1}{f\left(T_{ref}\right)}\right), \tag{3.55}$$

where

$$f\left(T\right) = f\left(T_{ref}\right) + \alpha_f\left(T - T_{ref}\right), \tag{3.56}$$

B is a constant, $f\left(T\right)$ and $f\left(T_{ref}\right)$ are the fractional free volumes at the testing temperature, T and the reference temperature, T_{ref} respectively, α_f is the expansivity of the free volume inside the polymer. Substitute equation 3.56 into 3.55, we obtain WLF equation.

$$\log a_T = \frac{-c_1\left(T - T_{ref}\right)}{c_2 + T - T_{ref}}, \tag{3.57}$$

where

$$c_1 = \frac{B}{2.303 f\left(T_{ref}\right)}, \tag{3.58}$$

$$c_2 = \frac{f\,(T_{ref})}{\alpha_f}. \tag{3.59}$$

c_1 and c_2 are positive constants that depend on the material and the reference temperature. These two constants for each material can be obtained from fitting equation 3.57 to a plot of shift factor, $\log a_T$ versus the testing temperature T (see Figure 3.42). The two constants for each material are shown in Table 3.2. For further fundamental discussion, see [36, 51]. From DMA and ultrasonic wave testing data, master curve for each material at the reference temperature (T_{ref}= 274 K or 1 °C) were determined (see Figures 3.43a-d). Note that, the reduced Young's storage and loss moduli from ultrasonic wave testing at 1 MHz in Figures 3.43a,b, and d were shifted using shift factor obtained from DMA data.

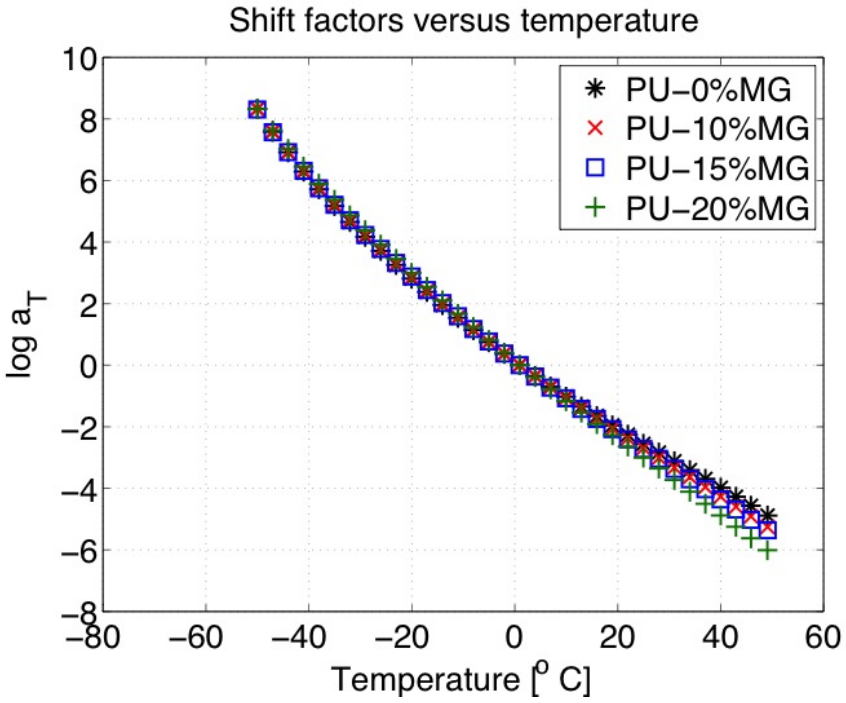

Figure 3.42: Shift factors, $\log a_T$ of PU-MG composites versus temperature

The shifting procedure based on the time-temperature superposition was done

Table 3.2: Constants c_1 and c_2 for PU-MG composites at $T_{ref} = 274\,\mathrm{K}$

	PU-0%MG	PU-10%MG	PU-15%MG	PU-20%MG
T_{ref} (K)	274	274	274	274
c_1	25.25	31.15	33.41	50.94
c_2 (K)	208.89	246.93	262	371.74

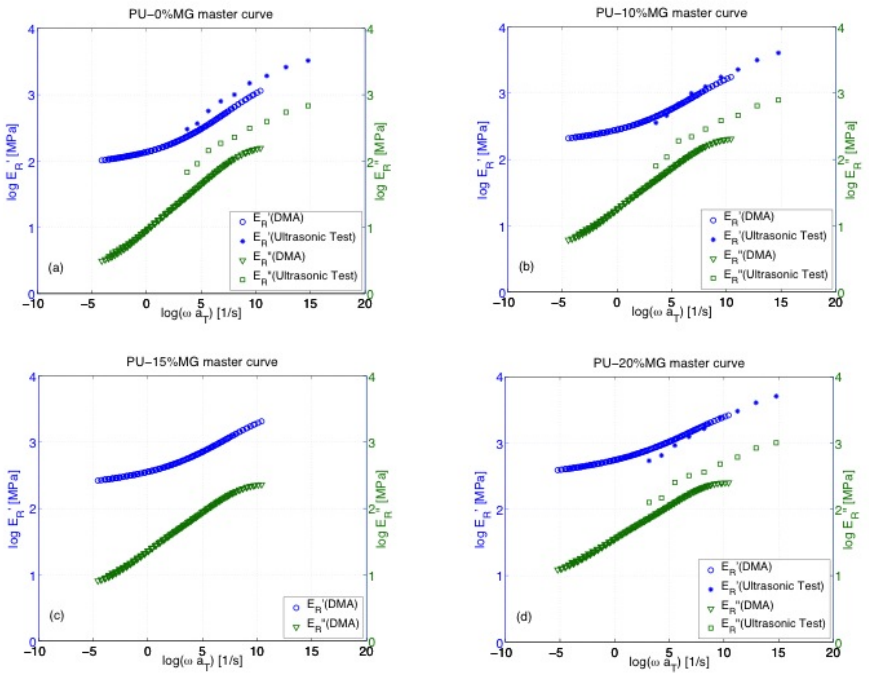

Figure 3.43: (a) Master curve of PU-0%MG (b) Master curve of PU-10%MG (c) Master curve of PU-15%MG (ultrasonic data was not collected for this case) (d) Master curve of PU-20%MG

with smooth transitions and therefore its application is qualitatively justified. As can be seen in Figures 3.43a-d, three regions on each master curve may be identified over the extended range of angular frequencies, considering DMA and ultrasonic wave testing data together. The storage modulus levels off, obviously, at low and, likely, at high reduced frequencies ωa_T. The plateau at low ωa_T represents rubbery zone. While, the plateau at high ωa_T represents glassy zone in which the material is very stiff. In the middle between the two plateaus, it represents the transition zone where

the behavior of the material is sensitive to frequency and temperature. As volume fraction of milled glass increases, the transition zone becomes smaller. In other words, the two plateau zones get close to each other. This is due to the fact that the material becomes more elastic or less frequency sensitive when more milled glass particles are added into the polyurea matrix. We can see that the reduced Young's storage modulus from DMA likely matches pretty well with that from ultrasonic wave testing; while, there is significant difference in the reduced loss modulus. Below $\log(\omega a_T) = 9$, the reduced loss moduli from DMA and Ultrasonic tests show similar trends. While, at $\log(\omega a_T)$ higher than 9, they deviate from each other. One possible reason is that the DMA data in this region are at the temperature close to $-50\,^{\circ}\mathrm{C}$ in which the materials are close to glassy state where the time-temperature superposition with WLF equation cannot be properly applied, thereby yielding unreliable loss modulus. While, the ultrasonic data of each material in this region are at temperature range of -20 to $-40\,^{\circ}\mathrm{C}$ that is higher than its glass transition temperature. It must be emphasized that the assumption of simple thermo-rheology is implicit in all such calculations. Note that since the MG fibers are not expected to introduce any further time-scales into this material (unless one deals with wavelengths that are comparable with their size and spacing), making such assumption for composites is somewhat equivalent to making it for pure PU. This issue has been addressed in detail elsewhere [31, 42, 47, 48, 52]. These frequency domain master curves of Young's storage and loss moduli can be used to explain viscoelastic behaviors of PUMG composites under unconfined uniaxial periodic excitation.

Time Domain Master Curve

Modeling of material response under complex histories, and design of polymer processing and applications often require the relaxation function, $E(t)$ or creep compliance, $D(t)$, instead of the storage and loss moduli, $E'(\omega)$ and $E''(\omega)$. Therefore it is of practical use to convert dynamic mechanical data from the frequency domain into the time domain. In this study, numerical methods of inter-conversions between the frequency and time domain moduli, and between relaxation and compliance functions are presented. Various inter-conversion methods can be found in [36, 49, 53, 54]. The relaxation and creep functions for solids in time domain can be represented in forms of Prony series as:

$$E(t) = E_e + \sum_{i=1}^{N} E_i e^{\frac{-t}{\tau_i}}, \tag{3.60}$$

$$D(t) = D_g + \sum_{i=1}^{N} D_i \left(1 - e^{\frac{-t}{\lambda_i}}\right), \tag{3.61}$$

where, E_e is equilibrium modulus as t goes to infinity, D_g is the instantaneous compliance at t equals to zero, E_i and D_i are relaxation and retardation strengths, and τ_i and λ_i are relaxation and retardation times. In frequency domain, the storage and loss moduli, $E'(\omega)$ and $E''(\omega)$ can be written as:

$$E'(\omega) = E_e + \sum_{i=1}^{N} \frac{(\omega\tau_i)^2 E_i}{(\omega\tau_i)^2 + 1}, \tag{3.62}$$

$$E''(\omega) = \sum_{i=1}^{N} \frac{\omega\tau_i E_i}{(\omega\tau_i)^2 + 1}. \tag{3.63}$$

Parameters τ_i, E_i, and N are unknown variables and can be found by simply fitting equations 3.62 and 3.63 to E'_R and E''_R data shown in Figure 3.43. The parameters E_i and τ_i are determined such that the sum of squared deviation between the predicted values and the experimental data is minimized (least squares nonlinear regression) [49]:

$$\text{error} = \sum_{j=1}^{m} \left\{ \left[\frac{E'(\omega_j)}{E'_R(\omega_j)} - 1 \right]^2 + \left[\frac{E''(\omega_j)}{E''_R(\omega_j)} - 1 \right]^2 \right\}, \tag{3.64}$$

where $E'_R(\omega_j)$ and $E''_R(\omega_j)$ are the experimental data from DMA at m frequencies ω_j. $E'(\omega_j)$ and $E''(\omega_j)$ are the calculated data from equations 3.62 and 3.63. Once parameters τ_i, E_i, and N are obtained from the least squares nonlinear regression, the relaxation function can be written based on equation 3.60. The retardation parameters λ_i, D_i, and D_g can then be calculated through the relationship between relaxation function and creep compliance in Laplace domain. Baumgaertel et al. has shown the very detailed calculation for polymeric liquid case [49]. Their method was later used to create the commercial software IRIS. However, it appears that some equations for the solid case described in the appendix of this reference require modification. The convolution integral relationship between the relaxation and creep functions transforms in the Laplace domain with variable s to:

$$\hat{E}(S)\,\hat{D}(S) = \frac{1}{S^2}. \tag{3.65}$$

Performing Laplace transform on equation 3.60, $\hat{E}(s)$ is:

$$\hat{E}(S) = \frac{E_e}{S} + \sum_{i=1}^{N} \frac{E_i}{S + \frac{1}{\tau_i}}. \tag{3.66}$$

Substitute equation 20 into 19, to obtain $\hat{D}(s)$ as:

$$\hat{D}(S) = \frac{1}{S} \frac{\frac{1}{E_0}\left[\prod_{k=1}^{N}\left(S+\frac{1}{\tau_k}\right)\right]}{\frac{E_e}{E_0}\left[\prod_{k=1}^{N}\left(S+\frac{1}{\tau_k}\right)\right] + S\sum_{i=1}^{N}\frac{E_i}{E_0}\left[\prod_{k=1,i}^{N}\left(S+\frac{1}{\tau_k}\right)\right]}, \tag{3.67}$$

where

$$E_0 = E_e + \sum_{i=1}^{N} E_i, \tag{3.68}$$

the notation $\prod_{k=1,i}^{N} a_k$ represents the multiplication of all a_k from $k = 1$ to N except a_i. The Laplace transform of Equation 3.61 can be written as:

$$\hat{D}(S) = \frac{A_0}{S} - \sum_{i=1}^{N} \frac{D_i}{S+\frac{1}{\lambda_i}}, \tag{3.69}$$

where

$$A_0 = D_g + \sum_{i=1}^{N} D_i. \tag{3.70}$$

By equating the denominator of equation 3.67 to that of equation 3.69, the N discrete retardation times, λ_i, may be calculated as the inverses of the real roots of the following polynomial equation for S:

$$\frac{E_e}{E_0}\left[\prod_{k=1}^{N}\left(S+\frac{1}{\tau_k}\right)\right] + S\sum_{i=1}^{N}\frac{E_i}{E_0}\left[\prod_{k=1,i}^{N}\left(S+\frac{1}{\tau_k}\right)\right] = \prod_{k=1}^{N}\left(S+\frac{1}{\lambda_k}\right). \tag{3.71}$$

Furthermore, the numerators of the partial fractions in equation 3.69 are

$$A_0 = \frac{1}{E_0}\left[\prod_{k=1}^{N}\frac{\lambda_k}{\tau_k}\right], \tag{3.72}$$

$$D_i = -\frac{1}{E_0}\frac{\left[\prod_{k=1}^{N}\left(1-\frac{\lambda_i}{\tau_k}\right)\right]}{\left[\prod_{k=1,i}^{N}\left(1-\frac{\lambda_i}{\lambda_k}\right)\right]}. \tag{3.73}$$

Once λ_i, D_i, and D_g (in equations 3.69 and 3.70) are found, the creep compliance can be calculated and plotted using equation 3.61.

The very good agreement between the experimental lines and the Prony series fits of the master curves are shown in Figure 3.44, and the parameters of the discrete relaxation and retardation spectra for all are presented in Figure 3.45a. The number of relaxation and retardation times, N is 23 for all materials. Baumgaertel et al. reported 8 and 18 modes for a blend of two monodisperse polystyrenes of different molecular weight and a commercial blend of tar and oil, respectively [49]. The number of relaxation and retardation times are higher due to the complexity of polyurea and its composites as solid phase separated elastomeric composites; a lower number terms for the discrete spectra leads to waviness in the calculated dynamic moduli; while, increasing the number of modes further rarely changes the error in equation 3.64. A method for developing computationally efficient Prony series for specific frequency ranges can be found in [31]. Figure 3.45b shows the time domain relaxation function and creep compliance for all composites calculated using equations 3.60 and 3.61. The relaxation function and creep compliance show two distinct regions of rubbery, and transitional behaviors with switch happening around 10^2 s for T_{ref}=274 K. As volume fraction of milled glass increases, the relaxation function increases, the creep compliance decreases, and the transitional stage becomes flatter or apparently less time-dependent possibly due to generally stiffer behavior of a higher volume fraction of glass in the polyurea matrix.

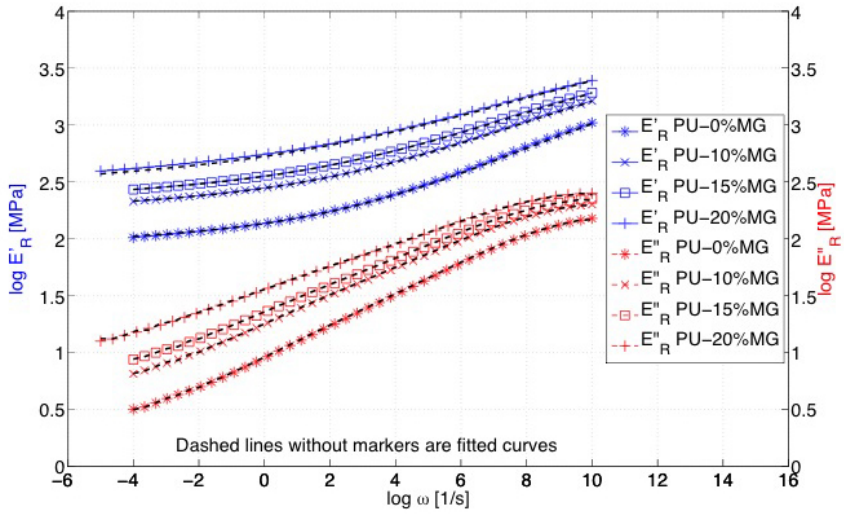

Figure 3.44: Comparisons between the measured E'_R and E''_R and the calculated E' and E''

3.4.5 Conclusions

In this study the dynamic properties of polyurea with various volume fractions of milled glass were studied using DMA at low frequencies and ultrasonics at high frequencies. PU-MG composites clearly demonstrate strong sensitivity to volume fraction of milled glass particles, temperature, and frequency. As volume fraction of milled glass increases, the composite becomes stiffer and lossier with a significant jump between 10% to 20% volume fraction of MG. Conversely, they become softer with increasing temperature. The high relative E'' (normalized with respect to pure PU) of the composites at high temperatures is observed in DMA; whereas, in ultrasonic tests, both relative L'' and G'' are flat over the entire range of tested temperature. Frequency dependent master curves of dynamic moduli for each material were created, using DMA and ultrasonic measurement data using time-temperature superposition model. It was observed that the Young's loss modulus values from ultrasonic measurements are higher than those predicted from DMA master curves, while

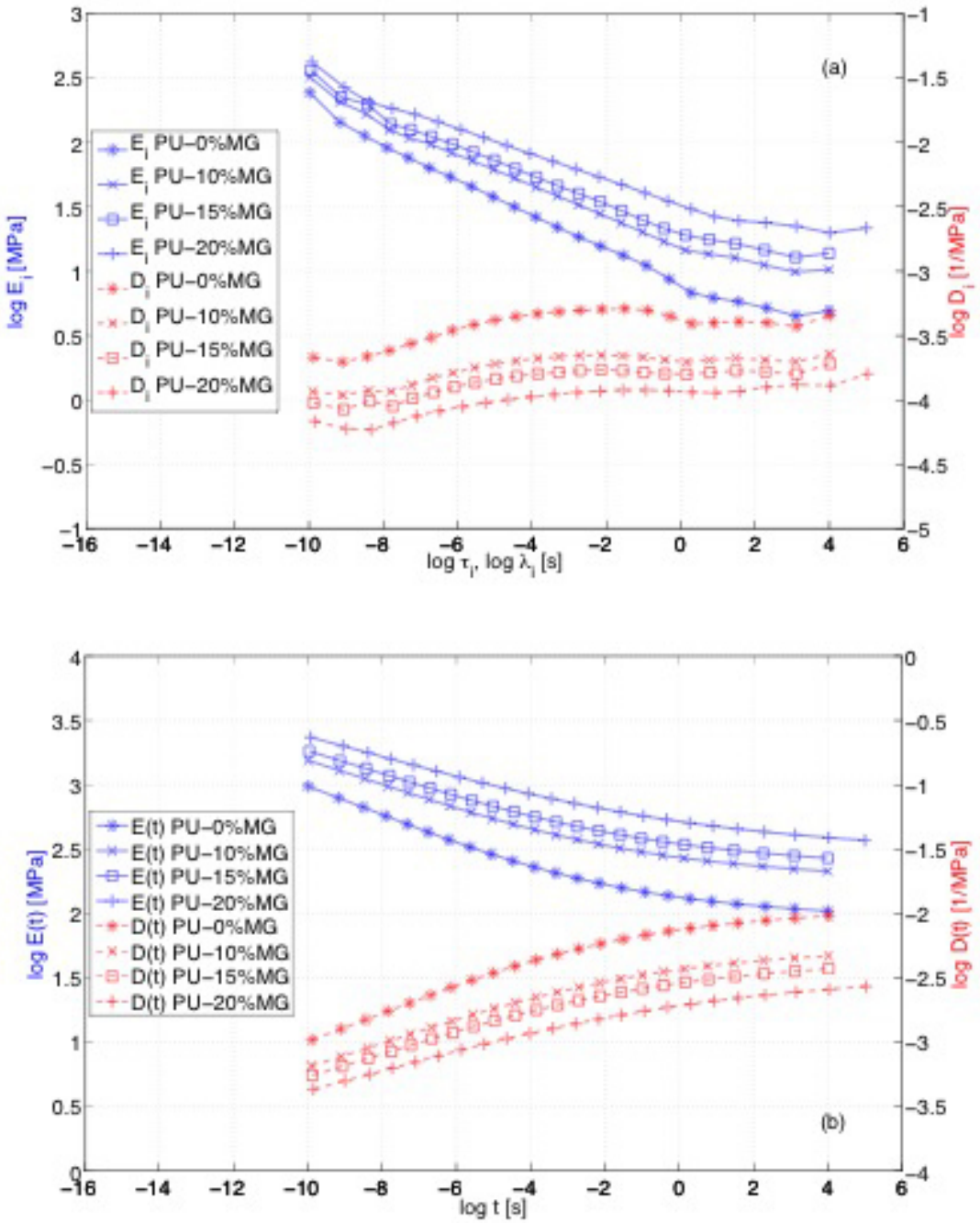

Figure 3.45: (a) Relaxation and retardation spectra (b) Relaxation function and creep compliance versus time

Young's storage modulus values correlated very well with the prediction from master curves. Time domain master curves, i.e. relaxation functions and creep compliances,

were also calculated. The discrete relaxation function can be used with commercial and other finite element software packages for design and analysis of composites. In the accompanying paper, the corresponding micromechanical models are presented to assist computational tools for estimating the mechanical properties of PU-MG composites [39]. The developed computational tools are not limited to PU-MG composite and may be used for other composites with similar microstructures.

3.5 A Novel Technique for Characterization of Elastomeric polyurea at kHz Frequencies

Elastomeric polyurea is a copolymer which has excellent chemical, thermal, and mechanical properties and is widely used as a coating material or protection material. The polyurea system used in this study is synthesized using Versalink P-1000 (Air Products) and Isonate 143L (Dow Chemicals). This polyurea has wide unique transitions of storage and loss moduli from rubber-like to glassy behaviors in which they extend from low to high frequencies. The characterization of polyurea is very challenging in the kHz frequency range, due to the long wave length and the dissipative nature of polyurea. In this study, we have developed a novel test technique by modifying the split Hopkins pressure bar and using ball impact to measure Young's storage and loss moduli of polyurea at kHz frequencies, which fills the frequency gap between dynamic mechanical analysis and ultrasonic wave measurement. The measured Young's storage and loss moduli from this technique are compared with the Young's storage and loss modulus master curves developed using experimental data of dynamic mechanical analysis and ultrasonic wave measurement. This technique is

a direct measurement which provides more reliable data in the kHz frequency range and can be used to evaluate the reliability, in the same frequency range, of other non-direct measurements including master curves. The usage of this technique is not limited to polyurea, it can also be used to characterize other polymeric materials at kHz frequencies.

3.5.1 Introduction

Elastomeric polyurea has excellent chemical, thermal, and mechanical properties. It can be used for chemical resistance (lab and factory floor protections) and truck bed abrasion protection [12]. Polyurea is tough and simultaneously dissipative. A recent application of polyurea is to improve the resistance of hard sturcture to failure [14] and ballistic penetration [15–17]. Moreover, it is also excellent for managing shock/impact-induced energy [46]. Polyurea has a unique relaxation behavior, which spans more than 10 decades on the logarithmic scale of frequency [31]. Its viscoelastic properties are highly sensitive to frequencies. Existing characterization techniques are not sufficient to directly measure its viscoelastic properties for the entire frequency range of its relaxation.

Towards the low frequency end, viscoelastic properties can be measured by dynamic mechanical analysis (DMA). The operating frequency range of modern DMA is in the order of 10^{-2} to 10^{2} Hz according to TA Instruments. For the high frequency end, ultrasonic wave measurement is the regular characterization technique. Normally testing frequency range of ultrasound spans from a little less than 50 kHz to 200 MHz [55]. The fundamental detail of this technique can be found in [56, 57]. Measurement at moderate frequency from 1 to several kHz is very challenging for ultrasonic wave

measurement since it requires large piezoelectric material and it also requires large transmitting media between transducers and the sample.

In order to fill the frequency gap between the regular operating frequency ranges of DMA and ultrasonic wave measurement, we have developed a novel measurement technique by modifying the split Hopkins pressure bar (SPHB) and using ball impact to measure Young's storage and loss moduli of polyurea at kHz frequencies. This new measurement is later on refereed to as acoustic ball impact test (ABI). Unlike standard operation of SPHB, we use an aluminum ball striker with diameter $\oslash_1 = 0.01905$ m (3/4 inch), incident and transmission aluminum bars with length $L = 1.219$ m (4 feet) each and diameter $\oslash_2 = 0.01905$ m (3/4 inch) to generate and propagate a compression wave pulse that contains low frequencies. The sample for this measurement is cylindrical and has the same diameter as the aluminum bars. The sample is placed between the incident and transmission similar to the sample location of the regular SPHB measurement. It is worth noting that this technique is considered as small deformation measurement. The tested sample maintains in original shape, and it is reusable. The impact force profile can be accurately estimated using Hertzian contact solution. The estimated impact force profile is used as a theoretical guidance to design the testing frequency content and the amplitude of the input compression pulse signal. We also integrated a temperature chamber, which enables us to test from -50 to 50 °C, considering viscoelastic properties of polymers are usually temperature-sensitive.

Incident, reflected, and transmitted signals are measured using two ultrasensitive semiconductor strain gages placed at the half-span of the two aluminum bars. Two tests with different sample lengths are required for determination of mate-

rial properties. Two transmitted signals from the two test are used to measure wave speed and attenuation in the material, using phase spectral analysis (PS) [58–61]. Transfer matrix method [62] together with the Incident, reflected, and transmitted wave signal from each test, is used to improve and validate the measured attenuation. The resulting wave speed and attenuation are used to calculate the Young's storage and loss moduli of the material. The Young's storage and loss moduli from this measurement are compared with the frequency domain master curves that were developed from the data of dynamic mechanical analysis (DMA). This test is not limited to polyurea characterization, and can be applied for other similar materials.

The following paper is organized as: Section 3.5.2 discusses design of the test and shows the experimental setup, Section 3.5.3 discusses design of the incident pulse, Section 3.5.4 presents sample fabrication, Section 3.5.5 provides the measurement and data analysis procedure, Section 3.5.6 shows results and discussions, and finally conclusions are discussed in Section 3.5.7.

3.5.2 Design of The Test and Experimental Setup

The SHPB measurement is a commonly used experimental technique to study behavior of metallic material at high strain rates [63–66]. However, if the specimen is a soft material, the acoustic impedance can be so low that the noise level often prevents proper interpretation of the transmitted signal obtained from a conventional SHPB experiment (Steel bar) [67]. Viscoelastic SHPB was developed and can provide measurable transmitted signal [68–70]; however it requires extensive effort and mathematical treatment of the signals obtained from the experiment due to the geometrical and material dispersions in the viscoelastic bar [68, 71].

To avoid material dispersion in the bar, two aluminum bars (7075-T6) of length L =1.219 m each and diameters $\oslash_2$ = 0.01905 m are used as the wave propagation medium in the ABI measurement. The high-strength aluminum alloy was chosen instead of conventional steel bar because at the same stress level, the lower Young's modulus of the aluminum alloy significantly increased the amplitude of the transmitted strain signal as compared to the steel bar [67].

The incident pulse is generated by the impact between an aluminum ball and the incident bar. The striker ball is made of the same grade of the aluminum as the aluminum bars and has diameter $\oslash_1$ = 0.01905 m. The reason to choose ball impact to generate incident pulse is because in such a way, the incident pulse can be a clear pure-compression bell-shaped signal. And importantly, the incident pulse can be modeled with Hertzian contact force such that the amplitude and frequency content of the pulse can be adjusted if necessary. The degree of impact depends on the velocity of the ball before impact. To control the ball velocity at impact, we developed a simple ball release system with a three-prong clamp to hold and release the ball, as in Figure 3.46. The ball is suspended by two strings in the form of V-shaped pendulum. The other ends of the two strings are hung on the horizontal pivot bar. The lengths of the strings and the height of the suspension pivot bar are adjustable to provide the desired ball impact speed and force (see Figure 3.46). In order to increase measurement sensitivity, two encapsulated Kulite G S/AGP-1000-300 semiconductor strain gages, which can operate up to 5000 microstrain in tension and 7000 microstrain in compression [72], were bonded on the side surface at the half-span of each bar (location S1 and S2) in the form of half Wheatstone bridge circuit (see Figure 3.47). The measured strain signals at S1 and S2 are sent through

BM-174-3 cables to the digital oscilloscope (Tektronix DPO 3014). To perform the ABI measurement at various temperatures, the temperature chamber, Sun Electronic System model ET1, is integrated into the measurement system (see Figure 3.47).

The length of the sample need to be estimated. In order to avoid the interference from multiple reflections, the length of the sample should be long enough to contain at least the longest length of one incident pulse in the sample. The longest length of the pulse occurs at the lowest testing temperature at which the wave speed is the maximum. By multiplying the maximum wave speed to the time period of the incident pulse (pulse width), the longest length of the pulse is obtained. The pulse width can be estimated using the Hertzian contact force model. In this test, the designed pulse width is around 0.06 ms (see Figure 3.50). However, we have no information on the wave speed in the material since it is the goal of this measurement. Therefore, the wave speed must be estimated. For our estimation, we used the wave speed in polyurea which is estimated from the square root of the Young's storage modulus (obtained from ultrasonic wave measurement at $-50\,^{\circ}\mathrm{C}$ and 1 MHz) divided by polyurea's density. The ultrasonic wave measurement result of polyurea can be found in [73]. The estimated wave speed is found to be around $1500\,\mathrm{m\,s^{-1}}$. Therefore, the length of the sample should be at least 0.09 m long ($1500\,\mathrm{m\,s^{-1}}$ x 0.06 ms). In this study, our polyurea samples with 10cm, 14cm, 16cm, 18cm are used.

3.5.3 Design of The Incident Pulse: Amplitude and Frequency Contents

The estimation of amplitude and rise time of the incident pulse is required in order to find out whether the frequency content in the incident pulse covers the desired

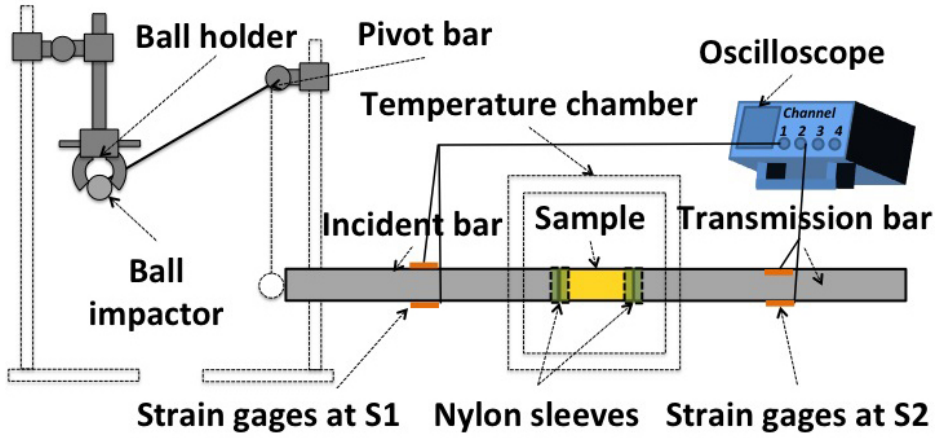

Figure 3.46: Schematic diagram of experimental setup

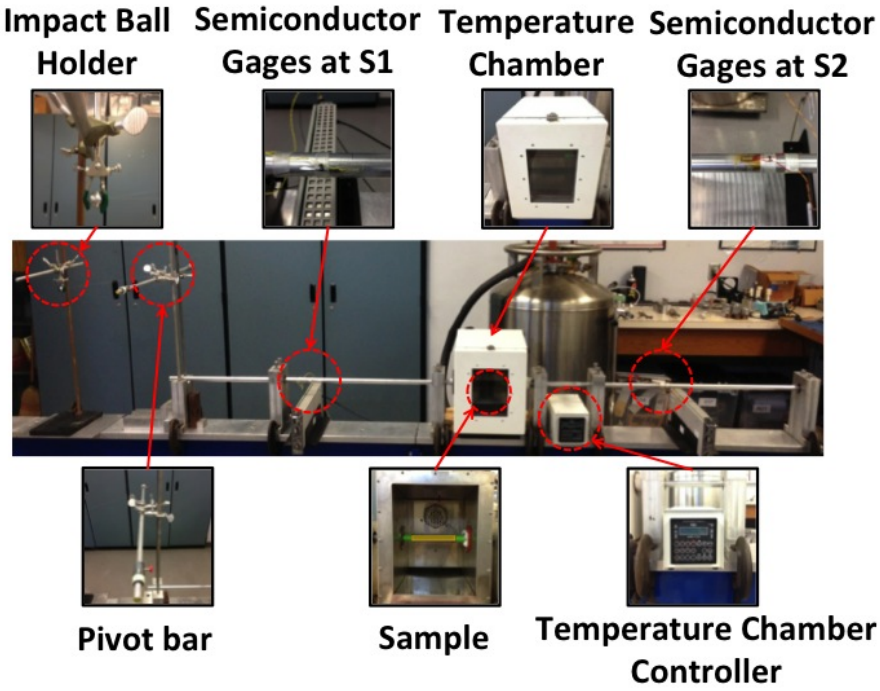

Figure 3.47: Real experimental setup

testing frequencies and whether amplitude at each frequency is strong enough to be measured by the strain gages on each bar. Since the ball and bars in ABI measurement are linearly elastic, the interaction force between the ball and incident bar can be represented through strongly nonlinear Hertzian interaction which is generally used in

the study of granular materials [74–77]. Due to the geometries of the impact surfaces of the ball and the incident bar, the force-deformation law is highly nonlinear and can be described by [74, 78, 79]:

$$F(\delta) = \tilde{k}\delta^{\frac{3}{2}}, \tag{3.74}$$

where

$$\tilde{k} = \frac{4}{3}E^*\sqrt{R^*}, \tag{3.75}$$

$$\frac{1}{\tilde{E}} = \frac{(1-\nu_1^2)}{E_1} + \frac{(1-\nu_2^2)}{E_2}, \tag{3.76}$$

$$\frac{1}{\tilde{R}} = \frac{1}{R_1} + \frac{1}{R_2}, \tag{3.77}$$

F is Hertzian contact force, $\tilde{k}$ is a constant, δ is the indentation, $\tilde{E}$ and $\tilde{R}$ are equivalent Young's modulus and relative radius of curvature of impact surface, respectively, E and ν are Young's modulus and Poisson's ratio, R is radius of curvature of impact surface, and the subscripts 1 and 2 refer to the ball and the bar. Figure 3.48 shows the schematic diagram of the impact problem between the ball and the bar. The ball is treated as point mass while the bar is treated as continuous mass. For our problem, the δ becomes:

$$\delta = u_1(t) - u_2(t, 0), \tag{3.78}$$

where $u_1(t)$ is displacement of the ball at time t, $u_2(t, 0)$ is the displacement of the impact surface of the incident bar at time t.

The normalized equations of motion governing the dynamics of the ball and

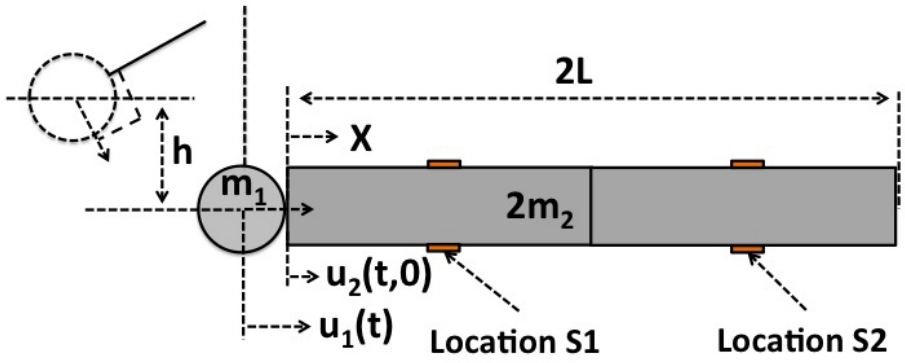

Figure 3.48: Schematic diagram of the impact problem between the ball and the bar

Table 3.3: All parameters for ABI calculation

$E_1 = E_2$	73.9	[GPa]
$\nu_1 = \nu_2$	0.33	-
$\rho_1 = \rho_2$	2807	[kg m^{-3}]
$\oslash_1 = \oslash_2$	1.905E-2	[m]
m_1	9.998E-3	[kg]
m_2	9.753E-1	[kg]
L	1.219	[m]
A	2.85E-4	[m^2]
R_1	9.47E-3	[m]
R_2	∞	[m]
D	35	[kg s^{-1}]
h	0.33	[m]

the bar are given by [74]:

$$\varepsilon \frac{d^2 U_1(\tau)}{d\tau^2} = -\left[U_1(\tau) - U_2(\tau,0)\right]^{\frac{3}{2}} H(U_1(\tau) - U_2(\tau,0)), \tag{3.79}$$

$$\frac{\partial U_2(\tau,0)}{d\tau} = \left[U_1(\tau) - U_2(\tau,0)\right]^{\frac{3}{2}} H(U_1(\tau) - U_2(\tau,0)), \tag{3.80}$$

where

$$U_1(\tau) = \beta^{-1} u_1(t), \tag{3.81}$$

$$U_2(\tau, 0) = \beta^{-1} u_2(t, 0), \tag{3.82}$$

$$\varepsilon = \frac{m_1}{2m_2}, \tag{3.83}$$

$$\tau = \psi^{-1} t, \tag{3.84}$$

$$\beta = \frac{E_2^2 A^2}{(2L)^2 \tilde{k}^2}, \tag{3.85}$$

$$\psi = \frac{2L}{c_0}, \tag{3.86}$$

$$c_0 = \sqrt{\frac{E_2}{\rho_2}}, \tag{3.87}$$

$U_1(\tau)$ is normalized displacement of the ball, $U_2(\tau, 0)$ is the normalized displacement of the impact surface of the incident bar, $H(\bullet)$ is the Heaviside step function, ε is mass ratio, τ is the normalized time, β and ψ are the normalized displacement and time factors, m_1 is the mass of the ball, m_2, ρ_2, L, and A are the mass, density, length, and cross-sectional area of one aluminum bar, c_0 is acoustic wave speed in aluminum bar. Generally, there is energy loss during impact from the dynamical interaction between the ball and the bar. This can be accounted by incorporating a viscous damping term

into equations 3.79 and 3.80 [77, 80]. The two equations become:

$$\varepsilon\frac{d^2U_1(\tau)}{d\tau^2} = -\left\{[U_1(\tau)-U_2(\tau,0)]^{\frac{3}{2}}+\eta\left[\frac{dU_1(\tau)}{d\tau}-\frac{\partial U_2(\tau,0)}{\partial\tau}\right]\right\} H(U_1(\tau)-U_2(\tau,0)), \tag{3.88}$$

$$\frac{\partial U_2(\tau,0)}{\partial\tau} = \left\{[U_1(\tau)-U_2(\tau,0)]^{\frac{3}{2}}+\eta\left[\frac{dU_1(\tau)}{d\tau}-\frac{\partial U_2(\tau,0)}{\partial\tau}\right]\right\} H(U_1(\tau)-U_2(\tau,0)), \tag{3.89}$$

where

$$\eta = \frac{LD}{m_2c_0}, \tag{3.90}$$

η and D are the normalized and the actual damping coefficient, respectively. Parameter D is obtained experimentally in [77] and is shown in Table 3.3. The initial conditions for the problem are:

$$U_1(0) = 0, \tag{3.91}$$

$$\frac{dU_1(0)}{d\tau} = \frac{\sqrt{2gh}}{\beta\psi}, \tag{3.92}$$

$$U_2(0,0) = 0. \tag{3.93}$$

$U_1(\tau)$, $U_2(\tau,0)$, $\frac{dU_1(\tau)}{d\tau}$, and $\frac{\partial U_2(\tau,0)}{\partial\tau}$ can be found by numerically solving equations 3.88 and 3.89 with initial conditions in equations 3.91, 3.92, and 3.93. All necessary parameters are shown in Table 3.3. Matlab function, ode43 was used to solve this problem. The unnormalized variables, $u_1(t)$, $u_2(t,0)$, $\frac{du_1(t)}{dt}$, and $\frac{\partial u_2(t,0)}{\partial t}$ can be cal-

culated with equations 3.81, 3.82, and 3.84. The the impact force that includes the effect of viscous damping can be calculated by:

$$F(t) = \tilde{k}\,[u_1(t) - u_2(t,0)]^{\frac{3}{2}}\,H(u_1(t) - u_2(t,0)). \tag{3.94}$$

The damping term is not included in equation 3.94 since it is already taken into account during the numerical calculation with equations 3.88 and 3.89. Adding damping to equation 3.94 does not effect much the profile of the impact force but it creates irregular tiny jump and drop at the head and tail of the force profile. To verify this impact force estimation, ABI measurement was performed without sample at 223 to 323 K with 10 K increments. Tests at various temperatures were conducted in order to determine the effect of temperature gradient on the two Aluminum bars since some parts of the aluminum bars are in the temperature chamber and some are outside the chamber (see Figure 3.46). The two aluminum bars were in contact and equilibrated at each temperature for 40 minutes. After that the ball was freed from the holder at the height of 0.33 m. The ball hit the incident bar at the left end. The compressive wave from the impact between the ball and the incident bar propagated through the incident and the transmission bars. The incident and the reflected strain signals were measured at strain gage S1 on the incident bar and the transmitted wave was measured on the strain gage S2 on the transmission bar (see Figure 3.48). The measured strain signals were then converted to force signals, using Young's modulus and cross-sectional area of the aluminum bar. The force signals are shown in Figure 3.49a. Then equation 3.94 was used to estimated force signal at impact location. Since the calculated force signal was not estimated at the measured force locations, it was then moved to locations S1 (half bar length) and S2 (one and a half bar length)

where the incident and transmitted signals were measured and dispersion corrected to include the effect of geometrical dispersion in the bars before comparison with the measured signals from ABI tests. The dispersion correction procedure can be found in [81]. The comparison between the calculated and the measured forces are shown in Figure 3.49a. Amplitude and frequency content of signals at S1 and S2 were then calculated, using Fast Fourier Transform (FFT) function in MATLAB and are shown in Figures 3.49b and 3.49c. As we can see, the amplitudes at S2 are slightly lower than those at S1. This is due to the fact that the two strain gages are not exactly the same. Therefore, the gage S1 was used as a baseline and the amplitude calibration factor for S2 was calculated by dividing amplitudes at S1 by those at S2. The calibration factor is shown in Figure 3.49d for 1 to 10 kHz. We can see that out force estimation is very close to the measurement. Therefore it verifies that our estimation is accurate and it can be used for designing the input pulse for other higher frequency range.

By changing calculation parameters, e.g. the drop height, the size and the properties of the ball, the profile of the impact pulse is changed, leading to the changes in amplitude and frequency contents of the pulse. Figure 3.50 shows how the pulse profile, the amplitude and frequency contents change, when a calculation parameter is changed while others are fixed. Figure 3.50a shows how the pulse profile changes when the diameter of the ball is changed. When the ball becomes bigger, the peak of pulse is higher and the duration of the pulse is wider. In other words, larger ball creates lower frequency pulse with higher signal strength (see Figure 3.50b). Figure 3.50c shows how the pulse profile changes when the drop height of the ball is changed. The higher the drop height, the higher the peak the pulse has. Unlike changing size of

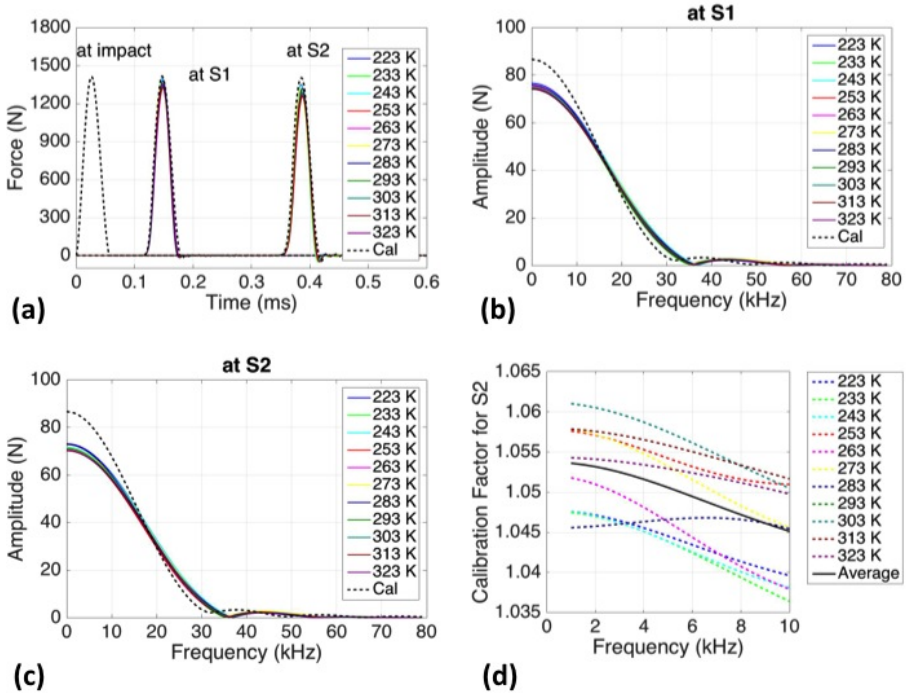

Figure 3.49: (a) The comparison between the measured and the calculated forces (b) Amplitudes of signal at S1 vs frequencies (c) Amplitudes of signal at S2 vs frequencies (d) Calibration factor for strain gage S2

the ball, changing the drop height does not change much the frequency content or duration of the signal (see Figure 3.50d). Figures 3.50e and 3.50g show how the pulse changes, when the ball properties, i.e. Young's modulus and Poisson's ratio change, respectively. We can see that when the ball becomes softer, it creates the pulse with lower frequency content (see Figure 3.50f). Adjusting Poisson's ratio almost does not change anything of the pulse (see Figures 3.50g and 3.50h).

3.5.4 Sample Fabrication

Polyurea samples are fabricated using Isonate 143L (Dow Chemical Company) and Versalink P-1000 (Air Product and Chemicals, Inc.). Isonate 143L is a polycarbodiimide-modified diphenylmethane diisocyanate that is liquid at room tem-

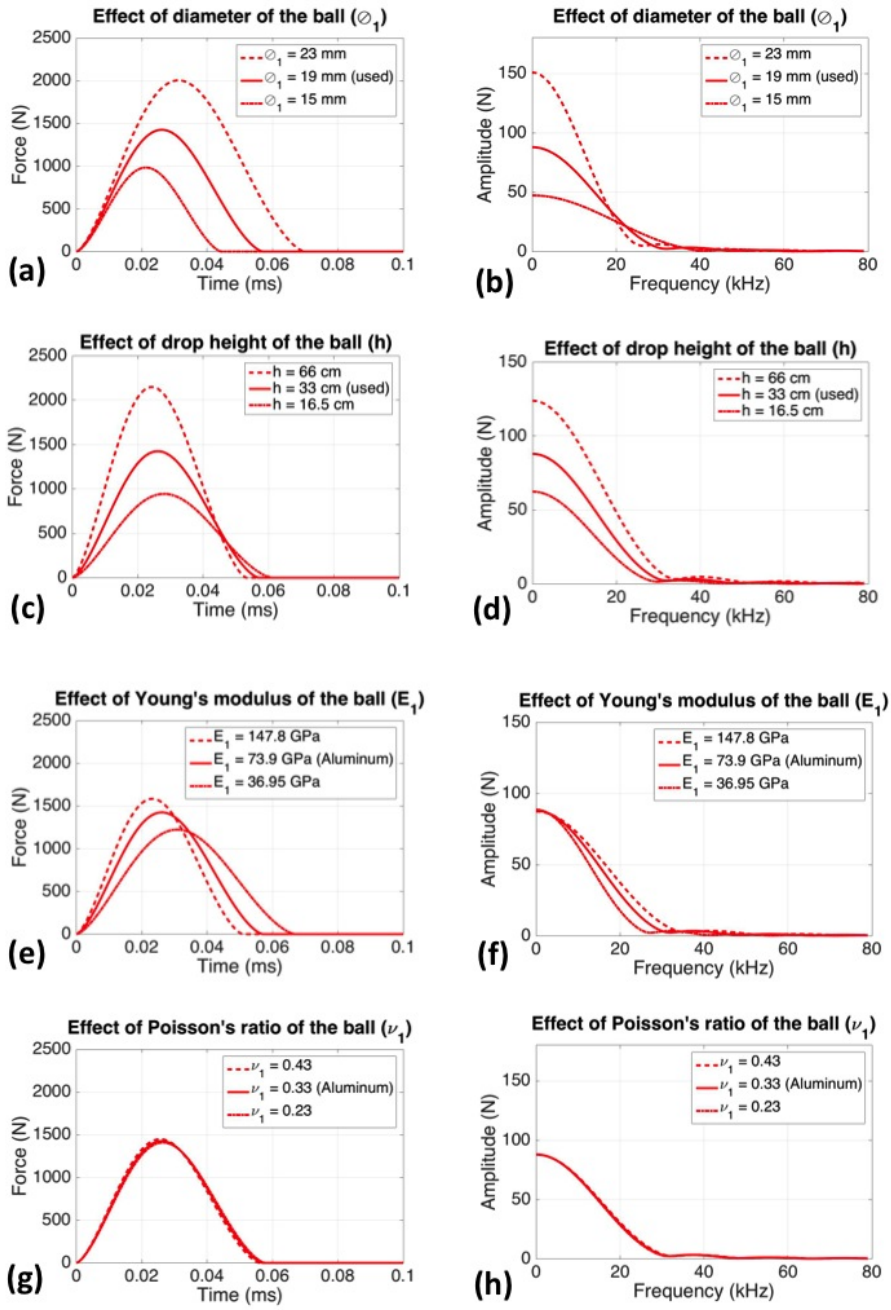

Figure 3.50: (a) Effect of $\oslash_1$ on force profile (b) Effect of $\oslash_1$ on amplitude and frequency contents (c) Effect of h on force profile (d) Effect of h on amplitude and frequency contents (e) Effect of E_1 on force profile (f) Effect of E_1 on amplitude and frequency contents (g) Effect of ν_1 on force profile (h) Effect of ν_1 on amplitude and frequency contents

perature. Versalink P-1000 is an oligomeric diamine, which is an amber liquid at ambient temperatures and can be mixed, cast and cured at room temperature. The stoichiometric ratio of Isonate 143L and Versalink P-1000 is controlled at 1.05:1 in the fabrication, since it has been shown that polyurea performs best at stoichiometric index 1.05 or higher [82]. The 5% extra isocyanate insures the completion of the chemical reaction.

The two components (Isonate 143L and Versalink P-1000) were first degassed at 1 torr while stirred by magnetic stir bars for an hour until most of the air bubbles were removed. Then appropriate amount of Isonate 143L was quickly added into Versalink P-1000, and the mixture was degassed for an additional 5 minutes under vacuum. The mixture was then transferred into the 1 foot long Teflon pipe using the experimental setup shown in the schematic drawing Figure 3.51a. The inner diameter of the Teflon pipe is 0.01905 m (3/4 inch), the same as the aluminum bars of the test setup. The valve at the bottom of the Teflon pipe was turned off at the end of the suction when the Teflon pipe was full. The Teflon pipe was set in the upright position after the polyurea suction to remove any air bubbles that could be trapped in the polyurea during the suction. The sample was cured in the desiccant chamber for two weeks before cutting and demolding.

The 0.3-m-long Teflon pipe with polyurea cast and cured inside was machined into sections of various lengths (see Figure 3.51b). Both ends of the polyurea samples were sanded with high accuracy such that the two ends of each sample were smooth and perpendicular to the axial direction. The final sample lengths were 4 cm, 6 cm, 8 cm, and 10 cm. These samples could be combined to make additional lengths for the test.

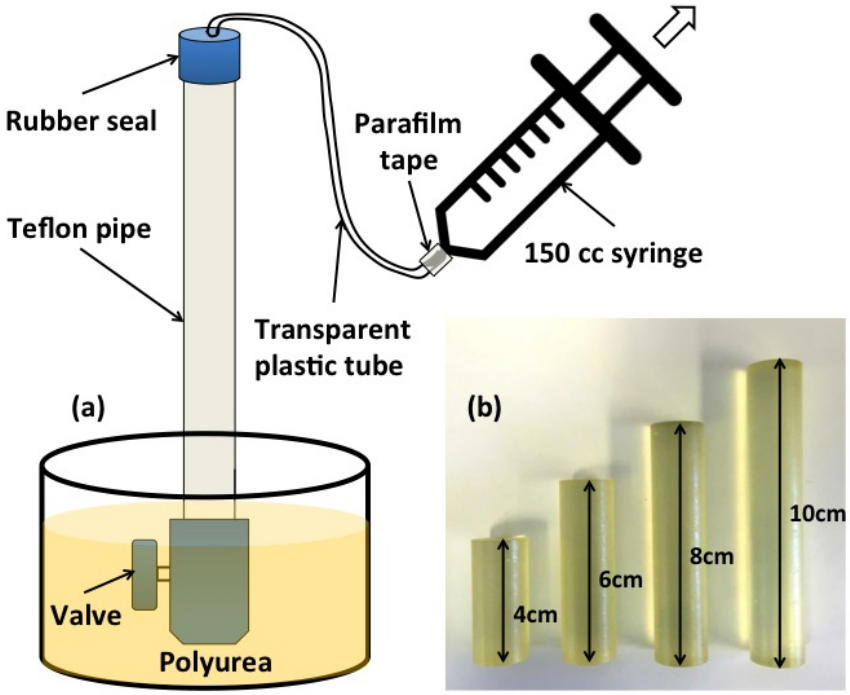

Figure 3.51: (a) Polyurea sample casting. (b) Machined polyurea bar samples of various lengths.

3.5.5 Measurement and Data Analysis Procedures

The unconfined modified Hopkinson bar testing is performed on polyurea sample from 223 to 323 K with 10 K increments. Two tests with two different sample lengths are required for measuring wave speed and attenuation of the sample. In test 1, a short sample is inside the temperature chamber and placed between the incident and transmission bars. The sample is aligned uniaxially with the bars. Two thin cylindrical sleeves made of nylon tape are used as support and alignment between the sample and bars (see Figure 3.46). Oil couplant is applied on all contact cross-sectional surfaces of the samples. Then the sample is equilibrated for 40 minutes at each testing temperature. The ball is set into place and held by the 3-prong clamp. The left cross-sectional surface of the incident bar is set at the location that the direction of the ball velocity when hitting the bar is perpendicular to the surface.

This location is consistent for all tests. After reaching thermal equilibrium, the ball impactor is released from the height of 0.33 m. The ball hits the incident bar at the left end. The compression wave from the impact between the ball and the incident bar propagates through the incident bar, the sample and the transmission bar, consecutively. The incident and the reflected signals are measured at strain gage S1 on the incident bar and the transmitted wave is measured on the strain gage S2 on the transmission bar. The signals are transmitted through BM-174-3 cables to a digital oscilloscope (Tektronix DPO3014) and recorded there (see Figure 3.46). The same procedure is followed for test 2 using a longer sample. The transmitted wave signals recorded at strain gage S2 from the two tests are used as inputs for phase spectral analysis (PS) to calculate attenuation, wave speed, Young's storage and loss moduli at each temperature. Transfer matrix calculation is then performed to improve and validate the calculated attenuation from PS, using the wave speed from PS and the information of incident, reflected, and transmitted waves that are recorded for each sample at each temperature. Figures 3.52a and 3.52b show examples of recorded signals at S1 and S2 on the incident and transmission bars, respectively. These signals are obtained from tests with 14-cm sample at 4 different temperatures.

Phase Spectral Analysis (PS)

At each testing temperature, the transmitted wave signals from the two tests with different sample lengths are converted to frequency domain using Fast Fourier Transform (FFT) function in MATLAB. Figure 3.52 shows examples of transmitted signals from tests with 14-cm sample at 4 different temperatures. As we can see, the tail of the transmission signals, which are the reflections, are cut off and replaced with

Table 3.4: Test matrix

Temperature	Sample pairs (length (cm), lenght (cm))	Tests per pair	Total
223 K	(10, 14), (10, 16), (10, 18)	2	6
233 K	(10, 14), (10, 16), (10, 18)	2	6
243 K	(10, 14), (10, 16), (10, 18)	2	6
253 K	(10, 14), (10, 16), (10, 18)	2	6
263 K	(10, 14), (10, 16), (10, 18)	2	6
273 K	(10, 14), (10, 16), (10, 18)	2	6
293 K	(10, 14), (10, 16), (10, 18)	2	6
303 K	(10, 14), (10, 16), (10, 18)	2	6
313 K	(10, 14), (10, 16), (10, 18)	2	6
323 K	(10, 14), (10, 16), (10, 18)	2	6

zero (see Figures 3.52b and 3.52d). After performing FFT, we obtain the complex amplitude (absolute amplitude and phase) of each frequency in the transmitted wave signals. The wave speed and attenuation can calculated using [58–60]:

$$c\left(f\right)=\frac{2\pi f\left(d_2-d_1\right)}{\left(\phi_2\left(f\right)-\phi_1\left(f\right)\right)}, \tag{3.95}$$

$$\alpha\left(f\right)=-\frac{1}{\left(d_2-d_1\right)}ln\left(\frac{A_2\left(f\right)}{A_1\left(f\right)}\right), \tag{3.96}$$

where c is wave speed, f is frequency of interest, d_1 and d_2 are lengths of samples in test 1 (thin) and test 2 (thick), respectively, ϕ_1 and ϕ_2 are unwrapped phases at frequency f from tests 1 and 2 respectively, α is attenuation per unit length, A_1 and A_2 are the absolute amplitudes at frequency f from tests 1 and 2, respectively. The Young's storage and loss moduli can be obtained from [20]:

$$E'=\frac{\rho c^2(1-r^2)}{(1+r^2)^2}, \tag{3.97}$$

$$E'' = \frac{2\rho c^2 r}{(1+r^2)^2}, \tag{3.98}$$

where

$$r = \frac{\alpha c}{\omega}, \tag{3.99}$$

$$E^* = E' + E''i, \tag{3.100}$$

E', E", and E^* are Young's storage, loss and complex moduli, respectively, ρ is the density of the sample, r is dimensionless parameter, and ω is angular frequency. At each temperature, 6 tests were performed see Table 3.4. The best wave speed, attenuation, Young's storage, and loss moduli at a given frequency and temperature are the average numbers over the 6 tests.

Transfer Matrix Calculation (TM)

Transfer matrix calculation is an effective method to calculate reflected, transmitted, and dissipated energies of a harmonic plane wave propagating through a one dimensional layered composite sandwiched between two homogeneous half-spaces, based on the given geometries and properties of each material component in the composite [62, 83, 84]. According to the one-dimensional propagations of harmonic waves, the displacement and stress in the polyurea sample are in the following forms:

$$u^S = ae^{i(\omega t - k^* x)} + be^{i(\omega t + k^* x)}, \tag{3.101}$$

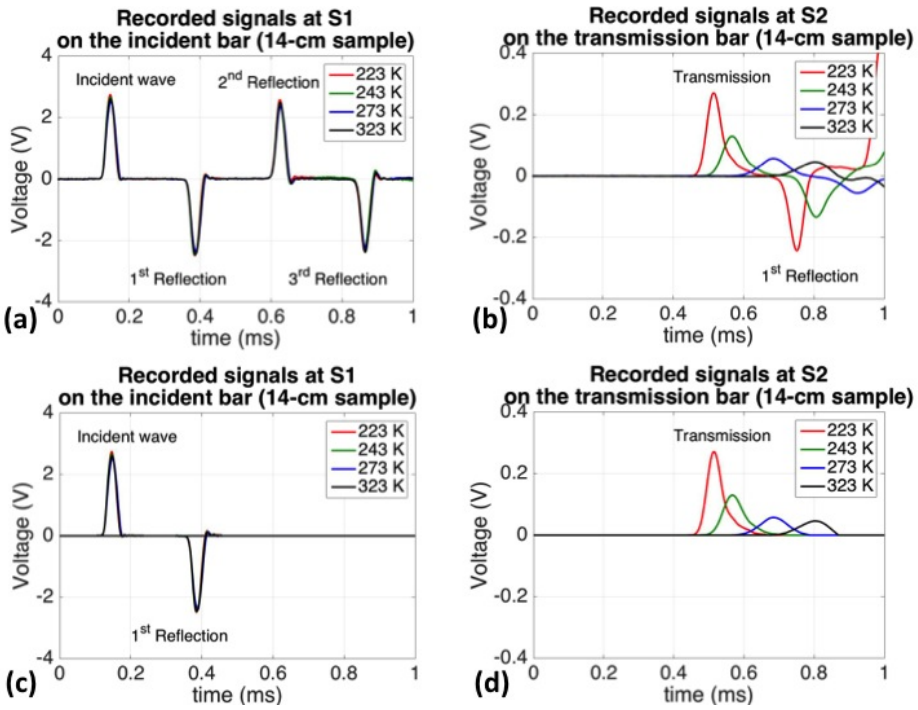

Figure 3.52: (a) recorded signals at S1 on the incident bar (b) recorded signals at S2 on transmission bar (c) Incident and 1^{st} reflected signals at S1 on incident bar (d) transmitted signals at S2 on the transmission bar.

$$\sigma^S = -ik^* E^* a e^{i(\omega t - k^* x)} + ik^* E^* b e^{i(\omega t + k^* x)}, \tag{3.102}$$

where

$$k^* = \frac{\omega}{c*}, \tag{3.103}$$

$$c^* = \sqrt{\frac{E^*}{\rho}}, \tag{3.104}$$

$u^S$and σ^S are the displacement and stress fields, a and b are unknown constants, k^* and c^* are the wavenumber and the complex wave speed in the polyurea sample, respectively. Similarly, the displacements and stresses in the incident and transmission bars have the same forms with the bars's properties. The first terms on the right hand

side of equations 3.101 and 3.102 are related to the wave propagating to the right, and the second terms are related to the wave propagating to the left. The relations between displacements and stresses at the left and right boundaries of the sample can be written as [62, 83]:

$$\begin{bmatrix} u_R^S \\ \sigma_R^S \end{bmatrix} = \boldsymbol{T} \begin{bmatrix} u_L^S \\ \sigma_L^S \end{bmatrix}, \tag{3.105}$$

where

$$\boldsymbol{T} = \begin{bmatrix} cos(kd) & \frac{-sin(kd)}{E^*k} \\ E^*ksin(kd) & cos(kd) \end{bmatrix}, \tag{3.106}$$

u_L^S and u_R^S are displacements in the sample at the left and the right boundaries respectively, σ_L^S and σ_R^S are the stresses in the sample at the left and the right boundaries respectively, $\boldsymbol{T}$ is the transfer matrix. Due to the continuities of displacements and stresses at the interfaces between the sample and the two bars, the displacements and stresses at the left and right boundaries can be written as:

$$\begin{aligned} u_L^S &= u^S(x=0) = u^{B1}(x=0) \\ &= \hat{A}_{In}e^{i(\omega t)} + \hat{A}_{Re}e^{i(\omega t)}, \end{aligned} \tag{3.107}$$

$$\begin{aligned} u_R^S &= u^S(x=d) = u^{B2}(x=d) \\ &= \hat{A}_{Tr}e^{i(\omega t - k_{B2}d)}, \end{aligned} \tag{3.108}$$

$$\begin{aligned} \sigma_L^S &= \sigma^S(x=0) = \sigma^{B1}(x=0) \\ &= -ik_{B1}E_{B1}\hat{A}_{In}e^{i(\omega t)} + ik_{B1}E_{B1}\hat{A}_{Re}e^{i(\omega t)}, \end{aligned} \tag{3.109}$$

$$\begin{aligned} \sigma_R^S &= \sigma^S(x=d) = \sigma^{B2}(x=d) \\ &= -ik_{B2}E_{B2}\hat{A}_{Tr}e^{i(\omega t - k_{B2}d)}, \end{aligned} \tag{3.110}$$

where

$$k_{B1} = \frac{\omega}{c_{B1}}, \tag{3.111}$$

$$k_{B2} = \frac{\omega}{c_{B2}}, \tag{3.112}$$

$$c_{B1} = \sqrt{\frac{E_{B1}}{\rho_{B1}}}, \tag{3.113}$$

$$c_{B2} = \sqrt{\frac{E_{B2}}{\rho_{B2}}}, \tag{3.114}$$

u^{B1} and u^{B2} are displacements in the incident and the transmission bars respectively, σ^{B1} and σ^{B2} are stresses in the incident and the transmission bars respectively, position $x = 0$ is at the left boundary of the sample, position $x = d$ is at the right boundary of the sample (see Figure 3.53), $\hat{A}$ is the amplitude of displacement, the subscripts In, Re, and Tr refer to incident, reflected, and transmitted waves, k_B, c_B, E_B, and ρ_B are the wavenumber, the wave speed, the Young's modulus, and the density of the bar, where the subscript 1 and 2 refers to the incident and transmission bars respectively, d is length of the sample (see Figure 3.53). From equations 3.107 - 3.110, equation 3.105 can be written in term of amplitudes of incident, reflected, and transmitted waves as:

$$\begin{bmatrix} \hat{A}_{Tr} \\ 0 \end{bmatrix} = \boldsymbol{K} \begin{bmatrix} \hat{A}_{In} \\ \hat{A}_{Re} \end{bmatrix}, \tag{3.115}$$

where

$$\boldsymbol{K} = \boldsymbol{D_{B2}^{-1}} \boldsymbol{B_{B2}^{-1}} \boldsymbol{T} \boldsymbol{B_{B1}}, \tag{3.116}$$

$$\boldsymbol{D_{B2}} = \begin{bmatrix} e^{-ik_{B2}d} & 0 \\ 0 & e^{ik_{B2}d} \end{bmatrix}, \tag{3.117}$$

$$\boldsymbol{B_{B2}} = \begin{bmatrix} 1 & 1 \\ -ik_{B2}E_{B2} & ik_{B2}E_{B2} \end{bmatrix}, \tag{3.118}$$

$$\boldsymbol{T} = \begin{bmatrix} cos(kd) & \frac{-sin(kd)}{E^*k} \\ E^*ksin(kd) & cos(kd) \end{bmatrix}, \tag{3.119}$$

$$\boldsymbol{B_{B1}} = \begin{bmatrix} 1 & 1 \\ -ik_{B1}E_{B1} & ik_{B1}E_{B1} \end{bmatrix}, \tag{3.120}$$

From equation 3.115, $\hat{A}_{Re}$ and $\hat{A}_{Tr}$ can be written in term of $\hat{A}_{In}$ as:

$$\hat{A}_{Re} = -\frac{K_{21}}{K_{22}} \hat{A}_{In}, \tag{3.121}$$

$$\hat{A}_{Tr} = \left(K_{11} - \frac{K_{12}K_{21}}{K_{22}} \right) \hat{A}_{In}, \tag{3.122}$$

where K_{ij} is component ij $(i, j = 1, 2)$ of the matrix $\boldsymbol{K}$. Since the energy of acoustic wave is proportional to the square of its amplitude, we then define energy reflection and transmission coefficients, RC and TC as:

$$RC = \left| \frac{A_-^{(0)}}{A_+^{(0)}} \right|^2 = \left| -\frac{K_{21}}{K_{22}} \right|^2, \tag{3.123}$$

$$TC = \left| \frac{A_+^{(Nm+1)}}{A_+^{(0)}} \right|^2 = \left| K_{11} - \frac{K_{12}K_{21}}{K_{22}} \right|^2 . \tag{3.124}$$

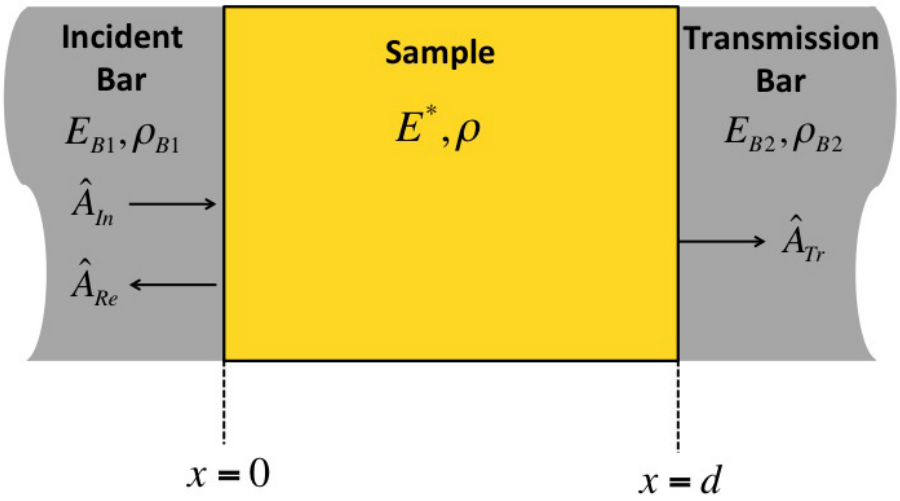

Figure 3.53: Displacement amplitudes of incident ($\hat{A}_{In}$), reflected ($\hat{A}_{Re}$), and transmitted ($\hat{A}_{Tr}$) waves at boundaries of the sample

When the transmitted wave signal is small, especially at high temperature, the measured attenuation from PS analysis might not be accurate . TM calculation can be used to improve and validate the measured attenuation. Consider a testing temperature, at a given frequency, f (or angular frequency, ω), only E^* of the sample is the input for TM calculation, assumed that the sample length (d), sample density (ρ) and the properties ($E_{B1}, E_{B2}, \rho_{B1}, \rho_{B2}$) of the two bars are known. E^* depends on wave speed and attenuation and can be calculated using equations 3.97 - 3.100. In TM calculation, the wave speed is the average wave speed obtained form PS and is fixed at each frequency. The attenuation is guessed and runs from 0 to $\frac{\omega}{c}$ neper/m, with $\frac{\omega}{c} \times 10^{-6}$ neper/m increments, where c is the average wave speed at the corresponding frequency from PS analysis. At a given frequency, the energy reflection

and transmission coefficients, RC and TC are calculated for each guessed attenuation using equations 3.123 and 3.124. These RC and TC from TM calculation are referred as RC_{CAL} and TC_{CAL} and will be compared with RC and TC obtained from experiment which are referred as RC_{EXP} and TC_{EXP}. To calculate RC_{EXP} and TC_{EXP}, the incident, reflected, and transmitted wave signals recorded from ABI measurement on the sample with the same length as in TM calculation are needed. Figures 3.52c and 3.52d show the examples of the incident, reflected, and transmitted signals from tests with 14-cm sample at four different temperatures. To be noted, the tails of the signals are already eliminated. At a given temperature, the amplitudes of the three signals as functions of frequency are obtained by performing FFT on the three signals. Then RC_{EXP} and TC_{EXP} are calculated for each frequency using equations 3.123, and 3.124. The acceptable attenuation at each frequency is the guessed attenuation that minimizes the following equation:

$$\begin{aligned} Error^i(f) &= \left(\frac{TC_{EXP}(f) - TC^i_{CAL}(f)}{TC_{EXP}(f)}\right)^2 \\ &\quad + \left(\frac{RC_{EXP}(f) - RC^i_{CAL}(f)}{RC_{EXP}(f)}\right)^2, \end{aligned} \tag{3.125}$$

where superscripted i refers to the i-th guessed attenuation. The same precess is applied on all data of other sample lengths. At a given temperature, the best attenuation at each frequency is obtained by averaging the 4 acceptable attenuations received from TM calculations of the 4 cases with different sample lengths; 10, 14, 16, and 18 cm. This process is repeated for all other testing temperatures.

3.5.6 Results and Discussions

The results from PS analysis are shown in figure 3.54. From our observation, we consider frequency in the range of 5 to 10 kHz for Polyurea since acoustic waves in the incident and transmission bars with frequencies below this range have wavelength longer than the length of the two bars and the acoustic waves in the sample with frequencies higher than this range are very dissipative and cannot be measured. Therefore the frequencies outside this range cannot be reliably measured by the current test setup. Figure 3.54a shows attenuation per unit length, α as a function of frequency. As we can see, α linearly increases with frequency in the range of 5 to 10 kHz, except at the two highest temperatures where it shows nonlinear behavior with the drop at high frequency. This nonlinear behavior can be corrected with TM calculation (see figure 3.55a). Figure 3.54b shows wave speed as a function of frequency at various temperatures. We can see that the wave speed slightly increases with frequency. This trend is less obvious at high temperature. The wave speed also increases as temperature decreases. This is due to that at low temperature polyurea becomes denser, stiffer, therefore vibrational energy can be transferred easier and faster. This trend is also observed in ultrasonic wave measurement [20, 73]. Figures 3.54c and 3.54d show E' and E" as functions of frequency. Similar to wave speed, E' increases with frequency. This trend is also observed in E'', except at the lowest temperatures where it slightly lower at high frequency. E'' can be improved using α from TM (see figure 3.55c).

Figure 3.55a shows α that is calculated using TM calculation with wave speed from PS analysis. As mentioned previously, TM calculation takes into account multiple reflection in the sample, thereby improving quality of attenuation measurement.

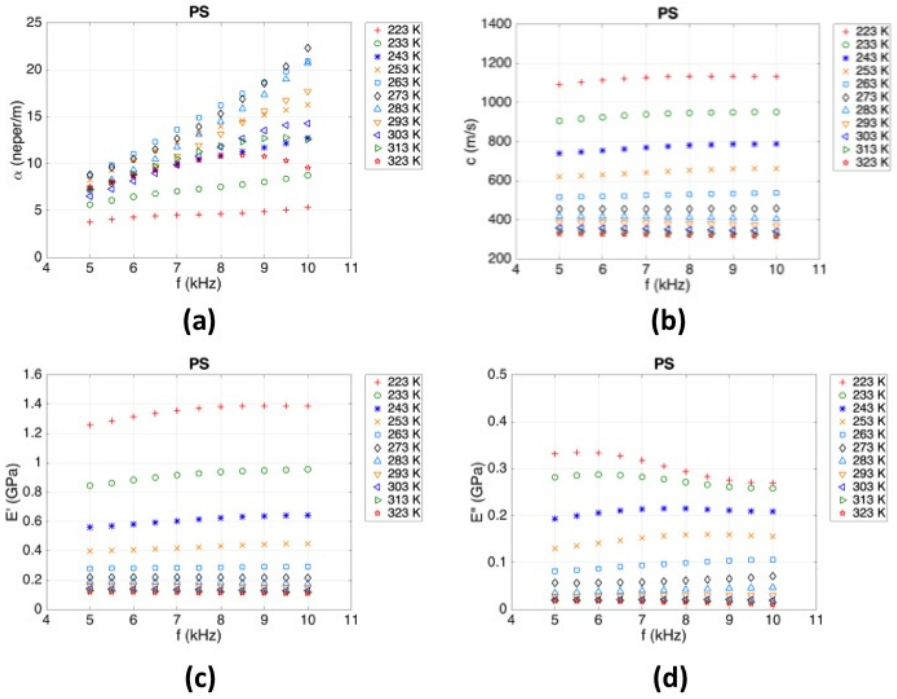

Figure 3.54: (a) α from PS versus frequency (b) c from PS versus frequency (c) E' from PS versus frequency (d) E'' from PS versus frequency

Moreover, in TM the attenuation was calculated using incident, reflected, and transmitted signals from single ABI test with one sample length while in PS it requires two transmitted signals from two ABI tests with two different sample lengths. Therefore, in TM calculation it minimizes error from the difference between the two environmental conditions of the two ABI tests. It is believed that the attenuation calculated with TM is more reliable. From figure 3.55a, it is apparent that α increases linearly with frequency. Its slope increases as temperature increases. At around 273 K and higher, α and its slope becomes saturated which is different from what we observed with α calculated using PS in figure 3.54a. Figure 3.56 shows the Comparison between attenuations from PS and TM as functions of temperature. At high frequency, α from PS develops a peak around 273 K and drops down, while α from TM develops a peak at around 283 K, gradually decreases, and converges to a number. As frequency

decreases, the peaks becomes smaller for the two cases. Figures 3.55b and 3.55c show E' and E'' calculated with wave speed, c from PS and attenuation, α from TM as functions of frequency. Clearly, E' and E'' increases with frequency except at 223 K where E'' exhibits fluctuation with increasing trend according to the behavior of the attenuation at the same temperature.

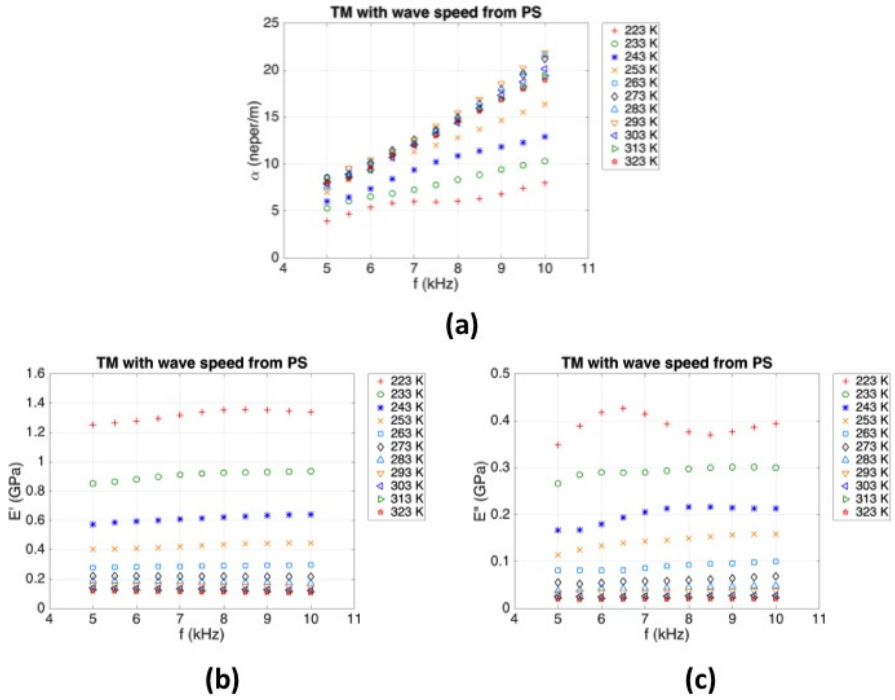

Figure 3.55: (a) α (calculated using TM with c from PS) versus frequency (b) $E^{'}$ (calculated with c from PS and α from TM) versus frequency (d) E" (calculated with c from PS and α from TM) versus frequency

Even though DMA tests are conducted at much lower frequencies than ABI test, and the sample deformation in the DMA test is totally different from the deformation in the wave propagation in a bar, it is still meaningful to compare the trend of the attenuation calculated form DMA test to the attenuation from ABI test. Figure 3.57 shows the Young's storage and loss moduli of polyurea fabricated from the same batch as the samples for ABI test. The detail of the DMA measurement

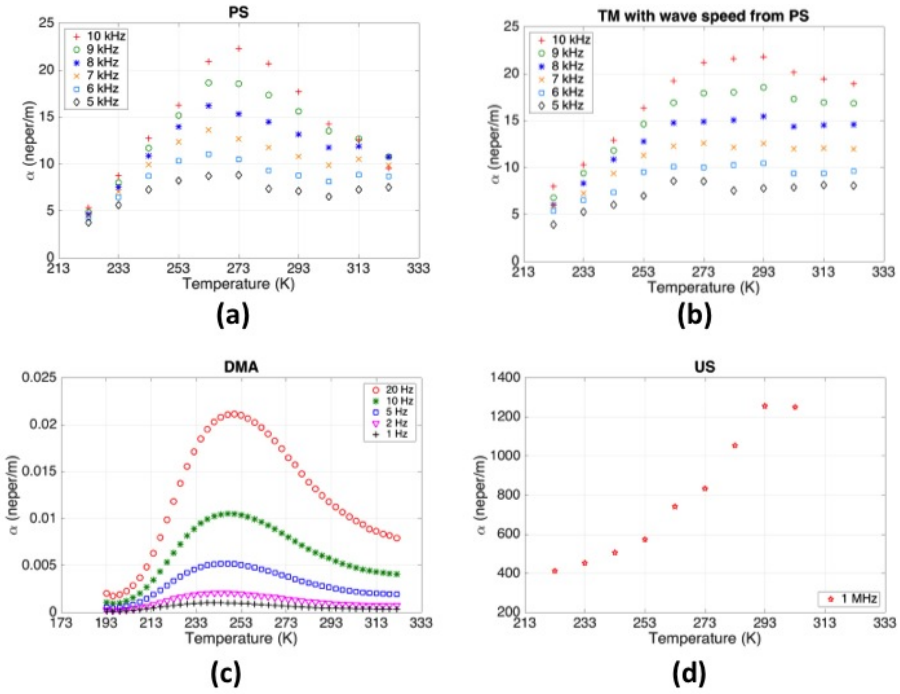

Figure 3.56: (a) attenuation from PS as a function of temperature (b) attenuation from TM as a function of temperature (c) attenuation from DMA as a function of temperature (d) attenuation from US as a function of temperature

can be found in [31, 73]. The attenuation can be calculated from the DMA data by the following equations:

$$\alpha_{DMA} = \frac{\omega r_{DMA}}{c_{DMA}}, \tag{3.126}$$

where

$$c_{DMA} = \sqrt{\frac{E'_{DMA}(1 + r_{DMA}^2)^2}{\rho(1 - r_{DMA}^2)}}, \tag{3.127}$$

$$r_{DMA} = \frac{-1 + \sqrt{1 + tan^2\delta_{DMA}}}{tan\delta_{DMA}}, \tag{3.128}$$

$$\tan\delta_{DMA} = \frac{E''_{DMA}}{E'_{DMA}}, \tag{3.129}$$

subscript DMA refers to data from DMA. E'_{DMA} and E''_{DMA} are Young's storage and loss moduli from DMA (shown in Figure 3.57). Equation 3.127 and 3.128 are derived by direct solving equations 3.97, and 3.98, using $\tan\delta_{DMA}$ defined in equation 3.129. Similarly, the attenuation can be calculated from the data of ultrasonic wave measurement (US) by replacing parameters with subscript DMA with the corresonding paprameters from US. Young's storage and loss moduli from US can be found in [73].

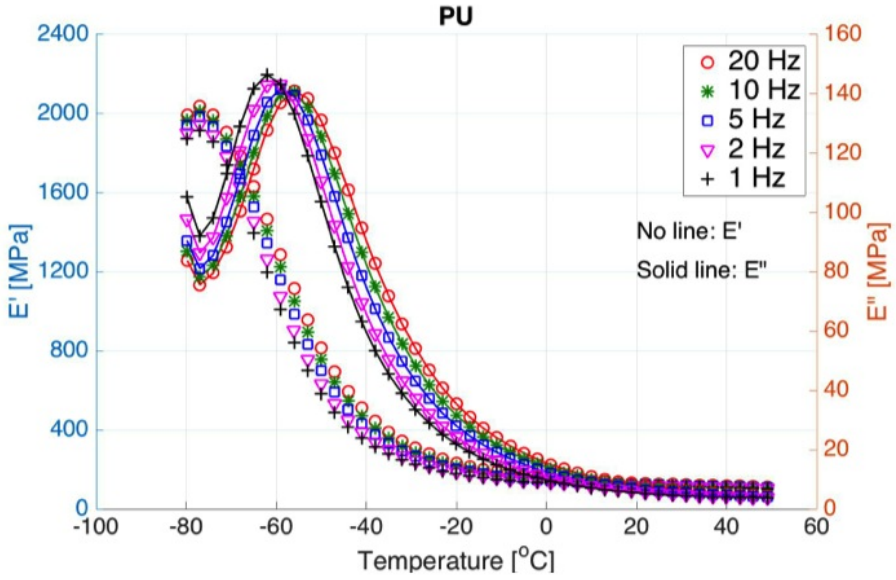

Figure 3.57: Young's storage and loss moduli from DMA

The attenuation of pure polyurea between 193 to 323 K, at 1 Hz, 2 Hz, 5 Hz, 10 Hz and 20 Hz is shown in Fig. 3.56c. It should be noted that equations 3.97, 3.98 and 3.99 are derived from wave propagation while DMA test is a single cantilever bending test, and they are very different measurement techniques. But the trend of the attenuation calculated from the DMA data are in consistent with the attenuation measured by the ABI test, especially after improvement with TM calculation (see

Figures 3.56b and 3.56c). As we can see, α_{DMA} develops a peak at around 247 K, gradually decreases, and converges to a number. We believe that this peak is an indiction of the glass transition in Polyurea; even though, it occurs at different temperature, compared to the temperature at the peak of E''_{DMA} which is widely used to determine the glass transition temperature T_g. This supports that T_g is not a discrete thermodynamic transition, but a temperature range over which the mobility of the polymer chains undergoes significant change. As expected, peaks of α_{DMA} occur at lower temperature, compared to the peaks of α from TM calculation since polyurea chains have higher mobilities at lower frequency, thereby requiring lower temperature to transform into glassy state. Figure 3.56d shows the attenuation of pure polyurea between 213 to 333 K, from US at 1 MHz. Interestingly, the attenuation calculated with US data has similar behavior, compared to attenuation from ABI test. Attenuation from US increases with increasing temperature and develops a peak around 293 K which is a little higher than peak of ABI test. However, above 303 K the trend of the attenuation from US cannot be revealed because of the lack of data above 303 K. Compare the trends of the three calculated attenuations from three different tests shown in Figures 3.56a-d, it suggests that the attenuation measured by the ABI test, can be improveed with TM calculation.

Figure 3.58a shows comparison between four master curves of polyurea constructed using data from three different methods; DMA, ABI, and ultrasonic wave measurement. The information on how to create a master curve can be found in [31, 73]. E'_R and E''_R are Young's storage and loss moduli at reference temperature, 274 K. Shift factor, $log(a_T)$ shown in figure 3.58b was obtained from shifting DMA data and was used to shift other test data. The shift factor can be fitted with

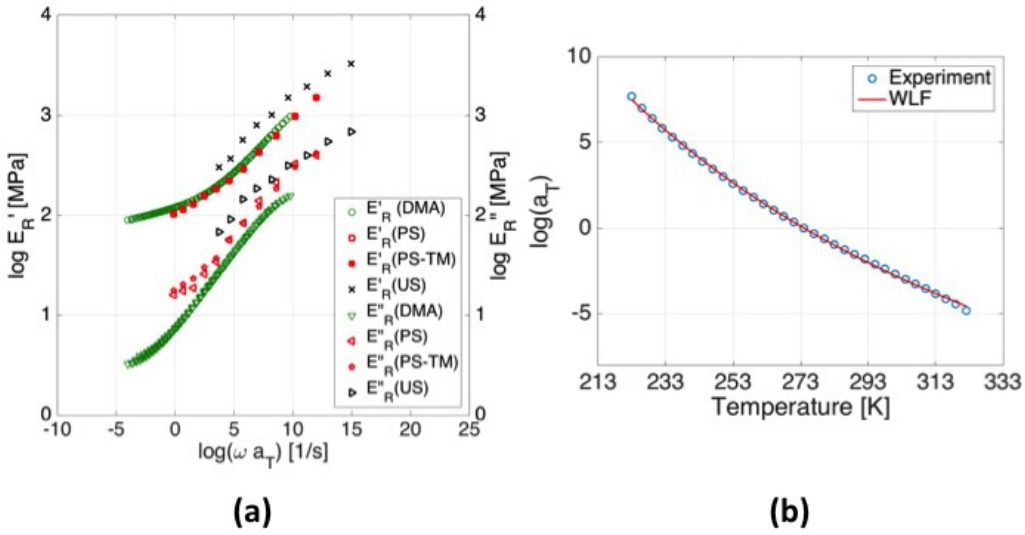

Figure 3.58: (a) master curve of polyurea (b) shift factor

the WLF equation which we found that the two constants c_1 and c_2 are 26.26 and 229.5, respectively. To be noted, DMA master curve was obtained from testing DMA sample fabricated in the same batch as all ABI samples while ultrasonic wave master curve were obtained from [73] with samples from different batch. E'_R and E''_R from ultrasonic wave measurement were calculated using longitudinal and shear moduli at 1 MHz and the temperature range of the measurement was from 223 to 303 K [73]. Due to the fact that, the Young's storage and loos moduli from ABI test are slightly increase with frequency, the two master curves (PS and PS-TM) were obtained by shifting Young's storage and loss moduli at 5 kHz, where PS refers to that E'_R and E''_R were calculated using attenuation and wave speed only from PS analysis while PS-TM means that E'_R and E''_R were calculated using wave speed from PS analysis and attenuation from TM calculation. As we can see, the two master curves (PS and PS-TM) are on top of each other on the logarithmic scale. E'_R from ABI test agrees very well with E'_R from DMA. Both E'_R from ABI test and DMA are lower than that

of ultrasonic wave measurement. E''_R from ABI test lie between those from DMA and Ultrasonic wave measurement, where E''_R from ultrasonic wave measurement is the highest among the three. It is worth noting that low frequency test technique tends to underestimate loss modulus at higher frequencies, while high frequency test technique tends to overestimate loss modulus at lower frequencies. The two possible reasons for this disagreement might be that (1) the ultrasonic wave samples were fabricated from different batch and (2) the three different test techniques are appropriate and accurate for different ranges of frequency. Interestingly, if we consider all master curves from the three test techniques, we can see the three common stages of polymeric materials; rubbery, transitional, and glassy stages. This introduces an idea for unifying the master curves from the three test techniques in our future work.

3.5.7 Conclusions

The characterization of polyurea is especially challenging in the kHz frequency range, due to the long wave length and the dissipative nature of polyurea. This study provides a novel testing technique, called acoustic ball impact measurement (ABI) to characterize polyurea's storage and loss moduli at kHz frequencies. The technique utilizes pendulum ball impact to generate a pulse containing kHz frequencies. Numerical calculation of the pulse profile is given so that the incident pulse profile, as well as amplitude and frequency contents of the pulse, can be adjusted if necessary. Two long bars as in split Hopkinson pressure bar experiment are used as wave propagating media. The bar materials are chosen to elastic materials, thereby eliminating material dispersion and simplifying analysis procedure compared to viscoelastic bar. In this work, the ball and bars are made of aluminum. Temperature chamber is equipped

to allow tests at various temperatures, in this case 223 to 323 K. Sample fabrication, measurement, and analysis procedures are proposed. Phase spectral analysis (PS) is used to analyze wave speeds and attenuations in Polyurea at various experimental conditions. Transfer matrix method (TM) is used to correct the measured attenuations from PS. The improved *alpha* from TM calculation shows similar trend as found in *alpha* calculated from DMA data. Young's storage and loss moduli of polyurea are calculated using wave speed and attenuation. Then Young's storage and loss moduli master curve from ABI measurement is created and compared with those from DMA and ultrasonic wave measurement. E'_R from ABI test agrees very well with E'_R from DMA. Both E'_R from ABI test and DMA are lower than that of ultrasonic wave measurement. $E"_R$ from ABI test lie between those from DMA and Ultrasonic wave measurement, where $E"_R$ from ultrasonic wave measurement is the highest among the three. The two possible reasons for the disagreement might be that (1) the ultrasonic wave samples were fabricated from different batch and (2) the three different test techniques are appropriate and accurate for different ranges of frequency. Interestingly, considering all master curves from the three test techniques together yield the three common stages of polymeric materials; rubbery, transitional, and glassy stages. This introduces an idea for unifying the master curves from the three test techniques in our future work. This new measurement technique is not limited to polyurea, it can also be used to characterize other similar materials at kHz frequencies.

Acknowledgements

Subchapter 3.4 is mostly a reprint of the material as it may appear in Mechanics of Materials, 2016, Nantasetphong, Wiroj; Jia, Zhanzhan; Amirkizhi, Alireza V.; Nemat-Nasser, Sia, Elsevier, 2016. Subchapter 3.5 is currently being prepared for submission for publication of the material. Nantasetphong, Wiroj; Jia, Zhanzhan; Amirkizhi, Alireza V.; Nemat-Nasser, Sia. This work has been conducted at the Center of Excellence for Advanced Materials (CEAM) at the University of California, San Diego, and has been supported through ONR Grant N00014-09-1-1126 and DARPA Grant RDECOM W91CRB-10-1-0006. This dissertation author was the primary investigator and author of this material.

3.A The Elastic Buckling Strength of Spherical Glass Shells

The whole detail of this appendix can be found in [33]. Only necessary detail will be presented here. The general expression for the elastic buckling pressure of a complete sphere, P_cr may be given as:

$$P_{cr} = \frac{KE\left(\frac{h}{R}\right)^2}{\sqrt{1-\nu^2}}, \tag{3.130}$$

where K is a buckling coefficient, E is Young's modulus, h is the shell thickness, R is the radius to the midsurface of the shell, and ν is Poisson's ratio. K for the classical small-deflection buckling is 1.15. Unfortunately, the data existing do not support the classical theory. The improvement based on nonlinear and large-deflection shell has

been done and found to have the same general form as equation 3.130. However the elastic buckling coefficient is one-fourth of K in equation 3.130. Based on nonlinear and large-deflection shell, equation 3.130 is changed to:

$$P_{cr} = \frac{KE\left(\frac{h}{R}\right)^2}{4\sqrt{1-\nu^2}}. \tag{3.131}$$

E and ν for phenolics are 4.83 GPa and 0.351. Average shell thickness and diameter of phenolic microballoon are 1 and 37 µm, respectively. To be noted, phenolic microballoon is a thermoset plastic, not glass. Thus, we needs to be cautious when using this theory for plastic microballoon.

Chapter 4

Material Behavior Modeling

4.1 Dynamic Mechanical Properties and Viscoelastic Master Curves

4.1.1 Background

The material in this section is mainly summarized from [36, 85–87]. Generally, a material is referred to as either a solid or a liquid. Its behavior depends on environmental conditions. An ideal solid is the material that is purely elastic. When a load is applied on the ideal solid or elastic material, its shape is deformed and the deformational energy is stored in the body of the material. The ability to store the deformational energy is called elasticity. When the load is released, it regains its original shape and the stored energy is released. This behavior is comparable to the behavior of an elastic spring. In general, this elastic behavior is described by Hooke's law, which states that stress (force per unit area) is a linear function of strain (deformation per unit initial length). They are related through a proportional constant

called modulus as follows:

$$\sigma = M\epsilon, \tag{4.1}$$

where M is the elastic modulus, σ and ϵ are the stress and the strain, respectively. Contrary to the ideal solid, an ideal liquid has no elasticity. It cannot store the deformational energy. When an ideal fluid is deformed, it flows, and when the applied load or deformation is removed, it cannot regain its initial shape but remains in its new deformed shape. Water can be taken as an example. When a shear stress is applied on water, the water flows. This behavior is referred to as viscous flow. For the ideal liquid, the shear stress is a linear relation of the rate of the shear strain as follows:

$$\tau = \eta \frac{d\gamma}{dt}, \tag{4.2}$$

where τ and γ are the shear stress and strain, respectively, η is the viscosity of the liquid. When η is constant or independent of the shear rate, the material is referred to as Newtonian. If the material exhibits a non-linear response to the shear rate, it is categorized as Non-Newtonian.

Due to the fact that most of engineering materials are not ideal solid and liquid, the concept of viscoelasticity is introduced. Viscoelasticity describes the behavior of materials that exhibit both elastic and viscous characteristics when undergoing deformation. A viscoelastic material will flow under an applied stress as time passes. When the stress is removed, the material will not completely recover. The strain that can be recovered represents the elastic part of the material, whereas the portion of strain that cannot be recovered represents the viscous part of the material. If the material can almost fully recover when the stress released, the material is more like

elastic solid. If the deformational strain almost cannot be recovered, the material is likely liquid. In general, viscoelastic materials have time-dependent mechanical properties. Two common time dependent phenomena that can be seen in viscoelastic materials are creep and relaxation. Creep can be described as the tendency of a viscoelastic material to move or deform slowly under an applied mechanical stress. In general, creep can be tested with creep experiment, which the constant stress is applied to the material and strain is measured as a function of time. Figure 4.1 shows a simple creep behavior where the measured strain increases with the exponential decay rate. Figure 4.1 is just an example. It is not the actual behavior of a real polymer. The creep experiment yields creep compliance, which is the ratio of the measured strain to constant applied stress.

$$D(t) = \frac{\epsilon(t)}{\sigma_o}, \tag{4.3}$$

where D is the creep compliance, σ_o is the applied constant stress, and ϵ is the measured strain.

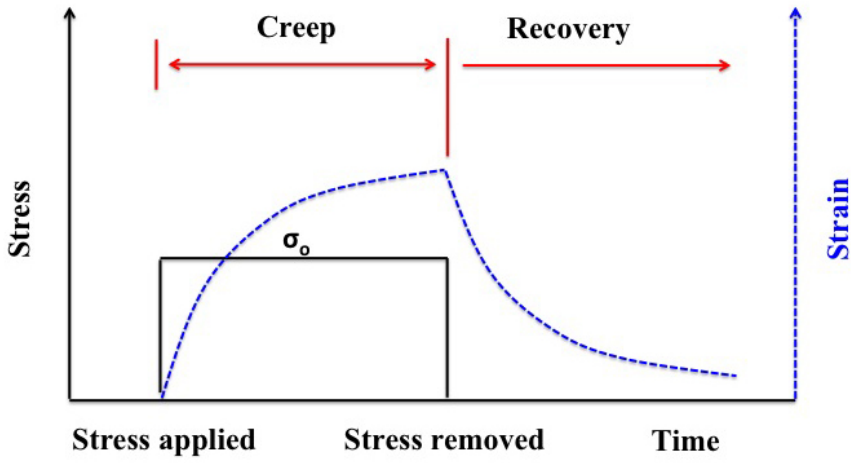

Figure 4.1: Creep versus time

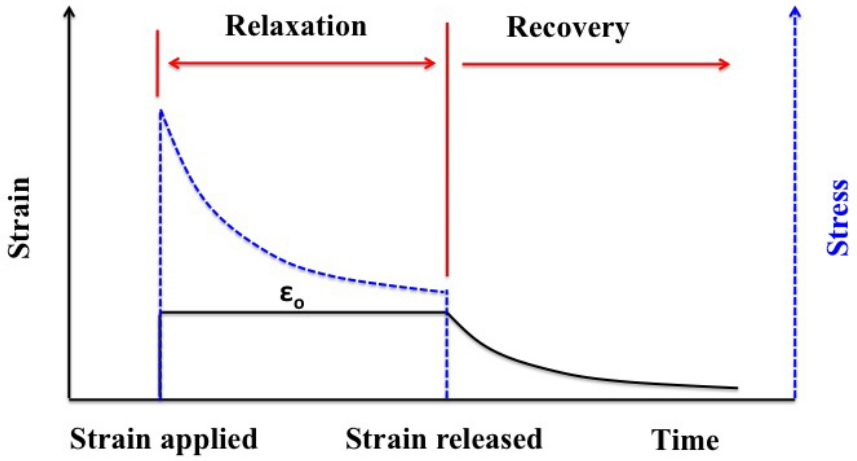

Figure 4.2: Relaxation versus time

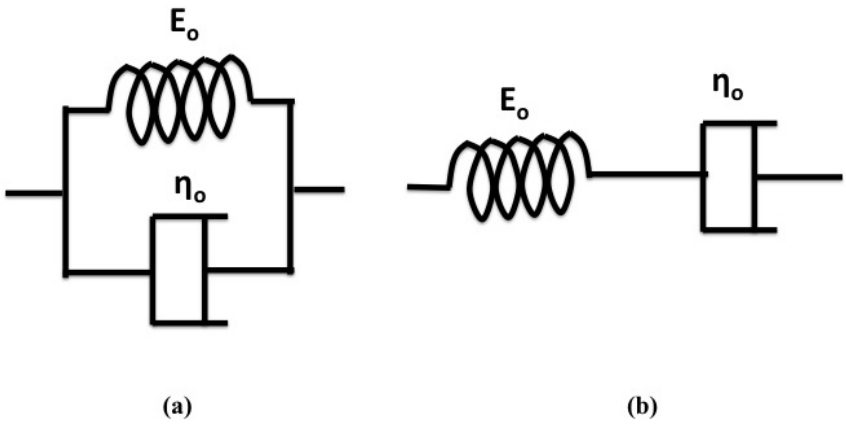

Figure 4.3: (a) Kelvin-Voigt model (b) Maxwell model

Relative to creep, stress relaxation describes how a polymer relieves stress under an applied constant strain. The relaxation modulus (see equation 4.4) can be calculated after testing the material under stress relaxation test, which the material is subjected to the constant strain and the stress is measured as a function of time. Figure 4.2 shows a simple relaxation behavior where the measured stress decays exponentially while the constant strain is applied. Figure 4.2 is just an example. It is

not the actual behavior of a real polymer.

$$E(t) = \frac{\sigma(t)}{\epsilon_o}, \tag{4.4}$$

where E is the relaxation modulus, ϵ_o is the applied constant strain, and σ is the measured stress. The behaviors of viscoelastic materials can be modeled for different loading conditions. Their viscoelastic behaviors are modeled using spring and dashpot in combination. The spring represents the elastic behavior while the dashpot represents the viscous behavior. Two simplest models, which are efficient for predicting simple creep and relaxation phenomena, are Kelvin-Voigt model and Maxwell model, respectively.

Kelvin-Voigt Model

The Kelvin-Voigt model consists of a Newtonian dashpot and a Hookean elastic spring connected in parallel, as shown in Figure 4.3a. Upon the application of a constant stress, the dashpot acts to exponentially decelerate the growth of strain with time. When the stress is removed, the dashpot again exponentially decelerates the recovery of strain, causing the material to gradually relax to its undeformed state (see Figure 4.1). The Kelvin-Voigt model effectively predict the simple creep of the simple viscoelastic materials; however it poorly describe the relaxation behavior of the material. Under constant strain (relaxation test), the Kevin-Voigt model predicts that the stress is constant such that the viscoelastic material behaves as if it is purely elastic. The verification of the Kevin-Voigt model is the following.

Consider creep test, the constant stress, σ_o is applied to the Kelvin-Voigt model. Since the dashpot and spring are parallel, the strain must be the same in

both elements while the stress must be the sum of the stresses in the two individual elements. Consider uniaxial extension case, the total stress can be written as:

$$\sigma_o = E_o \epsilon(t) + \eta_o \frac{d\epsilon(t)}{dt}, \tag{4.5}$$

where η_o is the extensional viscosity of the dashpot, E_o is stiffness of the spring. Simplify equation 4.5, we obtain:

$$\frac{d\epsilon(t)}{dt} + \frac{\epsilon(t)}{\tau_o} = \frac{\sigma_o}{\eta_o}, \tag{4.6}$$

where τ_o is defined as $\frac{\eta_o}{E_o}$. Equation 4.6 is a simple linear differential equation which can be solved using the integrating factor $e^{\frac{t}{\tau_o}}$ and integration between the limits $(0, \epsilon(0))$ and $(t, \epsilon(t))$. The solution is:

$$\epsilon(t) = \frac{\sigma_o}{E_o}\left(1 - e^{-\frac{t}{\tau_o}}\right) = \epsilon_o\left(1 - e^{-\frac{t}{\tau_o}}\right), \tag{4.7}$$

where ϵ_o is the strain of the Kevin-Voigt model as time t goes to ∞. The creep compliance is defined as:

$$D(t) = \frac{\epsilon(t)}{\sigma_o} = \frac{1}{E_o}\left(1 - e^{-\frac{t}{\tau_o}}\right) = D_o\left(1 - e^{-\frac{t}{\tau_o}}\right), \tag{4.8}$$

where D is the creep compliance, D_o is the compliance of the spring. Equation 4.7 can be used to explain the creep process shown in Figure 4.1.

For relaxation, the constant strain, ϵ_o is applied to the Kelvin-Voigt model. Since the applied strain is constant, the derivative of strain with respect to time is zero. Therefore, there is no stress in the dashpot component. The total stress,

equation 4.5, is reduced to:

$$\sigma(t) = E_o \epsilon_o. \tag{4.9}$$

The relaxation modulus is defined as:

$$E(t) = \frac{\sigma(t)}{\epsilon_o} = E_o, \tag{4.10}$$

where E is the relaxation modulus. For Kevin-Voigt model, the relaxation modulus is E_o which is constant. So the stress relaxation of the Kevin-Voigt model, equation 4.9 does not match the exponential decay of the relaxation process in Figure 4.2.

Maxwell Model

Maxwell model is much better for modeling the relaxation phenomenon. The Maxwell model is composed of a dashpot and an elastic spring connected in series, as shown in Figure 4.3b. The Maxwell model predicts that the stress under the application of constant strain (relaxation test) decays exponentially with time. This is very close to the actual behaviors of the viscoelastic materials. However, the Maxwell model estimates that under the application of constant stress (creep test), the strain increases linearly with time, whereas in reality the strain increases with exponentially decreasing rate. Since in Maxwell model the dashpot and spring are connected in series, the stresses on the two element are the same while the total strain (or total strain rate) is the summation of the strains (or strain rates) in the two individual elements. The mathematical derivation for relaxation process is as follows:

$$\frac{d\epsilon(t)}{dt} = \frac{1}{E_o}\frac{d\sigma(t)}{dt} + \frac{\sigma(t)}{\eta_o}. \tag{4.11}$$

Under relaxation test, the constant strain, ϵ_o is applied to the Maxwell model. The derivative of strain with respect to time is zero, so equation 4.11 becomes:

$$\frac{d\sigma\left(t\right)}{\sigma\left(t\right)} = -\frac{dt}{\tau_o}. \tag{4.12}$$

This equation can be solved by integration from $\sigma\left(0\right)$ at time $t = 0$ to $\sigma\left(t\right)$ at time t. The solution is:

$$\sigma\left(t\right) = \sigma\left(0\right) e^{-\frac{t}{\tau_o}}, \tag{4.13}$$

where $\sigma\left(0\right)$ can be considered as the stress in the spring element since stresses are equal in the two elements. Then, the relaxation modulus can be written as:

$$E\left(t\right) = \frac{\sigma\left(t\right)}{\epsilon_o} = \frac{\sigma\left(0\right)}{\epsilon_o} e^{-\frac{t}{\tau_o}} = E_o e^{-\frac{t}{\tau_o}}. \tag{4.14}$$

As we can see, the stress relaxation of the Maxwell model, equation 4.13 can excellently predict the exponential decay of the relaxation process shown in Figure 4.2.

For creep test, the model is subjected to an applied constant stress, σ_o. Therefore the derivative of stress with respect to time is zero. Equation 4.11 is reduced to:

$$\frac{d\epsilon\left(t\right)}{dt} = \frac{\sigma_o}{\eta_o}. \tag{4.15}$$

Integration of equation 4.15 from time $t = 0$ to time t yields:

$$\epsilon\left(t\right) = \epsilon_o + \frac{\sigma_o t}{\eta_o}. \tag{4.16}$$

Divide equation 4.16 with σ_o, the creep compliance is obtained.

$$D(t) = \frac{\epsilon(t)}{\sigma_o} = \frac{\epsilon_o}{\sigma_o} + \frac{t}{\eta_o} = D_o + \frac{t}{\eta_o}. \tag{4.17}$$

As we can see, the strain solution, equation 4.16, of the Maxwell model is linear with time. It cannot represent the creep process shown in Figure 4.1.

As mentioned earlier, Kevin-Voigt and Maxwell models are good only for simple creep and relaxation, which each of them has only one transition and is enough to be fitted with a single exponential term. In reality, the creep and relaxation behaviors of a real polymer deviate from the creep and relaxation behaviors shown in Figures 4.1 and 4.2. For real polymers, they might exhibit more complicated behaviors with many transitions in the creep and relaxation, which only single exponential term in Kevin-Voigt or Maxwell model is not enough to represent all the transitions. To overcome these deficiencies, models that consist of combinations of Maxwell and Kevin-Voigt elements have been proposed. Although an infinite number of such combinations is possible, we will consider only two models called, generalized Maxwell and generalized Kevin-Voigt models. The two models are shown in Figures 4.4 and 4.6, respectively. The treatments of other such models are completely analogous. The generalized Maxwell model allows us to effectively predict of experimental data of the relaxation to an arbitrary level of accuracy, depending on number of the Maxwell subunits, while the generalized Kevin-Voigt model is excellent for predicting creep up to very high level of accuracy, depending on number of the Kevin-Voigt subunits.

Generalized Maxwell Model

Consider a generalized Maxwell model in Figure 4.4, it has n Maxwell subunits connected in parallel. Each of Maxwell subunit has a spring and a dashpot which each of them has its own unique property, except that an extra subunit consisting of a single spring with stiffness E_e is added to track the behaviors of solid polymers which exhibit a plateau of relaxation modulus as time goes to ∞. Each of this unique pair of the spring and dashpot contributes to different relaxation mechanism of the modeled polymer. In other words, this pair of the spring and dashpot possesses a unique relaxation time which is defined as:

$$\tau_i = \frac{\eta_i}{E_i}, \tag{4.18}$$

where η_i, E_i, and τ_i are the viscosity of the dashpot and stiffness of the spring, and the relaxation time of the i-th pair respectively. If we consider all the relaxation times together, it represents a discrete relaxation spectrum of the modeled relaxation behavior. Figure 4.5 shows examples of the relaxation moduli in logarithmic scale predicted by the generalized Maxwell model with two subunits. There are two relaxation times at 1 min and 1000 min, therefore two relaxation mechanisms are observed at the corresponding times. Figure 4.5a represents the relaxation modulus in logarithmic scale with $E_e = 0$. As you can see, the modulus goes to zero as time goes to ∞, therefore representing the behavior of a polymer melt. Figure 4.5b represents the relaxation modulus with $E_e \neq 0$. As you can see, the relaxation modulus flattens out as time goes to ∞, therefore representing the behavior of a solid polymer. The mathematical representation of the model will be discussed in detail.

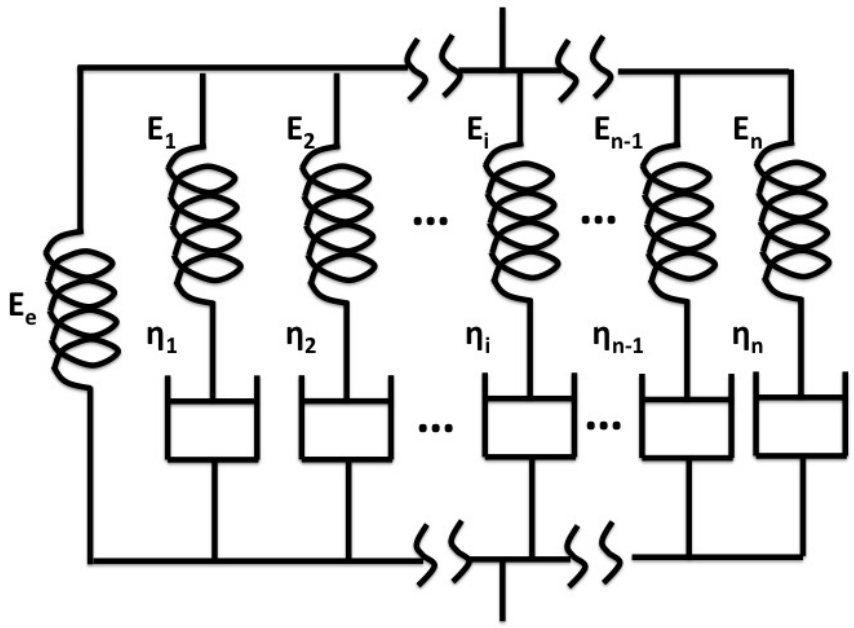

Figure 4.4: Generalized Maxwell model

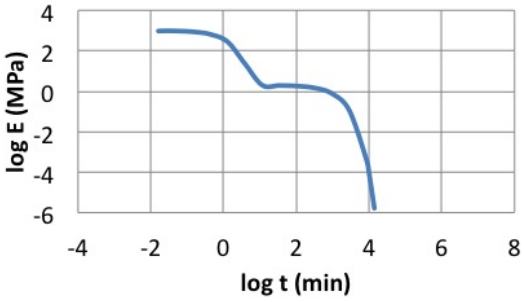

E_e	0	MPa
E_1	1000	MPa
η_1	1000	Mpa.min
τ_1	1	min
E_2	2	MPa
η_2	2000	Mpa.min
τ_2	1000	min

(a)

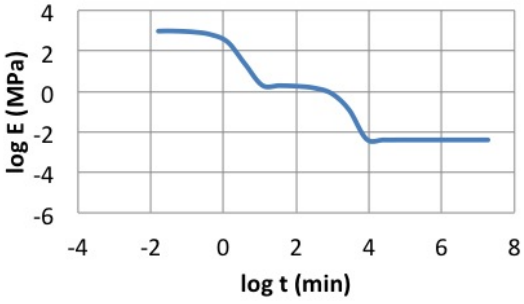

E_e	0.004	MPa
E_1	1000	MPa
η_1	1000	Mpa.min
τ_1	1	min
E_2	2	MPa
η_2	2000	Mpa.min
τ_2	1000	min

(b)

Figure 4.5: (a) An example of relaxation of a polymer melt (b) An example of relaxation of a solid polymer

When the generalized Maxwell model is subjected to a stress relaxation experiment, each subunit (dashpot + spring) shares the applied constant strain, ϵ_o. The total stress is the summation of the individual stresses experienced by each subunit. The derivative of strain with respective to time is zero. We can then write:

$$\begin{aligned}
\frac{d\epsilon(t)}{dt} &= 0 \\
&= \frac{1}{E_1}\frac{d\sigma_1(t)}{dt} + \frac{\sigma_1(t)}{\eta_1} \\
&= \frac{1}{E_2}\frac{d\sigma_2(t)}{dt} + \frac{\sigma_2(t)}{\eta_2} \\
&\vdots \\
&= \frac{1}{E_i}\frac{d\sigma_i(t)}{dt} + \frac{\sigma_i(t)}{\eta_i} \\
&\vdots \\
&= \frac{1}{E_{n-1}}\frac{d\sigma_{n-1}(t)}{dt} + \frac{\sigma_{n-1}(t)}{\eta_{n-1}} \\
&= \frac{1}{E_n}\frac{d\sigma_n(t)}{dt} + \frac{\sigma_n(t)}{\eta_n},
\end{aligned} \tag{4.19}$$

$$\sigma_e = E_e\epsilon_o, \tag{4.20}$$

$$\sigma(t) = \sigma_e + \sigma_1 + \sigma_2 + ... + \sigma_i + ... + \sigma_{n-1} + \sigma_n. \tag{4.21}$$

Similar to the regular Maxwell model, the partial stress in each subunit, $\sigma_i (i = 1, 2, 3, .., n)$ can be solved individually by integration from $\sigma_i(0)$ at time $t = 0$ to $\sigma_i(t)$ at time t. Substitute σ_e and all σ_i into equation 4.21 and divide with ϵ_o, the

relaxation modulus is obtained as:

$$E(t) = E_e + \sum_{i=1}^{n} E_i e^{-\frac{t}{\tau_i}}. \tag{4.22}$$

As we can see, the relaxation modulus of the generalized Maxwell model is the summation of the individual relaxation moduli of all subunits. Since the generalized Maxwell model will be used only for prediction of relaxation modulus in this study, the mathematical representation of creep will not be considered here.

Generalized Kelvin-Voigt Model

Consider a generalized Kelvin-Voigt model in Figure 4.6, it has n Kelvin-Voigt subunits connected in series. Similar to Maxwell subunit, each of Kelvin-Voigt subunit has a pair of a spring and a dashpot. The single spring with stiffness M_g is added to track the instantaneous creep response of polymers. Each of this unique pair of the spring and dashpot contributes to different retardation mechanism of the modeled polymer. In other words, this pair of the spring and dashpot possesses a unique retardation time which is defined as:

$$\lambda_i = \frac{\beta_i}{M_i}, \tag{4.23}$$

where β_i, M_i, and λ_i are the viscosity of the dashpot and stiffness of the spring, and the retardation time of the i-th pair in the generalized Kelvin-Voigt model respectively. If we consider all the retardation times together, it represents a discrete retardation spectrum of the modeled creep behavior. Figure 4.7 shows examples of the creep compliance in logarithmic scale predicted by the generalized Kelvin-Voigt

model with two subunits. There are two retardation times at 1 min and 1000 min, therefore two retardation mechanisms are observed at the corresponding times. Figure 4.7a represents the creep compliance in logarithmic scale with $M_g = \infty$. As you can see, the creep compliance at time $t \to 0$ is very small, which represents a stiff instantaneous creep response. Later it increases with exponential decay rate as time progresses. Figure 4.7b represents the creep compliance with a finite value of M_g. Apparently, the creep compliance instantaneously jumps at time $t \to 0$, which represents a softer instantaneous creep response. The smaller M_g yields larger jump of the creep compliance. The mathematical representation of the model will be discussed in detail.

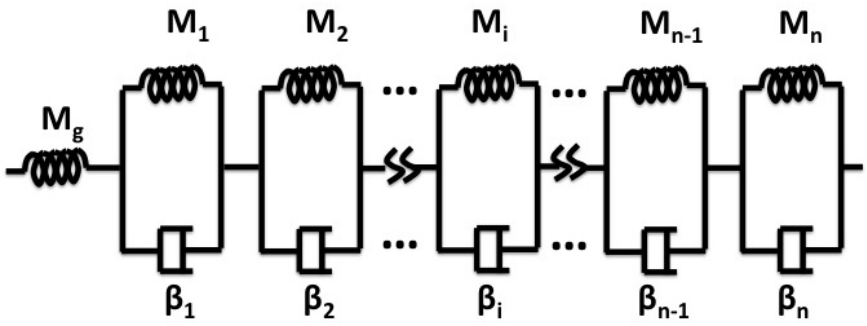

Figure 4.6: Generalized Kevin-Voigt model

When the generalized Kelvin-Voigt model is subjected to a creep experiment, each subunit (dashpot + spring) shares the applied constant stress, σ_o. The total strain is the summation of the individual strains experienced by each subunit. We

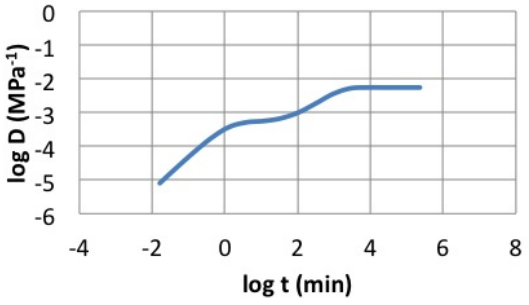

M_g	∞	MPa
M_1	2000	MPa
β_1	2000	MPa.min
λ_1	1	min
M_2	200	MPa
β_2	200000	MPa.min
λ_2	1000	min

(a)

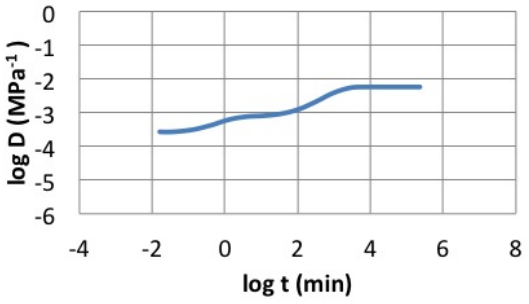

M_g	4000	MPa
M_1	2000	MPa
β_1	2000	MPa.min
λ_1	1	min
M_2	200	MPa
β_2	200000	MPa.min
λ_2	1000	min

(b)

Figure 4.7: (a) An example of creep without the stiffness M_g (b) An example of creep with the stiffness M_g

can then write:

$$\begin{aligned}
\sigma_o &= \epsilon_1(t) M_1 + \beta_1 \frac{d\epsilon_1(t)}{dt} \\
&= \epsilon_2(t) M_2 + \beta_2 \frac{d\epsilon_2(t)}{dt} \\
&\vdots \\
&= \epsilon_i(t) M_i + \beta_i \frac{d\epsilon_i(t)}{dt} \\
&\vdots \\
&= \epsilon_{n-1}(t) M_{n-1} + \beta_{n-1} \frac{d\epsilon_{n-1}(t)}{dt} \\
&= \epsilon_n(t) M_n + \beta_n \frac{d\epsilon_n(t)}{dt}, \qquad (4.24)
\end{aligned}$$

$$\epsilon_g = \frac{\sigma_o}{M_g}, \tag{4.25}$$

$$\epsilon(t) = \epsilon_g + \epsilon_1 + \epsilon_2 + ... + \epsilon_i + ... + \epsilon_{n-1} + \epsilon_n. \tag{4.26}$$

Similar to the regular Kelvin-Voigt model, the partial strain in each subunit, $\epsilon_i (i = 1, 2, 3, .., n)$ can be solved individually, using the integrating factor $e^{\frac{t}{\tau_i}}$ and integration between the limits $(0, \epsilon_i(0))$ and $(t, \epsilon_i(t))$. Then, the strain for the i-th subunit is:

$$\epsilon_i(t) = \frac{\sigma_o}{M_i}\left(1 - e^{-\frac{t}{\lambda_i}}\right), \tag{4.27}$$

Substitute ϵ_g and all ϵ_i from $i = 1$ to n into equation 4.26 and divide with σ_o, the creep compliance is obtained.

$$D(t) = \frac{1}{M_g} + \sum_{i=1}^{n} \frac{1}{M_i}\left(1 - e^{-\frac{t}{\lambda_i}}\right) = D_g + \sum_{i=1}^{n} D_i\left(1 - e^{-\frac{t}{\lambda_i}}\right). \tag{4.28}$$

where D_g and D_i are compliances of the single spring and the i-th spring in the i-th subunit. As we can see, the creep compliance of the generalized Kelvin-Voigt model is the summation of the individual creep compliances of all subunits. When the generalized Kelvin-Voigt model is subjected to the applied constant stress, at time $t = 0$ compliance of each subunit is zero due to the very stiff response of each dashpot in each subunit. Only the single spring with stiffness M_g is extended at time $t = 0$. As time passes, the Kelvin-Voigt subunits with smaller retardation times relax themselves first. The dashpot in each subunit relaxes and stretches itself and allows its paired spring to extend simultaneously. This process continues on with

the Kelvin-Voigt subunits with higher retardation times, leading to the increasing of the overall compliance as time passes. Since the generalized Kelvin-Voigt model will be used only for prediction of creep compliance in this study, the mathematical representation of relaxation of the model will not be considered here.

Boltzmann Superposition Principle

So far, we have learnt about relaxation and creep experiments, in which the constant strain and stress are applied on the test material, respectively. The measured stress of the uniaxial relaxation experiment can be presented by:

$$\sigma(t) = E(t)\,\epsilon_o, \tag{4.29}$$

where ϵ_o, E, and σ are the applied constant strain, uniaxial relaxation modulus, and the measured stress. The measured strain of the creep experiment is in the following form:

$$\epsilon(t) = D(t)\,\sigma_o, \tag{4.30}$$

where σ_o, D, and ϵ are the applied constant stress, compliance, and the measured strain. E and D depend on the viscoelastic behaviors of the tested polymer. They can be modeled with equations 4.22 and 4.28 up to arbitrary level of accuracy, depending on the number of the exponential terms. The applied loads in equations 4.29 and 4.30 are constants. One might imagine a case where the applied stress (or strain) is a function of time. This becomes challenging when one thinks about how to find the strain (or the stress) response. The Boltzmann superposition principle is one of the simplest but most powerful principles of polymer physics that can be used to solve

this problem. For linear viscoelasticity, we consider only small deformation where E and D do not change their forms during deformation. Consider the application of two small strain ϵ_0 and ϵ_1, at the times $t = 0$ and $t = s_1$, respectively. The Boltzmarn superposition principle states that the two strains act independently and the resultant stresses add linearly. Thus:

$$\sigma(t) = E(t)\,\epsilon_o + E(t - s_1)\,\epsilon_1. \tag{4.31}$$

Now consider a series of very tiny step strains, $d\epsilon_i$ applied to our polymer at time s_i where $i = 1, 2, 3, ..., n$, from Boltzmarn superposition principle the overall resultant stress would be:

$$\sigma(t) = \sum_{i=1}^{n} E(t - s_i)\,d\epsilon_i. \tag{4.32}$$

Considering a continuous strain application, $\epsilon(s)$, the increment of the applied strain is just the derivative of $\epsilon(s)$ times the increment of time, ds. Replacing the summation in equation 4.32 by an integration, we obtain:

$$\sigma(t) = \int_{-\infty}^{t} E(t - s)\,\frac{d\epsilon(s)}{ds}ds = \int_{-\infty}^{t} E(t - s)\,\dot{\epsilon}(s)\,ds. \tag{4.33}$$

This can apply to the case of continuous stress application. Then the resulting strain is:

$$\epsilon(t) = \int_{-\infty}^{t} D(t - s)\,\frac{d\sigma(s)}{ds}ds = \int_{-\infty}^{t} D(t - s)\,\dot{\sigma}(s)\,ds. \tag{4.34}$$

Modulus and Compliance in Frequency Domain

With the help of the Boltzmarn superposition principle, we can now consider the viscoelastic response of a polymer under an applied harmonic stress or strain.

Consider a unit harmonic strain which is in the following form:

$$\epsilon(t) = e^{i\omega t}, \tag{4.35}$$

where ω is an angular frequency. Differentiate equation 4.35, strain rate can then be written as:

$$\dot{\epsilon}(t) = i\omega e^{i\omega t}. \tag{4.36}$$

Substitute equations 4.36 and 4.22 into equation 4.33 and obtain:

$$\sigma(t) = \int_{-\infty}^{t} \left(E_e + \sum_{j=1}^{n} E_j e^{-\frac{t-s}{\tau_j}} \right) i\omega e^{i\omega s} ds. \tag{4.37}$$

After integration from $-\infty$ to t, we obtain:

$$\begin{aligned} \sigma(t) &= \left(\left[E_e + \sum_{j=1}^{n} \frac{E_j (\omega\tau_j)^2}{1 + (\omega\tau_j)^2} \right] + \left[\sum_{j=1}^{n} \frac{E_j \omega\tau_j}{1 + (\omega\tau_j)^2} \right] i \right) e^{i\omega t} \\ &= \left(E'(\omega) + E''(\omega) i \right) e^{i\omega t} \\ &= E^*(\omega) e^{i\omega t} \\ &= E^*(\omega) \epsilon(t), \end{aligned} \tag{4.38}$$

where

$$E^*(\omega) = E'(\omega) + E''(\omega) i, \tag{4.39}$$

$$E'(\omega) = E_e + \sum_{j=1}^{n} \frac{E_j (\omega\tau_j)^2}{1 + (\omega\tau_j)^2}, \tag{4.40}$$

$$E''(\omega) = \sum_{j=1}^{n} \frac{E_j \omega \tau_j}{1 + (\omega \tau_j)^2} i, \tag{4.41}$$

E^* is complex modulus, E' and E'' are real and imaginary parts of the complex modulus. E' is called storage modulus. It represents the elastic part of the polymer. E'' is called loss modulus. It represents the viscous part of the polymer. Similarly, if a unit harmonic stress is applied, one can write the harmonic strain response as:

$$\begin{aligned} \epsilon(t) &= \left(\left[D_g + \sum_{j=1}^{n} \frac{D_j}{1 + (\omega \lambda_j)^2} \right] + \left[\sum_{j=1}^{n} \frac{D_j \omega \lambda_j}{1 + (\omega \lambda_j)^2} \right] i \right) e^{i\omega t} \\ &= \left(D'(\omega) + D''(\omega) i \right) e^{i\omega t} \\ &= D^*(\omega) e^{i\omega t} \\ &= D^*(\omega) \sigma(t), \end{aligned} \tag{4.42}$$

where

$$D^*(\omega) = D'(\omega) + D''(\omega) i, \tag{4.43}$$

$$D'(\omega) = D_g + \sum_{j=1}^{n} \frac{D_j}{1 + (\omega \lambda_j)^2}, \tag{4.44}$$

$$D''(\omega) = \sum_{j=1}^{n} \frac{D_j \omega \lambda_j}{1 + (\omega \lambda_j)^2} i, \tag{4.45}$$

D^* is complex compliance, D' and D'' are real and imaginary parts of the complex compliance. D' is called storage compliance. D'' is called loss compliance. From equations 4.38 and 4.42, the complex modulus is an inverse of the complex compliance and vice versa. However this is not true for the relaxation modulus and the creep

compliance in time domain [36, 85, 87].

$$E^*(\omega) = \frac{1}{D^*(\omega)}. \tag{4.46}$$

Up to this point, we have showed the mathematical formulations for predicting the relaxation modulus and creep compliance in time domain and also the complex modulus and compliance in frequency domain. With these mathematical formulations, equations 4.22, 4.28, 4.40, 4.41, 4.44, and 4.45, one can predict material responses under either applied stress or strain in both time and frequency domians. Parameters in equation 4.22 for relaxation modulus is related to parameters in equations 4.40 and 4.41 for storage and loss moduli. Once we fit equation 4.22 to the experimental data obtained from relaxation experiment, we could use the resulting parameters to predict storage and loss moduli, using equations 4.40 and 4.41. The other way around is also doable when we have experimental data of storage and loss moduli which generally can be obtained from DMA experiment discussed in Section 3.2. This also applies to the relation between the creep compliance and the storage and loss compliances.

To be able to predict material behaviors of polymers for an inexhaustible range application, one needs to characterize the polymers over sufficiently long time or wide frequency window. However, in reality the experimental time window is too narrow, i.e. in the range of a fraction of a second to several days, and the experimental frequency window is not continuous due to the limitation of the testing devices, therefore the available data are not enough to cover the whole range of material behaviors, especially at very short and long term behaviors. This has been the interesting topic of many researches dealing with polymeric materials. According to experimental data

obtained from many tests on polymers, the viscoelastic modulus is found to be a function of time at a constant temperature and vice versa. According to this, the time-temperature correspondence theory is developed. Based on this theory, the long term behavior of a polymer may be measured by two different means. First, experiments for extended periods of time can be carried out at a given temperature, and the response measured directly. However, this means is time consuming due to the long response times of many polymers. The second method takes advantage of the principles of time-temperature correspondence wherein experiments are performed over a short time frame at various testing temperatures, a reference temperature is chosen, the experimental data at the reference temperature is fixed, and the rest at other temperatures are shifted using the time-temperature relation. The two methods are equivalent according to the principles of time-temperature superposition. The detail of time temperature superposition based on free volume concept will be discussed in the next section.

4.1.2 Time-Temperature Superposition (TTS) and Master Curve

Time-temperature superposition was firstly developed for the so called thermorheologically simple materials. For polymeric materials that are regarded as the thermorheologically simple materials, it requires that all relaxation or retardation times depend equally on temperature [52]. The relaxation (or ratardation) times at two different temperatures are related through:

$$a_T(T) = \frac{\tau_i(T)}{\tau_i(T_o)}, i = 1, 2, 3, ... \tag{4.47}$$

where a_T is the temperature-dependent shift function (shift factor) of the relaxation or retardation time. $\tau_i(T)$ and $\tau_i(T_o)$ are the i-th relaxation (or retardation) times at a temperature T and a reference temperature T_o. According to observations form experiments on various polymers, if T is higher than T_o, $\tau_i(T)$ is less than $\tau_i(T_o)$, and $a_T < 1$. This means that at temperature T the mechanism of a relaxation or molecular event is accelerated through the shortening of the relaxation time with the factor of a_T, compared to $\tau_i(T_o)$. If T is less than T_o, $\tau_i(T)$ is larger than $\tau_i(T_o)$, and $a_T > 1$. Therefore, the relaxation at T is decelerated, compared to at T_o. Thermorheologically simple materials allow time-temperature superposition, i.e., the shifting of isothermal segments into superposition to generate a master curve, thereby extending the time scale beyond the range that could normally be covered in a single experiment. An example of such a procedure is given in Figure 4.8. The relaxation modulus of a polymer from a tensile test, E is plotted as a function of time in logarithmic scale over a normal experimental time window, from 10^{-2} to 10^{2} hours, for various temperatures. A chosen reference temperature is 0 °C in this case. Thus, the isothermal data at 0 °C was fixed at its original position. The modulus-versus-time curves for the remaining isotherms were horizontally shifted towards this reference until an exact superposition is accomplished. Shifting of each isothermal curve results in a much larger, smooth continuous curve called a master curve. It can be seen that this procedure results in a dramatic increase in the range of the time scale. The inset is the plot of shift factor in the logarithmic scale, $\log a_T$, versus temperature. The shift factor represents the magnitude of shifting along the time axis, necessary for a specific isotherm to superimpose on its neighbor in the final master curve with respect to a given reference temperature. Generally, the $\log a_T$ versus temperature plot should be a smooth

monotonic curve, provided the mechanism of relaxation remains the same during the process. An inflection in the shift factor plot would be an indication of a change in the mechanism of the process which might invalidate the procedure. Normally, amorphous homopolymers and random copolymers with primarily single phase and single transition are thermorheologically simple materials. For thermorheologically complex materials that show two or more distinct distributions of relaxation times, each with its own time-temperature dependence, shifting of isothermal segments into superposition might generate misleading master curves. However, there is no evidence that prohibits us from applying the TTS principle on other complex polymers. So, the TTS should be used with caution when dealing complex polymers that show multiple transitions of their moduli.

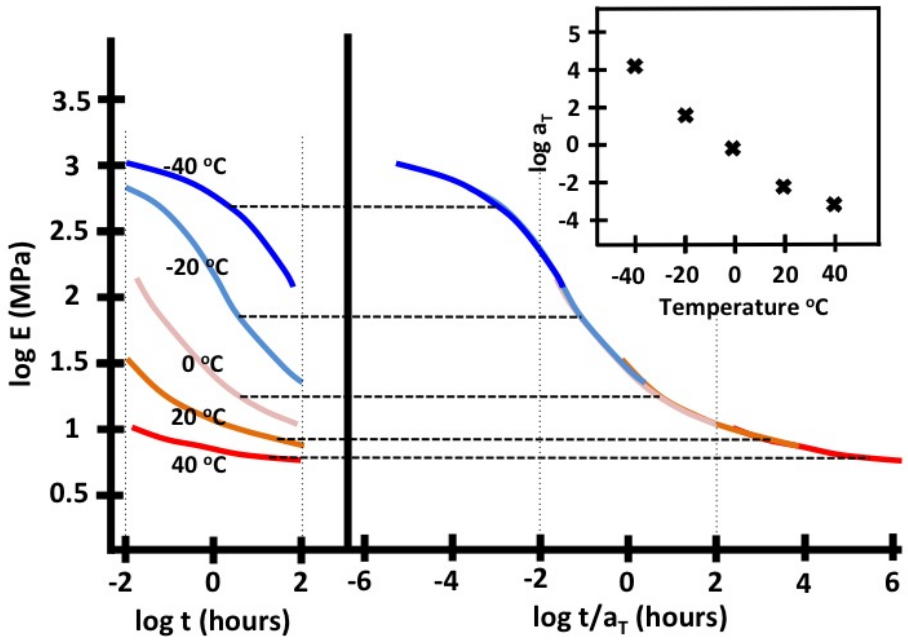

Figure 4.8: Shifting isothermal segments into a relaxation modulus master curve (The inset shows shift factor)

There are many theories for modeling the effect of temperature on time-

dependent behavior of polymers, for example, free volume [36, 51], excess configurational entropy [88,89], excess enthalpy [90], and chemical reaction based [91] theories. In this work, we will focus on the free-volume based theory which is one of the most well-known theory for modeling time-temperature correspondence above glass transition temperature, T_g. This free-volume concept was first introduced by Doolittle and Doolittle in their work on the viscosity of liquids [92]. The key concept is that the change in viscosity could be expressed by a simple function of the net available volume between the polymer molecules. The net available volume represents the free volume, which directly affects the mobility of the polymer chains. At a given temperature, T, the relation between the viscosity and the free volume is:

$$\eta\left(T\right) = A\mathrm{e}^{B\frac{V_\phi(T)}{V_f(T)}} = A\mathrm{e}^{B\frac{V(T)-V_f(T)}{V_f(T)}} = A\mathrm{e}^{B\left(\frac{1}{f(T)}-1\right)}, \tag{4.48}$$

where V_ϕ, V_f, V are the occupied, free, and total volumes, respectively, A and B are empirical material constants, f is the fractional free volume, defined as $\frac{V_f}{V}$. From equation 4.49, the relation between viscosities at two different temperatures can be written as:

$$\frac{\eta\left(T\right)}{\eta\left(T_o\right)} = \mathrm{e}^{B\left(\frac{1}{f(T)}-\frac{1}{f(T_o)}\right)}. \tag{4.49}$$

Williams, Landel, and Ferry adapted equation 4.49 for the viscoelastic behavior of polymers by letting [51]:

$$\frac{\eta\left(T\right)}{\eta\left(T_o\right)} = \frac{\tau_i\left(T\right)}{\tau_i\left(T_o\right)}. \tag{4.50}$$

From equations 4.47, 4.49, and 4.50, the temperature shift factor can be written as:

$$a_T = \frac{\tau_i\left(T\right)}{\tau_i\left(T_o\right)} = \mathrm{e}^{B\left(\frac{1}{f(T)}-\frac{1}{f(T_o)}\right)}. \tag{4.51}$$

In logarithmic form, equation 4.51 becomes:

$$\log a_T = \frac{B}{2.303}\left(\frac{1}{f(T)} - \frac{1}{f(T_o)}\right). \tag{4.52}$$

Williams et al. suggested that the fractional free volume is a linear function of temperature. They let:

$$f(T) = f(T_o) + \alpha_f (T - T_o), \tag{4.53}$$

where α_f is the isobaric expansivity. Substitute equation 4.53 into equation 4.52, we obatin:

$$\log a_T = -\frac{c_1 (T - T_o)}{c_2 + T - T_o}, \tag{4.54}$$

$$c_1 = \frac{B}{2.303} f(T_o), \tag{4.55}$$

$$c_2 = \frac{f(T_o)}{\alpha_f}. \tag{4.56}$$

Equation 4.54 is called WLF equation. To be noted, WLF equation should be used to model the time-temperautre correspondence above T_g. For temperature below T_g, it can be modeled with the shift factor in the form of Arrhenius rate of chemical reaction equation [91].

$$\log a_T = \frac{-\triangle E}{2.303R}\left(\frac{1}{T} - \frac{1}{T_o}\right) \tag{4.57}$$

where $\triangle E$ is activation energy and R is gas constant. We will not discuss the Arrhenius form shift factor here since in this work we tested polyurea and polyurea-based

composites above T_g.

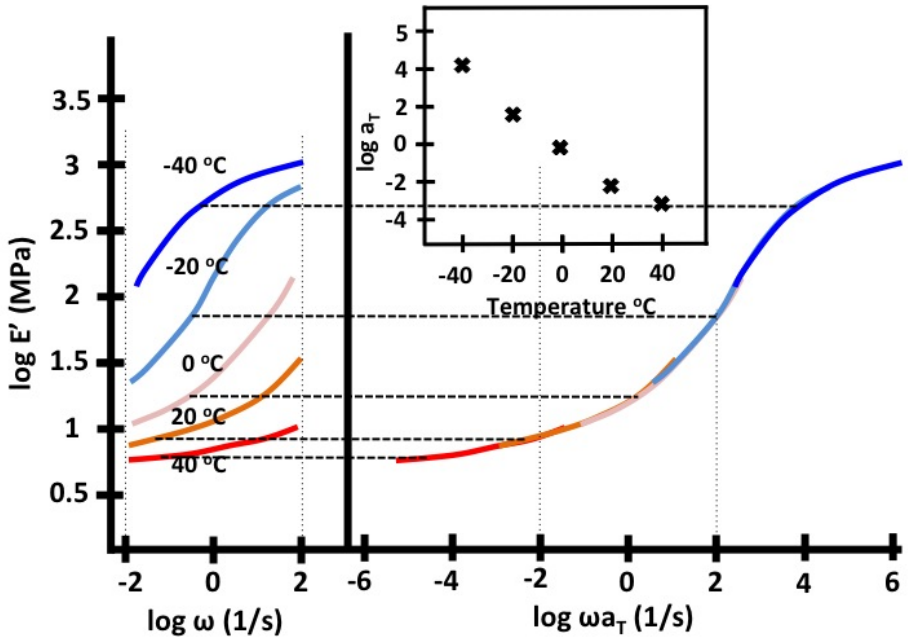

Figure 4.9: Shifting isothermal segments into a storage modulus master curve (The inset shows shift factor)

Equation 4.54 is used to fit the plot of shift factor versus temperature obtained experimentally by shifting isothermal curves into superposition as shown in Figure 4.8. Relaxation or creep tests at various temperatures generally require quite long experimental time. It is found that the data of time-temperature correspondence can also be obtained through the measurement in frequency domain, using dynamic mechanical analysis (DMA) discussed previously in Sections 3.2 and 3.4. Similar to relaxation test, DMA is performed over a short frequency range at various temperatures. The storage and loss moduli are obtained as functions of frequencies at various temperature. The plot of shift factor versus temperature can be found by shifting either storage or loss modulus. Shift factors from shifting storage and loss moduli are close. The average between the two are used. Figure 4.9 shows the process of shift-

ing storage-modulus-versus-frequency of a polymer. It is found that the shift factors from time-domain and frequency-domain measurement are very close. Equations 4.22 and 4.28 can be used to fit relaxation modulus and creep compliance master curves. Equations 4.40, 4.41 can be used to fit the storage and loss modulus master curves, and equations 4.44 and 4.45 can be used to fit the storage and loss compliance master curves, respectively. The models of the relaxation moduli and retardation compliances for polyurea and milled glass reinforced composites are shown in Section 3.4. The relation between relaxation modulus and creep compliance is also given in that section. If either one of them is known, the other one can be calculated without experiment [49].

So far, we have shown that the temperature which is a thermodynamic quantity has an influence on the relaxation and retardation mechanisms of polymeric materials. The time-temperature correspondence can be modeled based on the free volume concept by assuming that the decreasing in temperature reduces the micro-size free space between polymer molecules while increasing in temperature has an opposite effect. Therefore changing in temperature affects the mobility of the polymer chain, leading to the change in relaxation and retardation mechanisms. In the next chapter, the effect of pressure which is also a thermodynamic quantity is taken into account through the same free volume theory. It is assumed that increasing in pressure equivalently affects the free volume in a polymer in the same way as decreasing in temperature does.

4.2 Constitutive Modeling and Experimental Calibration of Pressure Effect for Polyurea Based on Free Volume Concept

In this study, the combined effect of pressure and temperature on the mechanical behavior of polyurea is experimentally characterized and integrated into a constitutive model based on Williams-Landel-Ferry (WLF) equation. The increase in pressure is related to a decrease in temperature, both pressure and temperature affecting the polymer's molecular free volume and thereby introducing a pressure-dependent term into the WLF equation. This modified WLF equation can represent viscoelastic properties of thermorheologically and piezorheologically simple materials over wide ranges of temperature and pressure. The model is derived based on Fillers and Tschoegl's original work, regarding the free volume as a state variable. Although in previous work, the effect of pressure was modeled as a linear (or quadratic) decrease in equivalent temperature, the present results and analysis demonstrate a nonlinear relationship, with a stronger effect at smaller pressures. The model provides a closed-form expression for the time scale shift factor for equivalent temperature in terms of temperature and pressure and its three-dimensional surface representation. The prediction of the present model agrees well with pressure shift factor data obtained from confined compression tests of polyurea, reported elsewhere, confirming our constitutive model and its experimental calibration procedure. A simplified model of the pressure effect was also developed which yields good approximate results. Both versions can be readily integrated into user-defined constitutive subroutines for explicit finite element modeling.

4.2.1 Introduction

The relation between relaxation times and temperature in viscoelastic materials has been studied over the past 60 years. Many researches have used the assumption of thermorheologically simple materials which allow time-temperature superposition and generate a master curve by shifting isothermal segments, thereby extending the experimental time window beyond the normal range of a single test [36, 51, 93, 94]. Many theories for modeling the effect of temperature on the time-dependent behavior of polymers are based on the free volume concept. Doolittle and Doolittle [92] proposed this idea in their work on the viscosity of liquids. They found that the change in viscosity due to the temperature might be expressed as a simple function of the net available volume between the polymer molecules, or free volume. William, Landel, and Ferry [51] extended this idea for application to polymers. They proposed that the fractional free volume, which is the ratio of free volume to total volume of a polymer, directly determines the mobility of the polymer chains, which in turn governs the time-dependent mechanical properties of the polymer. Above Tg, the effect of temperature on the time-dependent mechanical properties is traditionally modeled by the well-known WLF equation, in which the fractional free volume is approximated by a linear function of temperature [36, 51]. A more sophisticated free volume-based model was proposed by Knauss and Emri [95, 96]. Their model is able to predict nonlinear response of several polymers. They suggested that the fractional free volume should depend on the temperature, mechanical dilatation and swelling histories. In the case of negligible moisture and dilatational effects their model reduces to the WLF equation. Popelar and Liechti modified this model to include distortional effect by introducing a new term, similar to the dilatational one [97, 98]. Losi and Knauss

modified the free volume-based model for temperature below Tg [99]. Other than the fractional free volume concept, the effect of temperature can be modeled via other thermodynamic quantities, e.g. the excess configurational entropy [88, 89], the excess enthalpy [90], and the relaxation or retardation process as the physical counterpart of a chemical reaction [91].

While the effect of temperature on the viscoelastic properties of polymers is fairly well understood, relatively little information is available on the effect of pressure. Generally, volume is reduced as temperature is decreased and/or pressure is increased. One could equate the effect of pressure increase to that of temperature decrease following this rationale. Ferry and Stratton assumed that the fractional free volume decreases linearly with pressure, yielding an equation of shift factor that has the same form as WLF equation [100]. O'Reilly assumed that the fractional free volume is a function of the inverse of pressure, obtaining a simple exponential form for the shift factor [101]. However, it has been found that the dependence of the empirical shift distances on pressure could not be successfully described by either the Ferry-Stratton or the O'Reilly equation [102]. The present work shows that these two models are not appropriate for the behavior of polyurea in particular. Fillers and Tschoegl proposed that pressure is associated with the change in fractional free volume via compressibility, which is defined as the inverse of the tangential bulk modulus [52, 102]. They considered the fractional free volume to be a state variable depending on pressure and temperature and developed an equation for shift factor, which describes the pressure dependence and contains the WLF equation as a limiting case. They showed that shifting isobaric segments of mechanical properties of viscoelastic materials could yield the similar master curve as shifting the isothermal

segments. The materials that allow isobaric shifting are referred to as piezorheologically simple materials.

The change in fractional free volume due to pressure is related to the compressibility of the free volume, and the change due to the temperature is associated with the thermal expansivity. With the assumption of the fractional free volume being a state variable, its differential may be written accordingly as the sum of the two effects [102]. To consider the total change with pressure and temperature, Fillers and Tschoegl proposed two different integration paths; (1) integrate the pressure-dependent term at a fixed temperature first, followed by the temperature-dependent term at a fixed pressure, and (2) integrate the temperature-dependent term at a fixed pressure first, followed by the pressure-dependent term at a fixed temperature. They suggested that the first path is preferable since the first path requires knowledge of the pressure dependence of the expansivity while the second requires knowledge of the temperature dependence of the compressibility that is more difficult to determine. However, the second integration path yields the WLF equation as a limiting case without having to change its constants for each reference pressure. Moreover, one does not have to complete the stress relaxation test under pressure to obtain pressure-dependent parameters, as it is required with the first integration path. In this work, we extend Fillers and Tschoegl's work, utilizing the second integration path and designing the experimental framework to extract all desired constitutive parameters. For the sake of clarity in presentation, we will refer to this model as modified WLF equation (mWLF). However the original authors call it, the FMT model.

Polyurea, a block copolymer formed from the chemical reaction of diisocyanates with polyamines, was studied under high-pressure using ultrasonic measurements.

The test specimens were quasi-statically compressed in confined uniaxial deformation. The longitudinal ultrasonic wave speed in the sample was measured at various pressures and temperatures. Then, the longitudinal moduli at various temperature and pressure were calculated, using the wave speeds and densities of the samples, modified by the uniaxial strain. The testing pressure and temperature ranges in this study are 0.1 to 900 MPa and 223 to 303 K. The longitudinal moduli were used to relate the pressure increase to temperature decrease at ambient pressure that would have yielded the same longitudinal modulus. The mWLF model gives the necessary shifts along the time or frequency axes that would lead to overlapping and alignment of the measured isothermal and isobaric viscoelastic modulus curves. The shift factor may be considered as the combination of two parts that account for effects of temperature and pressure. All parameters controlling the time scale shifts needed for the effect of temperature may be obtained from the original WLF equation. Furthermore, one can construct a function that for a given applied pressure gives the equivalent reduction in temperature, which induces the similar change in material behavior as the applied pressure. All remaining parameters for the effect of pressure can be found by curve-fitting this function. The mWLF model can be presented by a three-dimensional surface of the necessary shift in time or frequency scale as a function of temperature and pressure. The model fits very well with the present experimental data. Moreover, when specialized to the appropriate experimental range (0-850 MPa and 215-313 K) the predictions of the model also agree quite well with the previous study on nonlinear viscoelastic behavior of polyurea, conducted by Chevellard et al [103].

4.2.2 Experiment

Material

Polyurea (PU) is a block copolymer formed from a chemical reaction of an aromatic isocyanate component (hard segment) and an amine-terminated resin blend component (soft segment). The aromatic isocyanate component, commercial name Isonate 143L is manufactured by Dow Chemicals [26]. It is a polycarbodiimide-modified diphenylmethane diisocyanate. It is in liquid form at room temperature and has a low viscosity and good storage stability down to 24 °C. The amine-terminated resin blend component, commercial name Versalink P-1000, is an oligomeric diamine, manufactured by Air Products [6]. It is a polytetramethyleneoxide-di-p-aminobenzoate and is liquid at room temperature, which allows it to be mixed, cast, and cured in ambient conditions. The reaction between Isonate 143L and Versalink P-1000 is generally very fast and insensitive to humidity and low temperatures. Theoretically, Isonate 143L and Versalink P-1000 should be mixed in a stoichiometric ratio of 1:1, i.e., the total number of isocyanate groups must equal the total number of amine groups in order to obtain complete chemical reaction. Holzworth et al. also showed that the stoichiometric ratio affects the mechanical properties of polyurea [4]. However, a slight 5% excess of Isonate 143L is typically recommended by the manufacturer to ensure that the reaction is completed and to create a lightly cross-linked polymer [6].

Sample Preparation

Samples were fabricated according to the process described in [4]. Teflon molds were used to cast test specimens with the geometry shown in Figure 4.10b.

This geometry was selected to match with the high-pressure cell described below. The polyurea specimens were cured for 2 weeks at room temperature in a humidity-controlled environmental chamber that maintains RH 10%. Twelve specimens were fabricated in one batch.

Experimental Setup

The test system consists of ultrasonic wave measurement setup, quasi-static confined loading setup, and temperature control chamber. The ultrasonic measurements were performed in the through-transmission mode, using a desktop computer with a Matec TB-1000 Toneburst card, two Panametrics videoscan longitudinal transducers (V103 Panametrics-NDT OLYMPUS), a 100:1 attenuator box, and a digital oscilloscope (Tektronix DPO3014) [50]. Toneburst signals of prescribed frequencies were generated from the card and split through BM-174-3 cables to the pitching transducer and the attenuator box, where the voltage was reduced by a factor of 100 to be measured on the scope. The received signal at the catching transducer was sent directly to the scope where the amplitude and travel time were measured.

Instron servo-hydraulic machine model 1332 was used as loading test machine. It has the capability to generate forces up to 100 kN. The compression mode was used in this study. MTS controller model 407 was used to control the force and displacement. Either displacement or force control can be selected. The loading rate is adjustable depending on the test condition. In this study, the force control mode was used with the slow loading rate of $67\,\mathrm{N\,s^{-1}}$ to ensure that sample was under quasi-static condition. An MTS environmental chamber model 651 was used to provide a cooling range from ambient to 144 K using liquid nitrogen. Testing temperature was

controlled by MTS temperature controller model 409.80.

To create quasi-hydrostatic conditions for the sample, a confinement cell was made of maraging steel (see Figure 4.10). The nearly cylindrical geometry and small size was chosen to achieve high pressures of 1000 MPa at the maximum force load of 100 kN, while avoiding failure. The cell structure has no sharp edge, thereby minimizing stress concentrations. Two vertical flat surfaces were machined on the two opposite sides of the cell where the two transducers were placed. Two pistons with the same cross-sectional shape of the sample were used for loading, while inside the cell, two filler columns were aligned to ensure that the sample surfaces were flat and parallel to the surfaces of the two transducers (see Figure 4.10). Screws, nuts, springs, fasteners, and cover plates were used to hold the test setup and to provide the constant applied load on the two transducers.

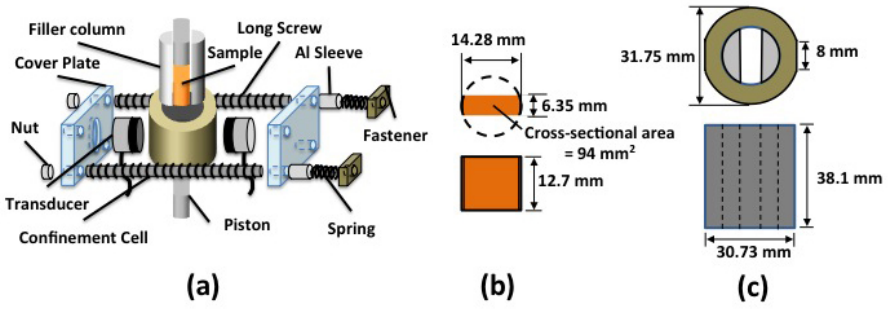

Figure 4.10: (a) Components of high-pressure test fixture (b) Sample (c) Confinement cell

Experimental Procedure

The confinement cell calibration process was done at ambient condition. The special shape of the cell lead to the complexity of the wave speed measurement; internal reflections and interferences. The measured transmission can be roughly

divided in two components (see Figure 4.11): traveling in a direct path through the sample and traveling around the cell body. The purpose of the cell calibration is to eliminate the effect of the second component from the measurement of time of travel in the cell (t_C). In calibration test 1, we filled the cell with water, sent ultrasonic wave through the cell, and recorded the input and received signals (see Figure 4.12a). We used water because the wave speed in water at room temperature was known ($1484\,\mathrm{m\,s^{-1}}$), and it could completely fill the cell without gaps. The received signal in test 1 consisted of both direct-path and the go-around components added (see Figure 4.11). In test 2, we repeated this for an empty cell. The received signal in test 2 is only the go-around component. Subtracting the received signal in test 2 from the received signal from test 1, the direct-path signal is obtained (see Figure 4.12b). Note that since the impedance mismatch between steel and water is very large, the effect of transmission into the water on the go-around signal is neglected. Furthermore, since we are only interested in the timing of the pulse, a small error in the amplitudes due to this assumption is not expected to affect the eventual results. Finally, the consistency of the shape and amplitude of the go-around signals in Figure 4.12a, fortifies the relevance of this assumption (the input pulses are the same in both tests). We estimated the total time of travel in the direct path (t_T) using the first peaks of the input and the direct-path signals (see Figure 4.12b). We calculated the time of travel in the water (t_W), using the known wave speed and gap width of 6.35 mm. The time of travel in the cell (t_C) can be found by subtracting t_W from t_T (see Figure 4.11). Since the cell is made of maraging steel, whose mechanical properties do not change much in the range of testing temperature and pressure, we assume that t_C is constant. This agreed with our observations on the wave speed in the steel as we varied the

temperature. We found that t_C equals 4.564 µs at 1 MHz. It will be used later in the wave speed measurement. Note that t_C can also be estimated by dividing the total thickness of the steel in the direct-path propagation with the known wave speed in the steel (5490 m s^{-1}). From this method, t_C is 4.442 µs which is in very close agreement with the value above.

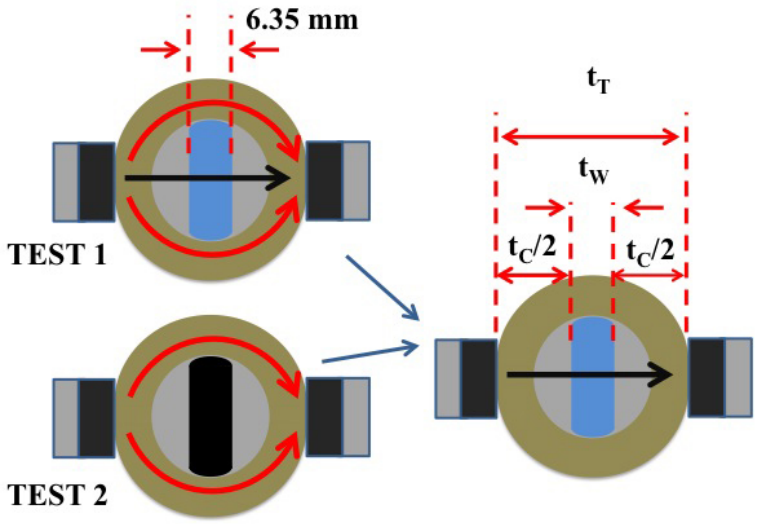

Figure 4.11: Confinement cell calibration; t_T is total time of travel of direct-path signal, t_C is half of time of travel in the cell, t_W is time of travel in the water. The gap thickness is 6.35 mm

After the cell calibration was finished, the wave speed measurement was performed. The testing temperature ranges from -50 to 30 °C with 10 °C steps. At each testing temperature, the sample was loaded from ambient pressure to 900 MPa. After loading, the sample could not be reused because it was deformed and loses its initial shape (though the material is highly elastic in compression, at very high pressures, it will extrude, in shear, through the very small gaps between the pistons and the cell body). Nine samples, all made in the same batch, were used for the nine testing temperatures. Before testing, dimensions and densities of all samples were measured.

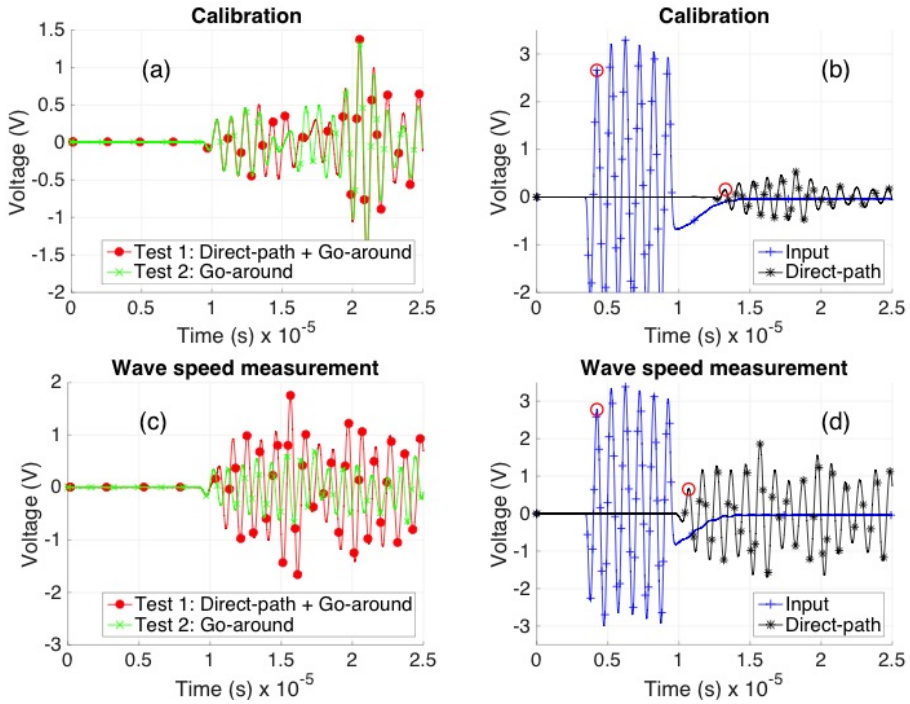

Figure 4.12: (a) Received signals from test 1 and 2 in cell calibration. (b) Total time of travel in the direct-path (t_T) of the calibration is equal to the time difference between the two red circles. (c) Received signals from test 1 and 2 in wave speed measurement. (d) Total time of travel in the direct-path (t_T) of the wave speed measurement is equal to the time difference between the two red circles. Note: The direct-path signal in (b) and (d) are obtained by subtracting the Go-around from the Direct-path + Go-around, in (a) and (c). The input signal is the same for all tests.

Longitudinal wave couplant was applied over all surfaces of the samples and where the cell touched the samples and the transducers. To measure the wave speed in the sample, two measurements were required at each testing temperature. In test 1, the sample was inserted into the confinement cell and capped with pistons from top and bottom (see Figure 4.10a). The two transducers were placed at the middle of the flat surfaces of the cell and locked in position with the two cover plates. In order to maintain relatively constant contact pressure between the transducers and the cell, two identical springs, fasteners and aluminum columns were employed together. The whole test fixture was held together by spring force (see Figure 4.10a). The test

fixture was then placed in an environmental chamber and the whole test fixture was equilibrated at the testing temperature for an hour, before the compressive load was applied on the sample at the loading rate of $67\,\mathrm{N\,s^{-1}}$. The polyurea sample in the cell was under quasi-hydrostatic conditions due to the slow loading rate and nearly incompressible nature of the elastomer. The testing pressure range is from 25 to 900 MPa, with 25 MPa increments up to 400 MPa and 50 MPa increments for the rest. At each pressure step, the loading machine was stopped and held at constant load, while the ultrasonic measurement was performed at nominal frequency 1 MHz, and data was recorded. The compressive force and axial displacement histories were measured by the load cell and linear variable differential transformer (LVDT), respectively. They were recorded in a Labview signal express text file for analysis. In test 2, the test fixture was assembled empty and was equilibrated in the environmental chamber at the same temperature as test 1 for an hour. No pressure was applied on test fixture, though the springs were tightened to the same level as test 1. After 1-hour equilibration, the signal was sent through the empty confinement cell to record the go-around signal for the given temperature. Example of recorded signals test 1 and test 2 from wave speed measurement are shown in Figure 4.12c.

Subtracting the received signal in test 2 (without sample) from the received signal from test 1 (with sample), the direct-path signal was obtained (see Figure 4.12d). The total time of travel in the direct path (t_T) was measured using the first peaks of the input and the direct-path signals (see Figure 4.12d). Subtracting t_C previously obtained from cell calibration process from t_T, the time of travel in the sample (t_S) at the testing temperature and pressure was obtained. We then repeated the process of finding t_S for other testing temperatures and pressures. Longitudinal wave speed

at each testing temperature and pressure can be calculated as:

$$v_L\left(T,P\right)=\frac{d_g}{t_S\left(T,P\right)}, \tag{4.58}$$

where the constant d_g =6.35 mm is the gap thickness shown in Figure 4.11, $t_S(T,P)$ and $v_L(T,P)$ are the time of travel in the sample and the longitudinal wave speed at testing temperature T and pressure P, respectively. Longitudinal wave speed at each testing temperature and pressure is shown in Figure 4.13a. Uniaxial quasi-static stress and strain of the sample were also calculated, using the recorded force, displacement histories, and initial dimension of the sample. Since polyurea is nearly incompressible material the confined compressive force creates quasi-hydrostatic pressure on the sample. Machine stiffness was also measured for correcting the measured strain in the sample.

$$\sigma=P=\frac{F\left(t\right)}{A}, \tag{4.59}$$

$$\epsilon\left(T,P\right)=\frac{d\left(T,P\right)-d\left(T,P_o\right)}{h}, \tag{4.60}$$

where σ is engineering stress (or pressure (P) in this particular case), $\epsilon\left(T,P\right)$ is compressive engineering strain at T and P, $F\left(t\right)$ is compressive force history, $d\left(T,P\right)$, and $d\left(T,P_o\right)$ are displacements at T and P, and T and P_o, respectively. h and A are the initial height and cross sectional area of the sample (see Figure 4.10b). The stress and strain are shown in Figure 4.13b. The slope of the stress-strain plot represents the tangential quasi-static longitudinal modulus (see Figure 4.13d). With the compressive strain at each temperature and pressure, polyurea density $\rho\left(T,P\right)$ can be calculated

as follows:

$$\rho\left(T,P\right)=\frac{\rho_o}{\left(1+3C_{TE}\left(T-T_o\right)+\epsilon\left(T,P\right)\right)}, \tag{4.61}$$

where ρ_o is the density of polyurea at room temperature T_o and ambient pressure, and C_{TE} is the thermal expansion coefficient of polyurea ($207\,\mu\mathrm{m\,m^{-1}\,K^{-1}}$). $\rho\left(T,P\right)$ is shown in Figure 4.13c. The 1 MHz dynamic longitudinal modulus at each temperature and pressure can be calculated as:

$$L\left(T,P\right)=\rho\left(T,P\right)\left[v_L\left(T,P\right)\right]^2, \tag{4.62}$$

where $L\left(T,P\right)$ is the dynamic longitudinal modulus at 1 MHz, temperature T, and pressure P. $L\left(T,P\right)$ is shown in Figure 4.13e.

Experimental results

During experiment, the samples were loaded slowly and step-wise from atmospheric pressure all the way to the maximum value of 900 MPa, and the ultrasonic data were collected at each pressure of interest. The unloading data were not considered here. The measured longitudinal wave speed is shown in Figure 4.13a. The wave speed at each temperature can be divided into two segments, with the first having a higher slope than the second. It is hypothesized that the bend in each line represents a transition in the material from rubber to glassy. As temperature decreases the glass transition point shifts toward lower pressure. At higher temperatures the transition point is more pronounced; while, at lower temperatures it exhibits a more gradual curve-like behavior. Figure 4.13b shows the compressive stress (to be an estimate of the pressure)-compressive strain plots. At $-50\,^{\circ}\mathrm{C}$ polyurea undergoes 11% strain

at 900 MPa; whereas, at 30 °C it takes 16% strain. Figure 4.13c shows the density of polyurea versus pressure. When pressure is above 300 MPa, the density measured at higher temperatures shows a higher slope, and all the curves converge to around 1200 $\mathrm{kg\,m^{-3}}$ at 900 MPa. Figure 4.13d represents quasi-static longitudinal modulus as a function of pressure. The data of quasi-static longitudinal modulus that obtains from the slope of the stress-strain plot are not clean due to the effect of the noise in the strain measurement, which requires very accurate displacement history. The overall trends with pressure and temperature are as expected. Figure 4.13e shows the ultrasonic longitudinal modulus (L) at 1 MHz. It increases with increasing pressure and decreasing temperature and is generally the quasi-static modulus, and they are of the same order of magnitude. The difference between them is around 20%. Similar to longitudinal wave speed, we can somewhat see the ultrasonic longitudinal modulus has two distinct segments; higher slope at the first segment and smaller slope at the second segment. However, due to the effect of density in longitudinal modulus (see equation 4.62), this behavior is less pronounced. Despite the less apparent glass transition bend point, its location is the same as in the longitudinal wave speed. Paterson did measurement of Young's moduli of polyureathane, as a function of pressure up to 1000 MPa at 20 °C and found similar behavior [104]. In Paterson's work, the glass transition of polyureathane occurs at around 400 MPa at 20 °C. Here the glass transition of polyurea happens at around 350 MPa at the same temperature. Paterson did not determine the glass transition temperature of polyurethane at atmospheric pressure; however, he provided the number from the supplier, −68 °C. For our polyurea sample, the glass transition is found to be around -50 to −60 °C [42]. At each temperature, the glass transition occurs when the 1 MHz dynamic longitudinal modulus

is higher than 8 GPa. Note that at lower temperatures, the glass transition point shifts toward lower pressure. Paterson did not test at other temperatures.

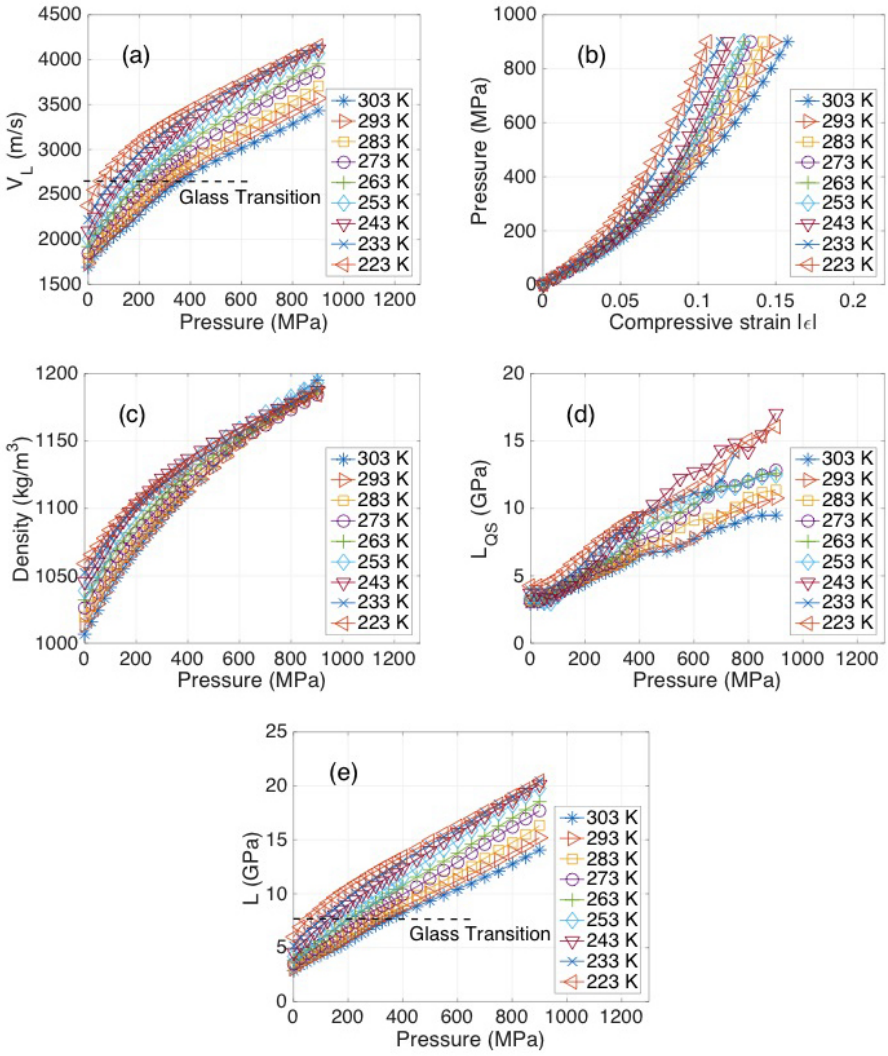

Figure 4.13: Longitudinal wave speed, v_L versus pressure. (b) Pressure versus compressive strain. (c) Density of polyurea versus pressure. (d) Quasi-static longitudinal modulus, L_{QS} versus pressure (e) Dynamic longitudinal modulus, L at 1 MHz versus pressure.

Analysis of the experimental data

In order to use the data of the longitudinal modulus for time-temperature-pressure superposition, a slight modification is needed. The 1 MHz longitudinal modulus at each temperature and pressure, $L(\omega, T, P)$ needs to be normalized, by a factor that depends theoretically on the density and temperature (vertical shift), based on the flexible chain theory [36, 52].

$$L_R(\omega, T, P) = L(\omega, T, P)\frac{\rho_{ref}T_{ref}}{\rho T}, \tag{4.63}$$

where $L_R(\omega, T, P)$ is the reduced longitudinal modulus. ω is the angular frequency. ρ_{ref} is the density of polyurea at reference temperature, T_{ref} and pressure, P_{ref}. For the following analysis, ρ_{ref} and T_{ref} can be arbitrary chosen since they are constant multipliers; so we use 1 for both of them. Figure 4.14a shows L_R as a function of pressure at each testing temperature.

Following Fillers and Tschoegl [102], the fractional free volume is considered a state variable that depends on pressure and temperature. Instead of dealing with both pressure and temperature separately, we seek to find a relation between pressure and temperature that yields the same state of the fractional free volume. It is worth noting that the fractional free volume is not calculated directly in our study. But it is associated to the reduced longitudinal modulus. If two different states of polyurea with different temperatures and pressures yield the same reduced longitudinal modulus, they are assumed to have the same fractional free volume. To do this, the following process is used:

1.Consider only data point below glass transition pressure, above which the

time-temperature-pressure superposition cannot be applied (see Figure 4.14a). Glass transition temperature of polyurea is around 213-223 K at atmospheric pressure [42, 103].

2.Consider data of a testing temperature and use interpolation to relate pressure to temperature that yields the same L_R (see Figure 4.14b). Collect pressure-temperature pairs.

3.Repeat the process for other testing temperatures.

Figure 4.14c shows the relation between pressure and temperature that give the same value of reduced dynamic longitudinal modulus L_R. Each line represents each testing temperature and maps the testing pressure to the corresponding testing temperature at 0.1 MPa (ambient pressure) that has the same L_R. Figure 4.14d relates the increasing in pressure to the amount of temperature reduction, depending on the initial temperature. Each line has different number of data points since the minimum temperature in the interpolation process is always $T_g = 223$ K. We remark that the reduction in temperature that is resulted from pressure may be different if we use longitudinal modulus at other frequencies. However, in the absence of any information on this point we assume that the difference is negligible.

4.2.3 Discussion

Figure 4.14a shows a point or a very narrow range for each testing temperature, where the slope of the reduced longitudinal modulus changes. At these transition pressures, the behavior of polyurea changes from rubber-like to glass-like. We limit the analysis in this paper to the rubbery range to be compatible with the free volume-based WLF approach. It can be seen in Figure 4.14c that the equivalent temperature

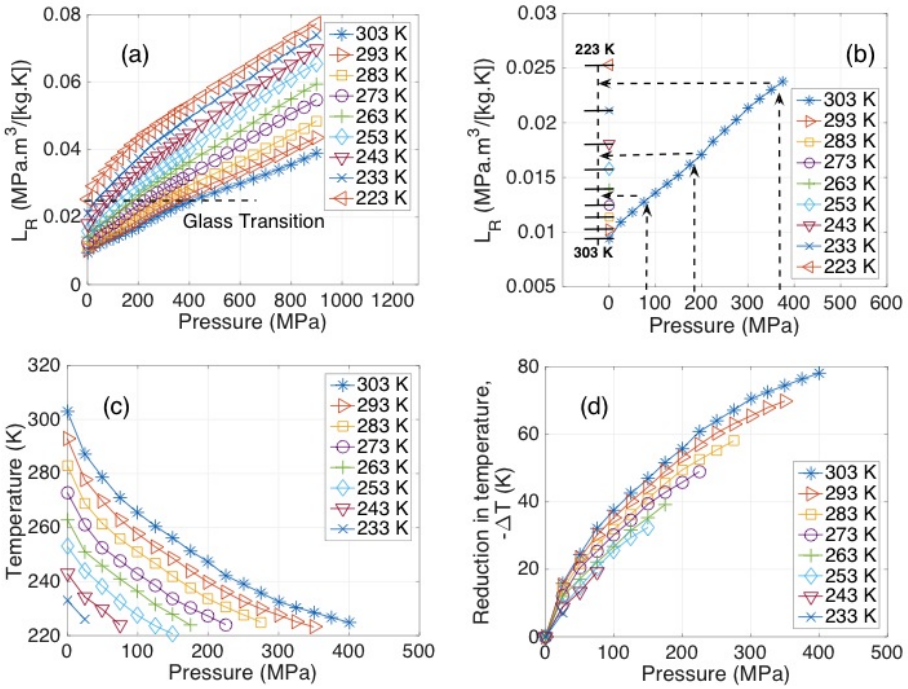

Figure 4.14: (a) The reduced dynamic longitudinal modulus, L_R versus pressure and temperature (b) Interpolation to find relation between temperature and pressure (c) The apparent temperature for a given actual temperature and applied pressure (d) Reduction in temperature versus pressure for a given actual temperature

is more sensitive at lower pressure values, suggesting that it might asymptotically approach to a limit value at high pressures. However, the material becomes glassy before that state is reached. Figure 4.14d supports this conclusion. If all the curves in this figure were to collapse on to a common one, a much simpler formulation would have been possible. In what follows, we will implement Fillers and Tschoegl's idea to derive the modified WLF equation (mWLF) for the general case of combined temperature and pressure effects [102].

Theory

The main idea of the modification of the WLF equation in this work follows that of Fillers and Tschoegl [52, 102]. However, we proposed an alternative material testing method compatible with the mWLF model and that is less time-consuming for nearly incompressible viscoelastic materials. The procedure is as follows. The shift factor, a_{TP}, is a function of fractional free volume defined as the ratio of the free volume inside a polymer to the total volume (free volume plus occupied volume) [36, 51]. It is expressed as,

$$\log a_{TP} = \frac{B}{2.303}\left(\frac{1}{f\left(T,P\right)} - \frac{1}{f\left(T_o,P_o\right)}\right), \tag{4.64}$$

where

$$f\left(T,P\right) = \frac{V_f\left(T,P\right)}{V\left(T,P\right)} = \frac{V_f\left(T,P\right)}{V_f\left(T,P\right)+V_\phi\left(T,P\right)}, \tag{4.65}$$

the factor B is a constant, $f\left(T,P\right)$ is the fractional free volume at temperature T and pressure P, $f\left(T_o,P_o\right)$ is the fractional free volume at reference temperature T_o and pressure P_o, $V_f\left(T,P\right)$, $V_\phi\left(T,P\right)$, and $V\left(T,P\right)$ are the temperature- and pressure-dependent free, occupied, and total volumes, respectively. The fractional free volume $f\left(T,P\right)$ is assumed to be conservative. The change of $f\left(T,P\right)$ does not depend on path. The differential of $f\left(T,P\right)$ or the infinitesimal change of $f\left(T,P\right)$ can be written as follows:

$$df\left(T,P\right) = \left(\frac{\partial f}{\partial T}\right)_P dT + \left(\frac{\partial f}{\partial P}\right)_T dP. \tag{4.66}$$

We integrate equation 4.66 from reference temperature T_o and pressure P_o to testing temperature T and pressure P, using a path that first keeps pressure fixed at P_o,

while increasing the temperature, followed by a segment that keeps the temperature fixed at T and increases the pressure:

$$\int_{T_o,P_o}^{T,P} df\,(T,P) = \int_{T_o}^{T} \left(\frac{\partial f}{\partial T}\right)_{P_o} dT + \int_{P_o}^{P} \left(\frac{\partial f}{\partial P}\right)_{T} dP. \tag{4.67}$$

Fillers and Tschoegl preferred a different integration path [102]; they integrated $\left(\frac{\partial f}{\partial P}\right)_{(T_o)}$ from P_o to P and $\left(\frac{\partial f}{\partial T}\right)_{P}$ from T_o to T. They chose to consider the pressure dependence of the expansivity of the free volume. In this work and consistent with the original WLF equation, only the expansivity of the free volume at ambient pressure is used. However, we have to deal with the temperature dependence of the compressibility of the free volume. Moreover, this choice of path suits our experimental data more seamless. The first term on the right of equation 4.67 relates to expansivity of the free volume at reference pressure and can be written as follows:

$$\int_{T_o}^{T} \left(\frac{\partial f}{\partial T}\right)_{P_o} dT = \int_{T_o}^{T} \alpha_f\,(P_o)\,dT = \alpha_f\,(P_o)\,[T - T_o]\,, \tag{4.68}$$

where $\alpha_f\,(P_o)$ is the expansivity of the free volume at reference pressure. Filler and Tschoegl suggested that the temperature dependence of $\alpha_f\,(P_o)$ could be neglected. Generally, $\alpha_f\,(P_o)$ could be obtained, using the material database of constants c_1 and c_2 in the WLF equation with the assumption that the constant B is equal to 1. It is rather difficult to obtain information of $\alpha_f\,(P_o)$ without this assumption; however, with our model, no such assumption is needed for determining $\alpha_f\,(P_o)$. We can obtain both $\alpha_f\,(P_o)$, and B using nonlinear regression analysis as shown below. The second term on the right of equation 4.67 relates to the compressibility of the free volume

that depends on both temperature and pressure and can be written as:

$$\int_{P_o}^{P} \left(\frac{\partial f}{\partial P}\right)_T dP = -\int_{P_o}^{P} \kappa_f (T,P)\, dP, \tag{4.69}$$

where

$$\kappa_f (T,P) = \kappa (T,P) - \kappa_\phi (T,P), \tag{4.70}$$

$\kappa_f (T,P)$, $\kappa (T,P)$, and $\kappa_\phi (T,P)$ are the compressibilities of the free volume, polymer, and occupied volume, respectively. The compressibility is the reciprocal of bulk modulus.

$$\kappa (T,P) = \frac{1}{K (T,P)}, \tag{4.71}$$

$$\kappa_\phi (T,P) = \frac{1}{K_\phi (T,P)}. \tag{4.72}$$

Bulk modulus of a polymeric material has approximately a linear dependence on pressure [102, 105] and can be written as:

$$K (T,P) = K (T,P_o) + k (T)\, P. \tag{4.73}$$

For nearly incompressible polymers, e.g. polyurea, Poisson's ratio is around 0.4 (low temperature, glass-like behavior) - 0.5 (high temperature, rubber-like behavior). Thus bulk modulus is significantly larger than shear modulus and one may approximate bulk modules with the longitudinal modulus L:

$$K (T,P) \approx L (T,P) = L (T,P_o) + l (T)\, P. \tag{4.74}$$

Our experimental observations confirm that the longitudinal modulus of polyurea is a linear function of pressure up to the glass transition (see Figure 4.13e), with a temperature-dependent slope. In this work, instead of using longitudinal modulus measured quasi statically, we use a more accurate longitudinal modulus that was measured at 1 MHz using ultrasonic wave measurement technique under pressure. Both moduli of course have similar behavior, and are of the same order of magnitude, thereby allowing us to use this replacement (see Figures 4.13d and 4.13e). $L\left(T,P_o\right)$ and $l\left(T\right)$ can be obtained from fitting equation 4.74 to the experimental data shown in Figure 4.13e. The results are shown in Figures 4.15b and 4.15c. The bulk modulus of the occupied volume is very difficult to measure experimentally. Filler and Tschoegl assumed that it has the same form as the bulk modulus of the polymer [52, 102], i.e.

$$K_\phi\left(T,P\right) \approx L_\phi\left(T,P\right) = L_\phi\left(T,P_o\right) + l_\phi\left(T\right)P. \tag{4.75}$$

$L_\phi\left(T,P\right)$, $L_\phi\left(T,P_o\right)$, and $l_\phi\left(T\right)$ are obtained using nonlinear regression analysis, after the final formulation is derived. Using equations 4.70-4.75, equation 4.69 can be integrated and yields:

$$\begin{aligned}\int_{P_o}^{P}\left(\frac{\partial f}{\partial P}\right)_T dP = -\Bigg[&\frac{1}{l\left(T\right)}\ln\left(\frac{1+\frac{l(T)}{L(T,P_o)}P}{1+\frac{l(T)}{L(T,P_o)}P_o}\right)\\ &-\frac{1}{l_\phi\left(T\right)}\ln\left(\frac{1+\frac{l_\phi(T)}{L_\phi(T,P_o)}P}{1+\frac{l_\phi(T)}{L_\phi(T,P_o)}P_o}\right)\Bigg].\end{aligned} \tag{4.76}$$

Combining equations 4.67, 4.68, and 4.76, we obtain:

$$f\left(T,P\right) = f\left(T_o,P_o\right) + \triangle f_{P_o}\left(T,T_o\right) - \triangle f_T\left(P,P_o\right), \tag{4.77}$$

where

$$\triangle f_{P_o}(T, T_o) = \int_{T_o}^{T} \left(\frac{\partial f}{\partial T}\right)_{P_o} dT = \alpha_f(P_o)\left[T - T_o\right], \tag{4.78}$$

$$\begin{aligned} \triangle f_T(P, P_o) &= -\int_{P_o}^{P} \left(\frac{\partial f}{\partial P}\right)_T dP \\ &= \frac{1}{l(T)} \ln\left(\frac{1 + \frac{l(T)}{L(T,P_o)}P}{1 + \frac{l(T)}{L(T,P_o)}P_o}\right) \\ &\quad -\frac{1}{l_\phi(T)} \ln\left(\frac{1 + \frac{l_\phi(T)}{L_\phi(T,P_o)}P}{1 + \frac{l_\phi(T)}{L_\phi(T,P_o)}P_o}\right), \end{aligned} \tag{4.79}$$

$\triangle f_{P_o}(T, T_o)$ is the change in fractional free volume due to temperature at reference pressure P_o, and $\triangle f_T(P, P_o)$ is the change in fractional free volume due to pressure at testing temperature T. Equation 4.77 can be modified in term of temperature as:

$$f(T, P) = f(T_o, P_o) + \triangle f_{P_o}(T, T_o) + \triangle f_{P_o}(T^*, T), \tag{4.80}$$

where

$$\triangle f_{P_o}(T^*, T) = -\triangle f_T(P, P_o), \tag{4.81}$$

$$\triangle f_{P_o}(T^*, T) = \alpha_f(P_o)\left[T^* - T\right], \tag{4.82}$$

$\triangle f_{P_o}(T^*, T)$ is the change in fractional free volume due to an equivalent temperature T^*. Instead of dealing directly with $\triangle f_T(P, P_o)$ in equation 4.77, we equate $-\triangle f_T(P, P_o)$ to $\triangle f_{P_o}(T^*, T)$. This allows us to relate the change in fractional free volume due to pressure to the change in fractional free volume due to virtual temperature that is defined in equation 4.82, i.e. the temperature that yields the same

change in fractional free volume as the applied pressure. Combining equations 4.79, 4.81, and 4.82, we obtain:

$$\begin{aligned} -\left[T^{*}-T\right] &= \frac{2.303}{\alpha_f\left(P_o\right) l\left(T\right)} \log\left(\frac{1+\frac{l(T)}{L(T,P_o)}P}{1+\frac{l(T)}{L(T,P_o)}P_o}\right) \\ &\quad -\frac{2.303}{\alpha_f\left(P_o\right) l_\phi\left(T\right)} \log\left(\frac{1+\frac{l_\phi(T)}{L_\phi(T,P_o)}P}{1+\frac{l_\phi(T)}{L_\phi(T,P_o)}P_o}\right). \end{aligned} \tag{4.83}$$

Equation 4.83 equates any change in pressure from reference pressure P_o at testing temperature T to the change in temperature from testing temperature T at reference pressure P_o. We can rewrite equation 4.83 as:

$$-\left[T^{*}-T\right] = c_3\left(T\right)\log\left(\frac{1+c_4\left(T\right)P}{1+c_4\left(T\right)P_o}\right) - c_5\left(T\right)\log\left(\frac{1+c_6\left(T\right)P}{1+c_6\left(T\right)P_o}\right), \tag{4.84}$$

where

$$c_3\left(T\right) = \frac{2.303}{\alpha_f\left(P_o\right) l\left(T\right)}, \tag{4.85}$$

$$c_4\left(T\right) = \frac{l\left(T\right)}{L\left(T,P_o\right)}, \tag{4.86}$$

$$c_5\left(T\right) = \frac{2.303}{\alpha_f\left(P_o\right) l_\phi\left(T\right)}, \tag{4.87}$$

$$c_6\left(T\right) = \frac{l_\phi\left(T\right)}{L_\phi\left(T,P_o\right)}, \tag{4.88}$$

$c_4\left(T\right)$ is a known parameter since we know $l\left(T\right)$ and $L\left(T,P_o\right)$ from ultrasonic wave testing under pressure, $c_3\left(T\right)$, $c_5\left(T\right)$ and $c_6\left(T\right)$ are unknown parameters that depend

on testing temperature T.

Substituting equation 4.77 into equation 4.64, we obtain:

$$\log a_{TP} = \frac{-B}{2.303 f\left(T_o, P_o\right)} \left(\frac{\triangle f_{P_o}\left(T, T_o\right) - \triangle f_T\left(P, P_o\right)}{f\left(T_o, P_o\right) + \triangle f_{P_o}\left(T, T_o\right) - \triangle f_T\left(P, P_o\right)} \right). \tag{4.89}$$

The shift factor $\log a_{TP}$ includes both temperature and pressure effects on time-dependent viscoelastic properties. Using equations 4.78-4.88, equation 4.89 can be written in more convenient from as:

$$\log a_{TP} = \frac{-c_1\left(T - T_o - \Omega\left(T, P\right)\right)}{c_2 + T - T_o - \Omega\left(T, P\right)}, \tag{4.90}$$

where

$$\Omega\left(T, P\right) = c_3\left(T\right) \log\left(\frac{1 + c_4\left(T\right) P}{1 + c_4\left(T\right) P_o} \right) - c_5\left(T\right) \log\left(\frac{1 + c_6\left(T\right) P}{1 + c_6\left(T\right) P_o} \right), \tag{4.91}$$

$$c_1 = \frac{B}{2.303 f\left(T_o, P_o\right)}, \tag{4.92}$$

$$c_2 = \frac{f\left(T_o, P_o\right)}{\alpha_f\left(P_o\right)}, \tag{4.93}$$

c_1 and c_2 are constants in original WLF equation, and $\Omega\left(T, P\right)$ is the additional pressure-dependent term that is introduced into the original WLF equation. Equation 4.90 represents the modified WLF equation that includes both effects of temperature and pressure. At the pressure equal to the reference pressure P_o, $\Omega\left(T, P\right)$ equals to 0 and equation 4.90 reduces to the original WLF equation.

Applications

The function $\log a_{TP}$ in equation 4.90 is the temperature-and-pressure- dependent logarithmic time shift required to bring data recorded at the testing temperature T and pressure P, into superposition with data recorded at the reference temperature T_o and pressure P_o. In this study, the reference temperature T_o and pressure P_o are 273 K and 0.1 MPa respectively. Materials that allow this superposition are called, thermorheologically and piezorheologically simple materials. Each polymer has different shift factor (though for temperature superposition, the WLF formula presents a very good uniform approximation formula for most polymers between T_g and T_g+100 K) and can be characterized through the parameters: c_1, c_2, $c_3(T)$, $c_4(T)$, $c_5(T)$, and $c_6(T)$. $L(T, P_o)$ and $l(T)$, which appear in $c_4(T)$ can be obtained from fitting equation 4.74 to the experimental data below glass transition pressure that is shown in Figure 4.13e. Figure 4.15a shows that the approximation and linearization in equation 4.74 agree very well with experimental data shown in Figure 4.13e. $L(T, P_o)$ and $l(T)$ are shown in Figures 4.15b and 4.15c, considering only data in the range between 243 and 303 K. We found that inverse of $l(T)$, which is a variable in parameter $c_3(T)$ is a linear function of temperature (see Figure 4.15d). It can be written in the following form:

$$\frac{1}{l(T)} = I_1 (T - I_2), \tag{4.94}$$

where I_1 and I_2 can be found from linear curve fitting. They are shown in Table 4.1. With a constant $\alpha_f(P_o)$, $c_3(T)$ can then be written in the following form:

$$c_3(T) = c_{31}(T - c_{32}), \tag{4.95}$$

where

$$c_{31} = \frac{2.303 I_1}{\alpha_f(P_o)}, \tag{4.96}$$

$$c_{32} = I_2, \tag{4.97}$$

c_{31} is an unknown constant to-be-found based on parameter $\alpha_f(P_o)$. $c_4(T)$ or $\frac{l(T)}{L(T,P_o)}$ can now be calculated using equation 4.86 and is shown in Figure 4.15e. As we can see, $c_4(T)$ is independent of the temperature in the range from 243 to 303 K. Therefore, we assume that $c_4(T)$ is constant and equal to the average of $c_4(T)$:

$$c_4(T) = \bar{c}_4(T) = c_4. \tag{4.98}$$

c_4 is shown in Table4.1. Due to the lack of information about parameters $c_5(T)$, and $c_6(T)$, we assume that $c_5(T)$ also has a linear form similar to $c_3(T)$, and $c_6(T)$ is constant similar to $c_4(T)$. This is quite reasonable assumption due to the similar characteristics between $c_3(T)$ and $c_5(T)$, and $c_4(T)$ and $c_6(T)$ (see equations 4.85-4.88).

With equations 4.95 to 4.98, and assumption that $c_5(T)$ and $c_6(T)$ are linear function of temperature and constant, respectively, a preliminary nonlinear regression analysis was performed using equation 4.84 (or equivalently equation 4.91) and data

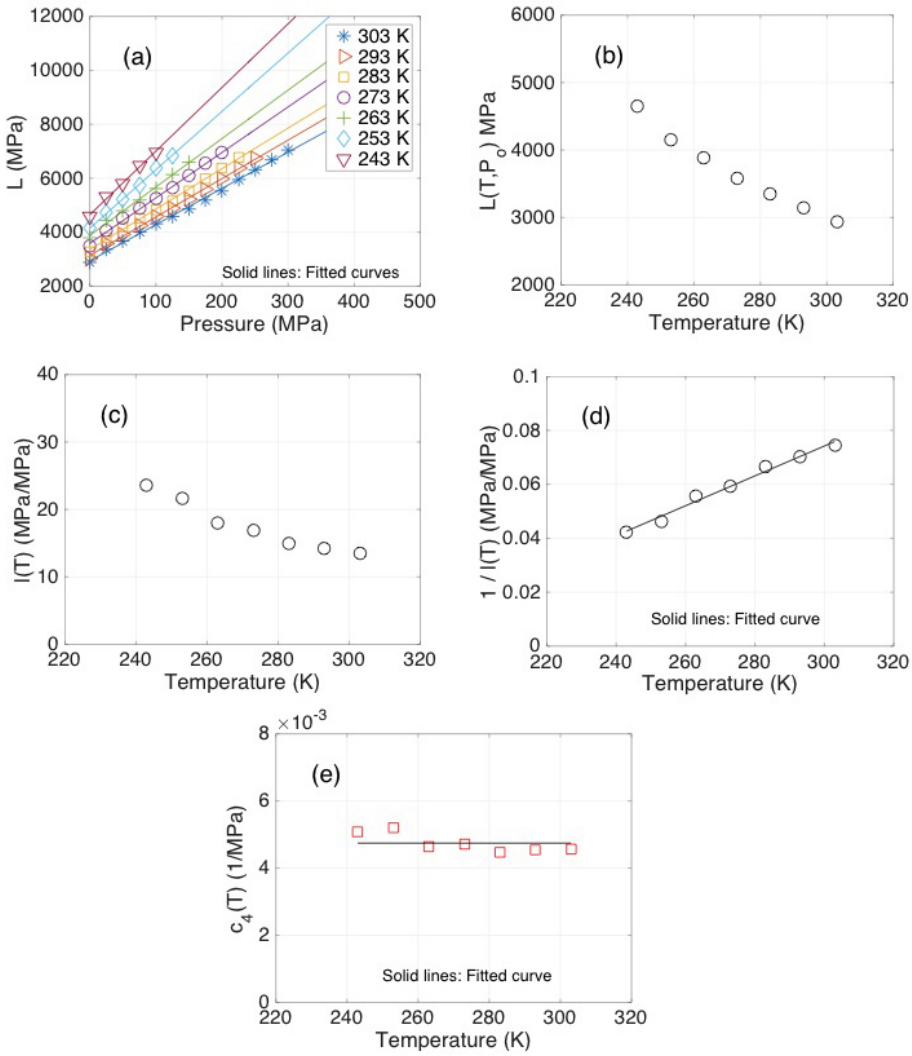

Figure 4.15: (a) Dynamic longitudinal modulus, L at 1 MHz versus pressure. (b) Longitudinal moduli, $L\,(T, P_o)$ at 1 MHz and atmospheric pressure versus temperature. (c) Slopes of longitudinal moduli, $l\,(T)$ at 1 MHz versus temperature. (d) Inverse of $l\,(T)$ at 1 MHz versus temperature. (e) $c_4\,(T)$ at 1 MHz versus temperature

in Figure 4.14d. The initial guess for $\alpha_f\,(P_o)$ was obtained using equations 4.92 and 4.93, with the assumption that parameter B is 1. Constants c_1 and c_2 were measured and recorded elsewhere [73]. They are shown in Table 4.1. The initial guesses for c_{51} and c_{52} were c_{31} and c_{32}, respectively. Constant c_4 was used as the initial guess for c_6. The results of the regression analysis are shown in Figure 4.16a. Constants c_{31}, c_{32},

c_4, c_{51}, c_{52}, c_6, and $\alpha_f(P_o)$ are given in Table 4.1. It is notable that c_{32} and c_{52} are very close to each other and are below the glass transition temperature of polyurea (213-223 K). As the temperature gets closer to these values, the effect of pressure on the shift factor diminishes. From the nonlinear regression analysis, we obtain all necessary parameters for the pressure-dependence in the mWLF equation. It can be written as:

$$\Omega(T,P) = c_{31}(T - c_{32}) \log\left(\frac{1 + c_4 P}{1 + c_4 P_o}\right) - c_{51}(T - c_{52}) \log\left(\frac{1 + c_6 P}{1 + c_6 P_o}\right), \qquad (4.99)$$

Equations 4.90, and 4.99, with parameters shown in Table 4.1 yields the full form of the modified WLF equation that includes temperature and pressure effects for polyurea at reference temperature (274 K) and pressure (0.1 MPa).

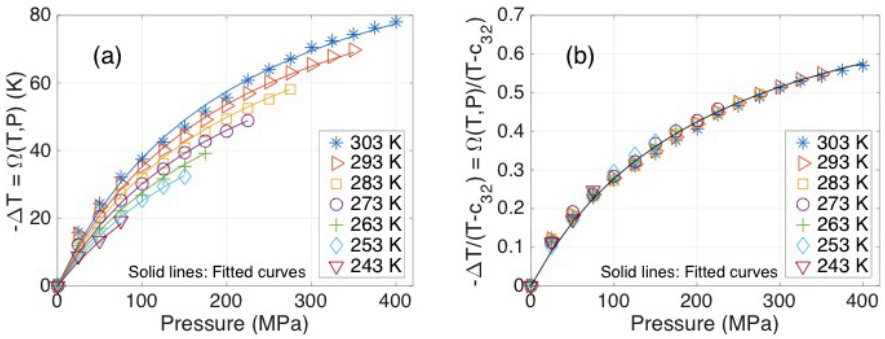

Figure 4.16: (a) Comparison between experimental data and the full model (equation 42) with parameters in Table 1. (b) Comparison between normalized experimental data and the normalized simplified model (equation 45) with parameters in Table 2.

With $\alpha_f(P_o)$, c_1, and c_2, the constants B, and $f(T_o, P_o)$ in the original WLF equation can be calculated, using equations 4.92 and 4.93. These parameters are shown in Table 4.1. It is interesting to note that the constant B is not equal to 1 as commonly assumed. Clearly the ratio of $\frac{B}{f(T_o,P_o)}$ is the physically important

Table 4.1: Parameters in full form modified WLF equation for polyurea

Polyurea			
B	0.839	c_1	25.25
$f\,(T_o, P_o)$	0.0144	c_2 (K)	208.9
$\alpha_f\,(P_o)$ (K^{-1})	6.91E-05	c_{31}	18.45
T_o (K)	274	c_4 (MPa^{-1})	0.00475
P_o (MPa)	0.1013	c_{51}	18.65
I_1 (K^{-1})	5.53E-04	c_{52} (K)	166.96
$I_2 = c_{32}$ (K)	165.94	c_6 (MPa^{-1})	0.00423

quantity related directly to the horizontal shift function. At this point, we have all the required parameters for the modified WLF equation. Effect of pressure is added as an additional variable into the original WLF equation. The original WLF line in temperature plane now becomes a surface in temperature and pressure space. Figure 4.17a shows the three-dimensional plot of the shift factor of polyurea. The glass transition temperature of polyurea is around 223 K at ambient pressure. For other conditions, we assume that the value of shift factor is constant at glass transition state and calculate glass transition temperatures at elevated pressures, in agreement with Fillers and Tschoegl. Their experimental results showed that the glass transition, at which polymers in their tests becomes glassy, occurs at a constant value of $\log a_{TP}$ [102].

Note that on the isobaric graph, the shift factor of polyurea is concave upward with respect to temperature (see Figure 4.17b); while on the isothermal graph, the shift factor is concave downward with respect to pressure (see Figure 4.17c). In other words, as pressure increases, its effect on the isothermal shift factor becomes less pronounced. This observation is compatible with the fact that at very high pressures there is less free volume available for polymer chains; thus, increasing pressure further

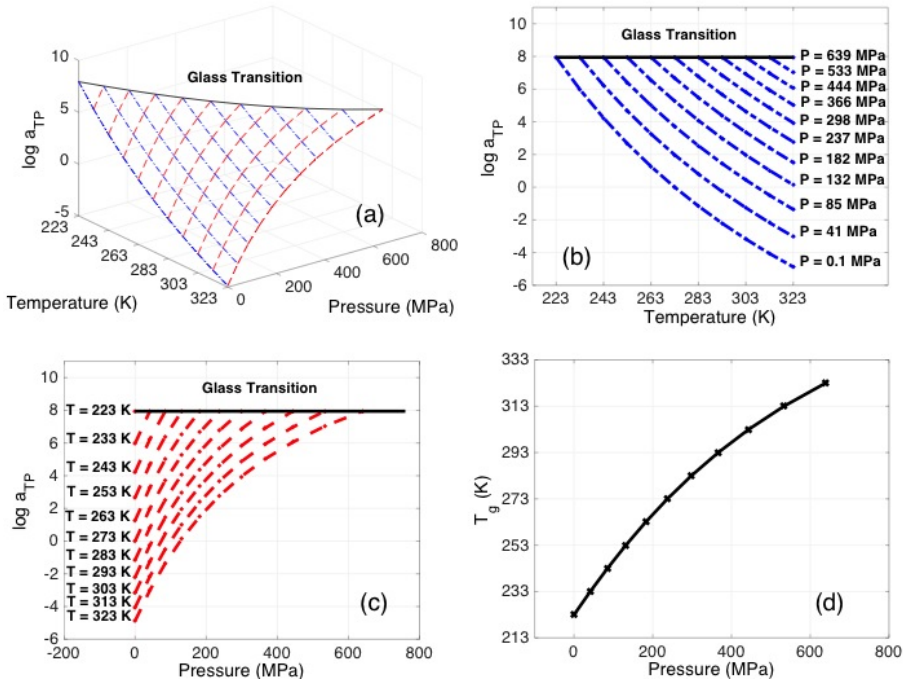

Figure 4.17: (a) Shift factor surface of polyurea (at reference temperature and pressure 273 K and 0.1 MPa respectively). (b) Isobaric shift factor versus temperature. (c) Isothermal shift factor versus pressure. (d) Glass transition temperature, T_g versus pressure.

would not have as much effect as it does at low pressures. This behavior is also found in the previous study on nonlinear viscoelastic behavior of polyurea by Chevellard et al [103]. They performed confined compression tests to extract bulk and shear moduli. Their pressure shift factor (shown as crosses in Figure 4.18) was obtained from shifting isobaric bulk moduli at different pressures to form a bulk modulus master curve at 273 K. They fitted the pressure shift factor with a quadratic equation (shown as dash-dotted line in Figure 4.18). The present model (shown as dashed line in Figure 4.18) reproduces their experimental data quite well, even though the present parameters were calibrated using longitudinal modulus data. In other words, the more efficient and less complicated process of measuring the longitudinal wave behavior under high pressure as described here could be utilized for a very good approximation of pressure

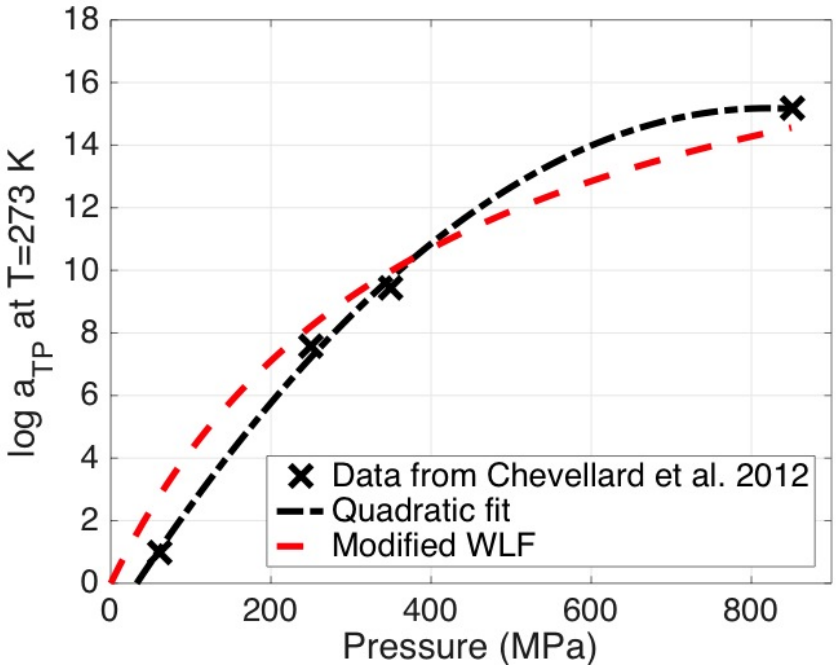

Figure 4.18: Comparison between the prediction from modified WLF model and experimental data obtained from the previous study on nonlinear viscoelastic behavior of polyurea by Chevellard et al [19] for reference temperature of 273 K and pressures at 62, 250, 370, and 850 MPa.

effect. Furthermore, the present model does not use a separable formulation for the effects of pressure and temperature, therefore preserving the coupling between the two; see equation 4.91. Finally, Figure 4.17d shows T_g as an increasing function of pressure, showing glassy response at room temperature under around 400 MPa confining pressure.

Simplification

Even though the pressure-dependent term (equation 4.99) can reflect the relation between the effects of temperature and pressure on the viscoelastic behavior of polyurea and fit excellently with the experimental data, a simpler from may be more convenient for calculation and finite element models. Thus, we have tried to

simplify equation 4.99 based on the observed trends that $c_3(T)$ and $c_5(T)$ are very close functions. The difference in the definition of these two functions, shown in equations 4.85 and 4.87, is between $l(T)$ and $l_\phi(T)$, i.e. the slopes of the longitudinal modulus of the polymer and that of the occupied volume (excluding free volume). Since the polymer chains occupy most of the space in a polymer, it is reasonable to assume that $l(T)$ and $l_\phi(T)$ are close. Note that this does not reflect the actual values of moduli, but their dependence on pressure. Thus one may enforce that $c_3(T)$ and $c_5(T)$ are identical with small potential loss of accuracy. Furthermore, since P_o, $c_4(T)$, and $c_6(T)$ all have small values, the denominators in the logarithmic terms in equation 4.99 may also be neglected with negligible effect on accuracy of the model. We can then write the simplified equation for equation 4.99 as:

$$\Omega'(T,P) = c_3'(T)\log\left(\frac{1+c_4'P}{1+c_6'P}\right), \tag{4.100}$$

where

$$c_3'(T) = c_{31}'(T - c_{32}'), \tag{4.101}$$

prime sign indicates parameters that relate to the simplified equation 4.100. $c_3'(T)$ has the same form as $c_3(T)$. We further prescribe c_{32}', c_4', and c_6' to have the same value as c_{32}, c_4, and c_6, respectively. It is noteworthy that when one normalizes the experimental data in Figure 4.14d through dividing by $(T - c_{32}')$ in equation 4.101, all curves collapse and lie on top of each other (see Figure 4.16b). Although the temperature c_{32}' is below the glass transition temperature, it represents an asymptotic state for the rubbery regimes independent of the applied pressure. It will be interesting to extend such characterization and analysis to the glassy regime to see how this behav-

ior transitions. However, is beyond the scope of the present work. Corresponding to this normalized data, equation 4.100 can be modified as:

$$\frac{\Omega'(T,P)}{T-c'_{32}} = c'_{31}\log\left(\frac{1+c'_4P}{1+c'_6P}\right). \tag{4.102}$$

Now one can perform another nonlinear regression analysis using equation 4.102 with the normalized data in Figure 4.16b to find c'_{31}. The initial guess for c'_{31} is c_{31} shown in Table 4.1. The result of this regression analysis is shown as solid line in Figure 4.16b. With c'_{31} and I_1 shown in Table 4.1, $\alpha'_f(P_o)$ can be calculated using equation 4.96 and is listed in Table 4.2. With $\alpha'_f(P_o)$, c_1, and c_2, the constants B', $f'(T_o,P_o)$ can be calculated, using equations 4.92, and 4.93. All primed parameters are shown in Table 4.2 and the rest, which are the same as unprimed parameters are shown in Table 4.1. Equations 4.90, and 4.100, with parameters c_1 and c_2 in Table 4.1 and all the primed parameters yields the simplified form of the modified WLF equation that includes temperature and pressure effects for polyurea at reference temperature (273 K) and ambient pressure.

Table 4.2: Constants for the simplified pressure-dependence formulation $\Omega'(T,P)$, equation 4.100 (The other are the same as unprimed series used in the full form equation 4.99, Table 4.1)

Polyurea			
B'	0.860	$\alpha'_f(P_o)$ (K^{-1})	7.079E-05
$f'(T_o,P_o)$	0.0148	c'_{31}	17.99

4.2.4 Conclusion

The standard WLF equation is modified to include the effect of pressure. The increase in pressure from ambient condition is related to a temperature reduction and therefore an additional pressure-dependent term is introduced into the original WLF equation. A final closed form expression is obtained based on a thermodynamics approach. This modified WLF equation was calibrated for polyurea with experimental data from ultrasonic longitudinal wave measurements under various pressures up to 900 MPa and temperatures as low as 243 K. The model can be represented by a three-dimensional shift surface in terms of temperature and pressure. The modified WLF equation results in a unique set of values for the parameters $\alpha_f(P_o)$, B, and $f(T_o, P_o)$. A simplified closed form expression for the pressure-dependent term is also presented which includes fewer fitting parameters since all the measurements at different temperatures collapsed onto a single line once divided by $(T - c'_{32})$, where c'_{32} appears as an asymptotic "freezing" temperature below T_g for the combined pressure and temperature effects on the elastomer in the rubbery regime. The full and simplified forms fit experimental data very closely. It is believed that this modified WLF equation could be used for other thermorheologically and piezorheologically simple materials under similar conditions and assumptions. Once all the necessary parameters are known, equation 4.90 can be used to predict the mechanical properties at any other pressure and temperature within the rubbery regime. The transition to glassy regime due to combination of increased pressure and decreased temperature is also derived based on the experimental results and can be described based on equation 4.90.

4.3 Numerical Model of Material Behavior for Finite Element Analysis

In this section, an experimentally-based constitutive model for polyurea, which is pressure- and temperature-dependent has been developed and improved to cover nonlinear effect of pressure on viscoelastic mechanism of polyurea. The model is improved based on the work of Amirkhizi et al. [9]. The nonlinear effect of pressure on viscoelastic modulus was obtained from the experimental result presented in the previous section. We will discuss the improvement of the constitutive model in detail and show how to implement it with finite element software. However, the improved model has not been used and validated with experimental data. The validation will be future work. This model can be used for small strain and finite strain with small rotation.

4.3.1 Background

The basic concept of linear viscoelasticity is discussed previously in Section 4.1. For small strain with the assumption of linear viscoelasticity, the stress at time t can be written in term of the history of the strain rate by:

$$\boldsymbol{\sigma}(t) = \int_{-\infty}^{t} \boldsymbol{\chi}(t - t') : \dot{\boldsymbol{\epsilon}}(t')\, dt', \tag{4.103}$$

where $\dot{\boldsymbol{\epsilon}}$ is the strain-rate tensor for small deformation, $\boldsymbol{\sigma}$ is Cauchy stress tensor, and $\boldsymbol{\chi}$ is the forth-order relaxation modulus tensor. This is similar to equation 4.33 except that $\dot{\epsilon}$ in equation 4.33 is the uniaxial strain-rate for small deformation and E

is relaxation modulus for uniaxial deformation. For finite strain and small rotation, equation 4.103 is changed to:

$$\boldsymbol{\sigma}(t) = \int_{-\infty}^{t} \boldsymbol{\chi}(t - t') : \mathbf{D}(t')\, dt', \tag{4.104}$$

where $\mathbf{D}$ is the deformation rate tensor which is the symmetric part of the velocity gradient. To be noted, $\mathbf{D}$ in this section is not the compliance defined earlier. For large rotation, the modification of equation 4.104 is required and can be found in [106,107]. For isotopic viscoelastic materials, the forth-order relaxation modulus tensor can be written as:

$$\boldsymbol{\chi}(t) = 3K(t)\,\tilde{\mathbf{E}^{\mathbf{1}}} + 2G(t)\tilde{\mathbf{E}^{\mathbf{2}}}, \tag{4.105}$$

where K and G are the bulk and shear relaxation moduli, $\tilde{\mathbf{E}^{\mathbf{1}}}$ and $\tilde{\mathbf{E}^{\mathbf{2}}}$ are the fourth-order tensors which are defined in term of components as:

$$\tilde{\mathrm{E}}^{1}_{ijkl} = \frac{\delta_{ij}\delta_{kl}}{3}, \tag{4.106}$$

$$\tilde{\mathrm{E}}^{2}_{ijkl} = 1^{(4s)}_{ijkl} - \tilde{\mathrm{E}}^{1}_{ijkl} = \left(\frac{\delta_{ik}\delta_{jl} + \delta_{il}\delta_{jk}}{2}\right) - \frac{\delta_{ij}\delta_{kl}}{3}, \tag{4.107}$$

where δ_{ij} is the Kronecker delta. These $\tilde{\mathbf{E}^{\mathbf{1}}}$ and $\tilde{\mathbf{E}^{\mathbf{2}}}$ are used to separate the deviatoric and the volumetric components of the deformation. Substitute equation 4.105 into euqation 4.104, the stress can be divided into two components:

$$\boldsymbol{\sigma}(t) = \mathrm{vol}(\boldsymbol{\sigma}) + \mathrm{dev}(\boldsymbol{\sigma}) \tag{4.108}$$

where

$$\mathrm{vol}\left(\boldsymbol{\sigma}\right) = \int_{-\infty}^{t} 3K\left(t-t'\right) : \frac{\mathrm{D_{ii}}\left(\mathrm{t}'\right)}{3}\mathbf{1^{(2)}}dt', \tag{4.109}$$

$$\begin{aligned}\mathrm{dev}\left(\boldsymbol{\sigma}\right) &= \int_{-\infty}^{t} 2G\left(t-t'\right) : \left(\mathbf{D}\left(t'\right) - \frac{\mathrm{D_{ii}}\left(\mathrm{t}'\right)}{3}\mathbf{1^{(2)}}\right)dt' \\ &= \int_{-\infty}^{t} 2G\left(t-t'\right) : \mathbf{D}'\left(t'\right)dt', \end{aligned} \tag{4.110}$$

$\mathbf{D'}$ is the deviatoric part of $\mathbf{D}$, $\mathrm{D_{ii}}$ is trace of $\mathbf{D}$, $\mathbf{1^{(2)}}$ is second-ordered unit tensor which is defined in term of component as: $1_{ij}^{(2)} = \delta_{ij}$. In general, for small deformation, K and G can be obtained from relaxation experiments. However, based on the work of Amirkhizi et al., the $\mathrm{vol}\left(\boldsymbol{\sigma}\right)$ was modeled with the well-known Arruda-Boyce model which is better for finite deformation [108].

$$\mathrm{vol}\left(\boldsymbol{\sigma}\right) = \kappa\frac{\ln J}{J}, \tag{4.111}$$

where κ is a modified bulk modulus that depends linearly on temperature, and J is the Jacobian of the deformation tensor, given by

$$\kappa\left(T\right) = \kappa\left(T_o\right) + m\left(T - T_o\right), \tag{4.112}$$

$$J = \mathrm{det}\mathbf{F}. \tag{4.113}$$

Due to the very high bulk modulus of polyurea, shear relaxation modulus, G can be estimated using the uniaxial relaxation modulus, E that has the same form as in

equation 4.22.

$$G(t) = \frac{E(t)}{2(1+\nu_{inst})}, \tag{4.114}$$

where ν_{inst} is the instantaneous Poisson's ratio which is 0.486 [9]. For isothermal deformation, G at reference temperature T_o is given by:

$$G_{ref}(t) = \frac{\left(E_e + \sum_{i=1}^{n} E_i e^{-\frac{t}{\tau_i}}\right)}{2(1+\nu_{inst})} = G_e + \sum_{i=1}^{n} G_i e^{-\frac{t}{\tau_i}}, \tag{4.115}$$

where G_e is the shear stiffness of the single spring shown in Figure 4.19, n is the total number of discrete shear relaxation spectra. It represents shear modulus of a polymer at equilibrium when t goes to ∞, G_i is the shear modulus of the the i-th spring in the i-th Maxwell subunit, τ_i is the relaxation time of the i-th pair of spring and dashpot, defined as $\frac{\eta_i}{G_i}$. Similar to E, G can be modeled with the generalized Maxwell model. Please see Section 4.1.1 for more detail of the generalized Maxwell model.

In reality, temperature of a polymer can change during deformation, especially for very fast deformation. When temperature increases or decreases from the reference temperature T_o, the shear modulus at T_o needs to be modified in two ways. Firstly, the shear modulus of each spring and viscosity of each dashpot in the generalized Maxwell model will be proportional to the ratio of the current temperature to the reference temperature (see Figure 4.20). This modification is referred to as vertical shift since it involves translation of the isothermal curves along the modulus-axis. Secondly, change in temperature affects the molecular relaxation process as discussed in the topic of time-temperature correspondence, Section 4.1.1. The relaxation time at the current temperature is adjusted with the shift factor, a_T at current temperature, T according to equation 4.47. In other words, the viscosity of each dashpot is also

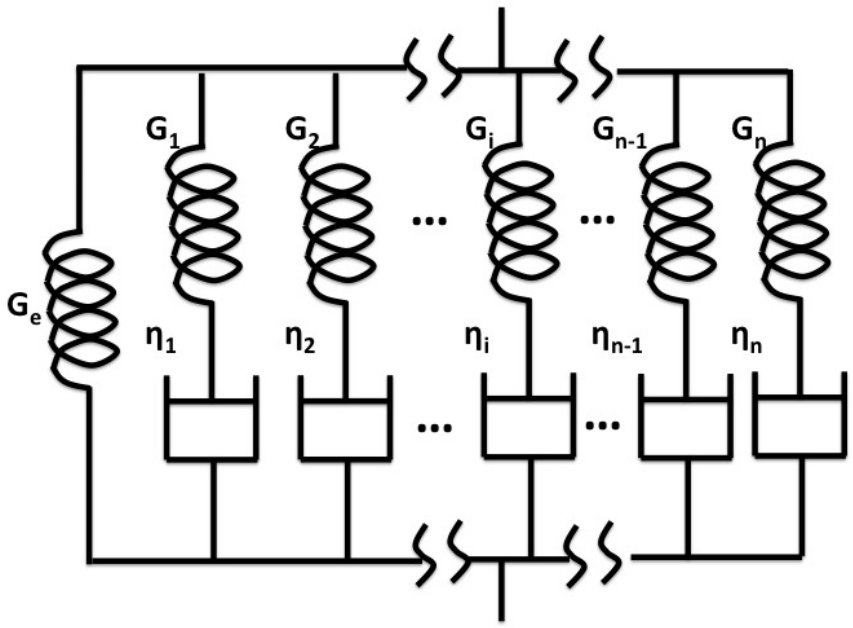

Figure 4.19: Generalized Maxwell model for shear modulus at reference temperature, T_o

multiplied with the shift factor at the current temperature (see Figure 4.20). Consider Figure 4.20, under an applied shear strain, $2\mathbf{D}'$, the shear stress can be written as:

$$\begin{aligned} \text{dev}\,(\boldsymbol{\sigma}) &= \boldsymbol{\sigma'}\,(t) \\ &= \boldsymbol{\sigma'_e}\,(t) + \sum_{i=1}^{n} \boldsymbol{\sigma_i'^{dp}}(t) \\ &= \boldsymbol{\sigma'_e}\,(t) + \sum_{i=1}^{n} \boldsymbol{\sigma_i'^{sp}}(t), \end{aligned} \tag{4.116}$$

where $\boldsymbol{\sigma'_e}$ is the shear stress in the single spring with shear modulus G_e, and it is defined as:

$$\boldsymbol{\sigma'_e}\,(t) = \frac{T(t)}{T_o} G_e\,(2\mathbf{D}'\,(t))\,, \tag{4.117}$$

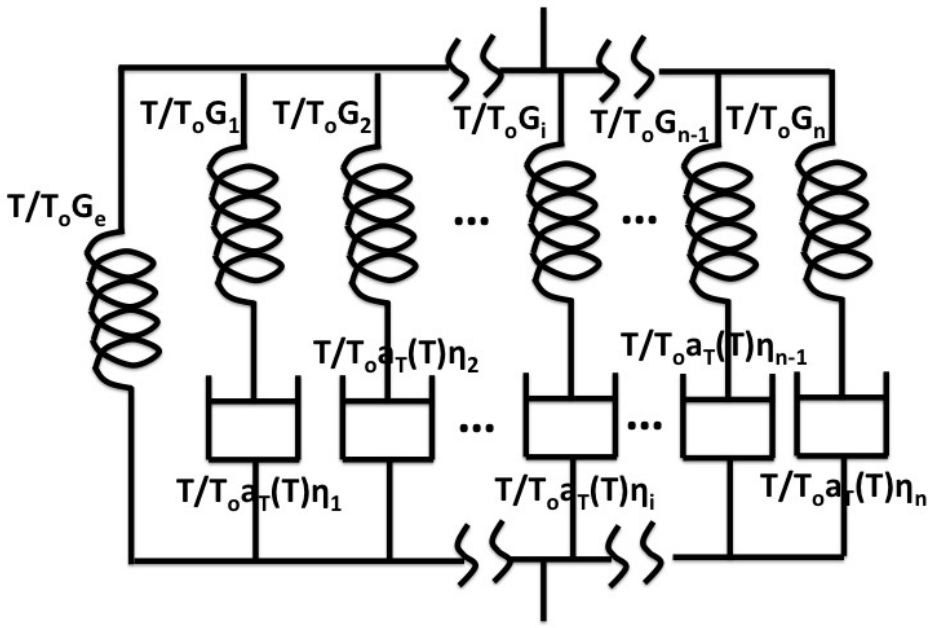

Figure 4.20: Generalized Maxwell model for shear modulus at temperature, T

$\boldsymbol{\sigma}_{\boldsymbol{i}}^{'\boldsymbol{dp}}$ is the shear stress in the i-th dashpot which is:

$$\boldsymbol{\sigma}_{\boldsymbol{i}}^{'\boldsymbol{dp}}(t) = a_T(T(t))\frac{T(t)}{T_o}\eta_i\left(2\dot{\mathbf{D}}_{\mathbf{i}}^{'\mathbf{dp}}(t)\right), \tag{4.118}$$

$\mathbf{D}_{\mathbf{i}}^{'\mathbf{dp}}$ is the time-dependent shear strain in the i-th dashpot, $\dot{\mathbf{D}}_{\mathbf{i}}^{'\mathbf{dp}}$ is the shear strain rate, $\boldsymbol{\sigma}_{\boldsymbol{i}}^{'\boldsymbol{sp}}$ is the shear stress in the i-th spring which is:

$$\begin{aligned}\boldsymbol{\sigma}_{\boldsymbol{i}}^{'\boldsymbol{sp}}(t) &= \frac{T(t)}{T_o}G_i\left(2\left(\mathbf{D}'(t) - \mathbf{D}_{\mathbf{i}}^{'\mathbf{dp}}(t)\right)\right) \\ &= \boldsymbol{\sigma}_{\boldsymbol{i}}^{'\boldsymbol{dp}}(t),\end{aligned} \tag{4.119}$$

$2\left(\mathbf{D}'(t) - \mathbf{D}_{\mathbf{i}}^{'\mathbf{dp}}(t)\right)$ is the time-dependent shear strain in the i-th spring. Substitute

equations 4.117 and 4.119 into equation 4.116, we obtain:

$$\mathrm{dev}\left(\boldsymbol{\sigma}\right)=\frac{T(t)}{T_o}G_e\left(2\mathbf{D}'\left(t\right)\right)+\sum_{i=1}^{n}\frac{T\left(t\right)}{T_o}G_i\left(2\left(\mathbf{D}'\left(t\right)-\mathbf{D}_{\mathbf{i}}^{'\mathbf{dp}}\left(t\right)\right)\right). \tag{4.120}$$

Since the i-th spring and the i-th dashpot are connected in series, the shear stresses in the spring and dashpot are equal. Equate equations 4.118 to 4.119, we obtain:

$$\begin{aligned} a_T(T\left(t\right))\frac{T\left(t\right)}{T_o}\eta_i\left(2\dot{\mathbf{D}}_{\mathbf{i}}^{'\mathbf{dp}}\left(t\right)\right) &= \frac{T\left(t\right)}{T_o}G_i\left(2\left(\mathbf{D}'\left(t\right)-\mathbf{D}_{\mathbf{i}}^{'\mathbf{dp}}\left(t\right)\right)\right) \\ \dot{\mathbf{D}}_{\mathbf{i}}^{'\mathbf{dp}}\left(t\right) &= \frac{\mathbf{D}'\left(t\right)-\mathbf{D}_{\mathbf{i}}^{'\mathbf{dp}}\left(t\right)}{a_T\left(T\left(t\right)\right)\tau_i}, \end{aligned} \tag{4.121}$$

where τ_i is $\frac{\eta_i}{G_i}$. From equation 4.121, it can be written as:

$$\frac{d\mathbf{D}_{\mathbf{i}}^{'\mathbf{dp}}\left(t\right)}{dt}+\frac{\mathbf{D}_{\mathbf{i}}^{'\mathbf{dp}}\left(t\right)}{a_T\left(T\left(t\right)\right)\tau_i}=\frac{\mathbf{D}'\left(t\right)}{a_T\left(T\left(t\right)\right)\tau_i}. \tag{4.122}$$

We then introduce a new time scale:

$$\xi\left(t\right)=\int_{-\infty}^{t}\frac{dt'}{a_T\left(T\left(t'\right)\right)}, \tag{4.123}$$

where ξ can be considered as the internal time scale that material feels at temperature T [109]. ξ is defined such that at $t=-\infty$, ξ is equal to 0. Its derivative with respect to the actual time scale is:

$$\frac{d\xi}{dt}=\frac{1}{a_T\left(T\left(t\right)\right)} \tag{4.124}$$

Using eqautions 4.124 and chain rule, equation 4.122 can be rewritten as,

$$\begin{aligned}
\frac{d\mathbf{D_i^{'dp}}(\xi)}{d\xi}\frac{d\xi}{dt}+\frac{\mathbf{D_i^{'dp}}(\xi)}{a_T(T(t))\tau_i} &= \frac{\mathbf{D'}(\xi)}{a_T(T(t))\tau_i} \\
\frac{d\mathbf{D_i^{'dp}}(\xi)}{d\xi}+\frac{\mathbf{D_i^{'dp}}(\xi)}{\tau_i} &= \frac{\mathbf{D'}(\xi)}{\tau_i}. \qquad (4.125)
\end{aligned}$$

Equation 4.125 is written in the ξ time scale. To solve for $\mathbf{D_i^{'dp}}$, we multiply equation 4.125 with $e^{\frac{\xi}{\tau_i}}$ and integrate from 0 to ξ.

$$\begin{aligned}
\frac{d\mathbf{D_i^{'dp}}(\xi)}{d\xi}e^{\frac{\xi}{\tau_i}}+\frac{\mathbf{D_i^{'dp}}(\xi)}{\tau_i}e^{\frac{\xi}{\tau_i}} &= \frac{\mathbf{D'}(\xi)}{\tau_i}e^{\frac{\xi}{\tau_i}} \\
\frac{d\left(\mathbf{D_i^{'dp}}(\xi)e^{\frac{\xi}{\tau_i}}\right)}{d\xi} &= \frac{\mathbf{D'}(\xi)e^{\frac{\xi}{\tau_i}}}{\tau_i} \\
\int_0^{\xi} d\left(\mathbf{D_i^{'dp}}(\xi')e^{\frac{\xi'}{\tau_i}}\right) &= \int_0^{\xi}\frac{\mathbf{D'}(\xi')e^{\frac{\xi'}{\tau_i}}}{\tau_i}d\xi' \\
\mathbf{D_i^{'dp}}(\xi) &= \int_0^{\xi}\frac{e^{\frac{-(\xi-\xi')}{\tau_i}}\mathbf{D'}(\xi')}{\tau_i}d\xi'. \qquad (4.126)
\end{aligned}$$

From equation 4.126, perform integrate by part, we obtain:

$$\mathbf{D_i^{'dp}}(\xi)=\mathbf{D'}(\xi)-\int_0^{\xi}e^{\frac{-(\xi-\xi')}{\tau_i}}\frac{d\mathbf{D'}(\xi')}{d\xi'}d\xi'. \qquad (4.127)$$

Equation 4.127 is in the ξ time scale. Convert equation 4.127 back to the actual time scale t, we get:

$$\mathbf{D_i^{'dp}}(\mathbf{t})=\mathbf{D'}(t)-\int_{-\infty}^{t}e^{\frac{-(\xi(t)-\xi(t'))}{\tau_i}}\frac{d\mathbf{D'}(t')}{dt'}dt'. \qquad (4.128)$$

Substitute equation 4.128 into equation 4.120, we obtain:

$$\begin{aligned}\operatorname{dev}(\boldsymbol{\sigma}) &= \frac{T(t)}{T_o}G_e\left(2\mathbf{D}'(\mathbf{t})\right)+\sum_{i=1}^{n}\frac{T(t)}{T_o}G_i\left(2\int_{-\infty}^{t}e^{\frac{-(\xi(t)-\xi(t'))}{\tau_i}}\frac{d\mathbf{D}'(\mathbf{t})}{dt'}dt'\right)\\ &= \int_{-\infty}^{t}2\frac{T(t)}{T_o}\left[G_e+\sum_{i=1}^{n}G_ie^{\frac{-(\xi(t)-\xi(t'))}{\tau_i}}\right]\frac{d\mathbf{D}'(\mathbf{t}')}{dt'}dt'. \qquad (4.129)\end{aligned}$$

Note that Pipkin pointed out about a ambiguity of the use of the current temperature T since there is no non-isothermal experimental evidence to suggest how T should be evaluated [109]. Another way is to allow T to change accordingly with D'. Then, $T(t)$ is replaced by $T(t')$. Equation 4.129 can be rewritten as:

$$\operatorname{dev}(\boldsymbol{\sigma})=\int_{-\infty}^{t}2\frac{T(t')}{T_o}\left[G_e+\sum_{i=1}^{n}G_ie^{\frac{-(\xi(t)-\xi(t'))}{\tau_i}}\right]\frac{d\mathbf{D}'(\mathbf{t}')}{dt'}dt'. \qquad (4.130)$$

Equation 4.130 is the form that is used in the work of Amirkhizi et al. [9]. From our preliminary investigation, it is found that the equations yields very close results if the change in temperature during deformation is small. So in this work, we will use equation 4.129 since it will be easier for us to estimate the change in temperature during deformation. Substitute equation 4.128 into equation 4.119, we obtain the stress in the i-th dashpot which is equal to the stress in the i-th spring, given by:

$$\boldsymbol{\sigma}_{\boldsymbol{i}}^{'\boldsymbol{dp}}(t)=\frac{T(t)}{T_o}2G_i\int_{-\infty}^{t}e^{\frac{-(\xi(t)-\xi(t'))}{\tau_i}}\frac{d\mathbf{D}'}{dt'}dt'. \qquad (4.131)$$

Substitute equation 4.128 into equation 4.121, we obtain the strain rate at the i-th dashpot, which is:

$$\dot{\mathbf{D}}_{\mathbf{i}}^{'\mathbf{dp}}(t)=\frac{1}{a_T(T(t))\,\tau_i}\int_{-\infty}^{t}e^{\frac{-(\xi(t)-\xi(t'))}{\tau_i}}\frac{d\mathbf{D}'}{dt'}dt'. \qquad (4.132)$$

At high strain rates, the deformation is essentially locally adiabatic. When the only available heat source is that from the dissipated mechanical energy at each dashpot and the conductive and convective heat losses are slow relative to the strain rates. The total rate of energy dissipation of all dashpots per unit volume, $\dot{W}^d(t)$ can be written as:

$$\dot{W}^d(t) = \sum_{i=1}^{n} \boldsymbol{\sigma}_{\boldsymbol{i}}^{\boldsymbol{'dp}}(t) : \dot{\mathbf{D}}_{\mathbf{i}}^{\mathbf{'dp}}(t) = \frac{T(t)}{T_o a_T(T(t))} \sum_{i=1}^{n} \frac{2G_i}{\tau_i} \mathbf{D}_{\mathbf{i}}^{\mathbf{'d}}(t) : \mathbf{D}_{\mathbf{i}}^{\mathbf{'d}}(t), \tag{4.133}$$

where

$$\mathbf{D}_{\mathbf{i}}^{\mathbf{'d}}(t) = \int_{-\infty}^{t} e^{\frac{-(\xi(t)-\xi(t'))}{\tau_i}} \frac{d\mathbf{D'}}{dt'} dt'. \tag{4.134}$$

Consider adiabatic process, the dissipated energy is absorbed and kept as heat in the system. The rate of energy dissipation is equal to the rate of heat stored in the system.

$$\dot{W}^d(t) = C_V \frac{dT(t)}{dt}. \tag{4.135}$$

where C_V is the heat capacity at constant volume (per unit original volume).Substitute equation 4.133 into equation 4.135 and solve for the incremental change of temperature, $\triangle T(t)$, we obtain:

$$\triangle T(t) = \triangle\xi \frac{T(t)}{C_V T_o} \sum_{i=1}^{n} \frac{2G_i}{\tau_i} \mathbf{D}_{\mathbf{i}}^{\mathbf{'d}}(t) : \mathbf{D}_{\mathbf{i}}^{\mathbf{'d}}(t), \tag{4.136}$$

where

$$\triangle\xi = \frac{\triangle t}{a_T(T(t))}. \tag{4.137}$$

4.3.2 Recurrence Relation for The Numerical Model

In this section, the recurrence relationship for $\mathbf{D_i'^d}(t)$ will be discussed according to the information in [9, 110]. Consider equation 4.134, $\mathbf{D_i'^d}(t_n)$ at a current numerical step n with a current time step t_n is given by:

$$\mathbf{D_i'^d}(t_n) = \int_{-\infty}^{t_n} e^{\frac{-(\xi(t_n)-\xi(t'))}{\tau_i}} \frac{d\mathbf{D}'}{dt'} dt'. \tag{4.138}$$

Similarly, consider at step $n+1$ where $t_{n+1} = t_n + \triangle t_n$, we obtain:

$$\mathbf{D_i'^d}(t_{n+1}) = \int_{-\infty}^{t_n+\triangle t_n} e^{\frac{-(\xi(t_n+\triangle t_n)-\xi(t'))}{\tau_i}} \frac{d\mathbf{D}'}{dt'} dt'. \tag{4.139}$$

Let consider the term $\xi(t_n + \triangle t_n)$. According to equation 4.123, this term can be written as:

$$\begin{aligned} \xi(t_n + \triangle t_n) &= \int_{-\infty}^{t_n+\triangle t_n} \frac{dt'}{a_T(T(t'))} \\ &= \int_{-\infty}^{t_n} \frac{dt'}{a_T(T(t'))} + \int_{t_n}^{t_n+\triangle t_n} \frac{dt'}{a_T(T(t'))} \\ &= \xi(t_n) + \triangle\xi, \end{aligned} \tag{4.140}$$

where

$$\triangle\xi = \frac{\triangle t_n}{a_T\left(T\left(\frac{t_{n+1}+t_n}{2}\right)\right)}. \tag{4.141}$$

Substitute equation 4.140 into equation 4.139, we obtain:

$$\begin{aligned}
\mathbf{D}_{\mathbf{i}}^{\prime\mathbf{d}}\left(t_{n+1}\right) &= \int_{-\infty}^{t_n+\triangle t_n} e^{\frac{-(\xi(t_n)+\triangle\xi-\xi(t'))}{\tau_i}} \frac{d\mathbf{D}'}{dt'} dt' \\
&= \int_{-\infty}^{t_n} e^{\frac{-\triangle\xi}{\tau_i}} e^{\frac{-(\xi(t_n)-\xi(t'))}{\tau_i}} \frac{d\mathbf{D}'}{dt'} dt' \\
&\quad + \int_{t_n}^{t_n+\triangle t_n} e^{\frac{-(\xi(t_n)+\triangle\xi-\xi(t'))}{\tau_i}} \frac{d\mathbf{D}'}{dt'} dt'. \qquad (4.142)
\end{aligned}$$

Consider the first term on the right hand side of equation 4.142, we have:

$$\begin{aligned}
\int_{-\infty}^{t_n} e^{\frac{-\triangle\xi}{\tau_i}} e^{\frac{-(\xi(t_n)-\xi(t'))}{\tau_i}} \frac{d\mathbf{D}'}{dt'} dt' &= e^{\frac{-\triangle\xi}{\tau_i}} \int_{-\infty}^{t_n} e^{\frac{-(\xi(t_n)-\xi(t'))}{\tau_i}} \frac{d\mathbf{D}'}{dt'} dt' \\
&= e^{\frac{-\triangle\xi}{\tau_i}} \mathbf{D}_{\mathbf{i}}^{\prime\mathbf{d}}\left(t_n\right). \qquad (4.143)
\end{aligned}$$

Consider the second term on the right hand side of equation 4.142, we have:

$$\begin{aligned}
\int_{t_n}^{t_n+\triangle t_n} e^{\frac{-(\xi(t_n)+\triangle\xi-\xi(t'))}{\tau_i}} \frac{d\mathbf{D}'}{dt'} dt' &\approx \left[e^{\frac{-(\xi(t_n)+\triangle\xi-\xi(t'))}{\tau_i}} \frac{d\mathbf{D}'\left(t'\right)}{dt'} \right]_{t'=\frac{t_{n+1}+t_n}{2}} \triangle t_n \\
&= \left[e^{\frac{-\left(\xi(t_n)+\triangle\xi-\xi\left(\frac{t_{n+1}+t_n}{2}\right)\right)}{\tau_i}} \frac{d\mathbf{D}'\left(\frac{t_{n+1}+t_n}{2}\right)}{dt'} \right] \triangle t_n \\
&= e^{\frac{-\left(\xi(t_n)+\triangle\xi-\xi\left(\frac{t_{n+1}+t_n}{2}\right)\right)}{\tau_i}} \left[\frac{d\mathbf{D}'\left(\frac{t_{n+1}+t_n}{2}\right)}{dt'} \triangle t_n \right] \\
&= e^{\frac{-\left(\xi(t_n)+\triangle\xi-\xi\left(t_n+\frac{t_{n+1}-t_n}{2}\right)\right)}{\tau_i}} \left[\mathbf{D}'\left(t_{n+1}\right)-\mathbf{D}'\left(t_n\right)\right]. \\
& \qquad (4.144)
\end{aligned}$$

Consider term $\xi\left(t_n+\frac{t_{n+1}-t_n}{2}\right)$ in equation 4.144, we have:

$$\begin{aligned}\xi\left(t_n+\frac{t_{n+1}-t_n}{2}\right) &= \int_{-\infty}^{t_n}\frac{dt'}{a_T\left(T\left(t'\right)\right)}+\int_{t_n}^{t_n+\frac{t_{n+1}-t_n}{2}}\frac{dt'}{a_T\left(T\left(t'\right)\right)}\\ &= \xi\left(t_n\right)+\frac{\frac{\triangle t_n}{2}}{a_T\left(T\left(\frac{3t_n+t_{n+1}}{4}\right)\right)}\\ &\approx \xi\left(t_n\right)+\frac{\triangle t_n}{2a_T\left(T\left(\frac{t_n+t_{n+1}}{2}\right)\right)}\\ &= \xi\left(t_n\right)+\frac{\triangle\xi}{2},\end{aligned} \tag{4.145}$$

where $\triangle\xi$ is defined in equation 4.141. Substitute equation 4.145 into equation 4.144, we obtain:

$$\begin{aligned}\int_{t_n}^{t_n+\triangle t_n} e^{\frac{-\left(\xi(t_n)+\triangle\xi-\xi(t')\right)}{\tau_i}}\frac{d\mathbf{D'}}{dt'}dt' &= e^{\frac{-\left(\xi(t_n)+\triangle\xi-\left(\xi(t_n)+\frac{\triangle\xi}{2}\right)\right)}{\tau_i}}\left[\mathbf{D'}\left(t_{n+1}\right)-\mathbf{D'}\left(t_n\right)\right]\\ &= e^{\frac{-\triangle\xi}{2\tau_i}}\left[\mathbf{D'}\left(t_{n+1}\right)-\mathbf{D'}\left(t_n\right)\right].\end{aligned} \tag{4.146}$$

Substitute equations 4.143 and 4.146 into equation 4.142, we obtain:

$$\mathbf{D_i^{'d}}\left(t_{n+1}\right)=e^{\frac{-\triangle\xi}{\tau_i}}\mathbf{D_i^{'d}}\left(t_n\right)+e^{\frac{-\triangle\xi}{2\tau_i}}\left[\mathbf{D'}\left(t_{n+1}\right)-\mathbf{D'}\left(t_n\right)\right] \tag{4.147}$$

Form equation 4.128, we can rewrite the strain in the i-th dashpot, $\mathbf{D_i^{'dp}}$ as:

$$\mathbf{D_i^{'dp}}(t_n)=\mathbf{D'}(t_n)-\mathbf{D_i^{'d}}\left(t_n\right) \tag{4.148}$$

The incremental change of the strain in the i-th dashpot from step n to $n+1$ can then be written as:

$$\triangle\mathbf{D_i^{'dp}}(t_n,t_{n+1})=\triangle\mathbf{D'}(t_n,t_{n+1})-\triangle\mathbf{D_i^{'d}}\left(t_n,t_{n+1}\right) \tag{4.149}$$

where

$$\triangle \mathbf{D}'(t_n, t_{n+1}) = \dot{\mathbf{D}}'(t) \triangle t = \mathbf{D}'(t_{n+1}) - \mathbf{D}'(t_n), \tag{4.150}$$

and from equation 4.147,

$$\begin{aligned} \triangle \mathbf{D}_{\mathbf{i}}^{'\mathbf{d}}(t_n, t_{n+1}) &= \mathbf{D}_{\mathbf{i}}^{'\mathbf{d}}(t_{n+1}) - \mathbf{D}_{\mathbf{i}}^{'\mathbf{d}}(t_n) \\ &= \left(e^{\frac{-\triangle \xi}{\tau_i}} - 1\right) \mathbf{D}_{\mathbf{i}}^{'\mathbf{d}}(t_n) + e^{\frac{-\triangle \xi}{2\tau_i}} \left[\mathbf{D}'(t_{n+1}) - \mathbf{D}'(t_n)\right]. \end{aligned} \tag{4.151}$$

Terms, $\mathbf{D}_{\mathbf{i}}^{'\mathbf{d}}(t)$ and $\triangle \mathbf{D}_{\mathbf{i}}^{'\mathbf{dp}}(t_n, t_{n+1})$ are similar to the terms, $\epsilon_d^i(t)$ and $\triangle \epsilon_c^i(t, \triangle t)$, respectively, in [9]. Now equation 4.129 can be written in numerical form as:

$$\mathrm{dev}\left(\boldsymbol{\sigma}(t_n)\right) = \frac{T(t_n)}{T_o} G_e \left(2\mathbf{D}'(t_n)\right) + \sum_{i=1}^{n} \frac{T(t_n)}{T_o} G_i \left(2\mathbf{D}_{\mathbf{i}}^{'\mathbf{d}}(t_n)\right) \tag{4.152}$$

4.3.3 Implementation of Temperature and Pressure Effect on Relaxation Mechanism

The effect of both pressure and temperature on the viscoelastic mechanism can be included into the previously discussed model by replacing the temperature-dependent shift factor $a_T(T(t))$ with the temperature-and-pressure-dependent shift factor $a_{TP}(T(t), P(t))$ that is obtain from Section 4.2, see equations 4.90 and 4.99. The rest of the model is still the same. Parameters for bulk and shear moduli for this model are shown in Table 4.3. These parameters are similar to parameters in [9]. Parameters for the temperature-and-pressure-dependent shift factor are shown in Table 4.1.

Table 4.3: Values of constitutive parameters used in this numerical model [9]

Polyurea			
T_o	273	C_V ($\mathrm{J\,mm^{-3}\,K^{-1}}$)	1.977E-03
C_{TE} ($\mathrm{K^{-1}}$)	2E-4	m ($\mathrm{GPa\,K^{-1}}$)	-0.15
n	4	$\kappa(T_o)$ (GPa)	4.948
G_e (GPa)	0.0224	G_1 (GPa)	0.01895
G_2 (GPa)	0.03777	G_3 (GPa)	0.08051
G_4 (GPa)	0.09726	τ_1 (ms)	463.4
τ_2 (ms)	0.06407	τ_3 (ms)	1.163E-4
τ_4 (ms)	7.321E-7		

Acknowledgements

In this chapter, Subchapter 4.2 has been submitted for publication of the material, as it may appear in Polymer, 2016, Nantasetphong, Wiroj; Amirkizhi, Alireza V.; Nemat-Nasser, Sia, Elsevier, 2016. The work in this chapter has been conducted at the Center of Excellence for Advanced Materials (CEAM) at the University of California, San Diego. This work has been supported through ONR grants N00014-09-1-1126 to University of California, San Diego and N00014-13-1-0392 to University of Massachusetts, Lowell. This dissertation author was the primary author of this material.

Chapter 5

Micromechanical Modeling

In this chapter, the micromechanical models are developed based on three approximations: (1) dilute random, (2) non-dilute random, and (3) non-dilute periodic distributions of inclusions. These models are used to find the overall mechanical properties of composite materials. The inputs of the models are only the mechanical properties, geometries, and volume fraction of each constituent in the modeled composite. Originally, these models were created for estimating mechanical properties of elastic composites; however Hashin showed that by replacement of the real elastic moduli by their complex counterparts (including storage and loss components), they can be directly utilized for viscoelastic composites [111]. In this work, The models are used to predict the overall quasi-static and dynamic mechanical properties of polymeric composites. For dynamic case, it is worth noting that the models yield pretty accurate results as long as the excitation wavelength of the applied load is not comparable to the dimensions of the inclusion phases in the composites. Due to a small number of the required inputs and short computational time, this mathematical model is considered as one of the most powerful tools for estimating the effective

properties of polymeric composites.

5.1 Composite with Dilute Random Distribution of Inclusions

In this section, two models, composite sphere and dilute random distribution of inclusions, will be considered. The composite sphere model will be discussed based on Hashin's original work [112] and a straightforward extension of Hashin's work by Lee and Westmann [113]. The dilute random distribution of inclusions is developed using Eshelby's equivalent inclusion method. It will be discussed based on Eshelby's original works [114, 115] and other useful references [116–118].

5.1.1 Composite Sphere Model (CS)

Consider three-phase heterogeneous material; matrix, shell, and core (see Figure 5.1). This model has the assumption that the composite model consists of infinitely extended matrix and an embedded two-phase spherical inclusion. The composite model has a representative volume V and is bounded by surface δV. The volume fraction of each phase is the same as those in the actual composite.

Overall bulk modulus of the composite

To find overall bulk modulus of the composite, we will consider two special cases of the boundary conditions, i.e., the prescribed uniform strain (linear displacement) and stress. These two special boundary conditions simplify the problem of elasticity and allows us to easily calculate the average stress and strain in the com-

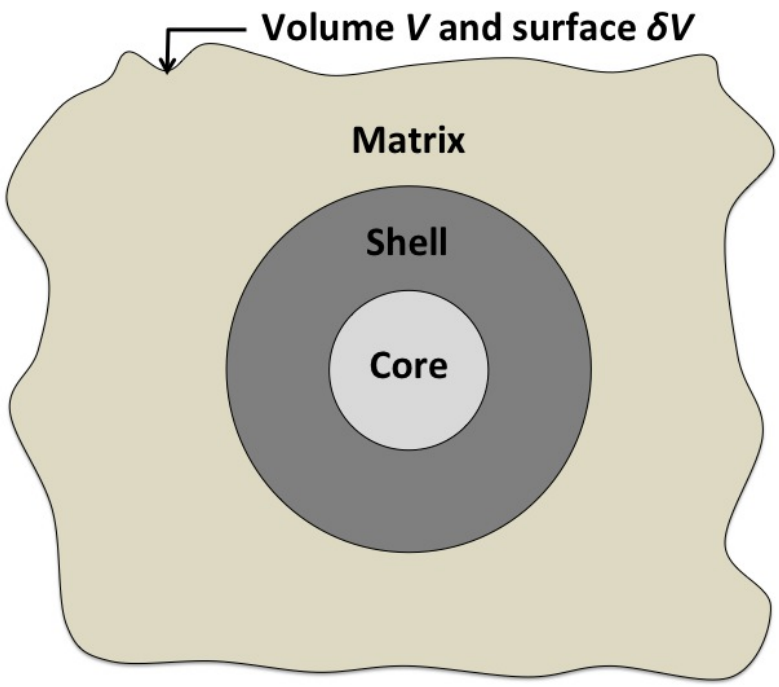

Figure 5.1: Three-phase heterogeneous material consisting of infinitely extended matrix and a two-phase spherical inclusion

posite. It is found that the average strain (stress) in the composite is equal to the applied uniform strain (stress) [116]. Since bulk modulus is related to only the change in volume of the material, it is necessary to determine only the volumetric part of the strain tensor and assume the deviatoric part to be zero. Consider the applied uniform strain, ϵ^o_{ij} as our first case, it is in the form of:

$$\epsilon^o_{ij} = \frac{1}{3}\epsilon^o \delta_{ij}, \tag{5.1}$$

where

$$\epsilon^o = \epsilon^o_{jj}, \tag{5.2}$$

δ_{ij} is the Kronecker delta. The range of the indices i and j is 1, 2, 3 and a repeated index denotes summation. The applied displacement at the surface δV of the composite

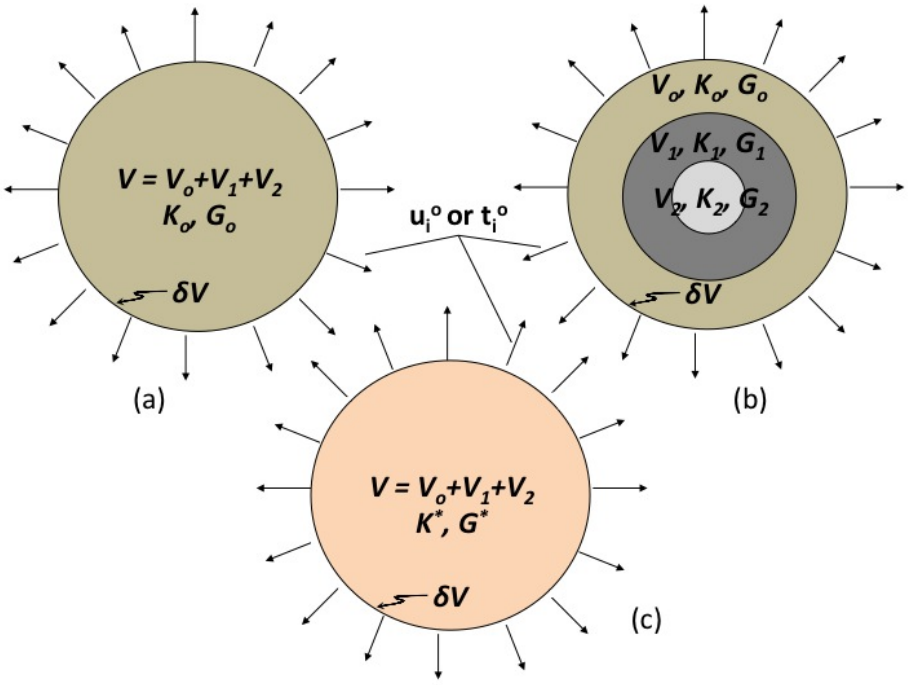

Figure 5.2: (a) Spherical homogeneous material under linear displacement or uniform traction (b) Heterogeneous material under linear displacement or uniform traction (c) Homogenized materials under linear displacement or uniform traction

is:

$$\begin{aligned} u_i^o &= \epsilon_{ij}^o x_j \\ &= \frac{1}{3}\epsilon^o \delta_{ij} x_j \\ &= \frac{1}{3}\epsilon^o x_i, \end{aligned} \tag{5.3}$$

where x_i denotes the spatial variables. To simplify our problem, the matrix of the model in Figure 5.1 is modified to be spherical (see Figure 5.2b). Subscript 0, 1, and 2 indicate matrix, shell, and core, respectively. The difference in strain energy between a loaded homogeneous solid (Figure 5.2a) and heterogeneous solid with the presence of inclusion (Figure 5.2b) is calculated. Assume the homogeneous and heterogeneous

bodies undergo the same surface displacement in equation 5.3, the total strain energy, $W^{o(\epsilon)}$ of homogeneous solid and the change in strain energy due to the existence of two-phase spherical inclusion $\delta W^{(\epsilon)}$ are expressed as [112, 113]:

$$W^{o(\epsilon)} = \frac{1}{2} K_0 \left(\epsilon^o\right)^2 V, \tag{5.4}$$

$$\delta W^{(\epsilon)} = \frac{1}{2} \int_{V_1} \left(K_1 - K_0\right) \epsilon^o \epsilon_{ii}^1 dV + \frac{1}{2} \int_{V_2} \left(K_2 - K_0\right) \epsilon^o \epsilon_{ii}^2 dV, \tag{5.5}$$

where K_0,K_1, and K_2 are bulk moduli of the matrix, shell, and core, respectively. V, V_1,and V_2 are total, shell, and core volumes, respectively. ϵ^o, ϵ_{ii}^1, and ϵ_{ii}^2 are the volumetric components of strains at surface δV, in the shell, and in the core, respectively. ϵ^o is constant while ϵ_{ii}^1 and ϵ_{ii}^2 are not constant, depending on the location in the shell and core respectively. The summation of equations 5.4 and 5.5 yield the total strain energy of the heterogeneous solid shown in Figure 5.2b.

$$\begin{aligned} W^{(\epsilon)} &= W^{o(\epsilon)} + \delta W^{(\epsilon)} \\ &= \frac{1}{2} K_0 \left(\epsilon^o\right)^2 V + \frac{1}{2} \int_{V_1} \left(K_1 - K_0\right) \epsilon^o \epsilon_{ii}^1 dV \\ &\quad + \frac{1}{2} \int_{V_2} \left(K_2 - K_0\right) \epsilon^o \epsilon_{ii}^2 dV, \end{aligned} \tag{5.6}$$

where $W^{(\epsilon)}$ is the total strain energy of the heterogeneous solid. To simplify the problem, instead of considering the heterogeneous solid, we consider the equivalent homogenized solid as shown in Figure 5.2c. We assume that the homogenized solid has the same total volume as the actual composite. Its properties are the same as the overall properties of the actual composite. The linear displacement boundary condi-

tion, equation 5.3 is also applied on the surface of the homogenized solid. Therefore, the total strain energy of the homogenized solid, $W^{(\epsilon)}$ is expressed as [112, 113]:

$$W^{(\epsilon)} = \frac{1}{2} K^* \left(\epsilon^o\right)^2 V, \tag{5.7}$$

where K^* is the bulk modulus of the homogenized solid which is the same as the overall bulk modulus of the heterogeneous solid.

If the stresses and strains in the inclusions are known, then $W^{(\epsilon)}$ can also be determined from equations 5.4-5.58. Equating then to equation 5.7, expressions for the effective bulk modulus, K^* is obtained. However, this is true for the case of very small volume fraction of inclusion because we equate the total energy of the homogenized solid to the total energy of the heterogeneous solid contains only single inclusion. Even though the volume fraction of the inclusion in the heterogeneous solid is the same as the actual composite, it does not take into account the effect of the interaction between the actual inclusions when calculating the total strain energy, equation 5.58. Thus, for finite fractional volume equating equation 5.58 to equation 5.7 clearly yield inaccurate overall bulk modulus, K^* of the actual composite. However, for finite volume fraction, an approximate upper bound on the bulk modulus can be obtained by using the variational theorems of the theory of elasticity. From the theorem of minimum potential energy, it states that when displacements are prescribed over the entire surface of an elastic body and the body forces vanish, then among the admissible displacement fields satisfying the boundary conditions, the actual displacements minimize the strain energy. Since we assume that the homogenized solid has the overall bulk modulus of the actual composite, the total strain energy of the homogenized solid calculated with its bulk modulus and the actual pre-

scribed linear displacement boundary condition (equation 5.3) would represent the total strain energy of the actual composite, therefore it is the minimum among all the total strain energies calculated with other methods, and can be showed as [112, 113]:

$$\begin{aligned} W^{(\epsilon)} &\leqslant W^{o(\epsilon)} + \delta W^{(\epsilon)} \\ \frac{1}{2}K^* \left(\epsilon^o\right)^2 V &\leqslant \frac{1}{2}K_0 \left(\epsilon^o\right)^2 V \\ &\quad + \frac{1}{2}\int_{V_1} \left(K_1 - K_0\right) \epsilon^o \epsilon^1_{ii} dV + \frac{1}{2}\int_{V_2} \left(K_2 - K_0\right) \epsilon^o \epsilon^2_{ii} dV. \end{aligned} \tag{5.8}$$

Since ϵ^o and V are arbitrary constants, divide $\frac{1}{2}\left(\epsilon^o\right)^2 V$ through equation 5.8 and obtain:

$$K^* \leqslant K_0 + \frac{1}{V}\int_{V_1} \left(K_1 - K_0\right) \frac{\epsilon^1_{ii}}{\epsilon^o} dV + \frac{1}{V}\int_{V_2} \left(K_2 - K_0\right) \frac{\epsilon^2_{ii}}{\epsilon^o} dV. \tag{5.9}$$

The two volumetric strains, ϵ^1_{ii} and ϵ^2_{ii} are not constants. ϵ^1_{ii} depends on position in the shell phase (inside V_1) while ϵ^2_{ii} depends on position in the core phase (inside V_2). Equation 5.9 can then be simplified further as:

$$K^* \leqslant K_0 + f_1 \left(K_1 - K_0\right) \frac{\bar{\epsilon}^1_{ii}}{\epsilon^o} + f_2 \left(K_2 - K_0\right) \frac{\bar{\epsilon}^2_{ii}}{\epsilon^o} = K^*_{up}, \tag{5.10}$$

where

$$f_1 = \frac{V_1}{V}, \tag{5.11}$$

$$f_2 = \frac{V_2}{V}, \tag{5.12}$$

$$\bar{\epsilon}_{ii}^{1} = \frac{1}{V_1}\int_{V_1} \epsilon_{ii}^{1} dV, \tag{5.13}$$

$$\bar{\epsilon}_{ii}^{2} = \frac{1}{V_2}\int_{V_2} \epsilon_{ii}^{2} dV, \tag{5.14}$$

f_1 and f_2 are fractional volumes of phases 1 (shell) and 2 (core), respectively, $\bar{\epsilon}_{ii}^{1}$ and $\bar{\epsilon}_{ii}^{2}$ are the volume-averaged volumetric strains in phases 1 and 2, respectively, K_{up}^{*} is the approximate upper bound of overall bulk modulus.

In a similar manner, the lower bound of the overall bulk modulus can be developed from the principle of minimum complementary energy and the applied uniform volumetric stress boundary condition.

$$\sigma_{ij}^{o} = \frac{1}{3}\sigma^{o}\delta_{ij}, \tag{5.15}$$

where

$$\sigma^{o} = \sigma_{jj}^{o}. \tag{5.16}$$

According to the applied unifrom stress, the applied uniform traction at the surface δV of the composite is:

$$t_i^o \;=\; \sigma_{ij}^{o} n_j, \tag{5.17}$$

where n_i are the components of the outward normal. Similar to the applied linear displacement case, the total strain energy of the heterogeneous solid under the applied

uniform traction is expressed as [112, 113]:

$$W^{(\sigma)} = W^{o(\sigma)} + \delta W^{(\sigma)}, \tag{5.18}$$

where

$$W^{o(\sigma)} = \frac{1}{2}\frac{(\sigma^o)^2}{9K_0}V, \tag{5.19}$$

$$\delta W^{(\sigma)} = \frac{1}{2}\int_{V_1}\frac{(K_0 - K_1)}{9K_0K_1}\sigma^o\sigma^1_{jj}dV + \frac{1}{2}\int_{V_2}\frac{(K_0 - K_2)}{9K_0K_2}\sigma^o\sigma^2_{jj}dV, \tag{5.20}$$

$W^{(\sigma)}$ and $W^{o(\sigma)}$ are the total strain energy of the heterogeneous and homogeneous solids (Figures 5.2a and 5.2b) under the applied uniform traction, $\delta W^{(\sigma)}$ is the energy difference between the two solids. Superscript (σ) refers to the applied uniform traction. The total strain energy of the homogenized solid under the applied uniform traction, $W^{(\sigma)}$ can be written as [112, 113]:

$$W^{(\sigma)} = \frac{1}{2}\frac{(\sigma^o)^2}{9K^*}V. \tag{5.21}$$

Similar to the upper bound, the lower bound of the bulk modulus can be developed from the principle of minimum complementary energy. From the theorem of minimum complementary energy, it states that when the tractions are prescribed over the entire surface of an elastic body and the body forces vanish, then among the admissible stress fields satisfying the equilibrium equations and the boundary conditions, the actual

stress minimizes the strain energy. Apply the theorem and obtain:

$$\begin{aligned} W^{(\sigma)} &\leqslant W^{o(\sigma)} + \delta W^{(\sigma)} \\ \frac{1}{2}\frac{(\sigma^o)^2}{9K^*}V &\leqslant \frac{1}{2}\frac{(\sigma^o)^2}{9K_0}V \\ &\quad + \frac{1}{2}\int_{V_1}\frac{(K_0-K_1)}{9K_0K_1}\sigma^o\sigma^1_{jj}dV + \frac{1}{2}\int_{V_2}\frac{(K_0-K_2)}{9K_0K_2}\sigma^o\sigma^2_{jj}dV. \end{aligned} \quad (5.22)$$

Since σ^o and V are arbitrary constants, divide $\frac{1}{18}(\sigma^o)^2 V$ through equation 5.22 and obtain:

$$\frac{1}{K^*} \leqslant \frac{1}{K_0} + \frac{1}{V}\int_{V_1}\frac{(K_0-K_1)}{K_0K_1}\frac{\sigma^1_{ii}}{\sigma^o}dV + \frac{1}{V}\int_{V_2}\frac{(K_0-K_2)}{K_0K_2}\frac{\sigma^2_{ii}}{\sigma^o}dV. \quad (5.23)$$

The two volumetric stress fields, σ^1_{ii} and σ^2_{ii} are not constants. σ^1_{ii} depends on position in the shell phase (inside V_1) while σ^2_{ii} depends on position in the core phase (inside V_2). Equation 5.9 can then be simplified further as:

$$K^* \geqslant K_0\left[1 + f_1\left(\frac{K_0}{K_1}-1\right)\frac{\bar{\sigma}^1_{ii}}{\sigma^o} + f_2\left(\frac{K_0}{K_2}-1\right)\frac{\bar{\sigma}^2_{ii}}{\sigma^o}\right]^{-1} = K^*_{low}, \quad (5.24)$$

where

$$\bar{\sigma}^1_{ii} = \frac{1}{V_1}\int_{V_1}\sigma^1_{ii}dV, \quad (5.25)$$

$$\bar{\sigma}^2_{ii} = \frac{1}{V_1}\int_{V_1}\sigma^2_{ii}dV, \quad (5.26)$$

$\bar{\sigma}^1_{ii}$ and $\bar{\sigma}^2_{ii}$ are the volume-averaged volumetric stresses in phases 1 and 2, respectively, K^*_{low} is the lower bound of overall bulk modulus. From equations 5.10 and 5.24, the

upper and lower bound of the overall bulk modulus of the composite are obtained:

$$K^*_{low} \leqslant K^* \leqslant K^*_{up}. \tag{5.27}$$

The formulation will be completed if one can calculate $\bar{\epsilon}^1_{ii}$, $\bar{\epsilon}^2_{ii}$, $\bar{\sigma}^1_{ii}$, and $\bar{\sigma}^2_{ii}$ in equations 5.13, 5.14, 5.25, and 5.26, respectively. Due to the facts that we have simplified and assumed that the matrix and the inclusion are perfect spherical and the deformation of the heterogeneous solid is spherically symmetric, the displacement fields, u^n_i have the following forms [112, 113]:

$$u^n_i = \left(A_n + \frac{B_n}{r^3} \right) x_i, \tag{5.28}$$

where $r = \sqrt{x_i x_i}$, $n = 0, 1, 2$ refers to matrix, shell, and core respectively, A_n and B_n are unknown constants. Since the displacement field is known and explicit, the strain and stress fields can be obtained from:

$$\epsilon^n_{ij} = \frac{1}{2} \left(\frac{\partial u^n_i}{\partial x_j} + \frac{\partial u^n_j}{\partial x_i} \right), \tag{5.29}$$

$$\sigma^n_{ij} = 3K_n \left(\frac{1}{3} \epsilon^n_{kk} \delta_{ij} \right) + 2G_n \left(\epsilon^n_{ij} - \frac{1}{3} \epsilon^n_{kk} \delta_{ij} \right). \tag{5.30}$$

Calculate $\bar{\epsilon}^1_{ii}$, $\bar{\epsilon}^2_{ii}$, $\bar{\sigma}^1_{ii}$, and $\bar{\sigma}^2_{ii}$, using equations 5.28, 5.29, and 5.30, we then obtain:

$$\bar{\epsilon}^1_{ii} = 3A_1, \tag{5.31}$$

$$\bar{\epsilon}_{ii}^{2} = 3A_2, \tag{5.32}$$

$$\bar{\sigma}_{ii}^{1} = 9K_1A_1, \tag{5.33}$$

$$\bar{\sigma}_{ii}^{2} = 9K_2A_2. \tag{5.34}$$

Substitute equations 5.31 and 5.32 into equation 5.10, the upper bound bulk modulus now is:

$$K_{up}^{*} = K_0 + f_1\left(K_1 - K_0\right)\frac{3A_1}{\epsilon^o} + f_2\left(K_2 - K_0\right)\frac{3A_2}{\epsilon^o}. \tag{5.35}$$

Substitute equations 5.33 and 5.34 into equation 5.24, the lower bound bulk modulus now is:

$$K_{low}^{*} = K_0\left[1 + f_1\left(\frac{K_0}{K_1} - 1\right)\frac{9K_1A_1}{\sigma^o} + f_2\left(\frac{K_0}{K_2} - 1\right)\frac{9K_2A_2}{\sigma^o}\right]^{-1}. \tag{5.36}$$

As we can see K_{up}^{*} and K_{low}^{*} depend on two constants A_1 and A_2 in the displacement field equation. To get for these two constants, one need to simultaneously solve for all the six unknown constants, (A_0, A_1, A_2, B_0, B_1, and B_2) in equation 5.28, using the continuity of displacement and traction at each phase boundary [112, 113]. For six unknowns, six independent equations are needed.

For the case of K_{up}^{*} the six independent equations obtained from the continuity of displacement and traction at each phase boundary are as follows:

$$\left(A_0 + \frac{B_0}{r_0^3}\right) = \frac{1}{3}\epsilon^o, \tag{5.37}$$

$$\left(A_0 + \frac{B_0}{r_1^3}\right) - \left(A_1 + \frac{B_1}{r_1^3}\right) = 0, \tag{5.38}$$

$$\left(A_1 + \frac{B_1}{r_2^3}\right) - \left(A_2 + \frac{B_2}{r_2^3}\right) = 0, \tag{5.39}$$

$$B_2 = 0, \tag{5.40}$$

$$\left(3K_0A_0 - \frac{4G_0B_0}{r_1^2}\right) - \left(3K_1A_1 - \frac{4G_1B_1}{r_1^2}\right) = 0, \tag{5.41}$$

$$\left(3K_1A_1 - \frac{4G_1B_1}{r_2^2}\right) - \left(3K_2A_2 - \frac{4G_2B_2}{r_2^2}\right) = 0, \tag{5.42}$$

where r_2 and r_1 are the inner and outer radii of the inclusion, r_0 is the radius of the composite (see Figure 5.3), G_0, G_1, and G_2 are the shear moduli of the matrix, shell, and core respectively.

For the case of K^*_{low}, the six independent equations are the same as those for K^*_{up}, except that equation 5.37 is replaced with the following equation:

$$\left(3K_0A_0 - \frac{4G_0B_0}{r_0^2}\right) = \frac{1}{3}\sigma^o. \tag{5.43}$$

After solving the boundary value problem, the six constants are obtained in term of ϵ^o and σ^o for the cases of K^*_{up} and K^*_{low} respectively. Substitute A_1 and A_2 for each case into equations 5.35 and 5.36, we obtain the the upper and lower bound bulk moduli.

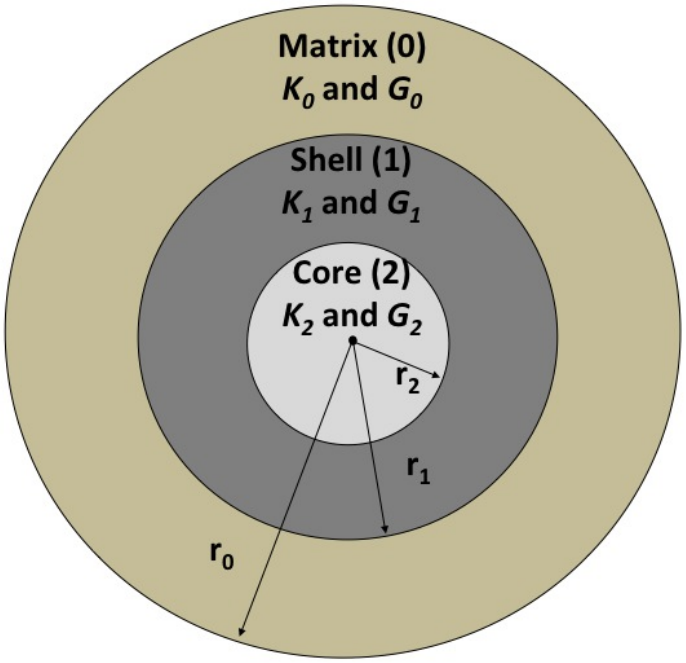

Figure 5.3: Dimension of spherical heterogeneous solid

Overall shear modulus of the composite

To find overall shear modulus of the composite, similar to the case of the overall bulk modulus we still consider the two special cases of the prescribed uniform strain (linear displacement) and stress. Since shear modulus is related to only the volume-conserving deformation of the material, it is necessary to determine only the deviatoric part of the strain tensor and assume the volumetric part to be zero. Consider the applied uniform shear strain, ϵ^o_{ij} as our first case, it is in the form of:

$$\epsilon^o_{ij} = \epsilon^{o'}_{ij} = \gamma^o \delta_{i1}\delta_{j2} + \gamma^o \delta_{i2}\delta_{j1}, \tag{5.44}$$

where

$$\gamma^o = \epsilon^o_{12} = \epsilon^o_{21} = \epsilon^{o'}_{12} = \epsilon^{o'}_{21}, \tag{5.45}$$

Prime ($'$) refers to the deviatoric part. The applied displacement at the surface δV of the composite is:

$$u_i^o = \gamma^o \delta_{i2} x_1 + \gamma^o \delta_{i1} x_2. \tag{5.46}$$

Similar to the case of the overall bulk modulus, the difference in strain energy between the loaded homogeneous solid (Figure 5.2a) and heterogeneous solid with the presence of inclusion (Figure 5.2b) is calculated. Assume the homogeneous and heterogeneous bodies undergo the same surface displacement in equation 5.46, the total strain energy, $W^{o(\epsilon)}$ of homogeneous solid and the change in strain energy due to the existence of two-phase spherical inclusion $\delta W^{(\epsilon)}$ are expressed as [112, 113]:

$$W^{o(\epsilon)} = 2G_0 \left(\gamma^o\right)^2 V, \tag{5.47}$$

$$\delta W^{(\epsilon)} = 2 \int_{V_1} \left(G_1 - G_0\right) \gamma^o \epsilon_{12}^{1'} dV + 2 \int_{V_2} \left(G_2 - G_0\right) \gamma^o \epsilon_{12}^{2'} dV, \tag{5.48}$$

where $\epsilon_{12}^{1'}$, and $\epsilon_{12}^{2'}$ are the deviatoric components of the strains in the shell, and in the core, respectively. ϵ^o is constant while ϵ_{ii}^1 and ϵ_{ii}^2 are not constant, depending on the location in the shell and core respectively. The summation of equations 5.47 and 5.48 yield the total strain energy of the heterogeneous solid shown in Figure 5.2b.

$$\begin{aligned} W^{(\epsilon)} &= W^{o(\epsilon)} + \delta W^{(\epsilon)} \\ &= 2G_0 \left(\gamma^o\right)^2 V + 2 \int_{V_1} \left(G_1 - G_0\right) \gamma^o \epsilon_{12}^{1'} dV \\ &\quad + 2 \int_{V_2} \left(G_2 - G_0\right) \gamma^o \epsilon_{12}^{2'} dV, \end{aligned} \tag{5.49}$$

where $W^{(\epsilon)}$ is the total strain energy of the heterogeneous solid. To simplify the problem, instead of considering the heterogeneous solid, we consider the equivalent homogenized solid as shown in Figure 5.2c. We assume that the homogenized solid has the same total volume as the actual composite. Its properties are the same as the overall properties of the actual composite. The linear displacement boundary condition, equation 5.46 is also applied on the surface of the homogenized solid. Therefore, the total strain energy of the homogenized solid, $W^{(\epsilon)}$ is expressed as [112, 113]:

$$W^{(\epsilon)} = 2G^* \left(\epsilon^o\right)^2 V, \tag{5.50}$$

where G^* is the shear modulus of the homogenized solid which is the same as the overall shear modulus of the heterogeneous solid.

Similar to the case of the overall bulk modulus we apply the theorem of minimum potential energy and obtain [112, 113]:

$$\begin{aligned} W^{(\epsilon)} &\leqslant W^{o(\epsilon)} + \delta W^{(\epsilon)} \\ 2G^* \left(\gamma^o\right)^2 V &\leqslant \frac{1}{2} G_0 \left(\gamma^o\right)^2 V \\ &\quad + 2\int_{V_1} \left(G_1 - G_0\right) \gamma^o \epsilon_{12}^{1'} dV + 2\int_{V_2} \left(G_2 - G_0\right) \gamma^o \epsilon_{12}^{2'} dV. \end{aligned} \tag{5.51}$$

Since γ^o and V are arbitrary constants, divide $2\left(\gamma^o\right)^2 V$ through equation 5.51 and obtain:

$$G^* \leqslant G_0 + \frac{1}{V}\int_{V_1} \left(G_1 - G_0\right) \frac{\epsilon_{12}^{1'}}{\gamma^o} dV + \frac{1}{V}\int_{V_2} \left(G_2 - G_0\right) \frac{\epsilon_{12}^{2'}}{\gamma^o} dV. \tag{5.52}$$

The two deviatoric strains, $\epsilon_{12}^{1'}$ and $\epsilon_{12}^{2'}$ are not constants. $\epsilon_{12}^{1'}$ depends on position in

the shell phase (inside V_1) while $\epsilon_{12}^{2'}$ depends on position in the core phase (inside V_2). Equation 5.52 can then be simplified further as:

$$G^* \leqslant G_0 + f_1 \left(G_1 - G_0\right) \frac{\bar{\epsilon}_{12}^{1'}}{\gamma^o} + f_2 \left(G_2 - G_0\right) \frac{\bar{\epsilon}_{12}^{2'}}{\gamma^o} = G_{up}^*, \tag{5.53}$$

where

$$\bar{\epsilon}_{12}^{1'} = \frac{1}{V_1} \int_{V_1} \epsilon_{12}^{1'} dV, \tag{5.54}$$

$$\bar{\epsilon}_{12}^{2'} = \frac{1}{V_2} \int_{V_2} \epsilon_{12}^{2'} dV, \tag{5.55}$$

$\bar{\epsilon}_{12}^{1'}$ and $\bar{\epsilon}_{12}^{2'}$ are the volume-averaged deviatoric strains in phases 1 and 2, respectively, G_{up}^* is the upper bound of overall shear modulus.

In a similar manner the lower bound of the overall shear modulus can be developed from the principle of minimum complementary energy and the applied uniform shear stress boundary condition.

$$\sigma_{ij}^o = \tau^o \delta_{i1} \delta_{j2} + \tau^o \delta_{i2} \delta_{j1}, \tag{5.56}$$

where

$$\tau^o = \sigma_{12}^o = \sigma_{21}^o = \sigma_{12}^{o'} = \sigma_{21}^{o'}. \tag{5.57}$$

Similar to the applied linear displacement case, the total strain energy of the

heterogeneous solid under the applied uniform stress is expressed as [112, 113]:

$$W^{(\sigma)} = W^{o(\sigma)} + \delta W^{(\sigma)}, \tag{5.58}$$

where

$$W^{o(\sigma)} = \frac{1}{2}\frac{(\tau^o)^2}{G_0}V, \tag{5.59}$$

$$\delta W^{(\sigma)} = \frac{1}{2}\int_{V_1}\frac{(G_0 - G_1)}{G_0 G_1}\tau^o \sigma_{12}^{1'} dV + \frac{1}{2}\int_{V_2}\frac{(G_0 - G_2)}{G_0 G_2}\tau^o \sigma_{12}^{2'} dV, \tag{5.60}$$

$W^{(\sigma)}$ and $W^{o(\sigma)}$ are the total strain energy of the heterogeneous and homogeneous solids (Figures 5.2a and 5.2b) under the applied uniform stress, $\delta W^{(\sigma)}$ is the energy difference between the two solids. The total strain energy of the homogenized solid under the applied uniform stress, $W^{(\sigma)}$ can be written as [112, 113]:

$$W^{(\sigma)} = \frac{1}{2}\frac{(\tau^o)^2}{G^*}V. \tag{5.61}$$

Similar to the upper bound, the lower bound of the shear modulus can be developed from the principle of minimum complementary energy:

$$\begin{aligned} W^{(\sigma)} &\leqslant W^{o(\sigma)} + \delta W^{(\sigma)} \\ \frac{1}{2}\frac{(\tau^o)^2}{G^*}V &\leqslant \frac{1}{2}\frac{(\tau^o)^2}{G_0}V \\ &\quad + \frac{1}{2}\int_{V_1}\frac{(G_0 - G_1)}{G_0 G_1}\tau^o \sigma_{12}^{1'} dV + \frac{1}{2}\int_{V_2}\frac{(G_0 - G_2)}{G_0 G_2}\tau^o \sigma_{12}^{2'} dV. \end{aligned} \tag{5.62}$$

Since τ^o and V are arbitrary constants, divide $\frac{1}{2}(\tau^o)^2 V$ through equation 5.62 and

obtain:

$$\frac{1}{G^*} \leqslant \frac{1}{G_0} + \frac{1}{V}\int_{V_1} \frac{(G_0 - G_1)}{G_0 G_1}\frac{\sigma_{12}^{1'}}{\tau^o}dV + \frac{1}{V}\int_{V_2} \frac{(G_0 - G_2)}{G_0 G_2}\frac{\sigma_{12}^{2}}{\tau^o}dV. \tag{5.63}$$

The two deviatoric stresses, $\sigma_{12}^{1'}$ and $\sigma_{12}^{2'}$ are not constants. $\sigma_{12}^{1'}$ depends on position in the shell phase (inside V_1) while $\sigma_{12}^{2'}$ depends on position in the core phase (inside V_2). Equation 5.63 can then be simplified further as:

$$G^* \geqslant G_0 \left[1 + f_1\left(\frac{G_0}{G_1} - 1\right)\frac{\bar{\sigma}_{12}^{1'}}{\tau^o} + f_2\left(\frac{G_0}{G_2} - 1\right)\frac{\bar{\sigma}_{12}^{2'}}{\tau^o}\right]^{-1} = G_{low}^*, \tag{5.64}$$

where

$$\bar{\sigma}_{12}^{1'} = \frac{1}{V_1}\int_{V_1} \sigma_{12}^{1'}dV, \tag{5.65}$$

$$\bar{\sigma}_{12}^{2'} = \frac{1}{V_1}\int_{V_1} \sigma_{12}^{2'}dV, \tag{5.66}$$

$\bar{\sigma}_{12}^{1'}$ and $\bar{\sigma}_{12}^{2'}$ are the volume-averaged 12 components of the deviatoric stresses in phases 1 and 2, respectively, G_{low}^* is the lower bound of overall shear modulus. From equations 5.53 and 5.64, the upper and lower bound of the overall shear modulus of the composite are obtained:

$$G_{low}^* \leqslant G^* \leqslant G_{up}^*. \tag{5.67}$$

The formulation will be completed if one can calculate $\bar{\epsilon}_{12}^{1'}$, $\bar{\epsilon}_{12}^{2'}$, $\bar{\sigma}_{12}^{1'}$, and $\bar{\sigma}_{12}^{2'}$ in equations 5.54, 5.55, 5.65, and 5.66, respectively. Due to the facts that we have simplified and assumed that the matrix and the inclusion are perfect spherical, the displacement

field, u_i^n under shear has the following forms [112, 113]:

$$u_i^n = A_n\varphi_{,i} + r_1^5 B_n\psi_{,i} + C_n\frac{1}{r_1^2}\left[r^2\varphi_{,i} + \alpha_n x_i\varphi\right] + D_n r_1^3\left[r^2\psi_{,i} + \beta_n x_i\psi\right], \tag{5.68}$$

where

$$\varphi = x_1 x_2, \tag{5.69}$$

$$\psi = \frac{x_1 x_2}{r^5}, \tag{5.70}$$

$$\alpha_n = -\frac{(12K_n + 34G_n)}{15K_n + 11G_n}, \tag{5.71}$$

$$\beta_n = \frac{(3K_n + 6G_n)}{G_n}, \tag{5.72}$$

$$r = \sqrt{x_i x_i}, \tag{5.73}$$

r_1 is the radius of the outer radius of the inclusion. subscript $, i$ refers to differentiation with respect to x_i, $n = 0, 1, 2$ refers to matrix, shell, and core respectively, A_n, B_n, C_n, and D_n are unknown constants. The strain and stress fields are shown in equations 5.29 and 5.30 respectively.

Calculate $\bar{\epsilon}_{12}^{1'}$, $\bar{\epsilon}_{12}^{2'}$, $\bar{\sigma}_{12}^{1'}$, and $\bar{\sigma}_{12}^{2'}$, using equations 5.68, 5.29, and 5.30, we then obtain:

$$\bar{\epsilon}_{12}^{1'} = A_1 + \frac{1}{5}(5 + \alpha_1) C_1 \left[\frac{1 - \left(\frac{r_2}{r_1}\right)^5}{1 - \left(\frac{r_2}{r_1}\right)^3}\right], \tag{5.74}$$

$$\bar{\epsilon}_{12}^{2'} = A_2 + \frac{1}{5}\left(5+\alpha_2\right) C_2 \left(\frac{r_2}{r_1}\right)^2, \tag{5.75}$$

$$\bar{\sigma}_{12}^{1'} = 2G_1 \left(A_1 + \frac{1}{5}\left(5+\alpha_1\right) C_1 \left[\frac{1-\left(\frac{r_2}{r_1}\right)^5}{1-\left(\frac{r_2}{r_1}\right)^3}\right]\right), \tag{5.76}$$

$$\bar{\sigma}_{12}^{2,} = 2G_2 \left(A_2 + \frac{1}{5}\left(5+\alpha_2\right) C_2 \left(\frac{r_2}{r_1}\right)^2\right). \tag{5.77}$$

Substitute equations 5.74 and 5.75 into equation 5.53, the upper bound shear modulus now is:

$$G_{up}^{*} = G_0 \left[1 + \sum_{n=1}^{2} f_n \frac{\left(G_n - G_0\right)}{G_0} \frac{\left(A_n + \frac{1}{5}\left(5+\alpha_n\right) F_n\right)}{\tau^o}\right], \tag{5.78}$$

where

$$F_1 = C_1 \left[\frac{1-(d)^5}{1-(d)^3}\right], \tag{5.79}$$

$$F_2 = C_2 \left(d\right)^2, \tag{5.80}$$

$$d = \frac{r_2}{r_1}. \tag{5.81}$$

Substitute equations 5.76 and 5.77 into equation 5.64, the lower bound shear modulus now is:

$$G_{low}^{*} = G_0 \left[1 + \sum_{n=1}^{2} f_n \left(\frac{G_0}{G_n} - 1\right) \frac{2G_n \left(A_n + \frac{1}{5}\left(5+\alpha_n\right) F_n\right)}{\tau^o}\right]^{-1}. \tag{5.82}$$

As we can see G_{up}^{*} and G_{low}^{*} depend on four constants A_1, A_2, C_1, and C_2 in

the displacement field equation 5.68. To get for these four constants, one need to simultaneously solve for all the twelve unknown constants, (A_0, A_1, A_2, B_0, B_1, B_2, C_0, C_1, C_2, D_0, D_1, and D_2) in equation 5.68, using the continuity of displacement and traction at each phase boundary [112,113]. For twelve unknowns, twelve independent equations are needed.

For the case of G^*_{up} the twelve independent equations obtained from the continuity of displacement and traction at each phase boundary are as follows:

$$\gamma^o = A_0 + \frac{C_0}{f^{\frac{2}{3}}} + fD_0 + f^{\frac{5}{3}}B_0, \tag{5.83}$$

$$0 = \alpha_0 C_0 - 5f^{\frac{5}{3}}D_0 + f^{\frac{5}{3}}\beta_0 D_0 - 5f^{\frac{7}{3}}B_0, \tag{5.84}$$

$$0 = A_0 - A_1 + C_0 - C_1 + B_0 - B_1 + D_0 - D_1, \tag{5.85}$$

$$0 = -5B_0 + 5B_1 + \alpha_0 C_0 - \alpha_1 C_1 - 5D_0 + 5D_1 + \beta_0 D_0 - \beta_1 D_1, \tag{5.86}$$

$$0 = A_1 + d^2 C_1 + \frac{D_1}{d^3} + \frac{B_1}{d^5} - A_2 - d^2 C_2 - \frac{D_2}{d^3} - \frac{B_2}{d^5}, \tag{5.87}$$

$$0 = (\alpha_1 C_1) - (\alpha_2 C_2) + \frac{5\,(B_2 - B_1)}{d^7} + \frac{(\beta_1 - 5)\,D_1}{d^5} - \frac{(\beta_2 - 5)\,D_2}{d^5}, \tag{5.88}$$

$$0 = B_2, \tag{5.89}$$

$$0 = D_2, \tag{5.90}$$

$$\begin{aligned} 0 &= 2A_0G_0 - 2A_1G_1 - 8B_0G_0 + 8B_1G_1 + 4C_0G_0 - 4C_1G_1 + \alpha_0C_0G_0 \\ &\quad -\alpha_1C_1G_1 + \beta_0D_0G_0 - \beta_1D_1G_1 - 6D_0G_0 + 6D_1G_1, \end{aligned} \tag{5.91}$$

$$\begin{aligned} 0 &= 40B_0G_0 - 40B_1G_1 + \frac{4C_0G_0}{3} - \frac{4C_1G_1}{3} + \frac{2\alpha_0C_0G_0}{3} - \frac{2\alpha_1C_1G_1}{3} \\ &\quad +28D_0G_0 - 28D_1G_1 - 6\beta_0D_0G_0 + 6\beta_1D_1G_1 + 4C_0K_0 - 4C_1K_1 \\ &\quad +5\alpha_0C_0K_0 - 5\alpha_1C_1K_1 - 6D_0K_0 + 6D_1K_1, \end{aligned} \tag{5.92}$$

$$\begin{aligned} 0 &= 2A_1G_1 - 2A_2G_2 + (4+\alpha_1)\,G_1d^2C_1 - (4+\alpha_2)\,G_2d^2C_2 \\ &\quad +\frac{(\beta_1-6)\,G_1D_1}{d^3} - \frac{(\beta_2-6)\,G_2D_2}{d^3} - \frac{8B_1G_1}{d^5} + \frac{8B_2G_2}{d^5}, \end{aligned} \tag{5.93}$$

$$\begin{aligned} 0 &= \frac{40B_1G_1}{d^5} - \frac{40B_2G_2}{d^5} + \frac{4}{3}C_1G_1d^2 - \frac{4}{3}C_2G_2d^2 \\ &\quad +\frac{2}{3}\alpha_1C_1G_1d^2 - \frac{2}{3}\alpha_2C_2G_2d^2 + \frac{28D_1G_1}{d^3} - \frac{28D_2G_2}{d^3} - \frac{6\beta_1D_1G_1}{d^3} \\ &\quad +\frac{6\beta_2D_2G_2}{d^3} + 4C_1K_1d^2 - 4C_2K_2d^2 + 5\alpha_1C_1K_1d^2 - 5\alpha_2C_2K_2d^2 \\ &\quad -\frac{6D_1K_1}{d^3} + \frac{6D_2K_2}{d^3}, \end{aligned} \tag{5.94}$$

where f is the volume fraction of the inclusion ($f = f_1 + f_2$).

For the case of G^*_{low}, the twelve independent equations are the same as those for G^*_{up}, except that equations 5.83 and 5.84 are replaced with the following equatios:

$$\tau^o = 2A_0G_0 - 8B_0G_0f^{\frac{5}{3}} + \frac{4C_0G_0}{f^{\frac{2}{3}}} + \frac{\alpha_0G_0C_0}{f^{\frac{2}{3}}} - 6fD_0G_0 + \beta_0fD_0G_0, \tag{5.95}$$

$$\begin{aligned} 0 &= 40B_0G_0f^{\frac{5}{3}} + \frac{4C_0G_0}{3f^{\frac{2}{3}}} + \frac{2\alpha_0G_0C_0}{3f^{\frac{2}{3}}} + 28fD_0G_0 - 6\beta_0fD_0G_0 \\ &\quad + \frac{4C_0K_0}{f^{\frac{2}{3}}} + \frac{5\alpha_0C_0K_0}{f^{\frac{2}{3}}} - 6fD_0K_0. \end{aligned} \tag{5.96}$$

After solving the boundary value problem, the twelve constants are obtained in term of γ^o and τ^o for the cases of G^*_{up} and G^*_{low} respectively. Substitute A_1, A_2, C_1, and C_2 for each case into equations 5.78 and 5.82, we obtain the the upper and lower bound shear moduli.

CS Model VS Experiment

CS model is used to predict complex longitudinal and shear moduli of phenolic microballoon filled polyurea (PUPMB) composites. There are three PUPMB composites with different volume fraction of the microballoon, 0.1, 0.2, and 0.4. Pristine polyurea samples were also created for comparison. The experimental data were obtained from ultrasonic longitudinal and shear measurements at 1 MHz, 20 °C, and ambient pressure. The longitudinal storage and loss moduli were calculated from the measured longitudinal wave speed and attenuation in the materials, while The shear storage and loss moduli were calculated from the measured shear wave speed and attenuation. The experiment detail and procedure can be found in Section 3.3.

With regard to computation, the inputs for CS model are the two complex moduli of each phase, inner and outer radii of the microballoon, and volume fraction. Table 5.1 shows longitudinal storage and loss moduli, L' and L'', and shear storage

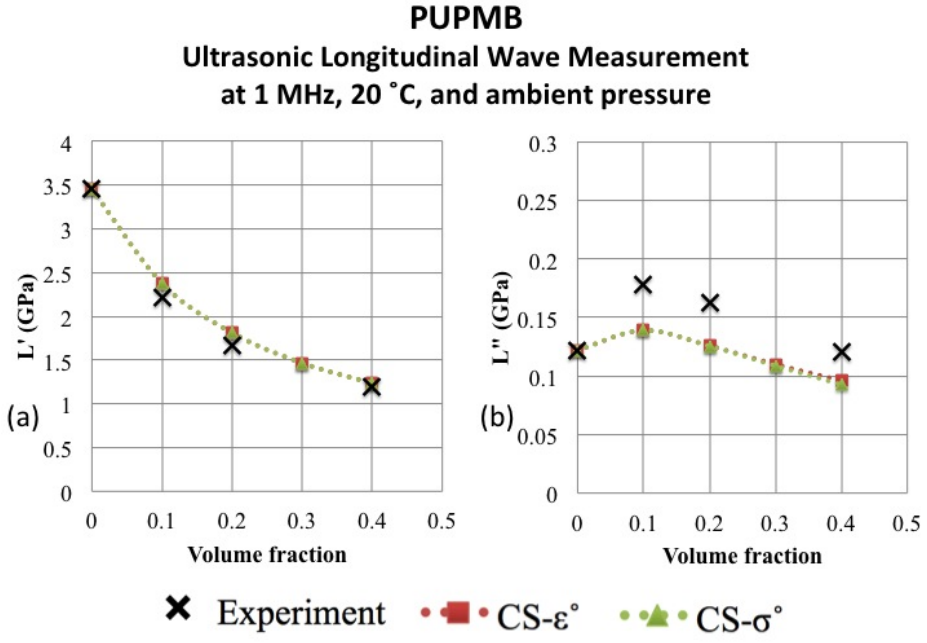

Figure 5.4: CS-model: (a) Storage longitudinal modulus, L' of PUPMB versus volume fraction (b) Loss longitudinal modulus, L'' of PUPMB versus volume fraction

and loss moduli, G' and G'' of all phases in PUPMB composite. The matrix is polyurea. For microballoom, the shell is phenolic while the core is void. Since we want to predict the mechanical properties of PUPMB composites at 1 MHz, 20 °C, and ambient pressure, the input properties need to be from the same testing condition. For the polyurea matrix phase, the properties were measured in-house with the same measurement and condition as in PUPMB. While, the properties of the shell phase (phenolic) were obtained elsewhere from Hartmann's work [119]. It is worth noting that Hartmann conducted the longitudinal and shear ultrasonic wave measurements at 1.8 MHz which is higher than our experiments. Since there is no other data for phenolic at 1 MHz, the data at 1.8 MHz were used in our calculation. The properties of core phase (void) are zero. Table 5.2 shows the geometries and apparent density

of the microballoon. The inner and outer radii were the average number that was obtained in-house from the observation of 237 microballoon under microscope. The size distribution is shown in Figure 3.12. With properties in Tables 5.1 and 5.2, the calculations were done for PUPMB with 0.1, 0.2, 0.3, and 0.4 volume fraction of the microballoon. To be noted, density is not an input for our models.

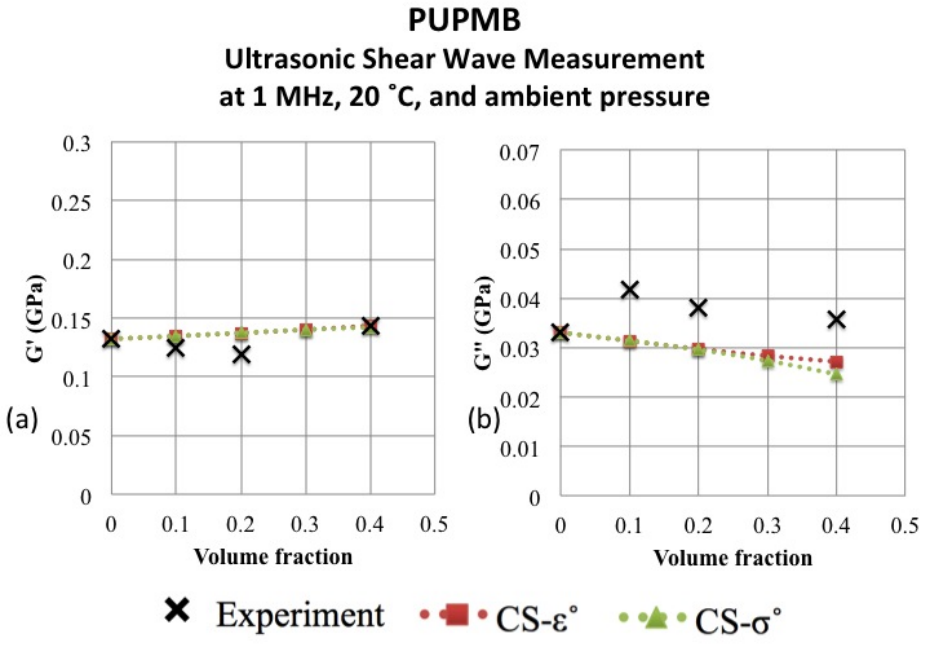

Figure 5.5: CS-model: (a) Storage shear modulus, G' of PUPMB versus volume fraction (b) Loss shear modulus, G'' of PUPMB versus volume fraction

Figure 5.4a shows L' of PUPMB as a function of volume fraction. The experimental result are compared with the calculation results from the CS models with uniform strain ϵ^o and uniform stress σ^o assumption. As we can see L' decrease nonlinearly with volume fraction of the microballoon. The rate of the decrease is faster at low volume fraction. The CS-ϵ^o and CS-σ^o are on top of each other. The computation results agree excellently with the experimental result. Figure 5.4b shows L'' of

PUPMB as a function of volume fraction. Apparently, L'' behaves differently from L'. L'' increases as volume fraction changes from 0 to 0.1. Above 0.1 volume fraction, L'' decrease with increasing volume fraction. The computation results from CS-ϵ^o and CS-σ^o are very close and can predict the trend of L''. However, CS-ϵ^o and CS-σ^o are around 20% lower than the experiment. This can be expected since we do not have accurate input properties for phenolic. We do not know whether our phenolic is the same as that in Harmann's work. Different type or stoichiometric ratio of reactants in phenolic could yield the different of mechanical properties of the resulting phenolic polymer. Moreover, Harmann did the test at the frequency slightly higher than our frequency. It is worth noting that the longitudinal wave speed in phenolic is not sensitive to degree of crosslinking and fabrication condition but attenuation is. Due to the fact that L' depends mainly on longitudinal wave speed and L'' depends mostly on attenuation, we tend to believe that L' of the phenolic that we obtained from Harmann's work would be more comparable to our phenolic microballoon than L''. This might be the reason that the our prediction of L' is a lot better than the prediction of L''.

Table 5.1: Properties of each phase in PUPMB for micromechanical modeling

	Polyurea (Matrix)	Phenolics (Shell)	Void (Core)
L' (GPa)	3.4625	9.8601	0
L'' (GPa)	0.1223	0.2338	0
G' (GPa)	0.1320	2.1268	0
G'' (GPa)	0.0331	0.1087	0
ρ ($\mathrm{g\,cm^{-3}}$)	1.1	1.223	0

Figure 5.5a shows G' of PUPMB as a function of volume fraction. As we can see from experiment, G' is quite flat over the range of 0-0.4 volume fraction of the

Table 5.2: Average dimensions and density of phenolic microballoon for micromechanical modeling

Phenolic Microballoon	
Inner Radius (µm)	17.25
Outer Radius (µm)	18.5
Apparent Density ($\mathrm{g\,cm^{-3}}$)	0.231

microballoon. CS-ϵ^o and CS-σ^o for G' are very close similar to the case of L'. The computation results agree excellently with the experimental result. Figure 5.5b shows G'' of PUPMB as a function of volume fraction. According to the experimental result, G'' behaves similar to L'', except that the trend is not as obvious as L''. G'' increases as volume fraction changes from 0 to 0.1, and then above 0.1 G'' gradually decrease with increasing volume fraction. The computation result from CS-ϵ^o is slightly higher than that from CS-σ^o at high volume fraction. CS-ϵ^o and CS-σ^o predict that the G'' should gradually decrease with increasing volume fraction of the microballoon. They underestimate the experimental result by around 25%. Similar to the case of longitudinal modulus, we estimate G' accurately and significantly underestimate G''. The reason is similar to what we discussed previously for the case of L' and L''.

5.1.2 Dilute Random Distributions of Inclusion Model (DD)

In this section, the micromechanical models for estimating the overall mechanical properties of composite with short fibers or spherical inclusions are discussed. The models are based on dilute randomly distributed inclusions method. A general idea is that a two-phase composite material can be divided by proportion of its constituents as matrix (having more volume) and filler (having less volume). The total volume of the composite V is the summation between the volume occupied by the filler (fiber)

V_Ω and the volume occupied by the matrix V_m. The volume fractions of the fiber, f_Ω, and matrix, f_m, are defined as:

$$f_\Omega = \frac{V_\Omega}{V}, \tag{5.97}$$

$$f_m = \frac{V_m}{V}. \tag{5.98}$$

The summation between f_Ω and f_m is unity. Consider a composite located with respect to x_1, x_2,and x_3 rectangular coordinates. $\boldsymbol{x}$ is the position vector. The inclusion and the matrix have constant elasticity tensors $\boldsymbol{C^\Omega}$ and $\boldsymbol{C^m}$ (or constant compliance tensors $\boldsymbol{D^\Omega}$ and $\boldsymbol{D^m}$), respectively. $\boldsymbol{C^\Omega}$ and $\boldsymbol{D^\Omega}$, and $\boldsymbol{C^m}$ and $\boldsymbol{D^m}$ are inverses of each other. When the composite material is under applied load, the strain field $\boldsymbol{\epsilon}(\boldsymbol{x})$ and stress field $\boldsymbol{\sigma}(\boldsymbol{x})$ inside the composite will be non-uniform on the microscale and can be written as:

$$\boldsymbol{\epsilon}(\boldsymbol{x}) = \begin{cases} \boldsymbol{\epsilon^\Omega}(\boldsymbol{x}) &= \boldsymbol{D^\Omega} : \boldsymbol{\sigma^\Omega}(\boldsymbol{x}) \quad \text{in inclusion} \\ \boldsymbol{\epsilon^m}(\boldsymbol{x}) &= \boldsymbol{D^m} : \boldsymbol{\sigma^m}(\boldsymbol{x}) \quad \text{in matrix,} \end{cases} \tag{5.99}$$

$$\boldsymbol{\sigma}(\boldsymbol{x}) = \begin{cases} \boldsymbol{\sigma^\Omega}(\boldsymbol{x}) &= \boldsymbol{C^\Omega} : \boldsymbol{\epsilon^\Omega}(\boldsymbol{x}) \quad \text{in inclusion} \\ \boldsymbol{\sigma^m}(\boldsymbol{x}) &= \boldsymbol{C^m} : \boldsymbol{\epsilon^m}(\boldsymbol{x}) \quad \text{in matrix,} \end{cases} \tag{5.100}$$

where $\boldsymbol{\epsilon^\Omega}(\boldsymbol{x})$ and $\boldsymbol{\epsilon^m}(\boldsymbol{x})$ are strain fields in the inclusion and the matrix, $\boldsymbol{\sigma^\Omega}(\boldsymbol{x})$ and $\boldsymbol{\sigma^m}(\boldsymbol{x})$ are stress fields in the inclusion and the matrix. The solution of these non-uniform fields is a formidable problem. However, many useful results can be obtained in terms of the average stress and strain [116, 120]. The volume-averaged stress $\bar{\boldsymbol{\sigma}}$ is defined as the average of the point-wise stress $\boldsymbol{\sigma}(\boldsymbol{x})$ over the volume V

and can be written as:

$$\bar{\boldsymbol{\sigma}} = f_\Omega \bar{\boldsymbol{\sigma}}^{\boldsymbol{\Omega}} + f_m \bar{\boldsymbol{\sigma}}^{\boldsymbol{m}} = f_\Omega \bar{\boldsymbol{\sigma}}^{\boldsymbol{\Omega}} + (1 - f_\Omega)\, \bar{\boldsymbol{\sigma}}^{\boldsymbol{m}}, \tag{5.101}$$

where $\bar{\boldsymbol{\sigma}}^{\boldsymbol{\Omega}}$ and $\bar{\boldsymbol{\sigma}}^{\boldsymbol{m}}$ are the average stresses over inclusion and matrix volumes, respectively. The average strains for the total volume $\bar{\boldsymbol{\epsilon}}$, inclusion $\bar{\boldsymbol{\epsilon}}^{\boldsymbol{\Omega}}$, and matrix $\bar{\boldsymbol{\epsilon}}^{\boldsymbol{m}}$ are defined similarly.

$$\bar{\boldsymbol{\epsilon}} = f_\Omega \bar{\boldsymbol{\epsilon}}^{\boldsymbol{\Omega}} + f_m \bar{\boldsymbol{\epsilon}}^{\boldsymbol{m}} = f_\Omega \bar{\boldsymbol{\epsilon}}^{\boldsymbol{\Omega}} + (1 - f_\Omega)\, \bar{\boldsymbol{\epsilon}}^{\boldsymbol{m}}. \tag{5.102}$$

From equations 5.99-5.102, one can write constitutive equations for the composite as:

$$\bar{\boldsymbol{\sigma}} = \bar{\boldsymbol{C}} : \bar{\boldsymbol{\epsilon}} = f_\Omega \boldsymbol{C}^{\boldsymbol{\Omega}} : \bar{\boldsymbol{\epsilon}}^{\boldsymbol{\Omega}} + f_m \boldsymbol{C}^{\boldsymbol{m}} : \bar{\boldsymbol{\epsilon}}^{\boldsymbol{m}}, \tag{5.103}$$

where $\bar{\boldsymbol{C}}$ is the unknown overall elasticity tensor of the composite. Similarly, the constitutive equations in term of compliance tensors can be defined as:

$$\bar{\boldsymbol{\epsilon}} = \bar{\boldsymbol{D}} : \bar{\boldsymbol{\sigma}} = f_\Omega \boldsymbol{D}^{\boldsymbol{\Omega}} : \bar{\boldsymbol{\sigma}}^{\boldsymbol{\Omega}} + f_m \boldsymbol{D}^{\boldsymbol{m}} : \bar{\boldsymbol{\sigma}}^{\boldsymbol{m}}, \tag{5.104}$$

where $\bar{\boldsymbol{D}}$ is the unknown overall compliance tensor of the composite. To be noted, equations 5.103 and 5.104 can also be proved through the integral of the strain energy over total volume of the composite V [112, 116, 120]. Consider applied uniform strain $\boldsymbol{\epsilon}^{\boldsymbol{o}}$ (linear displacement) and applied uniform stress $\boldsymbol{\sigma}^{\boldsymbol{o}}$ boundary conditions. The average strain and stress over total volume of a composite that is subjected to these

two special boundary conditions can be showed as [116, 120]:

$$\bar{\boldsymbol{\epsilon}} = \boldsymbol{\epsilon}^{\boldsymbol{o}}, \tag{5.105}$$

$$\bar{\boldsymbol{\sigma}} = \boldsymbol{\sigma}^{\boldsymbol{o}}. \tag{5.106}$$

Using equations 5.101-5.106, the constitutive equations reduce to:

$$\bar{\boldsymbol{C}} : \boldsymbol{\epsilon}^{\boldsymbol{o}} = \boldsymbol{C}^{\boldsymbol{m}} : \boldsymbol{\epsilon}^{\boldsymbol{o}} + f_{\Omega} \left(\boldsymbol{C}^{\boldsymbol{\Omega}} - \boldsymbol{C}^{\boldsymbol{m}} \right) : \bar{\boldsymbol{\epsilon}}^{\boldsymbol{\Omega}}, \tag{5.107}$$

$$\bar{\boldsymbol{D}} : \boldsymbol{\sigma}^{\boldsymbol{o}} = \boldsymbol{D}^{\boldsymbol{m}} : \boldsymbol{\sigma}^{\boldsymbol{o}} + f_{\Omega} \left(\boldsymbol{D}^{\boldsymbol{\Omega}} - \boldsymbol{D}^{\boldsymbol{m}} \right) : \bar{\boldsymbol{\sigma}}^{\boldsymbol{\Omega}}. \tag{5.108}$$

$\boldsymbol{\epsilon}^{\boldsymbol{o}}$ and $\boldsymbol{\sigma}^{\boldsymbol{o}}$ are arbitrary constants. If the relation between $\bar{\boldsymbol{\epsilon}}^{\boldsymbol{\Omega}}$ (or $\bar{\boldsymbol{\sigma}}^{\boldsymbol{\Omega}}$) and $\boldsymbol{\epsilon}^{\boldsymbol{o}}$ (or $\boldsymbol{\sigma}^{\boldsymbol{o}}$) is known, one could solve for $\bar{\boldsymbol{C}}$ (or $\bar{\boldsymbol{D}}$). This idea was first introduced by Hill through the introduction of strain- and stress-concentration tensors [120].

$$\bar{\boldsymbol{\epsilon}}^{\boldsymbol{\Omega}} = \boldsymbol{P}^{\boldsymbol{\Omega}} : \boldsymbol{\epsilon}^{\boldsymbol{o}}, \tag{5.109}$$

$$\bar{\boldsymbol{\sigma}}^{\boldsymbol{\Omega}} = \boldsymbol{Q}^{\boldsymbol{\Omega}} : \boldsymbol{\sigma}^{\boldsymbol{o}}, \tag{5.110}$$

where $\boldsymbol{P}^{\boldsymbol{\Omega}}$ and $\boldsymbol{Q}^{\boldsymbol{\Omega}}$ are the strain- and stress-concentration tensors, respectively. Substitute equations 5.109 and 5.110 into equations 5.107 and 5.108, $\bar{\boldsymbol{C}}$ and $\bar{\boldsymbol{D}}$ are in the following forms:

$$\bar{\boldsymbol{C}} = \boldsymbol{C}^{\boldsymbol{m}} + f_{\Omega} \left(\boldsymbol{C}^{\boldsymbol{\Omega}} - \boldsymbol{C}^{\boldsymbol{m}} \right) : \boldsymbol{P}^{\boldsymbol{\Omega}}, \tag{5.111}$$

$$\bar{\boldsymbol{D}} = \boldsymbol{D}^m + f_\Omega \left(\boldsymbol{D}^\Omega - \boldsymbol{D}^m \right) : \boldsymbol{Q}^\Omega. \tag{5.112}$$

At this point on, we will discuss about the two methods to find the tensors $\boldsymbol{P}^\Omega$ and $\boldsymbol{Q}^\Omega$. For DD model, $\boldsymbol{P}^\Omega$ and $\boldsymbol{Q}^\Omega$ can be found, using the Eshelby's equivalent inclusion theory [114–116, 118]. Eshelby solved an elasticity problem of a system consisting of an ellipsoidal particle in an infinite matrix and obtained a formulation for elastic stress field in and around the ellipsoidal particle. By changing the geometry parameters in the ellipsoid particle, one can use Eshelby's result to model the stress and strain fields around various types of inclusions, for example, sphere, prolate ellipsoid which can represent short fiber, and etc.

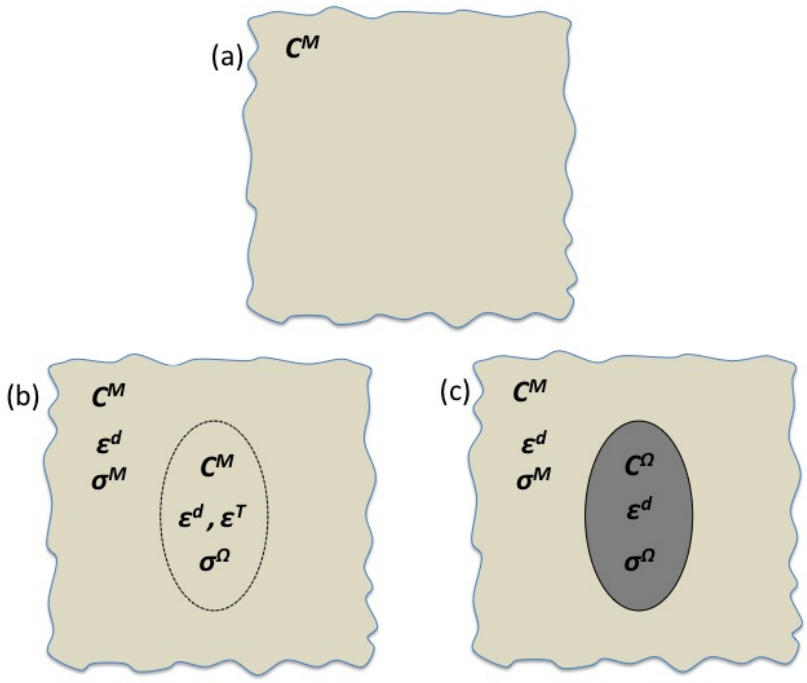

Figure 5.6: (a) A solid at stress-free state (b) An ellipsoidal region in the solid undergoes a transformation strain $\boldsymbol{\epsilon}^{\boldsymbol{T}}$ (c) A heterogenous solid without the transformation strain but has the same stress, $\boldsymbol{\sigma}^\Omega$ in the ellipsoidal region

Consider an infinite solid body with stiffness $\boldsymbol{C^m}$ that is initially at its stress-free stage (see Figure 5.6a). Suppose that an ellipsoidal region in the solid undergoes some type of transformation such that, if it were a separate body, it would acquire a uniform strain $\boldsymbol{\epsilon^T}$ with no surface traction or stress. $\boldsymbol{\epsilon^T}$ is called the transformation strain, or the eigenstrain. In fact the region is bonded to the matrix, so when the transformation occurs the whole body develops some disturdation strain $\tilde{\boldsymbol{\epsilon}}^{\boldsymbol{d}}$ relative to its shape before the transformation (see Figure 5.6b). Eshelby proved that within this ellipsoidal region the strain $\tilde{\boldsymbol{\epsilon}}^{\boldsymbol{d}}$ is uniform. It is related to $\boldsymbol{\epsilon^T}$ by [114, 116–118]:

$$\tilde{\boldsymbol{\epsilon}}^{\boldsymbol{d}} = \boldsymbol{S^{\Omega}} : \boldsymbol{\epsilon^T}, \tag{5.113}$$

where $\boldsymbol{S^{\Omega}}$ is Eshelby's tensor. It is independent of the material properties of the ellipsoidal region. It is completely defined in terms of the aspect ratio of the ellipsoidal region and the elastic parameters of the surrounding matrix. Now consider a solid with an ellipsoidal inclusion (having the same geometry as the ellipsoidal region) with a different stiffness $\boldsymbol{C^{\Omega}}$, but no transformation strain (see Figure 5.6c). The presence of the ellipsoidal inclusion also introduces the disturbation strain $\tilde{\boldsymbol{\epsilon}}^{\boldsymbol{d}}$. Subject both the solid with the transformed ellipsoidal region and the heterogeneous solid with ellipsoidal inclusion to a uniform applied strain $\boldsymbol{\epsilon^o}$ at infinity. Our goal is to find the relation between the strain field in the ellipsoidal inclusion and $\boldsymbol{\epsilon^o}$; in other words, the strain concentration factor discussed previously. We then compare these two cases. The strain in the ellipsoidal inclusion can be found by adjusting the transformation strain such that it gives the two cases the same stress and strain distributions.

For solid with the transformation strain in the ellipsoidal region, the stress in

the ellipsoidal region is:

$$\bar{\boldsymbol{\sigma}}^{\boldsymbol{\Omega}} = \boldsymbol{C}^{\boldsymbol{m}} : \left(\boldsymbol{\epsilon}^{\boldsymbol{o}} + \tilde{\boldsymbol{\epsilon}}^{\boldsymbol{d}} - \boldsymbol{\epsilon}^{\boldsymbol{T}}\right). \tag{5.114}$$

$\boldsymbol{\epsilon}^{\boldsymbol{T}}$ has the negative sign since it behaves oppositely, compared with $\tilde{\boldsymbol{\epsilon}}^{\boldsymbol{d}}$. In other words, if the the ellipsoidal region is expanding (transformation strain is positive), the areas around would try to maintain its shape by pushing back, therefore negative disturbation strain. For solid with the ellipsoidal inclusion, the stress in the ellipsoid is just the product of the multiplication between the stiffness of the ellipsoid and the strain in the ellipsoid:

$$\bar{\boldsymbol{\sigma}}^{\boldsymbol{\Omega}} = \boldsymbol{C}^{\boldsymbol{\Omega}} : \bar{\boldsymbol{\epsilon}}^{\boldsymbol{\Omega}}, \tag{5.115}$$

where

$$\bar{\boldsymbol{\epsilon}}^{\boldsymbol{\Omega}} = \boldsymbol{\epsilon}^{\boldsymbol{o}} + \tilde{\boldsymbol{\epsilon}}^{\boldsymbol{d}}. \tag{5.116}$$

Since this is the problem of infinitely extended solid with the single inclusion, the average strain in the heterogeneous solid is identical to the uniform applied strain, given by

$$\bar{\boldsymbol{\epsilon}} = \boldsymbol{\epsilon}^{\boldsymbol{o}}. \tag{5.117}$$

Equate equation 5.114 to 5.115 and obtain:

$$\boldsymbol{C}^{\boldsymbol{m}} : \left(\boldsymbol{\epsilon}^{\boldsymbol{o}} + \tilde{\boldsymbol{\epsilon}}^{\boldsymbol{d}} - \boldsymbol{\epsilon}^{\boldsymbol{T}}\right) \;=\; \boldsymbol{C}^{\boldsymbol{\Omega}} : \left(\boldsymbol{\epsilon}^{\boldsymbol{o}} + \tilde{\boldsymbol{\epsilon}}^{\boldsymbol{d}}\right). \tag{5.118}$$

From equation 5.116, we obtain:

$$\boldsymbol{C}^{\boldsymbol{m}} : \left(\bar{\boldsymbol{\epsilon}}^{\boldsymbol{\Omega}} - \boldsymbol{\epsilon}^{\boldsymbol{T}}\right) \;=\; \boldsymbol{C}^{\boldsymbol{\Omega}} : \bar{\boldsymbol{\epsilon}}^{\boldsymbol{\Omega}}. \tag{5.119}$$

Solve for $\boldsymbol{\epsilon^T}$:

$$\boldsymbol{\epsilon^T} = \boldsymbol{D^m} : \left(\boldsymbol{C^m} - \boldsymbol{C^\Omega}\right) : \bar{\boldsymbol{\epsilon}}^{\boldsymbol{\Omega}}. \tag{5.120}$$

Substitute equation 5.120 into 5.113, we obtain:

$$\tilde{\boldsymbol{\epsilon}}^{\boldsymbol{d}} = \boldsymbol{S^\Omega} : \boldsymbol{D^m} : \left(\boldsymbol{C^m} - \boldsymbol{C^\Omega}\right) : \bar{\boldsymbol{\epsilon}}^{\boldsymbol{\Omega}}. \tag{5.121}$$

Substitute equation 5.121 into 5.116, we obtain $\bar{\boldsymbol{\epsilon}}^{\boldsymbol{\Omega}}$:

$$\bar{\boldsymbol{\epsilon}}^{\boldsymbol{\Omega}} = \left[\mathbf{1^{(2)}} + \boldsymbol{S^\Omega} : \boldsymbol{D^m} : \left(\boldsymbol{C^\Omega} - \boldsymbol{C^m}\right)\right]^{-1} : \bar{\boldsymbol{\epsilon}}, \tag{5.122}$$

where $\mathbf{1^{(2)}}$ is the second order identity tensor. The strain concentration tensor, $\boldsymbol{P^\Omega}$ for DD model is given by:

$$\boldsymbol{P^{\Omega-DD}} = \left[\mathbf{1^{(2)}} + \boldsymbol{S^\Omega} : \boldsymbol{D^m} : \left(\boldsymbol{C^\Omega} - \boldsymbol{C^m}\right)\right]^{-1}, \tag{5.123}$$

where $\boldsymbol{P^{\Omega-DD}}$ is the $\boldsymbol{P^\Omega}$ for DD model. Substitute equation 5.123 into 5.111, we obtain the overall elasticity tensor of the composite with dilute randomly distributed and uniaxially oriented ellipsoidal inclusion, which is given by:

$$\bar{\boldsymbol{C}} = \boldsymbol{C^m} + f_\Omega \left(\boldsymbol{C^\Omega} - \boldsymbol{C^m}\right) : \left[\mathbf{1^{(2)}} + \boldsymbol{S^\Omega} : \boldsymbol{D^m} : \left(\boldsymbol{C^\Omega} - \boldsymbol{C^m}\right)\right]^{-1}. \tag{5.124}$$

Equation 5.124 can be used for many composites with different types of inclusions. It can be done by choosing the Eshelby's tensor such that it matches with the type of inclusion in the composite. Eshelby's tensors for spherical and prolate ellipsoid

inclusions are shown in Appendix 5.A. $\boldsymbol{C^m}$ and $\boldsymbol{C^\Omega}$ are isotropic and can be written in the following forms:

$$\boldsymbol{C^n} = \lambda^n \mathbf{1^{(2)}} \otimes \mathbf{1^{(2)}} + 2G^n \mathbf{1^{(4S)}}, \tag{5.125}$$

where n can be Ω or m, $\mathbf{1^{(4S)}}$ is the forth-order symmetric identity tensor, λ^n is Lamé constant, and G^n is shear modulus. λ^n and G^n can be complex number if it is a viscoelastic material. It can also be written in term of components as:

$$C^n_{ijkl} = \lambda^n \delta_{ij}\delta_{kl} + 2G^n \left(\frac{1}{2} \left[\delta_{ik}\delta_{jl} + \delta_{il}\delta_{jk} \right] \right), \tag{5.126}$$

where the indices,i, j, k, l = 1,2,3, and δ_{ij} is Kronecker delta which is defined as:

$$\delta_{ij} = \begin{cases} 0 & \text{if } i \neq j \\ 1 & \text{if } i = j \end{cases} \tag{5.127}$$

The DD model is developed based on the assumption that it has only single inclusion embedded in the infinitely extended matrix, therefore it does not take into account the effect of interaction between inclusions. It is appropriate for predicting mechanical properties of composite with low volume fraction of inclusion. Figures 5.7a shows a composite with dilute randomly distributed and uniaxially oriented prolate ellipsoid inclusions. It can also represent composite with uniaxially oriented fibers by adjusting the dimensions of the prolate ellipsoid such that its volume and aspect ratio agree with those of the fiber. The major axis of the prolate ellipsoid points in the x_1 direction. However, this model can be modified to represent composites with

in-plane oriented prolate ellipsoids and with randomly oriented prolate ellipsoids (see Section 5.4). Figure 5.7b shows composite with dilute randomly distributed spherical inclusions.

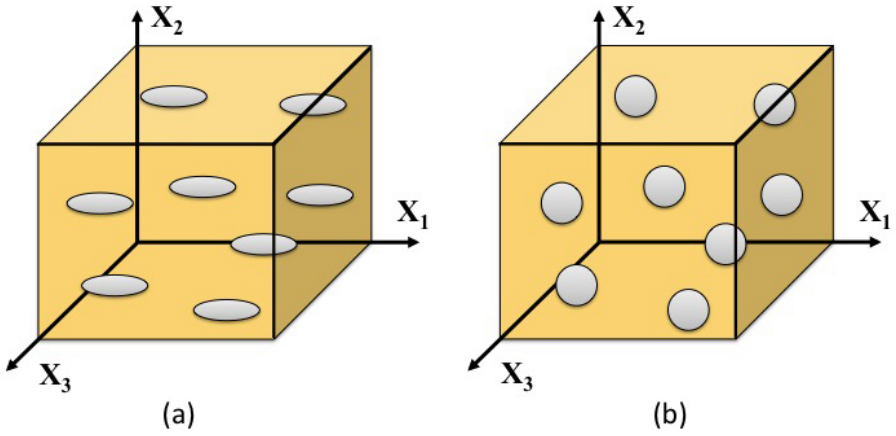

Figure 5.7: (a) Composite with dilute randomly distributed and uniaxially oriented prolate ellipsoid inclusions (b)Composite with dilute randomly distributed spherical inclusions

DD Model VS Experiment

This model is used to predict the overall mechanical properties of milled glassed reinforced polyurea composites at different volume fractions. The result and discussion are shown in Section 5.4.

5.2 Composite with Finite Volume Fraction and Random Distribution of Inclusions (MT)

In this section, our models for composite with Finite Volume Fraction and Random Distribution of Inclusions are developed based on Mori and Tanaka's work

[121]. Benveniste has provided a thorough and clear explanation of the Mori-Tanaka approach [122]. Tucker et al. has summarized and shown how to develop the model [118]. Here we will discuss and show the derivation of the model in detail. We will refer the models developed in this section as Mori-Tanaka models (MT). Our goal here is to find the strain concentration factor, $\boldsymbol{P}^{\boldsymbol{\Omega}}$ in equation 5.111 for MT models. Equation 5.111 with the strain concentration factor that is obtained using MT approach yields the model for composite with finite volume fraction and random distribution of inclusions.

In Mori-Tanaka approach and contrary to the dilute models, the inclusions may interact with each other through modifications in far-field strain to average strain in the matrix [116, 118]. The Mori-Tanaka assumption is that, when many identical particles are introduced in the composite, the average strain in the inclusion is given by [118]:

$$\bar{\boldsymbol{\epsilon}}^{\boldsymbol{\Omega}} = \boldsymbol{P}^{\boldsymbol{\Omega}-\boldsymbol{DD}} : \bar{\boldsymbol{\epsilon}}^{\boldsymbol{m}}, \tag{5.128}$$

where $\boldsymbol{P}^{\boldsymbol{\Omega}-\boldsymbol{DD}}$ is shown in equation 5.123. To obtain equation 5.128, the average strains in matrix and inclusion, $\bar{\boldsymbol{\epsilon}}^{\boldsymbol{m}}$ and $\bar{\boldsymbol{\epsilon}}^{\boldsymbol{\Omega}}$ are expressed as:

$$\bar{\boldsymbol{\epsilon}}^{\boldsymbol{m}} = \boldsymbol{\epsilon}^{\boldsymbol{o}} + \tilde{\boldsymbol{\epsilon}}^{\boldsymbol{m}}, \tag{5.129}$$

$$\bar{\boldsymbol{\epsilon}}^{\boldsymbol{\Omega}} = \boldsymbol{\epsilon}^{\boldsymbol{o}} + \tilde{\boldsymbol{\epsilon}}^{\boldsymbol{m}} + \tilde{\boldsymbol{\epsilon}}^{\boldsymbol{\Omega}}, \tag{5.130}$$

where $\tilde{\boldsymbol{\epsilon}}^{\boldsymbol{m}}$ and $\tilde{\boldsymbol{\epsilon}}^{\boldsymbol{\Omega}}$ are the disturbation strains in the matrix and inclusion, respectively.

From Eshelby's equivalent inclusion, $\tilde{\boldsymbol{\epsilon}}^{\boldsymbol{\Omega}}$ is related to transformation strain by:

$$\tilde{\boldsymbol{\epsilon}}^{\boldsymbol{\Omega}} = \boldsymbol{S}^{\boldsymbol{\Omega}} : \boldsymbol{\epsilon}^{\boldsymbol{T}}. \tag{5.131}$$

Apply the previously discussed Eshelby's equivalent inclusion and substitute equation 5.130 into equation 5.119, we obtain

$$\boldsymbol{C}^{\boldsymbol{m}} : \left(\boldsymbol{\epsilon}^{\boldsymbol{o}} + \tilde{\boldsymbol{\epsilon}}^{\boldsymbol{m}} + \tilde{\boldsymbol{\epsilon}}^{\boldsymbol{\Omega}} - \boldsymbol{\epsilon}^{\boldsymbol{T}}\right) = \boldsymbol{C}^{\boldsymbol{\Omega}} : \left(\boldsymbol{\epsilon}^{\boldsymbol{o}} + \tilde{\boldsymbol{\epsilon}}^{\boldsymbol{m}} + \tilde{\boldsymbol{\epsilon}}^{\boldsymbol{\Omega}}\right). \tag{5.132}$$

From equations 5.130-5.133, we have:

$$\begin{aligned}
\boldsymbol{C}^{\boldsymbol{m}} : \left(\bar{\boldsymbol{\epsilon}}^{\boldsymbol{\Omega}} - \bar{\boldsymbol{\epsilon}}^{\boldsymbol{T}}\right) &= \boldsymbol{C}^{\boldsymbol{\Omega}} : \bar{\boldsymbol{\epsilon}}^{\boldsymbol{\Omega}} \\
\left(\boldsymbol{C}^{\boldsymbol{\Omega}} - \boldsymbol{C}^{\boldsymbol{m}}\right) : \bar{\boldsymbol{\epsilon}}^{\boldsymbol{\Omega}} &= -\boldsymbol{C}^{\boldsymbol{m}} : \boldsymbol{S}^{\boldsymbol{\Omega}^{-1}} : \tilde{\boldsymbol{\epsilon}}^{\boldsymbol{\Omega}} \\
\tilde{\boldsymbol{\epsilon}}^{\boldsymbol{\Omega}} &= -\boldsymbol{S}^{\boldsymbol{\Omega}} : \boldsymbol{D}^{\boldsymbol{m}} : \left(\boldsymbol{C}^{\boldsymbol{\Omega}} - \boldsymbol{C}^{\boldsymbol{m}}\right) : \bar{\boldsymbol{\epsilon}}^{\boldsymbol{\Omega}}.
\end{aligned} \tag{5.133}$$

Substitute equations 5.129 and 5.133 into 5.130, we obtain:

$$\bar{\boldsymbol{\epsilon}}^{\boldsymbol{\Omega}} = \left[\mathbf{1}^{(\mathbf{2})} + \boldsymbol{S}^{\boldsymbol{\Omega}} : \boldsymbol{D}^{\boldsymbol{m}} : \left(\boldsymbol{C}^{\boldsymbol{\Omega}} - \boldsymbol{C}^{\boldsymbol{m}}\right)\right]^{-1} : \bar{\boldsymbol{\epsilon}}^{\boldsymbol{m}}. \tag{5.134}$$

Equation 5.134 is exactly equation 5.128. Substitute equation 5.128 (or 5.134) into 5.102, we obtain:

$$\begin{aligned}
\bar{\boldsymbol{\epsilon}} &= f_{\Omega}\boldsymbol{P}^{\boldsymbol{\Omega}-\boldsymbol{DD}}\bar{\boldsymbol{\epsilon}}^{\boldsymbol{m}} + (1 - f_{\Omega}) : \bar{\boldsymbol{\epsilon}}^{\boldsymbol{m}} \\
\bar{\boldsymbol{\epsilon}} &= \left[f_{\Omega}\boldsymbol{P}^{\boldsymbol{\Omega}-\boldsymbol{DD}} + (1 - f_{\Omega})\,\mathbf{1}^{(\mathbf{2})}\right] : \bar{\boldsymbol{\epsilon}}^{\boldsymbol{m}}.
\end{aligned} \tag{5.135}$$

From equation 5.102, we can write:

$$\bar{\boldsymbol{\epsilon}}^{\boldsymbol{m}} = \frac{\bar{\boldsymbol{\epsilon}} - f_{\Omega}\bar{\boldsymbol{\epsilon}}^{\boldsymbol{\Omega}}}{1 - f_{\Omega}}. \tag{5.136}$$

Substitute equation 5.135 into 5.136 and solve for $\bar{\boldsymbol{\epsilon}}^{\boldsymbol{\Omega}}$ in term of $\bar{\boldsymbol{\epsilon}}$, we obtain:

$$\bar{\boldsymbol{\epsilon}}^{\boldsymbol{\Omega}} = \boldsymbol{P}^{\boldsymbol{\Omega-MT}} : \bar{\boldsymbol{\epsilon}}, \tag{5.137}$$

where

$$\boldsymbol{P}^{\boldsymbol{\Omega-MT}} = \left[(1 - f_{\Omega})\,\mathbf{1}^{(\mathbf{2})} + f_{\Omega}\boldsymbol{P}^{\boldsymbol{\Omega-DD}}\right]^{-1} : \boldsymbol{P}^{\boldsymbol{\Omega-DD}}. \tag{5.138}$$

Substitute equation 5.138 into 5.111, we obtain the overall elasticity tensor of the composite with finite volume fraction and random distribution of uniaxially oriented ellipsoidal inclusions, which is given by:

$$\bar{\boldsymbol{C}} = \boldsymbol{C}^{\boldsymbol{m}} + f_{\Omega}\left(\boldsymbol{C}^{\boldsymbol{\Omega}} - \boldsymbol{C}^{\boldsymbol{m}}\right) : \left[(1 - f_{\Omega})\,\mathbf{1}^{(\mathbf{2})} + f_{\Omega}\boldsymbol{P}^{\boldsymbol{\Omega-DD}}\right]^{-1} : \boldsymbol{P}^{\boldsymbol{\Omega-DD}}. \tag{5.139}$$

Equation 5.124 can be used for many composites with different types of inclusions. It can be done by choosing the Eshelby's tensor such that it matches with the type of inclusion in the composite. $\boldsymbol{C}^{\boldsymbol{\Omega}}$, $\boldsymbol{C}^{\boldsymbol{m}}$, and $\boldsymbol{P}^{\boldsymbol{\Omega-DD}}$ are shown in equations 5.125 and 5.123. Eshelby's tensors for spherical and prolate ellipsoid inclusions are shown in Appendix 5.A.

The MT model indirectly takes into account the effect of interaction between inclusions by assuming that the each particle sees a far field strain equal to the average strain in the matrix. Figures 5.8a shows a composite with finite volume fraction and random distribution of uniaxially oriented ellipsoidal inclusions. It can also represent

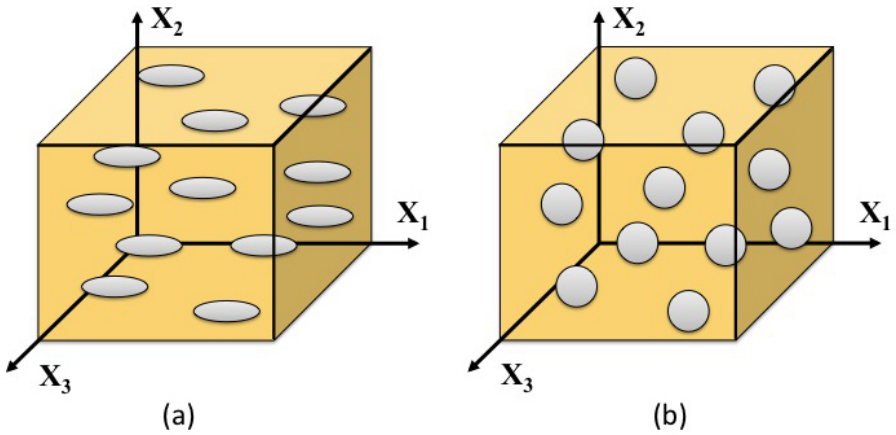

Figure 5.8: (a) Composite with finite volume fraction and random distribution of uniaxially oriented ellipsoidal inclusions (b) Composite with finite volume fraction and random distribution of spherical inclusions

composite with uniaxially oriented fibers by adjusting the dimensions of the prolate ellipsoid such that its volume and aspect ratio agree with those of the fiber. The major axis of the prolate ellipsoid points in the x_1 direction. However, this model can be modified to represent composites with in-plane oriented prolate ellipsoids and with randomly oriented prolate ellipsoids (see Section 5.4). Figure 5.8b shows composite with with finite volume fraction and random distribution of spherical inclusions.

MT Model VS Experiment

This model is used to predict the overall mechanical properties of milled glassed reinforced polyurea composites at different volume fractions. The result and discussion are shown in Section 5.4.

5.3 Composite with Finite Volume Fraction and Periodic Distribution of Inclusions (P)

In this part, we present a static homogenization method for the material with periodic microstructure based on micromechanical consideration of the volume averages of the field variables. This theory is firmly established in the literatures (see [116, 123, 124]). The models in this section are developed based on the periodic distribution of inclusions, in which the inclusion can be void or solid and can have various shapes. At high volume fraction, this method accounts for the interaction between particles in a more direct manner than Mori-Tanaka method. However, this method might not appropriately represent the microstructure of a composite material that has inclusions randomly distributed in the matrix. Despite this concern, the assumption of periodicity has been proved very powerful in predicting mechanical properties of composites with high inclusion-interaction effects and random distribution of inclusions [116]. Two models are developed for (1) composite with periodically distributed cylindrical inclusions and (2) composite with periodically distributed two-phase spherical inclusions

5.3.1 Composite with Periodically Distributed Cylindrical Inclusions (P-CI)

Consider an infinitely extended, homogeneous, isotropic, elastic solid. When the uniform stress is prescribed on the boundary of the solid, the strain within the solid would be uniform and vice versa. Suppose now that instead of being homogeneous, the infinite solid contains periodically distributed inclusions of common size and elastic

properties, in such a manner that the body may be regarded as a collection of infinite unit cells of identical dimensions, each containing one inclusion. The presence of inclusions with different elasticity, from that of the matrix disturbs the uniform stress and strain fields.

The disturbed stress $\boldsymbol{\sigma}(\boldsymbol{x})$ and strain $\boldsymbol{\epsilon}(\boldsymbol{x})$ fields are now considered as periodic fields due to geometric periodicity of the material. The elasticity and compliance tensors are not uniform anymore but periodic in space. An elastic solid with periodically distributed inhomogeneities can be homogenized by introduction of suitable periodically disturbed eigenstrains or eigenstresses. This homogenization method is similar to the transformation strain in Eshelby's equivalent inclusion method discussed previously, except that here. In this approach, the actual periodic elasticity tensor of the solid $\boldsymbol{C^P}(\boldsymbol{x})$ is replaced with a reference constant elasticity tensor $\boldsymbol{C}$ and a suitable periodic eigenstrain $\boldsymbol{\epsilon^*}(\boldsymbol{x})$ (eigenstress $\boldsymbol{\sigma^*}(\boldsymbol{x})$) field. The uniform solid with constant elasticity tensor $\boldsymbol{C^P}(\boldsymbol{x})$, is referred to as the equivalent homogeneous solid. U, M, and Ω denote unit cell, matrix, and inclusion respectively. Defined the domain of a typical unit cell, U, by

$$U = \{\boldsymbol{x}; -a_i < x_i < a_i \, (i = 1, 2, 3)\}, \tag{5.140}$$

$$V_U = 8a_1a_2a_3, \tag{5.141}$$

where $\boldsymbol{x}$ is a position vector or a typical point in the unit cell, $2a_i$ are the dimensions of parallelepiped unit cell in x_i direction, V_U is the total volume of the unit cell U.

Introduce a variable $\boldsymbol{\xi}$ where

$$\xi_i = \xi_i\left(n_i\right) = \frac{n_i \pi}{a_i}\left(n_i = 0, \pm 1, \pm 2, ...;\ i \text{ not summed};\ i = 1, 2, 3\right). \tag{5.142}$$

A field variable $\boldsymbol{Q}$ is periodic and can be represented in Fourier series form as:

$$\boldsymbol{Q}\left(\boldsymbol{x}\right) = \sum_{\boldsymbol{\xi}} F\boldsymbol{Q}\left(\boldsymbol{\xi}\right) e^{i\boldsymbol{x}\cdot\boldsymbol{\xi}}, \tag{5.143}$$

or

$$\boldsymbol{Q}\left(\boldsymbol{x}\right) = \langle \boldsymbol{Q} \rangle + \boldsymbol{Q^P}\left(\boldsymbol{x}\right), \tag{5.144}$$

where

$$\langle \boldsymbol{Q} \rangle = \frac{1}{V_U} \int_U \boldsymbol{Q}\left(\boldsymbol{x}\right) dV_x, \tag{5.145}$$

$$\boldsymbol{Q^P}\left(\boldsymbol{x}\right) = \sum_{\boldsymbol{\xi} \neq \boldsymbol{0}} F\boldsymbol{Q}\left(\boldsymbol{\xi}\right) e^{i\boldsymbol{x}\cdot\boldsymbol{\xi}}, \tag{5.146}$$

$$F\boldsymbol{Q}\left(\boldsymbol{\xi}\right) = \frac{1}{V_U} \int_U \boldsymbol{Q}\left(\boldsymbol{x}\right) e^{-i\boldsymbol{x}\cdot\boldsymbol{\xi}} dV_x, \tag{5.147}$$

$\langle \boldsymbol{Q} \rangle$ represents the averaged value of the field variable over the unit cell. $\boldsymbol{Q^P}\left(\boldsymbol{x}\right)$, which is periodic with zero mean value, represents the local deviations from the average value. Due to the periodicity of the material, $\boldsymbol{\epsilon}\left(\boldsymbol{x}\right)$, $\boldsymbol{\sigma}\left(\boldsymbol{x}\right)$, $\boldsymbol{\epsilon^*}\left(\boldsymbol{x}\right)$, and $\boldsymbol{\sigma^*}\left(\boldsymbol{x}\right)$ can be written as in equation 5.144.

To relate field variable in the equivalent homogenized solid to those in the original heterogeneous solid with periodic structure, the following consistency conditions is used

$$\boldsymbol{C^P}\left(\boldsymbol{x}\right):\boldsymbol{\epsilon}\left(\boldsymbol{x}\right)=\boldsymbol{C}:\left(\boldsymbol{\epsilon}\left(\boldsymbol{x}\right)-\boldsymbol{\epsilon^*}\left(\boldsymbol{x}\right)\right)\text{ For }\boldsymbol{x}\text{ in }U, \tag{5.148}$$

where $\boldsymbol{C^P}\left(\boldsymbol{x}\right)$ is the actual periodic elasticity tensor and $\boldsymbol{C}$ is the reference constant elasticity tensor of the homogenized solid. Normally, $\boldsymbol{C}$ is chosen to be identical to elasticity tensor of the matrix phase. However, this is not restriction. $\boldsymbol{\epsilon^*}\left(\boldsymbol{x}\right)$ is introduced to compensate for the effect of the homogenization of the elasticity tensor. For the case of an isotropic reference material, $\boldsymbol{C}$ can be described with two constant material parameters. The following is its index form.

$$C_{ijkl}=\lambda\delta_{ij}\delta_{kl}+2\mu\left(\frac{1}{2}\left[\delta_{ik}\delta_{jl}+\delta_{il}\delta_{jk}\right]\right), \tag{5.149}$$

where λ and μ are Lamé constant. one of the forms of λ is $K-\frac{2}{3}G$ where K and G are bulk and shear moduli respectively, while μ is G. The equilibrium equation can be written in the following form:

$$\nabla\boldsymbol{\sigma}\left(\boldsymbol{x}\right)=\nabla\left(\boldsymbol{C^P}\left(\boldsymbol{x}\right):\boldsymbol{\epsilon}\left(\boldsymbol{x}\right)\right)=0\text{ For }\boldsymbol{x}\text{ in }U. \tag{5.150}$$

Substitute equation 5.148 into 5.150, we obtain:

$$\nabla\left(\boldsymbol{C}:\left(\boldsymbol{\epsilon}\left(\boldsymbol{x}\right)-\boldsymbol{\epsilon^*}\left(\boldsymbol{x}\right)\right)\right)=0. \tag{5.151}$$

Due to that the symmetry of $\boldsymbol{C}$, we can write equation 5.151 in term of displacement

field $\boldsymbol{u}(\boldsymbol{x})$ as [116]:

$$\begin{aligned} 0 &= \nabla\left(\boldsymbol{C} : \left(\nabla \otimes \boldsymbol{u}(\boldsymbol{x}) - \boldsymbol{\epsilon}^{*}(\boldsymbol{x})\right)\right), \\ 0 &= \nabla\left(\boldsymbol{C} : \left(\nabla \otimes \boldsymbol{u}(\boldsymbol{x})\right)\right) - \nabla\left(\boldsymbol{C} : \boldsymbol{\epsilon}^{*}(\boldsymbol{x})\right), \end{aligned} \tag{5.152}$$

where $\otimes$ is dyadic operator. Noting that equations 5.152 and 5.150 are equivalent, related by equation 5.148. Using Fourier series form of each field variable, equation 5.152 becomes:

$$0 = -\boldsymbol{\xi} \cdot \boldsymbol{C} : [\boldsymbol{\xi} \otimes F\boldsymbol{u}(\boldsymbol{\xi})] - i\boldsymbol{\xi} \cdot \boldsymbol{C} : F\boldsymbol{\epsilon}^{*}(\boldsymbol{\xi}) \text{ For } \boldsymbol{\xi} \neq 0. \tag{5.153}$$

From equation 5.153, now we can relate displacement and strain to eigenstrain in the $\boldsymbol{\xi}$ domain as:

$$F\boldsymbol{u}(\boldsymbol{\xi}) = -i\left[\boldsymbol{\xi} \cdot \boldsymbol{C} : \boldsymbol{\xi}\right]^{-1} \cdot \left[\boldsymbol{\xi} \cdot \boldsymbol{C} : F\boldsymbol{\epsilon}^{*}(\boldsymbol{\xi})\right], \tag{5.154}$$

$$\begin{aligned} F\boldsymbol{\epsilon}(\boldsymbol{\xi}) &= \frac{1}{2} \cdot \left[\boldsymbol{\xi} \otimes F\boldsymbol{u}(\boldsymbol{\xi}) + F\boldsymbol{u}(\boldsymbol{\xi}) \otimes \boldsymbol{\xi}\right] \\ &= \operatorname{sym}\left[\boldsymbol{\xi} \otimes (\boldsymbol{\xi} \cdot \boldsymbol{C} \cdot \boldsymbol{\xi})^{-1} \otimes \boldsymbol{\xi}\right] : \boldsymbol{C} : F\boldsymbol{\epsilon}^{*}(\boldsymbol{\xi}), \end{aligned} \tag{5.155}$$

where sym stands for the symmetric part of the corresponding fourth-order tensor. From equations 5.144-5.147 and equation 5.155, strain field in term spatial variable $\boldsymbol{x}$ has the following form:

$$\boldsymbol{\epsilon}(\boldsymbol{x}) = \langle \boldsymbol{\epsilon} \rangle + \boldsymbol{\epsilon}^{\boldsymbol{P}}(\boldsymbol{x}), \tag{5.156}$$

where

$$\langle \boldsymbol{\epsilon} \rangle = \frac{1}{V_U} \int_U \boldsymbol{\epsilon}\left(\boldsymbol{x}\right) dV_x, \tag{5.157}$$

$$\boldsymbol{\epsilon^P}\left(\boldsymbol{x}\right) = \sum_{\boldsymbol{\xi} \neq 0} F\boldsymbol{S^P}\left(\boldsymbol{\xi}\right) : \left(\frac{1}{V_U} \int_U \boldsymbol{\epsilon^*}\left(\boldsymbol{y}\right) e^{i(\boldsymbol{x}-\boldsymbol{y})\cdot\boldsymbol{\xi}} dV_y \right), \tag{5.158}$$

$$\begin{aligned} F\boldsymbol{S^P}\left(\boldsymbol{\xi}\right) &= \text{sym}\left[\boldsymbol{\xi} \otimes \left(\boldsymbol{\xi}\cdot\boldsymbol{C}\cdot\boldsymbol{\xi}\right)^{-1} \otimes \boldsymbol{\xi}\right] : \boldsymbol{C} \\ &= F\boldsymbol{S^1}\left(\boldsymbol{\xi}\right) - \frac{1}{1-\nu} F\boldsymbol{S^2}\left(\boldsymbol{\xi}\right) + \frac{\nu}{1-\nu} F\boldsymbol{S^3}\left(\boldsymbol{\xi}\right), \end{aligned} \tag{5.159}$$

$$F\boldsymbol{S^1}\left(\boldsymbol{\xi}\right) = 2\text{sym}\left(\bar{\boldsymbol{\xi}} \otimes \boldsymbol{1^{(2)}} \otimes \bar{\boldsymbol{\xi}}\right), \tag{5.160}$$

$$F\boldsymbol{S^2}\left(\boldsymbol{\xi}\right) = \bar{\boldsymbol{\xi}} \otimes \bar{\boldsymbol{\xi}} \otimes \bar{\boldsymbol{\xi}} \otimes \bar{\boldsymbol{\xi}}, \tag{5.161}$$

$$F\boldsymbol{S^3}\left(\boldsymbol{\xi}\right) = \bar{\boldsymbol{\xi}} \otimes \bar{\boldsymbol{\xi}} \otimes \boldsymbol{1^{(2)}}, \tag{5.162}$$

$$\bar{\boldsymbol{\xi}} = \frac{\boldsymbol{\xi}}{\xi} = \frac{\boldsymbol{\xi}}{\sqrt{\xi_i \xi_i}}. \tag{5.163}$$

$F\boldsymbol{S^P}\left(\boldsymbol{\xi}\right)$ in index notation form is as follows:

$$FS^P_{ijkl}(\boldsymbol{\xi}) = FS^1_{ijkl}(\boldsymbol{\xi}) - \frac{1}{1-\nu} FS^2_{ijkl}(\boldsymbol{\xi}) + \frac{\nu}{1-\nu} FS^3_{ijkl}(\boldsymbol{\xi}), \tag{5.164}$$

where

$$FS^1_{ijkl}(\boldsymbol{\xi}) = \frac{1}{2}\left\{\bar{\xi}_j\left(\delta_{il}\bar{\xi}_k + \delta_{ik}\bar{\xi}_l\right) + \bar{\xi}_i\left(\delta_{jl}\bar{\xi}_k + \delta_{jk}\bar{\xi}_l\right)\right\}, \tag{5.165}$$

$$FS^2_{ijkl}(\boldsymbol{\xi}) = \bar{\xi}_i\bar{\xi}_j\bar{\xi}_k\bar{\xi}_l, \tag{5.166}$$

$$FS^3_{ijkl}(\boldsymbol{\xi}) = \bar{\xi}_i\bar{\xi}_j\delta_{kl}, \tag{5.167}$$

$$\bar{\xi}_i = \frac{\xi_i}{\sqrt{\xi_k\xi_k}}. \tag{5.168}$$

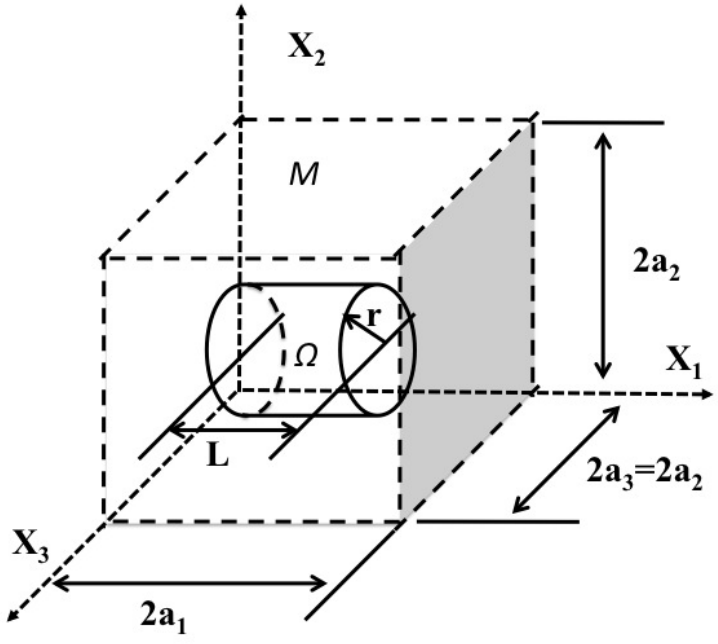

Figure 5.9: A unit cell of composite with periodically-distributed and uniaxially-oriented cylindrical inclusions

Consider a unit cell, U of composite with periodically distributed and uniaxially oriented cylindrical inclusions (Figure 5.9). M is matrix with the uniform elasticity tensor $\boldsymbol{C}$ and Ω is inclusion with uniform elasticity tensor $\boldsymbol{C^{\Omega}}$. The following is the elasticity tensor of the composite:

$$\boldsymbol{C^{P}}\left(\boldsymbol{x}\right) = \boldsymbol{H}\left(\boldsymbol{x}; M\right)\boldsymbol{C} + \boldsymbol{H}\left(\boldsymbol{x}; \Omega\right)\boldsymbol{C^{\Omega}}, \tag{5.169}$$

where $\boldsymbol{H}\left(\boldsymbol{x}; M\right)$ and $\boldsymbol{H}\left(\boldsymbol{x}; \Omega\right)$ are the Heaviside step functions associated with points in M and Ω, respectively. For the equivalent homogeneous solid for homogenization, the matrix elasticity $\boldsymbol{C}$ is used. Then, the eigenstrians are nonzero only in $\boldsymbol{C^{\Omega}}$, i.e.,

$$\boldsymbol{\epsilon^{*}}\left(\boldsymbol{x}\right) = \boldsymbol{H}\left(\boldsymbol{x}; \Omega\right)\boldsymbol{\epsilon^{*}}\left(\boldsymbol{x}\right). \tag{5.170}$$

The consistency condition (equation 5.148) is now changed to the following equation:

$$\begin{aligned} \boldsymbol{C^{\Omega}} : \boldsymbol{\epsilon}\left(\boldsymbol{x}\right) &= \boldsymbol{C} : \left(\boldsymbol{\epsilon}\left(\boldsymbol{x}\right) - \boldsymbol{\epsilon^{*}}\left(\boldsymbol{x}\right)\right) \text{ For } \boldsymbol{x} \text{ in } \Omega, \\ \boldsymbol{C^{\Omega}} : \left(\langle\boldsymbol{\epsilon}\rangle + \boldsymbol{\epsilon^{P}}\left(\boldsymbol{x}\right)\right) &= \boldsymbol{C} : \left(\langle\boldsymbol{\epsilon}\rangle + \boldsymbol{\epsilon^{P}}\left(\boldsymbol{x}\right) - \boldsymbol{\epsilon^{*}}\left(\boldsymbol{x}\right)\right). \end{aligned} \tag{5.171}$$

When a uniform overall strain, $\boldsymbol{\epsilon^{o}}$ is prescribed on the boundary of the composite. The volume average strain, $\langle\boldsymbol{\epsilon}\rangle$ is equal to $\boldsymbol{\epsilon^{o}}$. Equation 5.171 becomes:

$$\boldsymbol{C^{\Omega}} : \left(\boldsymbol{\epsilon^{o}} + \boldsymbol{\epsilon^{P}}\left(\boldsymbol{x}\right)\right) = \boldsymbol{C} : \left(\boldsymbol{\epsilon^{o}} + \boldsymbol{\epsilon^{P}}\left(\boldsymbol{x}\right) - \boldsymbol{\epsilon^{*}}\left(\boldsymbol{x}\right)\right). \tag{5.172}$$

We assume that the eigenstrain, $\boldsymbol{\epsilon^{*}}\left(\boldsymbol{x}\right)$ in the inclusion Ω is constant and equal to its average $\overline{\boldsymbol{\epsilon}}^{*}$. The average consistency condition over the volume of phase Ω can be

expressed as:

$$\boldsymbol{C}^{\boldsymbol{\Omega}} : \left(\boldsymbol{\epsilon}^{\boldsymbol{o}} + \bar{\boldsymbol{\epsilon}}^{\boldsymbol{P}}\right) = \boldsymbol{C} : \left(\boldsymbol{\epsilon}^{\boldsymbol{o}} + \bar{\boldsymbol{\epsilon}}^{\boldsymbol{P}} - \bar{\boldsymbol{\epsilon}}^{*}\right) \text{ in } \Omega, \tag{5.173}$$

where $\bar{\boldsymbol{\epsilon}}^{\boldsymbol{P}}$ is average disturbance (periodic) strain over the inclusion phase. From equation 5.158 and the assumption that $\boldsymbol{\epsilon}^{*}(\boldsymbol{x})$ is constant in Ω and zero outside, $\bar{\boldsymbol{\epsilon}}^{\boldsymbol{P}}$ can be written as:

$$\begin{aligned} \bar{\boldsymbol{\epsilon}}^{\boldsymbol{P}} &= \frac{1}{V_\Omega}\int_\Omega \boldsymbol{\epsilon}^{\boldsymbol{P}}(\boldsymbol{x}) dV_x \\ &= \frac{1}{V_\Omega}\int_\Omega \left[\sum_{\boldsymbol{\xi}\neq 0} F\boldsymbol{S}^{\boldsymbol{P}}(\boldsymbol{\xi}) : \left(\frac{1}{V_U}\int_U e^{i(\boldsymbol{x}-\boldsymbol{y})\cdot\boldsymbol{\xi}} dV_y\right)\bar{\boldsymbol{\epsilon}}^{*}\right] dV_x \end{aligned} \tag{5.174}$$

or

$$\bar{\boldsymbol{\epsilon}}^{\boldsymbol{P}} = \boldsymbol{S}^{\boldsymbol{P}} : \bar{\boldsymbol{\epsilon}}^{*}, \tag{5.175}$$

where

$$\boldsymbol{S}^{\boldsymbol{P}} = \sum_{\boldsymbol{\xi}\neq 0} f_\Omega g(-\boldsymbol{\xi})\, g(\boldsymbol{\xi})\, F\boldsymbol{S}^{\boldsymbol{P}}(\boldsymbol{\xi}), \tag{5.176}$$

$$g(\boldsymbol{\xi}) = \frac{1}{V_\Omega}\int_\Omega e^{i\boldsymbol{x}\cdot\boldsymbol{\xi}} dV_x, \tag{5.177}$$

$$f_\Omega = \frac{V_\Omega}{V_U}. \tag{5.178}$$

This $\boldsymbol{S}^{\boldsymbol{P}}$ is a forth-order tensor equivalent to Eshelby's tensor, except that it is for

periodic composite. The $g(\boldsymbol{\xi})$ for the inclusion with cylindrical shape pointing in the x_1 direction is as follows [116].

$$g(\boldsymbol{\xi}) = \frac{2J_1(t)}{t}\left(\frac{\sin\frac{z}{2}}{\frac{z}{2}}\right), \tag{5.179}$$

where

$$t = 2\pi\alpha n_1, \tag{5.180}$$

$$z = \sqrt{\frac{4\pi f_\Omega}{\alpha}}\sqrt{n_2^2 + n_3^2}, \tag{5.181}$$

$$\alpha = \frac{L}{2a_1}, \tag{5.182}$$

$$f_\Omega = \frac{\pi r^2 L}{8a_1a_2a_3}, \tag{5.183}$$

J_1 is the order 1 Bessel function of first kind, r and L are radius and length of the cylindrical inclusion (see Figure 5.9). Substitute equation 5.175 into 5.173, we obtain:

$$\boldsymbol{C^\Omega} : \left(\boldsymbol{\epsilon^o} + \boldsymbol{S^P} : \bar{\boldsymbol{\epsilon}}^*\right) = \boldsymbol{C} : \left(\boldsymbol{\epsilon^o} + \left(\boldsymbol{S^P} - \boldsymbol{1^{(4S)}}\right) : \bar{\boldsymbol{\epsilon}}^*\right) \text{ in } \Omega. \tag{5.184}$$

Consider equation 5.148, average the consistency condition over the volume of unit

cell, we arrive at:

$$\boldsymbol{C^P} : \boldsymbol{\epsilon^o} = \boldsymbol{C} : (\boldsymbol{\epsilon^o} - f_\Omega \bar{\boldsymbol{\epsilon}}^*) \,. \tag{5.185}$$

Substituting from equation 5.184 for $\bar{\boldsymbol{\epsilon}}^*$ into equation 5.185, and in view of the fact that $\boldsymbol{\epsilon^o}$ is arbitrary, obtain an explicit expression for overall elasticity tensor as follows:

$$\boldsymbol{C^P} = \boldsymbol{C} - f_\Omega \boldsymbol{C} : \left(\left(\boldsymbol{C} - \boldsymbol{C^\Omega} \right)^{-1} : \boldsymbol{C} - \boldsymbol{S^P} \right)^{-1} . \tag{5.186}$$

Equation 5.186 with $g(\boldsymbol{\xi})$ in equation 5.179 is predicting the effective elasticity tensor of composite with periodically distributed and uniaxially oriented fibers. The fiber axis in the x_1 direction. However, this model can be modified to represent composites with in-plane oriented fibers and with randomly oriented fibers (see Section 5.4). Figure 5.10a shows composite with periodically distributed and uniaxially oriented cylindrical inclusions.

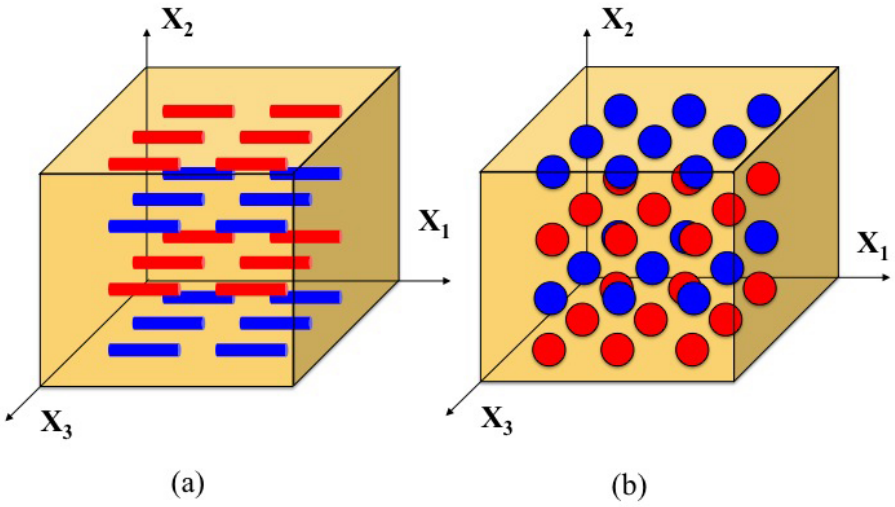

Figure 5.10: (a) Composite with periodically distributed and uniaxially oriented cylindrical inclusions (b) Composite with periodically distributed spherical inclusion

5.3.2 Composite with Periodically Distributed Spherical Inclusions (P-SI)

By replacing $g(\boldsymbol{\xi})$ in equation 5.179 with $g(\boldsymbol{\xi})$ for inclusion with spherical shape, equation 5.186 yield a model for composite with periodically distributed spherical inclusions. $g(\boldsymbol{\xi})$ for inclusion with spherical shape is [116]:

$$g(\boldsymbol{\xi}) = \frac{3}{(R\xi)^3}\left[(\sin(R\xi) - R\xi\cos(R\xi))\right], \tag{5.187}$$

where R is the radius of the spherical inclusion. Figure 5.10b shows composite with periodically distributed spherical inclusion.

5.3.3 Composite with Periodically Distributed Two-Phase Spherical Inclusions (P-2PSI)

The unbound elastic solid containing periodically distributed two-phase spherical inclusions is considered. Two-phase spherical inclusion refers to the spherical-shaped inclusion with spherical shell covering outside. By adjusting properties of each phase, the inclusion can also represent hollow sphere, single-phase solid sphere, and void. When each phase in the inclusion has the same properties, it is considered as uniform solid sphere. If the moduli of each phase are set to zero, the whole inclusion turns into void, while if only the moduli of the inner phase is set to zero, the inclusion turns into hollow sphere. A cubic unit cell containing two-phase spherical inclusion at the center of the cube is considered as the representative volume element of the composite with periodically distributed two-phase spherical inclusions (see Figure 5.11). The composite consists of matrix M, shell Ω_1, and core Ω_2. $\boldsymbol{C}$,

$\boldsymbol{C^1}$, and $\boldsymbol{C^2}$ are elasticity tensors of matrix, shell, and core, respectively (see Figure 5.12a). Similar to the previous section, homogenization technique is used to simplify the problem. The composite is replaced by the equivalent homogeneous solid with elasticity tensor $\boldsymbol{C}$ (the same as elasticity of the matrix phase). To compensate the mismatch between the elasticity tensor of the homogenized solid and the actual periodic composite, eigenstrains $\boldsymbol{\epsilon^{*1}(x)}$ and $\boldsymbol{\epsilon^{*2}(x)}$ are introduced in the shell and the core phases, respectively (see Figure 5.12b). The general idea of the model was already discussed in Section 5.3.1. However, when each unit cell contains three-phase elastic solids with different elastic moduli and geometries, some equations need to be modified.

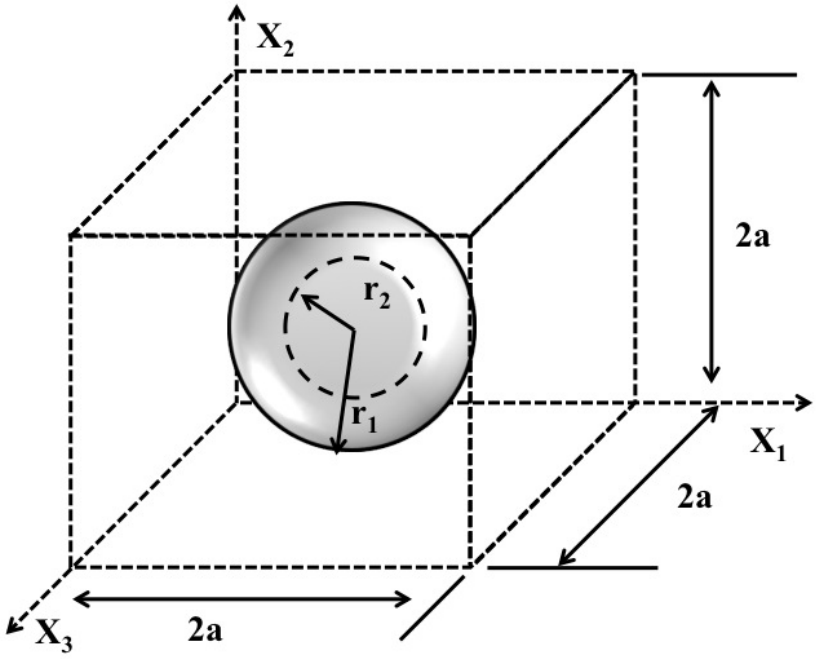

Figure 5.11: A unit cell of composite with periodically-distributed two-phase spherical inclusions

The elasticity tensor of the composite with periodically distributed two-phase

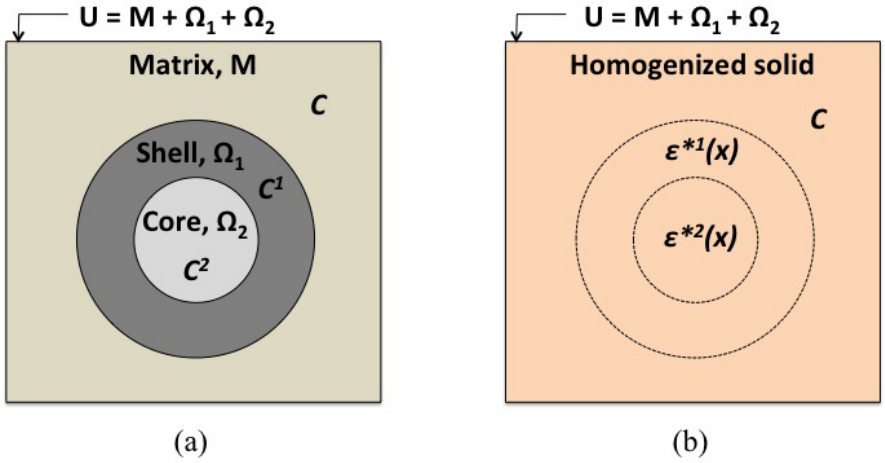

Figure 5.12: (a) Composite with periodically-distributed two-phase spherical inclusions (b) An equivalent homogeneous solid

spherical inclusions can be presented as follows:

$$\boldsymbol{C^P}\left(\boldsymbol{x}\right) = \boldsymbol{H}\left(\boldsymbol{x}; M\right)\boldsymbol{C} + \boldsymbol{H}\left(\boldsymbol{x}; \Omega_1\right)\boldsymbol{C^1} + \boldsymbol{H}\left(\boldsymbol{x}; \Omega_2\right)\boldsymbol{C^2}, \tag{5.188}$$

where $\boldsymbol{H}\left(\boldsymbol{x}; M\right)$, $\boldsymbol{H}\left(\boldsymbol{x}; \Omega_1\right)$, and $\boldsymbol{H}\left(\boldsymbol{x}; \Omega_2\right)$ are the Heaviside step functions associated with points in M, Ω_1 and Ω_2, respectively. The reference elasticity tensor of the equivalent homogeneous solid is the matrix elasticity $\boldsymbol{C}$. Then the eigenstrians are nonzero only in Ω_1 and Ω_2, i.e.,

$$\boldsymbol{\epsilon^{*1}}\left(\boldsymbol{x}\right) = \boldsymbol{H}\left(\boldsymbol{x}; \Omega_1\right)\boldsymbol{\epsilon^{*1}}\left(\boldsymbol{x}\right), \tag{5.189}$$

$$\boldsymbol{\epsilon^{*2}}\left(\boldsymbol{x}\right) = \boldsymbol{H}\left(\boldsymbol{x}; \Omega_2\right)\boldsymbol{\epsilon^{*2}}\left(\boldsymbol{x}\right). \tag{5.190}$$

The consistency condition, equation 5.171 is now changed to the following equations:

$$\boldsymbol{C^1} : \left(\langle \boldsymbol{\epsilon} \rangle + \boldsymbol{\epsilon^P}\left(\boldsymbol{x}\right)\right) = \boldsymbol{C} : \left(\langle \boldsymbol{\epsilon} \rangle + \boldsymbol{\epsilon^P}\left(\boldsymbol{x}\right) - \boldsymbol{\epsilon^{*1}}\left(\boldsymbol{x}\right)\right) \text{ For } \boldsymbol{x} \text{ in } \Omega_1, \tag{5.191}$$

$$\boldsymbol{C^2} : \left(\langle \boldsymbol{\epsilon} \rangle + \boldsymbol{\epsilon^P}\left(\boldsymbol{x}\right)\right) = \boldsymbol{C} : \left(\langle \boldsymbol{\epsilon} \rangle + \boldsymbol{\epsilon^P}\left(\boldsymbol{x}\right) - \boldsymbol{\epsilon^{*2}}\left(\boldsymbol{x}\right)\right) \text{ For } \boldsymbol{x} \text{ in } \Omega_2. \tag{5.192}$$

When a uniform overall strain, $\boldsymbol{\epsilon^o}$ is prescribed on the boundary of the composite. The volume average strain, $\langle \boldsymbol{\epsilon} \rangle$ is equal to $\boldsymbol{\epsilon^o}$. Equations 5.191 and 5.192 become:

$$\boldsymbol{C^1} : \left(\boldsymbol{\epsilon^o} + \boldsymbol{\epsilon^P}\left(\boldsymbol{x}\right)\right) = \boldsymbol{C} : \left(\boldsymbol{\epsilon^o} + \boldsymbol{\epsilon^P}\left(\boldsymbol{x}\right) - \boldsymbol{\epsilon^{*1}}\left(\boldsymbol{x}\right)\right) \text{ For } \boldsymbol{x} \text{ in } \Omega_1, \tag{5.193}$$

$$\boldsymbol{C^2} : \left(\boldsymbol{\epsilon^o} + \boldsymbol{\epsilon^P}\left(\boldsymbol{x}\right)\right) = \boldsymbol{C} : \left(\boldsymbol{\epsilon^o} + \boldsymbol{\epsilon^P}\left(\boldsymbol{x}\right) - \boldsymbol{\epsilon^{*2}}\left(\boldsymbol{x}\right)\right) \text{ For } \boldsymbol{x} \text{ in } \Omega_2. \tag{5.194}$$

Then we assume that the eigenstrain $\boldsymbol{\epsilon^{*1}}\left(\boldsymbol{x}\right)$ and $\boldsymbol{\epsilon^{*1}}\left(\boldsymbol{x}\right)$ are constants and equal to their averages $\bar{\boldsymbol{\epsilon}}^{\boldsymbol{*1}}$ and $\bar{\boldsymbol{\epsilon}}^{\boldsymbol{*2}}$, respectively. From equations 5.193 and 5.194, The average consistency conditions in Ω_1 and Ω_2 can be written as:

$$\boldsymbol{C^1} : \left(\boldsymbol{\epsilon^o} + \bar{\boldsymbol{\epsilon}}^{\boldsymbol{P1}}\right) = \boldsymbol{C} : \left(\boldsymbol{\epsilon^o} + \bar{\boldsymbol{\epsilon}}^{\boldsymbol{P1}} - \bar{\boldsymbol{\epsilon}}^{\boldsymbol{*1}}\right) \text{ in } \Omega_1, \tag{5.195}$$

$$\boldsymbol{C^2} : \left(\boldsymbol{\epsilon^o} + \bar{\boldsymbol{\epsilon}}^{\boldsymbol{P2}}\right) = \boldsymbol{C} : \left(\boldsymbol{\epsilon^o} + \bar{\boldsymbol{\epsilon}}^{\boldsymbol{P2}} - \bar{\boldsymbol{\epsilon}}^{\boldsymbol{*2}}\right) \text{ in } \Omega_2, \tag{5.196}$$

where $\bar{\boldsymbol{\epsilon}}^{\boldsymbol{P1}}$ and $\bar{\boldsymbol{\epsilon}}^{\boldsymbol{P1}}$ are the average isturbance (periodic) strains in Ω_1 and Ω_2, re-

spectively. From equations 5.158 and 5.174, $\bar{\boldsymbol{\epsilon}}^{\boldsymbol{P1}}$ and $\bar{\boldsymbol{\epsilon}}^{\boldsymbol{P2}}$ can be expressed as:

$$\bar{\boldsymbol{\epsilon}}^{\boldsymbol{P\alpha}} = \boldsymbol{S}^{\boldsymbol{P}}(\alpha,\beta) : \bar{\boldsymbol{\epsilon}}^{*\boldsymbol{\beta}} \ \ (\alpha,\beta = 1,2), \tag{5.197}$$

where

$$\boldsymbol{S}^{\boldsymbol{P}}(\alpha,\beta) = \sum_{\boldsymbol{\xi}\neq 0} f_\beta g_\beta(-\boldsymbol{\xi})\, g_\alpha(\boldsymbol{\xi})\, F\boldsymbol{S}^{\boldsymbol{P}}(\boldsymbol{\xi}), \tag{5.198}$$

$$g_\alpha(\boldsymbol{\xi}) = \frac{1}{V_{\Omega_\alpha}} \int_{\Omega_\alpha} e^{i\boldsymbol{x}\cdot\boldsymbol{\xi}} dV_x, \tag{5.199}$$

$$f_\alpha = \frac{V_{\Omega_\alpha}}{V_U}, \tag{5.200}$$

V_{Ω_1}, V_{Ω_2} and V_U are volumes of shell, core and entire unit cell, respectively. The $g_\alpha(\boldsymbol{\xi})$ for the composite with periodically distributed two-phase spherical inclusion model in Figure 5.11 can be calculated by:

$$\begin{aligned} g_1(\boldsymbol{\xi}) \;=\; & \frac{3}{\xi^3\left(r_1^3 - r_2^3\right)^3}\left(\sin(r_1\xi) - r_1\xi\cos(r_1\xi)\right) \\ & -\frac{3}{\xi^3\left(r_1^3 - r_2^3\right)^3}\left(\sin(r_2\xi) - r_2\xi\cos(r_2\xi)\right), \end{aligned} \tag{5.201}$$

$$g_2(\boldsymbol{\xi}) = \frac{3}{(r_2\xi)^3}\left[\left(\sin(r_2\xi) - r_2\xi\cos(r_2\xi)\right)\right]. \tag{5.202}$$

With equation 5.197, equations 5.195 and 5.196 can be rewritten as:

$$\begin{aligned}\boldsymbol{C^1} : \left(\boldsymbol{\epsilon^o} + \boldsymbol{S^P}\left(1,1\right) : \bar{\boldsymbol{\epsilon}}^{*\mathbf{1}} + \boldsymbol{S^P}\left(1,2\right) : \bar{\boldsymbol{\epsilon}}^{*\mathbf{2}}\right) \\ = \boldsymbol{C} : \left(\boldsymbol{\epsilon^o} + \left(\boldsymbol{S^P}\left(1,1\right) - \mathbf{1}^{(4S)}\right) : \bar{\boldsymbol{\epsilon}}^{*\mathbf{1}} + \boldsymbol{S^P}\left(1,2\right) : \bar{\boldsymbol{\epsilon}}^{*\mathbf{2}}\right), \end{aligned} \tag{5.203}$$

$$\begin{aligned}\boldsymbol{C^2} : \left(\boldsymbol{\epsilon^o} + \boldsymbol{S^P}\left(2,1\right) : \bar{\boldsymbol{\epsilon}}^{*\mathbf{1}} + \boldsymbol{S^P}\left(2,2\right) : \bar{\boldsymbol{\epsilon}}^{*\mathbf{2}}\right) \\ = \boldsymbol{C} : \left(\boldsymbol{\epsilon^o} + \boldsymbol{S^P}\left(2,1\right) : \bar{\boldsymbol{\epsilon}}^{*\mathbf{1}} + \left(\boldsymbol{S^P}\left(2,2\right) - \mathbf{1}^{(4S)}\right) : \bar{\boldsymbol{\epsilon}}^{*\mathbf{2}}\right). \end{aligned} \tag{5.204}$$

From equation 5.148, average the consistency condition over the volume of unit cell, we arrive at

$$\boldsymbol{C^P} : \boldsymbol{\epsilon^o} = \boldsymbol{C} : \left(\boldsymbol{\epsilon^o} - f_1\bar{\boldsymbol{\epsilon}}^{*\mathbf{1}} - f_2\bar{\boldsymbol{\epsilon}}^{*\mathbf{2}}\right), \tag{5.205}$$

where $\boldsymbol{C^P}$ is the overall elasticity tensor of composite with periodically distributed two-phase spherical inclusion. $\bar{\boldsymbol{\epsilon}}^{*\mathbf{1}}$ and $\bar{\boldsymbol{\epsilon}}^{*\mathbf{2}}$ can be obtained from the solution of the set of two linear tensorial equations 5.203 and 5.204.

P Model VS Experiment

The P model for composite with periodically distributed cylindrical inclusion was used to predict the overall mechanical properties of milled glassed reinforced polyurea composites at different volume fractions. The result and discussion are shown in Section 5.4. The P-SI and P-2PSI models were used to estimate the longitudinal and shear complex moduli of phenolic microballoon filled polyurea composites. The result of these two models will be compared with the result of CS model in Sec-

tion 5.1.1. The experimental data were obtained from ultrasonic longitudinal and shear measurements at 1 MHz, 20 °C, and ambient pressure. The longitudinal storage and loss moduli were calculated from the measured longitudinal wave speed and attenuation in the materials, while The shear storage and loss moduli were calculated from the measured shear wave speed and attenuation. The experiment detail and procedure can be found in Section 3.3. Discussion on the experimental result was already done in the Section 5.1.1. So in this section, we will just compare the results of periodic models to that of the CS model.

Table 5.3: Properties of phenolic microballoon obtained from CS model (volume fraction of void in the microballoon is 0.81)

Phenolic Microballoon	
L' (GPa)	0.6961
L'' (GPa)	0.0292
G' (GPa)	0.1904
G'' (GPa)	0.0092

With regard to calculation, two model based on periodic distribution of inclusion are used. One is composite with periodically distributed two phase spherical inclusions (P-2PSI) and the other one is composite with periodically distributed single phase spherical inclusions (P-SI). The inputs for P-2PSI model are the same as inputs for CS-model (see Section 5.1.1). The inputs for P-SI model are a little different. The properties of the matrix phase in P-SI are the same as CS-model. Since P-SI model also requires the mechanical properties of the whole phenolic microballoon (shell+core). Therefore the overall properties of the microballoon were not calculated using CS model with the properties of phenolic, and geometries of the microballoon shown in Tables 5.1 and 5.2, respectively. From the apparent density of phenolic microballoon (in Table 5.2) and density of phenolic polymer (in Table 5.1), the volume

fraction of the void in the phenolic microballon can be calculated and found to be 0.81. The CS model was used to estimated the overall properties of the microballoon because the model was developed based on spherical geometry which is identical to the shape of the microballoon. The overall longitudinal and shear complex moduli of the microballoon are the average between the results from CS-ϵ^o and CS-σ^o and are shown in Table 5.3. Properties of polyurea in Table 5.1 and properties of the microballoon in Table 5.3 were used as inputs for P-SI model.

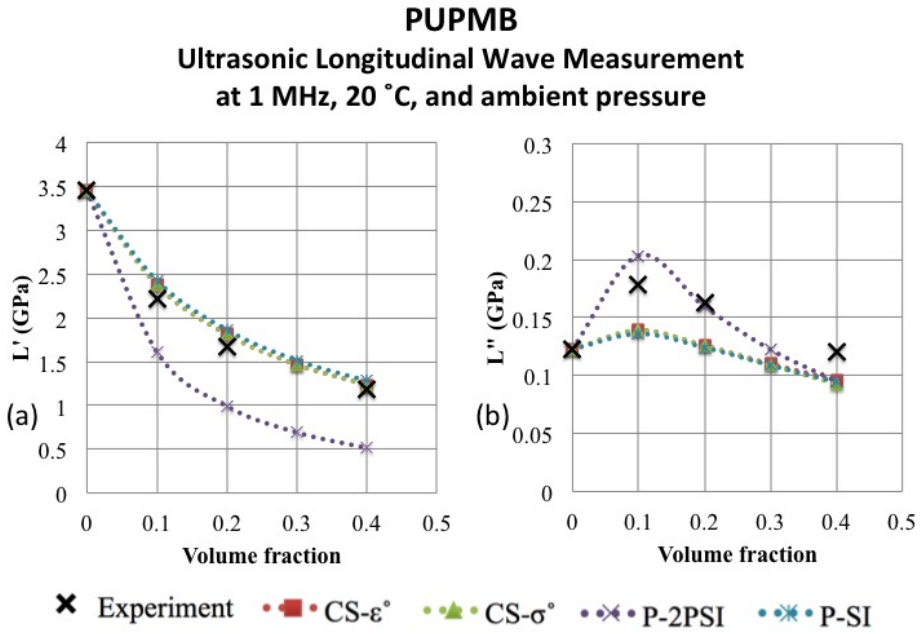

Figure 5.13: P and CS models: (a) Storage longitudinal modulus, L' of PUPMB versus volume fraction (b) Loss longitudinal modulus, L'' of PUPMB versus volume fraction

Figure 5.13a shows L' of PUPMB versus volume fraction. P-2PSI poorly underestimate L' while P-SI agrees with experimental result and CS model. The reason might be the P-2PSI directly and strongly take into account the effect of the periodic distribution of the void phase, leading to the drop in the longitudinal storage

modulus. Figure 5.13b shows L'' of PUPMB versus volume fraction. Interestingly, the result from P-2PSI is in very good agreement with experimental result, while P-SI underestimates experimental result but agrees with CS model. As discussed previously in section 5.1.1, we do not have accurate input properties of the phenolic polymer, the better prediction of P-2PSI for L'' might be an artifact and cannot be concluded at the moment.

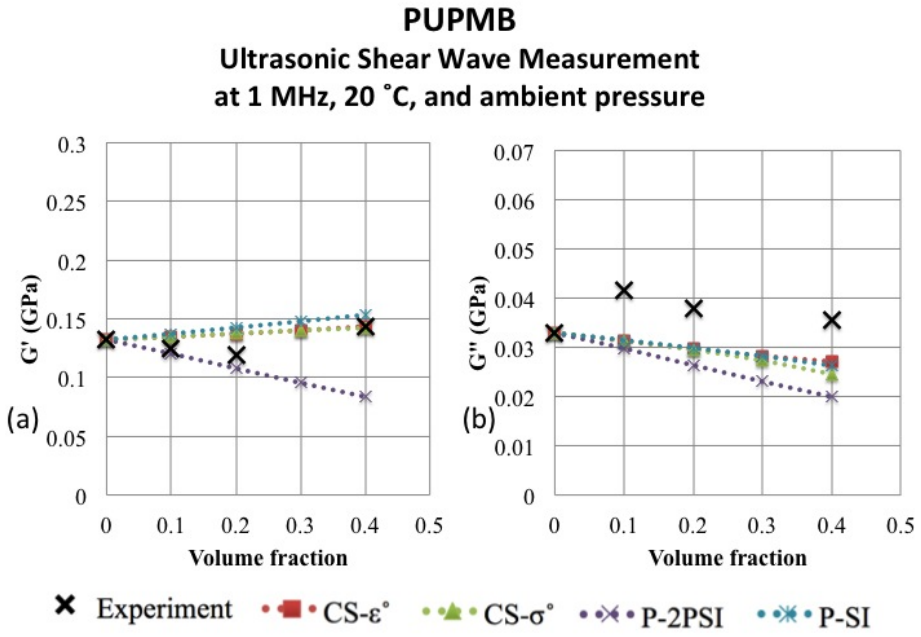

Figure 5.14: P and CS models: (a) Storage shear modulus, G' of PUPMB versus volume fraction (b) Loss shear modulus, G'' of PUPMB versus volume fraction

Figure 5.14a shows G' of PUPMB versus volume fraction. P-2PSI poorly underestimate G' at 0.4 volume fraction of the microballoon, while P-SI agrees with experimental result and the CS model. For G'' in Figure 5.13b, P-2PSI is worst in estimation, while the result from P-SI agrees with CS-ϵ^o model but underestimate the experimental result.

It seems that the greater drop in moduli predicted by P-2PSI suggests that the model did account for the effect of the presence of the void in the microballoon, while P-SI model take into account the interaction between the microballoons but in the softer manner since the mismatch properties between the shell and the core of the microballoon was homogenized and averaged using CS model. It is difficult to conclude which model is the best since we do not have accurate input for the phenolic phase. To find the best model, we might need to replace the viscoelastic phenolic microballoon with other elastic particles with known mechanical properties and geometries. This will be future work.

5.4 Dynamic Properties of Polyurea-Milled Glass Composites Part II: Micromechanical Modeling

In Part I, the results of experimental evaluation of the mechanical properties of pure polyurea (PU) and polyurea with milled glass composites (PU-MG) in low (1-20 Hz) and high (0.5-1.5 MHz) frequency ranges [73] have been reported, focusing on the dependence of these properties on frequency, temperature, and the milled glass volume fraction. Here, we report the results of the corresponding micromechanical modeling. The models are developed, based on three different approximations: (1) dilute random, (2) non-dilute random, and (3) non-dilute periodic distributions of inclusions. Different orientation distributions of fibers, e.g. uniaxial parallel, in-plane random, and 3D random are considered and their results are compared with experimentally measured data presented in [73]. Moreover, the computational results are used to construct master curves of dynamic Young's storage and loss moduli and

compare these with those constructed from experimental data. Three dimensional random and in-plane random calculation results are compared with the dynamic longitudinal and shear moduli of PU-MG composites obtained from ultrasonic wave measurements. These comparisons demonstrated that, as expected, the orientation distribution of the short fibers was affected by the thickness of the composite sample, and this effect was manifested in overall elasticity tensor of the composite.

5.4.1 Introduction

Polyurea with milled glass composites (PU-MG) are introduced and their mechanical behavior was experimentally characterized and reported in an accompanying paper [73]. In this paper, micromechanical models that describe their behavior with varying geometrical and mathematical complexity are presented.

One of the first models for short-fiber composites is the shear lag model developed by Cox [125]. Later, Eshelby solved the elasticity problem of an ellipsoidal inclusion embedded in infinitely large matrix for the elastic stress field in and around the inclusion [114, 115]. In these celebrated works, he showed that within an ellipsoidal inclusion the strain field is uniform, and is related to a uniform transformation strain through a tensor now commonly referred to as Eshelby's tensor. The tensor depends only on the inclusion aspect ratios and the matrix elastic constants [117]. By letting the inclusion be a prolate ellipsoid, one can use Eshelby's results to find the stiffness of a composite with cylindrical fibers at dilute concentrations [116, 126]. For non-dilute discontinuous fiber composite models, the interaction between fibers is taken into account either directly or indirectly. Mori and Tanaka proposed that the average strain in the fiber should be proportional to the average strain in the matrix.

This idea was used to treat non-dilute composite materials [121]. Taya and Mura applied Eshelby's and Mori-Tanaka's ideas to create models to predict the longitudinal modulus of a short-fiber composite containing fiber-end cracks in resin [127]. Another approach to account for finite fiber volume fraction is the self-consistent method. In the self-consistent method, one has to numerically find the properties of a composite in which a single particle is embedded in an infinite matrix that has the, yet unknown, average properties of the composite. The solution of the self-consistent approach for some composites may require using iterative scheme [128, 129]. Nemat-Nasser and coworkers [116, 123, 124] developed a method based on the periodic distribution of inclusions, in which the inclusion can be void or solid and can have various shapes. At high volume fraction, this method accounts for the interaction between particles in a more direct manner than either Mori-Tanaka or self-consistent methods. However, this method might not appropriately represent the microstructure of a composite material that has inclusions randomly distributed in the matrix. Despite this concern, the assumption of periodicity has been proved very powerful in predicting mechanical properties of composites with high inclusion-interaction effects and random distribution of inclusions [116,123,124]. Another method that accounts for the interaction between inclusion and their surrounding matrix material in a direct manner is the double inclusion model (or three-phase model) developed by Hori and Nemat-Nasser [130]. It is the generalized version of the Mori-Tanaka method. The model uses averaging scheme and produces the overall moduli of two-phase composites with greater flexibility and effectiveness than the self-consistent and the Mori-Tanaka method. The average stress and strain in a typical inclusion is estimated by embedding the typical inclusion in a finite ellipsoidal region of matrix elasticity and then this double inclu-

sion is embedded in an infinite uniform solid with the yet-unknown overall elasticity of the composite [116, 130]. By replacing the yet-unknown overall elasticity with the elasticity of the matrix, the model gives the Mori-Tanaka or two-phase model, while setting it as the unknown composite value gives the self-consistent estimate in the case both inclusions are coaxial. In general, other estimates may be achieved by any choice of combination of inclusion, matrix, and composite material properties. For other interesting methods, Tucker III and Liang have provided a thorough literature review [118].

In this study, micromechanical models were developed based on 3 different methods: (1) dilute random, (2) non-dilute random, and (3) non-dilute periodic distributions of inclusions. The first method implements Eshelby's works [114–117]. The second method uses Mori-Tanaka averaging method [116, 118, 121, 127]. The third method follows Nemat-Nasser and coworkers' works [116, 123, 124]. In contrast with method 1, methods 2 and 3 take into account the effect of particles interaction in two different unit cell structures. Each method has its own advantage. The dilute random distribution is the least complex approach and takes less computational time, but it is less accurate for high volume fractions of inclusions. The non-dilute random distribution of inclusions improves the accuracy of method 1, while it takes the same computational time. The non-dilute periodic distribution of inclusions requires more computational time due to the calculation of Fourier series representation of field variables [116, 123, 124], but it provides the most accurate results among the three-presented methods. In each method, three models with different fiber orientations; uniaxial, in-plane random, and 3D random orientations were addressed using proper averaging techniques. Originally, these models were created for estimating mechan-

ical properties of elastic composites; however Hashin showed that by replacement of the real elastic moduli by their complex counterparts (including storage and loss components), they can be directly utilized for viscoelastic composites [111].

5.4.2 Theory

Consider the applied uniform strain ϵ^o (linear displacement) or uniform stress σ^o on boundary of a composite. The average strain $\bar{\epsilon}$ or stress $\bar{\sigma}$ over total volume of the composite will be:

$$\bar{\boldsymbol{\epsilon}} = \boldsymbol{\epsilon^o}, \tag{5.206}$$

$$\bar{\boldsymbol{\sigma}} = \boldsymbol{\sigma^o}, \tag{5.207}$$

respectively [116]. The overall constitutive tensors for the composite can be written as:

$$\bar{\boldsymbol{C}} : \boldsymbol{\epsilon^o} = \boldsymbol{C^m} : \boldsymbol{\epsilon^o} + f_\Omega \left(\boldsymbol{C^\Omega} - \boldsymbol{C^m} \right) : \bar{\boldsymbol{\epsilon}}^{\boldsymbol{\Omega}}, \tag{5.208}$$

$$\bar{\boldsymbol{D}} : \boldsymbol{\sigma^o} = \boldsymbol{D^m} : \boldsymbol{\sigma^o} + f_\Omega \left(\boldsymbol{D^\Omega} - \boldsymbol{D^m} \right) : \bar{\boldsymbol{\sigma}}^{\boldsymbol{\Omega}}, \tag{5.209}$$

based on the calculated average stress and strain tensors, respectively. f_Ω is the volume fraction of the fiber, $\bar{\boldsymbol{C}}$, $\boldsymbol{C^\Omega}$, and $\boldsymbol{C^m}$ are the (to be determined) overall elasticity tensor of the composite, the elasticity tensor of the fiber, and the elasticity tensor of the matrix, respectively, $\bar{\boldsymbol{D}}$, $\boldsymbol{D^\Omega}$, and $\boldsymbol{D^m}$ are the (to be determined) overall compliance tensor of the composite, the compliance tensor of the fiber and the compliance tensor of the matrix, respectively, $\bar{\boldsymbol{\epsilon}}^{\boldsymbol{\Omega}}$ and $\bar{\boldsymbol{\sigma}}^{\boldsymbol{\Omega}}$ are the average strain

and stress over the fiber volume. $\boldsymbol{\epsilon^o}$ and $\boldsymbol{\sigma^o}$ are arbitrary. For a fundamental proof, see [116]. If the relation between $\bar{\boldsymbol{\epsilon}}^{\boldsymbol{\Omega}}$ ($\bar{\boldsymbol{\sigma}}^{\boldsymbol{\Omega}}$) and $\boldsymbol{\epsilon^o}$ ($\boldsymbol{\sigma^o}$) is known, one could solve for $\bar{\boldsymbol{C}}$ ($\bar{\boldsymbol{D}}$). $\bar{\boldsymbol{\epsilon}}^{\boldsymbol{\Omega}}$ and $\bar{\boldsymbol{\sigma}}^{\boldsymbol{\Omega}}$ may be related to $\boldsymbol{\epsilon^o}$ and $\boldsymbol{\sigma^o}$ as:

$$\bar{\boldsymbol{\epsilon}}^{\boldsymbol{\Omega}} = \boldsymbol{P}^{\boldsymbol{\Omega}} : \boldsymbol{\epsilon^o}, \tag{5.210}$$

$$\bar{\boldsymbol{\sigma}}^{\boldsymbol{\Omega}} = \boldsymbol{Q}^{\boldsymbol{\Omega}} : \boldsymbol{\sigma^o}, \tag{5.211}$$

where $\boldsymbol{P}^{\boldsymbol{\Omega}}$ and $\boldsymbol{Q}^{\boldsymbol{\Omega}}$ are introduced as tensors to transform $\boldsymbol{\epsilon^o}$ and $\boldsymbol{\sigma^o}$ to $\bar{\boldsymbol{\epsilon}}^{\boldsymbol{\Omega}}$ and $\bar{\boldsymbol{\sigma}}^{\boldsymbol{\Omega}}$, respectively. Note that in [118, 120], these tensors are denoted by letters A and B. Substitute equations 5 and 6 into 3 and 4,to write $\bar{\boldsymbol{C}}$ and $\bar{\boldsymbol{D}}$ as:

$$\bar{\boldsymbol{C}} = \boldsymbol{C}^{\boldsymbol{m}} + f_{\Omega}\left(\boldsymbol{C}^{\boldsymbol{\Omega}} - \boldsymbol{C}^{\boldsymbol{m}}\right) : \boldsymbol{P}^{\boldsymbol{\Omega}}, \tag{5.212}$$

$$\bar{\boldsymbol{D}} = \boldsymbol{D}^{\boldsymbol{m}} + f_{\Omega}\left(\boldsymbol{D}^{\boldsymbol{\Omega}} - \boldsymbol{D}^{\boldsymbol{m}}\right) : \boldsymbol{Q}^{\boldsymbol{\Omega}}. \tag{5.213}$$

The three methods listed earlier provide different approximations to tensors $\boldsymbol{P}^{\boldsymbol{\Omega}}$ and $\boldsymbol{Q}^{\boldsymbol{\Omega}}$. Since micromechanical models for composites with short fibers based on dilute random, non-dilute random, and non-dilute periodic distributions of inclusions are well established in literatures [114–118, 123, 124], only the important theoretical aspects and the necessary modifications of the models will be discussed here.

Dilute Random Distributions of Inclusions (DD Model)

This model considers an infinitely extended matrix with uniform-sized prolate spheroid inclusions in the matrix. Due to the low volume fraction (dilute model) the inclusions do not interact with the adjacent particles. Therefore the far-field strain (stress) experienced by any inclusion equals to the globally applied strain (stress). The average strain (stress) in the inclusion is proportional to the applied strain (stress) [116]. The shape of the prolate spheroid differs from the actual shape of the milled glass fiber. However, the prolate spheroid has a relatively long semi-major axis compared to the two equal semi-minor axes ($l/r >> 1$) and could be considered a reasonable representation of the milled glass fibers. Geometry and dimensions of the prolate spheroid are shown in Figure 5.17a and Table 5.4.

Figure 5.15a represents the structure of a uniaxial composite. The superscripted DD will be used to indicate all models developed from the method based on dilute random distribution of inclusions. Tensors $\boldsymbol{P}^{\boldsymbol{\Omega-DD}}$ and $\boldsymbol{Q}^{\boldsymbol{\Omega-DD}}$ for the composite can be written as [116]:

$$\boldsymbol{P}^{\boldsymbol{\Omega-DD}} = \left(\boldsymbol{C}^{\boldsymbol{m}} - \boldsymbol{C}^{\boldsymbol{\Omega}}\right)^{-1} : \boldsymbol{C}^{\boldsymbol{m}} : \left(\left(\boldsymbol{C}^{\boldsymbol{m}} - \boldsymbol{C}^{\boldsymbol{\Omega}}\right)^{-1} : \boldsymbol{C}^{\boldsymbol{m}} - \boldsymbol{S}^{\boldsymbol{\Omega}}\right)^{-1}, \tag{5.214}$$

$$\begin{aligned}\boldsymbol{Q}^{\boldsymbol{\Omega-DD}} = &\left(\boldsymbol{D}^{\boldsymbol{m}} - \boldsymbol{D}^{\boldsymbol{\Omega}}\right)^{-1} : \boldsymbol{D}^{\boldsymbol{m}} : \Big(\left(\boldsymbol{D}^{\boldsymbol{m}} - \boldsymbol{D}^{\boldsymbol{\Omega}}\right)^{-1} : \boldsymbol{D}^{\boldsymbol{m}} \\ &- \left(\boldsymbol{1}^{\boldsymbol{4S}} - \boldsymbol{D}^{\boldsymbol{m}-1} : \boldsymbol{S}^{\boldsymbol{\Omega}} : \boldsymbol{D}^{\boldsymbol{m}}\right)\Big)^{-1},\end{aligned} \tag{5.215}$$

where $\boldsymbol{1}^{(\boldsymbol{4s})}$ is forth-order symmetric identity tensor (see [116], section 15.5), $\boldsymbol{S}^{\boldsymbol{\Omega}}$ is the Eshelby's tensor (see [116], section 7.3), $\boldsymbol{C}^{\boldsymbol{m}}$ and $\boldsymbol{C}^{\boldsymbol{\Omega}}$ can be expressed in the index notation forms as shown in [116] section 15.6 and [124], $\boldsymbol{D}^{\boldsymbol{m}}$ and $\boldsymbol{D}^{\boldsymbol{\Omega}}$ can be found

by taking inverse of $\boldsymbol{C^m}$ and $\boldsymbol{C^\Omega}$, respectively. Note that since Eshelby's tensor is constant over the volume of an ellipsoid, the point-wise and average expressions are identical. Substitute equations 9 and 10 into 7 and 8, to obtain the overall elasticity and compliance tensor $\boldsymbol{\bar{C}^{DD}}$ and $\boldsymbol{\bar{D}^{DD}}$ for composite with dilute randomly distributed and uniaxially oriented prolate spheroid inclusions (see [116], section 7.4):

$$\boldsymbol{\bar{C}^{DD}} = \boldsymbol{C^m} - f_\Omega \boldsymbol{C^m} : \Big(\big(\boldsymbol{C^m} - \boldsymbol{C^\Omega} \big)^{-1} : \boldsymbol{C^m} - \boldsymbol{S^\Omega} \Big)^{-1}, \tag{5.216}$$

$$\begin{aligned} \boldsymbol{\bar{D}^{DD}} = \boldsymbol{D^m} - f_\Omega \boldsymbol{D^m} : \Big(& \big(\boldsymbol{D^m} - \boldsymbol{D^\Omega} \big)^{-1} : \boldsymbol{D^m} \\ & - \big(\boldsymbol{1^{4S}} - \boldsymbol{D^{m-1}} : \boldsymbol{S^\Omega} : \boldsymbol{D^m} \big) \Big)^{-1}. \end{aligned} \tag{5.217}$$

Note that based on equations 5.216 and 5.217, $\boldsymbol{\bar{C}^{DD}}$ and $\boldsymbol{\bar{D}^{DD}}$ are not exact inverse of each other [116]. The error involved here is only acceptable up to around 10% volume fraction of inclusion. So, $\boldsymbol{\bar{C}^{DD}}$ and $\boldsymbol{\bar{D}^{DD}}$ can only be used at low volume fractions. In this work, $\boldsymbol{\bar{C}^{DD}}$ Dwill be used for computation. Due to the anisotropy of the prolate spheroid inclusion, $\boldsymbol{\bar{C}^{DD}}$ is transversely isotropic, while $\boldsymbol{C^m}$ and $\boldsymbol{C^\Omega}$ are isotropic.

While equation 5.216 gives the overall elasticity tensor for a uniaxial orientation distribution, it can also be used to give the overall elasticity tensor for a composite with dilute randomly distributed and in-plane randomly oriented prolate spheroid inclusions (see Figure 5.15b) through integration. The modification can be made by calculating various elasticity tensors at all in-plane fiber-angle orientations, θ_β, using a second order rotational tensor $\boldsymbol{Q^\beta}$, which is defined in [116] as $\boldsymbol{Q^\alpha}$ in Section 6.4 for 2D problem, with $Q^\beta_{33} = 1$ and $Q^\beta_{13} = Q^\beta_{31} = Q^\beta_{23} = Q^\beta_{32} = 0$, and averaging the

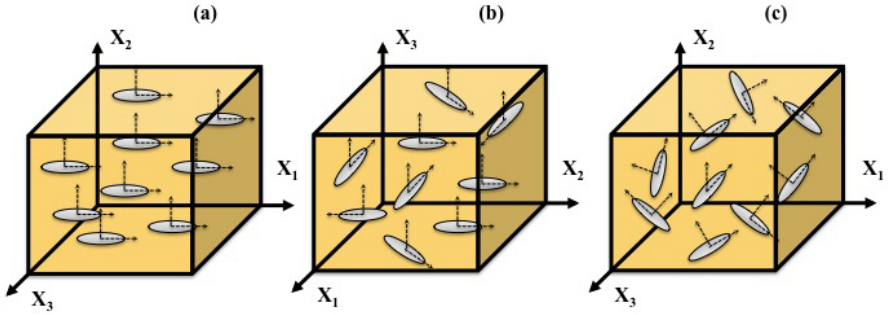

Figure 5.15: Models based on dilute and non-dilute random distributions of inclusions: (a) Uniaxially-oriented distribution, where semi-major axis is always parallel to X_1 axis (b) In-plane randomly oriented distribution, where semi-major axis always lies on X_1X_2-plane (c) 3D randomly oriented distribution

elasticity tensors of all in-plane orientation angles. The overall elasticity tensor for this composite, $\bar{\boldsymbol{C}}^{\boldsymbol{DD-in-plane}}$, can be expressed as:

$$\bar{\boldsymbol{C}}^{\boldsymbol{DD-in-plane}} = \left\{ \frac{1}{2\pi} \int_0^{2\pi} \bar{C}^{DD}_{pqrs} Q^{\beta}_{ip} Q^{\beta}_{jq} Q^{\beta}_{kr} Q^{\beta}_{ls} d\theta_{\beta} \right\} \boldsymbol{e_i} \otimes \boldsymbol{e_j} \otimes \boldsymbol{e_k} \otimes \boldsymbol{e_l}, \qquad (5.218)$$

where Q^{β}_{ip}, Q^{β}_{jq}, Q^{β}_{kr}, and Q^{β}_{ls} are the ip, jq, kr, and ls components of $\boldsymbol{Q^{\beta}}$ (i, j, k, l, p, q, r, $s = 1, 2, 3$), $\bar{C}^{DD}_{pqrs}$ is the $pqrs$ component of $\bar{\boldsymbol{C}}^{\boldsymbol{DD}}$ in equation 5.216, $\boldsymbol{e_i}$, $\boldsymbol{e_j}$, $\boldsymbol{e_k}$, and $\boldsymbol{e_l}$ are unit normal vectors. Similarly, equation 5.216 can be used for 3D randomly oriented distributions (see Figure 5.15c). We use $\boldsymbol{Q^{\gamma}}$, which is defined in [116] as $\boldsymbol{Q^{\alpha}}$ in Section 6.6 with index permutation $1 \rightarrow 2 \rightarrow 3 \rightarrow 1$ due to the different orientation between the crack (in [116]) and the fiber (for our case), and average the elasticity tensors of all orientations in three-dimensional space. The overall elasticity tensor for this composite, $\bar{\boldsymbol{C}}^{\boldsymbol{DD-3D}}$, can be written as:

$$\bar{\boldsymbol{C}}^{\boldsymbol{DD-3D}} = \left\{ \frac{1}{4\pi} \int_0^{2\pi} \int_0^{\pi} \bar{C}^{DD}_{pqrs} Q^{\gamma}_{ip} Q^{\gamma}_{jq} Q^{\gamma}_{kr} Q^{\gamma}_{ls} \sin\varphi_{\gamma} d\varphi_{\gamma} d\theta_{\gamma} \right\} \boldsymbol{e_i} \otimes \boldsymbol{e_j} \otimes \boldsymbol{e_k} \otimes \boldsymbol{e_l}, \quad (5.219)$$

where Q^{γ}_{ip}, Q^{γ}_{jq}, Q^{γ}_{kr}, and Q^{γ}_{ls} are the ip, jq, kr, and ls components of $\boldsymbol{Q}^{\gamma}$.

Non-Dilute Random Distributions of Inclusions (MT Model)

In Mori-Tanaka approach and contrary to the dilute models, the inclusions may interact with each other through modifications in far-field strain to average strain in the matrix [116, 118, 121]. The superscripted MT will be used to indicate all models developed from the method based on non-dilute random distribution of inclusions. Tensors $\boldsymbol{P^{\Omega-MT}}$ for the composite can be written as (see [118], $\boldsymbol{A^{MT}}$ and $\boldsymbol{A^{Eshelby}}$ are equivalent to our $\boldsymbol{P^{\Omega-MT}}$ and $\boldsymbol{P^{\Omega-DD}}$, respectively. Our equation 5.214 yields the same result as equation 35 in [118]):

$$\boldsymbol{P^{\Omega-MT}} = \boldsymbol{P^{\Omega-DD}} : \left[(1-f_{\Omega})\,\boldsymbol{1^{4S}} + f_{\Omega}\boldsymbol{P^{\Omega-DD}}\right]^{-1}, \tag{5.220}$$

Substitute equation 5.220 into equation 5.212, to obtain the overall elasticity tensor $\boldsymbol{\bar{C}^{MT}}$ of the composite with non-dilute randomly distributed and uniaxially oriented inclusions:

$$\begin{aligned} \boldsymbol{\bar{C}^{MT}} &= \boldsymbol{C^{m}} - f_{\Omega}\left(\boldsymbol{C^{\Omega}} - \boldsymbol{C^{m}}\right) : \boldsymbol{P^{\Omega-DD}} : \\ &\quad \left[(1-f_{\Omega})\,\boldsymbol{1^{4S}} + f_{\Omega}\boldsymbol{P^{\Omega-DD}}\right]^{-1}. \end{aligned} \tag{5.221}$$

The same averaging approach as the one used in Section 5.4.2 may be used to estimate the properties for the other configurations shown in Figures 5.15b and 5.15c.

Periodic Distributions of Inclusions (P Model)

The composite models based on this method may be regarded as a collection of infinite unit cells of identical dimensions, each containing one inclusion. The inclusion could have any geometric shape, e.g. cubic, sphere, cylinder, and etc [116,123]. In this case for PU-MG composite, the inclusion has cylindrical shape, which has the same dimensions as those of the milled glass fiber. The orientation of the inclusion can be chosen arbitrary. The overall elasticity (or compliance) of the composite with the chosen orientation of the inclusion can then be calculated using the overall elasticity (or compliance) of the composite with the uniaxially aligned inclusions and a rotation tensor that corresponds to the orientation of the inclusion [116]. Figure 5.17b shows a unit cell or representative volume element (RVE) of the composite with uniaxially aligned short fiber.

Figure 5.16a represents the structure of a uniaxially oriented periodic composite. The superscripted P will be used to indicate all models developed based on the periodic distribution of inclusions. The tensors $\boldsymbol{P^{\Omega-P}}$ can be written as (for complete detail, please see [116], Chapter 12):

$$\boldsymbol{P^{\Omega-P}} = \left(\boldsymbol{C^m} - \boldsymbol{C^\Omega}\right)^{-1} : \boldsymbol{C^m} : \left(\left(\boldsymbol{C^m} - \boldsymbol{C^\Omega}\right)^{-1} : \boldsymbol{C^m} - \boldsymbol{S^P}\right)^{-1}, \qquad (5.222)$$

where $\boldsymbol{S^P}$ is a fourth order tensor equivalent to Eshelby's tensor [116]. Substituting equation 5.222 into 5.212, the overall elasticity tensor $\boldsymbol{\bar{C}^P}$ of the composite with periodically distributed and uniaxially oriented cylindrical inclusions is obtained [116]:

$$\boldsymbol{\bar{C}^P} = \boldsymbol{C^m} - f_\Omega \boldsymbol{C^m} : \left(\left(\boldsymbol{C^m} - \boldsymbol{C^\Omega}\right)^{-1} : \boldsymbol{C^m} - \boldsymbol{S^P}\right)^{-1}. \qquad (5.223)$$

Due to the periodicity and geometry of the unit cell, $\bar{\boldsymbol{C}}^{\boldsymbol{P}}$ has cubic symmetry, while $\boldsymbol{C}^{\boldsymbol{m}}$ and $\boldsymbol{C}^{\boldsymbol{\Omega}}$ are isotropic. Note that in this case the overall compliance tensor $\bar{\boldsymbol{D}}^{\boldsymbol{P}}$ and $\bar{\boldsymbol{C}}^{\boldsymbol{P}}$ are exactly each other's inverse [116].

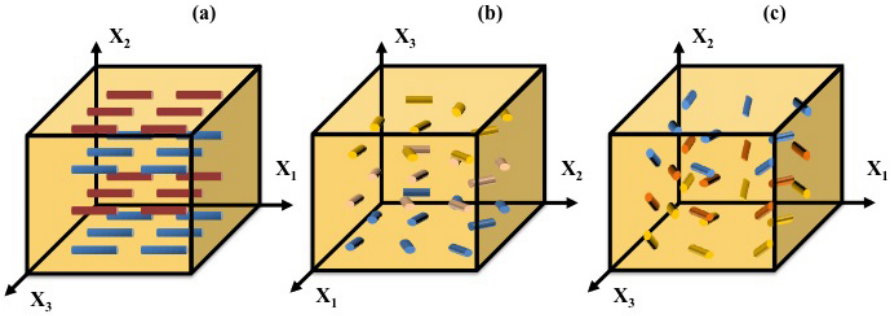

Figure 5.16: Models based on periodic distribution of inclusions: (a) Uniaxially oriented distribution, where fiber axis is always parallel to X_1 axis (b) In plane oriented distribution, where fiber axis always lies on X_1X_2-plane (c) 3D randomly oriented distribution

Similar integration in equation 5.218 can be used to calculate $\bar{\boldsymbol{C}}^{\boldsymbol{P-in-plane}}$, shown in Figure 5.16b. However, for the configuration in Figure 5.16c, an intermediate step is required. Due to that the $\bar{\boldsymbol{C}}^{\boldsymbol{P}}$ in equation 5.223 has cubic symmetry, we have to modify $\bar{\boldsymbol{C}}^{\boldsymbol{P}}$ to be transversely isotropic as is the case of $\bar{\boldsymbol{C}}^{\boldsymbol{DD}}$ and $\bar{\boldsymbol{C}}^{\boldsymbol{MT}}$ in equations 5.216 and 5.221. The modification can be done, using a second order rotation tensor $\boldsymbol{Q}^{\boldsymbol{\delta}}$ defined similar to $\boldsymbol{Q}^{\boldsymbol{\beta}}$ presented above with index permutation $1 \rightarrow 2 \rightarrow 3 \rightarrow 1$. The resulting tensor $\bar{\boldsymbol{C}}^{\boldsymbol{P-tr}}$ includes the effect of interaction of the inclusions in a periodic matrix, but, keeping the orientation of semi-major axis of the inclusions fixed, it averages over all other possible lattice orientations:

$$\bar{\boldsymbol{C}}^{\boldsymbol{P-tr}} = \left\{ \frac{1}{2\pi} \int_0^{2\pi} \bar{C}^P_{pqrs} Q^{\delta}_{ip} Q^{\delta}_{jq} Q^{\delta}_{kr} Q^{\delta}_{ls} d\theta_{\delta} \right\} \boldsymbol{e_i} \otimes \boldsymbol{e_j} \otimes \boldsymbol{e_k} \otimes \boldsymbol{e_l}, \tag{5.224}$$

where Q^{δ}_{ip}, Q^{δ}_{jq}, Q^{δ}_{kr}, and Q^{δ}_{ls} are the ip, jq, kr, and ls components of $\boldsymbol{Q}^{\boldsymbol{\delta}}$. Note

that, both $\bar{\boldsymbol{C}}^{\boldsymbol{P-tr}}$ and $\bar{\boldsymbol{C}}^{\boldsymbol{P-in-plane}}$ are transversely isotropic. However, the difference is that $\bar{\boldsymbol{C}}^{\boldsymbol{P-in-plane}}$ has axial symmetry around X_3 axis of the model shown in Figure 5.16b; while $\bar{\boldsymbol{C}}^{\boldsymbol{P-tr}}$ has axial symmetry around X_1 axis of the model shown in Figure 5.16a. Then the overall elasticity tensor of the composite shown in Figure 5.16c, $\bar{\boldsymbol{C}}^{\boldsymbol{P-3D}}$, can be calculated as:

$$\begin{aligned} \bar{\boldsymbol{C}}^{\boldsymbol{P-3D}} &= \left\{ \frac{1}{4\pi} \int_0^{2\pi} \int_0^{\pi} \bar{C}^{P-tr}_{pqrs} Q^{\gamma}_{ip} Q^{\gamma}_{jq} Q^{\gamma}_{kr} Q^{\gamma}_{ls} \sin\varphi_{\gamma} d\varphi_{\gamma} d\theta_{\gamma} \right\} \\ & \quad \boldsymbol{e_i} \otimes \boldsymbol{e_j} \otimes \boldsymbol{e_k} \otimes \boldsymbol{e_l}, \end{aligned} \tag{5.225}$$

5.4.3 Computation Parameters

All models based on dilute random, non-dilute random, and non-dilute periodic distributions of inclusions require similar material and geometric input parameters, i.e. geometry of the inclusion, volume fraction, and two mechanical properties of each phase in the composites. However, the periodic distribution model also requires the dimensions of unit cell.

Geometries of The Inclusions

To use the constant Eshelby's tensor, prolate spheroid shape is used to model the milled glass fiber in all random distribution models (see Figure 5.17a). The volume of the prolate spheroid is taken equal to the average volume of the milled glass fibers. The semi-major axis a_1 is equated to half of the average length L of the milled glass fibers, the semi-minor axes $a_2 = a_3$ are then calculated based on the volume equation. For all models based on periodic approximation, the actual cylindrical shape is used, with the same dimensions as those of the average milled glass fiber (see Figure 5.17b).

Table 5.4 shows geometries of inclusions in micromechanical models.

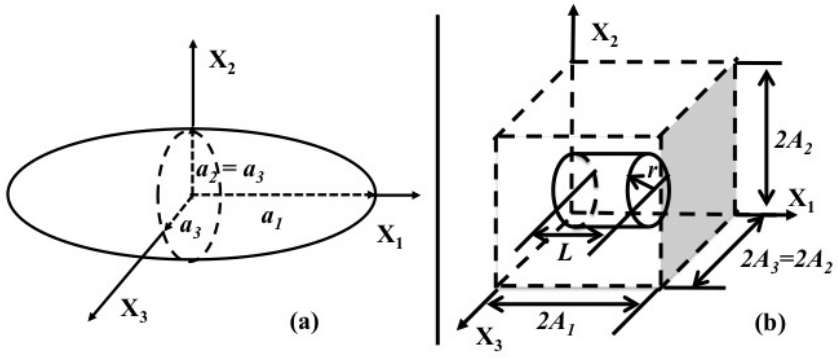

Figure 5.17: (a) Geometry of a prolate spheroid (b) Geometry of a periodic unit cell and short cylindrical fiber

Table 5.4: Geometries of inclusions used in the micromechanical models

Inclusion	L or $2a_1$ (µm)	r or $a_2 = a_3$ (µm)	Volume (µm^3)
Prolate Spheroid	200	9.8	40212
Cylinder	200	8	40212

Dimensions of The Periodic Unit Cell

The exact dimensions of the unit cell in the periodic model have to be estimated since the microstructure is not in fact periodic. Consider the geometry of a unit cell shown in Figure 5.17b. We assume that each fiber in the PU-MG composites is equal-distant apart from the unit cell wall in the X_1, X_2, and X_3 directions. With the known dimensions of the cylindrical inclusion at the center of the cell, the unit cell dimensions $2A_1$, $2A_2$, and $2A_3$ can be calculated for each volume fraction. Table 5.5 shows the dimensions of unit cell for three volume fractions.

For the analysis of DMA results, the volume fractions of inclusion are 0.1, 0.15, and 0.20. The volume fractions are 0.05, 0.1, and 0.2 for ultrasonic wave tests.

Table 5.5: Dimensions of the periodic unit cells

Volume Fraction	$2A_1$ (µm)	$2A_2 = 2A_3$ (µm)
0.05	241.69	57.69
0.1	226.17	42.17
0.15	218.99	34.99
0.2	214.61	30.61

Mechanical Properties for Computation to Compare with DMA Experiment

Shear storage modulus, G, and Poisson's ratio, ν, of the fully elastic milled glass fiber are listed in Table 5.6 and assumed to be constants in all calculations. For polyurea matrix phase, we have the complex dynamic Young's modulus obtained from the DMA measurement as shown in the accompanying experimental paper [73], Figure 4. We also use the quasi-static longitudinal moduli obtained from confined compression tests. In the confined compression test, polyurea sample is laterally confined in a steel compression cell under applied uniaxial load. The sample contraction and applied force were recorded. Quasi-static longitudinal modulus L can be calculated from the slope of the curve in the linear region [41]. The quasi-static longitudinal moduli from -50 to 30 °C with 10 °C increments are shown in Table 5.7. Other data points can be calculated, using interpolation (and extrapolation above 30 °C). In the modeling, the properties of polyurea are complex numbers. The Young's storage modulus is a real number and the Young's loss modulus is an imaginary number. The quasi-static longitudinal modulus is considered real (neglecting small loss, $L''/L' << 1$), and assumed frequency-insensitive within 0-20 Hz. With these two moduli, other viscoelastic properties of polyurea can be found using regular elastic

modulus interrelation for isotropic material.

Table 5.6: Mechanical properties of milled glass fiber [131]

Milled Glass	
G	ν
(GPa)	
30.34	0.2

Table 5.7: Quasi-static longitudinal modulus of pure polyurea [41]

Temperature	L
(°C)	(GPa)
-50	3.8223
-40	3.3925
-30	3.1351
-20	2.8624
-10	2.8213
0	2.7802
10	2.6066
20	2.4575
30	2.2405

Mechanical Properties for Computation to Compare with Ultrasonic Wave Experiment

The two mechanical properties of milled glass are constants for all calculations and are listed in Table 5.6. Two viscoelastic properties (longitudinal and shear moduli) of pure polyurea for ultrasonic-wave-test modeling are given in [73], Figure 9. Other mechanical properties can be found using typical interrelations between elastic moduli.

5.4.4 Results and Discussion

DMA Result

We calculated the viscoelastic properties of PU-MG composites under DMA measurement, using the models shown previously and compared them with the experimental results reported in part I of this paper [73]. Scanning electron microscopy revealed that milled glass fibers are randomly distributed and oriented in the all PU-MG composite samples for DMA measurement. Thus, 3D random orientation models are used to calculate the overall dynamic Young's moduli of the PU-MG composites. Hashin has showed that by replacing the real elastic moduli of each phase in micromechanical models of elastic composites with their complex counterparts (storage and loss components), one can directly utilize them for viscoelastic composites [111]. Shear G^* and bulk K^* moduli for each model are calculated as:

$$G^* = G' + G''i = \bar{M}^{3D}_{2323} = \bar{M}^{3D}_{3131} = \bar{M}^{3D}_{1212}, \tag{5.226}$$

$$K^* = K' + K''i = \frac{\bar{M}^{3D}_{ijkl}}{9}, \tag{5.227}$$

where $\bar{M}^{3D}_{2323}$, $\bar{M}^{3D}_{3131}$, and $\bar{M}^{3D}_{1212}$ are the 2323, 3131, and 1212 components of the tensor $\bar{\boldsymbol{C}}^{\boldsymbol{DD-3D}}$ (equation 5.219) or $\bar{\boldsymbol{C}}^{\boldsymbol{MT-3D}}$ or $\bar{\boldsymbol{C}}^{\boldsymbol{P-3D}}$ (equation 5.225), depending on what model is used. $\bar{M}^{3D}_{ijij}$ is the summation of the components with repeated indices $(i, j = 1, 2, 3)$. K' and K'' are bulk storage and loss moduli. Then dynamic Young's

moduli E^* can be calculated as:

$$E^* = E' + E''i = \frac{9K^*G^*}{3K^* + G^*}, \tag{5.228}$$

where E' and E'' are Young's storage and loss moduli.

Within the typical testing frequency range (1-20 Hz) of DMA measurement, the dynamic Young's moduli of PU-MG composites are not strong functions of the frequency, therefore only the experimental and the computational values at 1 and 20 Hz are compared over the temperature range of -50 to 50 °C and shown in Figure 5.18. We can see that the calculations from the three models are able to predict the trends of both storage and loss moduli of PU-10%MG (see Figures 5.18a and 5.18d). As expected the three models agree very well with the experimental results. Since the volume fraction of milled glass is very small, the particle interaction does not significantly affect the mechanical properties of the composite. As volume fraction of milled glass increases to 15% (see Figures 5.18b and 5.18e), we observe that among the three models, the dilute distribution (DD-3D) model underestimates Young's storage modulus. The non-dilute model based on Mori-Tanaka (MT-3D) approach slightly underestimates the Young's storage modulus while the periodic model (P-3D), agrees very well with experiment for both the Young's storage and loss moduli. As the volume fraction of milled glass increases up to 20% (see Figures 5.18c and 5.18f), calculations of Young's storage modulus of the PU-MG composite from DD-3D and MT-3D models are significantly lower than experiments (around 20%-50% lower), while the calculations of the Young's loss modulus are around 15% higher at temperature below $-40\,^{\circ}\mathrm{C}$ and around 30% lower above $-40\,^{\circ}\mathrm{C}$. It is noteworthy that the prediction of the P-3D model is always closer to experimental results than both other

models. This observation proves that the method based on periodic distribution of inclusions is very powerful in predicting the mechanical properties of composites with randomly distributed inclusions at high volume fraction of inclusions, even though the model does not appropriately represent the actual random micro-structure of the composites. The reason may be that it takes into account directly the interaction between adjacent particles through the evaluations of stress and strain fields in the particles, which dominates and has high influence on the mechanical properties of the composites [116, 123].

Figure 5.19 shows the comparison between master curves and shift factors constructed using experimental data and the computational master curves and shift factors constructed using calculation data based on the P-3D model for PU-10%MG, PU-15%MG, and PU-20%MG. The procedure to construct a master curve for a PU-MG composite is discussed in the accompanying paper [73]. We can see that for all three volumes, the computational master curves are able to track the trends of DMA data. They agree excellently with each other, especially at 10% and 15% volume fractions. The discrepancy between computation and DMA data becomes larger at 20% volume fraction (see Figure 5.19c). At this volume fraction, the P-3D model slightly underestimates the experimental Young's storage modulus master curve. The estimation improves as frequency increases. The loss master curves also show reasonable agreement. The largest deviation happens at the very low frequency range. This may be due to two factors (1) we assumed that the quasi-static longitudinal loss modulus of the polyurea is zero in our calculations and (2) extrapolation was performed to calculate the quasi-static longitudinal modulus at high temperature (above 30 °C) which corresponds to low frequency in the master curve.

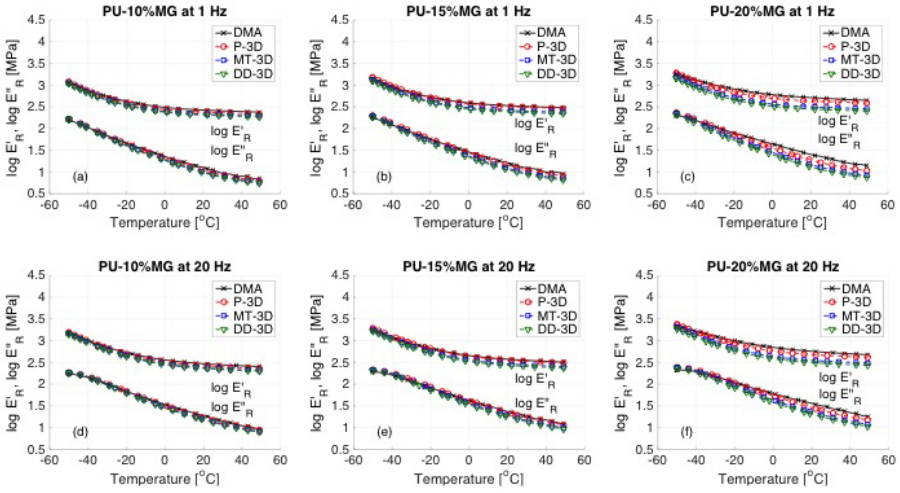

Figure 5.18: $\log E'_R$ and $\log E''_R$ versus temperature: (a) PU-10%MG at 1 Hz (b) PU-15%MG at 1 Hz (c) PU-20%MG at 1 Hz (d) PU-10%MG at 20 Hz (e) PU-15%MG at 20 Hz (f) PU-20%MG at 20 Hz

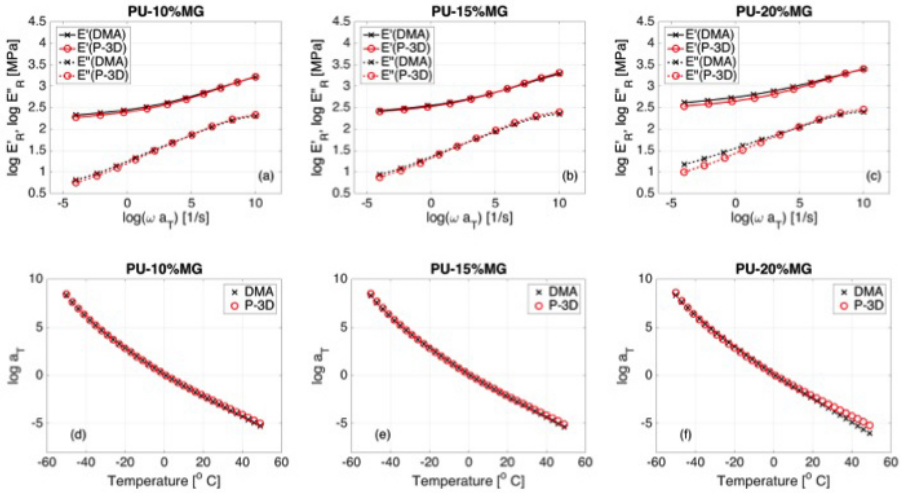

Figure 5.19: (a) master curves of PU-10%MG versus angular frequency (b) master curves of PU-15%MG versus angular frequency (c) master curves of PU-20%MG versus angular frequency (d) $\log a_T$ of PU-10%MG versus temperature (e) $\log a_T$ of PU-15%MG versus temperature (f) $\log a_T$ of PU-20%MG versus temperature

Ultrasonic Wave Testing Result

From our previous study, scanning electron microscopy revealed that milled glass fibers are randomly distributed and oriented in all longitudinal-wave-test sam-

ples but tend to lie parallel to the surfaces of the shear-wave-test samples since the shear-wave-test samples are much thinner than longitudinal-wave-test samples and were compressed between two glass sheets during the fabrication process [73]. Corresponding to this observation, micromechanical models are used to investigate and confirm the observation. All the three 3D random orientation models and the three in-plane orientation models were used in order to calculate the overall dynamic longitudinal and shear moduli of the PU-MG composites. They were compared with the results of ultrasonic wave experiments at 1 MHz from -50 to 30 °C with 10 °C step for PU-5%MG, PU-10%MG and PU-20%MG composites.

The computational longitudinal and shear moduli (L^* and G^*) for the models with the 3D random orientation of fiber can be found as:

$$L^* = L' + L''i = \bar{M}^{3D}_{1111} = \bar{M}^{3D}_{2222} = \bar{M}^{3D}_{3333}, \tag{5.229}$$

$$G^* = G' + G''i = \bar{M}^{3D}_{2323} = \bar{M}^{3D}_{3131} = \bar{M}^{3D}_{1212}, \tag{5.230}$$

where $\bar{\boldsymbol{M}}^{\boldsymbol{3D}}$ represents any of the tensors $\bar{\boldsymbol{C}}^{\boldsymbol{DD-3D}}$, $\bar{\boldsymbol{C}}^{\boldsymbol{MT-3D}}$, or $\bar{\boldsymbol{C}}^{\boldsymbol{P-3D}}$. For the in-plane orientation:

$$L^* = L' + L''i = \bar{M}^{in-plane}_{3333}, \tag{5.231}$$

$$G^* = G' + G''i = \bar{M}^{in-plane}_{2323} = \bar{M}^{in-plane}_{3131}, \tag{5.232}$$

where $\bar{\boldsymbol{M}}^{\boldsymbol{in-plane}}$ represents any of the tensors $\bar{\boldsymbol{C}}^{\boldsymbol{DD-in-plane}}$, $\bar{\boldsymbol{C}}^{\boldsymbol{MT-in-plane}}$, or

$\bar{C}^{P-in-plane}$.

Figure 5.20 shows experimental and computational dynamic longitudinal moduli of PU-5%MG, PU-10%MG, and PU-20%MG at 1 MHz. Unlike comparisons of Young's storage and loss moduli in the previous section, there is no significant difference among the results calculated from the three different models (DD, MT, and P). The difference between the orientations is nevertheless significant with $3D$ random cases performing much better than in-plane cases. At 20% volume fraction, the $3D$ (and in-plane) models underestimate longitudinal loss modulus, while they precisely estimate longitudinal storage modulus (see Figures 5.20c and 5.20f).

The experimental and computational dynamic shear moduli of PU-5%MG, PU-10%MG, and PU-20%MG at 1 MHz are shown in Figure 5.21. Similarly, there is no significant difference among the results calculated from three different models based on the three approaches (DD, MT, and P). The models deviate based on the orientation of fibers. The experimental results generally lie between the two distributions. In most cases, they tend to be closer toward the results of the in-plane orientation models, especially when we consider the shear storage modulus or for the lower volume fractions. The exception is for the loss modulus at the highest volume fraction, 20% (see Figure 5.21f). The storage modulus at 20% and lower temperatures also is a case where the experimental results appear to be in the middle of both models (see Figure 5.21c). It is possible that at higher volume fractions, the fibers are not permitted to align in plane to the fullest extent, considering they may prevent each other from rotation, while at lower volume fractions, the fluid flow and pressure induces this preferential plane alignment.

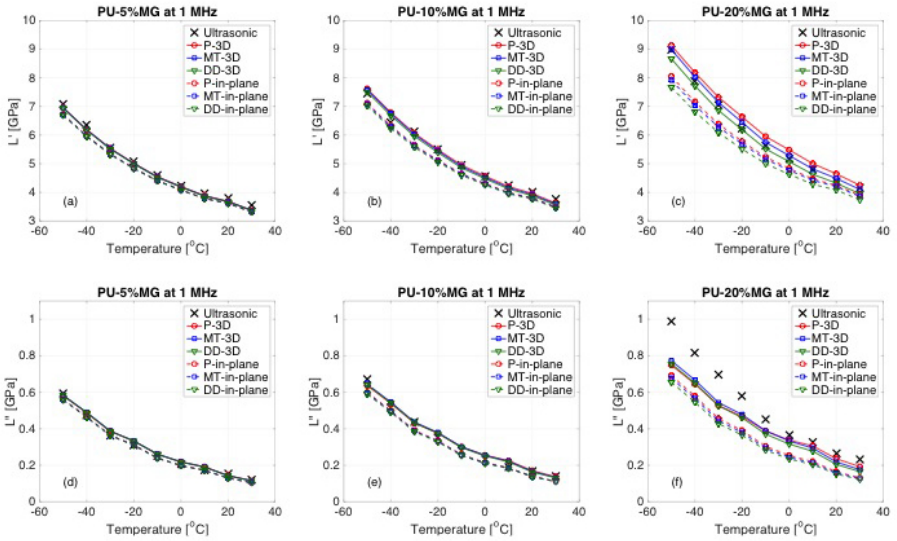

Figure 5.20: (a) L' of PU-5%MG versus temperature (b) L' of PU-10%MG versus temperature (c) L' of PU-20%MG versus temperature (d) L'' of PU-5%MG versus temperature (e) L'' of PU-10%MG versus temperature (f) L'' of PU-20%MG versus temperature

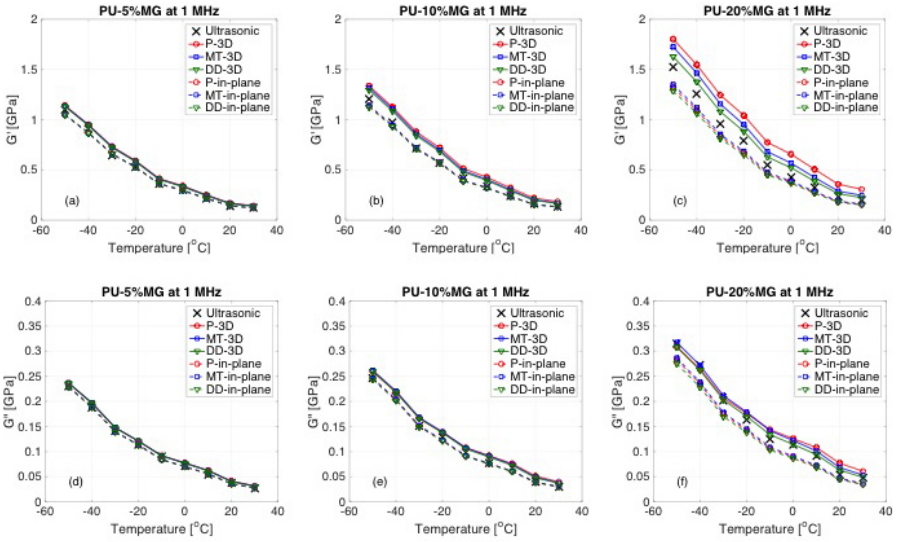

Figure 5.21: (a) G' of PU-5%MG versus temperature (b) G' of PU-10%MG versus temperature (c) G' of PU-20%MG versus temperature (d) G'' of PU-5%MG versus temperature (e) G'' of PU-10%MG versus temperature (f) G'' of PU-20%MG versus temperature

5.4.5 Conclusion

We have developed micromechanical models, based on three assumptions: (1) dilute random (DD), (2) non-dilute random (MT), and (3) periodic (P) distributions of inclusions. In each method, three models with different fiber orientations: uniaxial, in-plane, and 3D, were developed. The models were used to study the dynamic behaviors of PU-MG composites at 5%, 10%, 15%, and 20% volume fractions of milled glass. The DD and MT models require less computational cost compared to P model, but are less accurate for high volume fractions of inclusions. Comparison with the experimental results from DMA measurement proves that the models based on periodic distribution of inclusions is the most accurate in predicting mechanical properties of composites with randomly distributed inclusions at higher volume fractions. The periodic model was used to calculate and construct the master curves of the Young's storage and loss moduli. The computations were compared with the master curves from DMA experiment with very good agreement at 10% and 15% volume fractions of milled glass. At 20% volume fraction, the discrepancy between computations and experimental data becomes larger as expected. The reason might be that (1) we assumed that the quasi-static longitudinal loss modulus of the polyurea is zero in our calculations and (2) extrapolation was performed to calculate the quasi-static longitudinal modulus of polyurea matrix phase at higher temperatures (above 30 °C) which correspond to lower frequencies in the master curve. All models were used to estimate the dynamic longitudinal and shear moduli of PU-MG composites under ultrasonic wave measurement. The computational results were compared with experimental results. The comparisons are able to reveal the orientation of fibers in the tested samples with the models in general able to distinguish between the aligned

distributions of particulates for the thinner samples compared to 3D random orientations in thicker samples. All the models developed in this study could be used for other polymer-based composites with the similar microstructure to the PU-MG composite.

Acknowledgements

Subchapter 5.4 is a reprint of the material, as it appears in Mechanics of Materials, 2016, Nantasetphong, Wiroj; Amirkizhi, Alireza V.; Jia, Zhanzhan; Nemat-Nasser, Sia, Elsevier, 2016. The work in this chapter has been conducted at the Center of Excellence for Advanced Materials (CEAM) at the University of California, San Diego, and has been supported through ONR under grant N00014-09-1-1126 to the University of California, San Diego. This dissertation author was the primary author of this material.

5.A Eshelby's Tensors

The components of Eshelby's tensor $\boldsymbol{S}^{\boldsymbol{\Omega}}$ for prolate spheroid (see Figure 5.22) with respect to a rectangular Cartesian coordinate system are listed below [116, 117]. All calculation and proof detail can be found in reference [114–117].

$$S^{\Omega}_{1111} = \frac{3}{8\pi\,(1-\nu)} a_1^2 I_{11} + \frac{1-2\nu}{8\pi\,(1-\nu)} I_1 \tag{5.233}$$

$$S^{\Omega}_{1122} = \frac{1}{8\pi\,(1-\nu)} a_2^2 I_{12} - \frac{1-2\nu}{8\pi\,(1-\nu)} I_1 \tag{5.234}$$

$$S^{\Omega}_{1133} = \frac{1}{8\pi\left(1-\nu\right)} a_3^2 I_{13} - \frac{1-2\nu}{8\pi\left(1-\nu\right)} I_1 \tag{5.235}$$

$$S^{\Omega}_{1212} = \frac{\left(a_1^2+a_2^2\right)}{16\pi\left(1-\nu\right)} I_{12} + \frac{1-2\nu}{16\pi\left(1-\nu\right)} \left(I_1+I_2\right) \tag{5.236}$$

All other non-zero components are obtained by cyclic permutation of (1, 2, 3). The components which cannot be obtained by cyclic permutation are zero; for instance $S^{\Omega}_{1112} = S^{\Omega}_{1223} = S^{\Omega}_{1232} = 0$

$$I_2 = I_3 = \frac{2\pi a_1 a_3^2}{\left(a_1^2-a_3^2\right)^{\frac{3}{2}}} \left[\frac{a_1}{a_3}\left(\frac{a_1^2}{a_3^2}-1\right)^{\frac{1}{2}} - \cosh^{-1}\frac{a_1}{a_3}\right] \tag{5.237}$$

$$I_1 = 4\pi - 2I_2 \tag{5.238}$$

$$I_{12} = I_{13} = I_{21} = I_{31} = \frac{I_2 - I_1}{\left(a_1^2-a_2^2\right)} \tag{5.239}$$

$$3I_{11} = \frac{4\pi}{a_1^2} - 2I_{12} \tag{5.240}$$

$$I_{22} = I_{33} = I_{23} = I_{32} \tag{5.241}$$

$$I_{22} = \frac{\pi}{a_2^2} - \frac{I_2 - I_1}{4\left(a_1^2-a_2^2\right)} \tag{5.242}$$

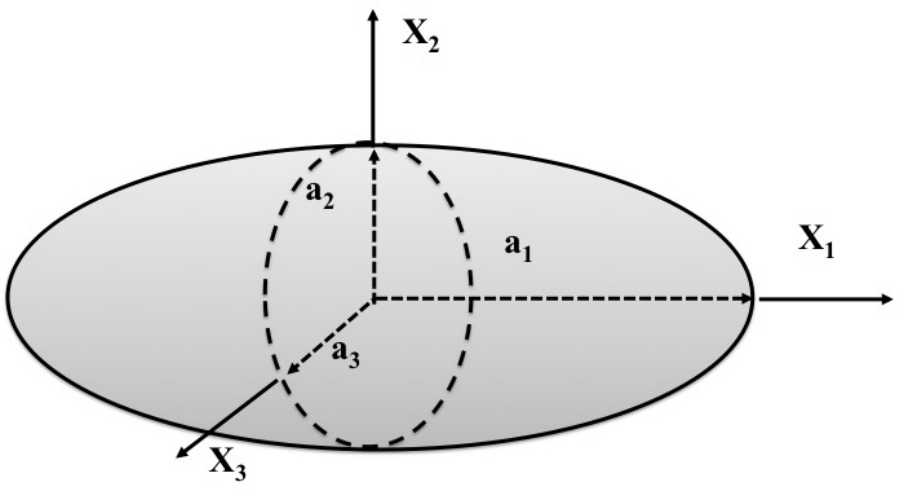

Figure 5.22: Prolate spheroid ($a_2 = a_3 < a_1$) and its geometry

Eshelby's tensor $\boldsymbol{S}^{\boldsymbol{\Omega}}$ for sphere in term of its components is given by:

$$S^{\Omega}_{ijkl} = \frac{5\nu - 1}{15\,(1-\nu)}\delta_{ij}\delta_{kl} + \frac{4 - 5\nu}{15\,(1-\nu)}\left(\delta_{ik}\delta_{jl} + \delta_{il}\delta_{jk}\right) \tag{5.243}$$

Chapter 6

Design of One-Dimensional Periodic Layered Composites for Acoustic Applications

In this chapter, the analysis of acoustic wave propagation in a one- dimensional periodic layered composite is discussed. To design the periodic layered composite, there are three components needed to be considered: (1) acoustic band structure, (2) effective dynamic properties, and (3) energy reflection and transmission coefficients. The acoustic band structure shows the relation between frequency and wavenumber. An acoustic wave with a given frequency would be allowed to pass the periodic layered composite if it has at least one wavenumber associated with the given frequency in the band structure plot. This is also called pass band. On the other hands, if there is no wavenumber associated with the given frequency, the periodic layered composite does not allow any acoustic wave to pass at that frequency. This phenomenon shows up in the acoustic band structure as a gap. Therefore it is referred to as a band

gap. A transfer of energy of an acoustic wave propagating from a medium to another medium depends on acoustic impedances of the two media. If the impedances of the two media are matched, the energy of the propagating acoustic wave will be completely transferred from the first medium to the second medium. If there is a mismatch, certain amount of energy will get reflected back, depending on the degree of the mismatch. The impedance of a homogeneous material is the square root of its density multiplied by its dynamic modulus. For a periodic layered composite, it consists of many homogeneous constituents each of which has it own dynamic properties. Therefore the effective or overall dynamic properties of the periodic layer composite is required in order to characterize it as a whole. In this research, the dynamic homogenization using field variable averaging method is used to calculate effective impedance of the periodic layered composite. In addition, transfer matrix method is used to provide an exact solution for calculating the energy reflection and transmission at the interfaces between the periodic layered composite and two surrounding homogenous half-spaces (see Figure 6.1).

6.1 Band Structure Calculation for One-Dimensional Periodic Layer Composites

In this section the band structure calculation based on transfer matrix method is discussed [62,83]. Consider a one-dimensional periodic layered composite consisting of an infinite number of identical repeated unit cells shown in Figure 6.2. The wave

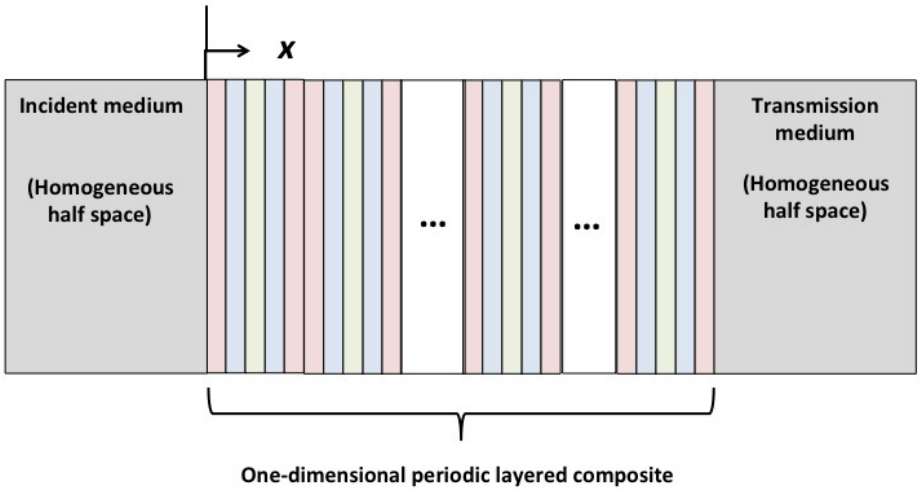

Figure 6.1: A one-dimensional periodic layered composite with two surrounding homogenous half-spaces

equation for the longitudinal waves that propagate in the x-direction is:

$$\frac{\partial^2 u\left(x,t\right)}{\partial t^2} = c_{(j)}^2 \frac{\partial^2 u\left(x,t\right)}{\partial x^2}, \tag{6.1}$$

where u is the displacement, x and t are spatial and time variables, $c_{(j)}$ is the longitudinal wave speed in the j-th layer of the composite. The general solution for displacement in each layer can be expressed as the superposition of two longitudinal waves traveling in opposite directions.

$$u\left(x,t\right) = \left[A_+^{(j)} e^{ik_{(j)}x} + A_-^{(j)} e^{-ik_{(j)}x}\right] e^{-i\omega t}, \tag{6.2}$$

where

$$k_{(j)} = \frac{\omega}{c_{(j)}}, \tag{6.3}$$

ω is angular frequency, $A_+^{(j)}$ and $A_-^{(j)}$ are the amplitudes of the waves traveling in positive and negative x-direction in j-th layer, respectively. k is the wavenumber in

the j-th layer. The stress, σ in the periodic layered composite can be written as:

$$\sigma(x,t) = E_{(j)}\frac{\partial u(x,t)}{\partial x}, \tag{6.4}$$

where

$$E_{(j)} = \rho_{(j)}c_{(j)}^2, \tag{6.5}$$

$\rho_{(j)}$ is density of the j-th layer, $E_{(j)}$ is the modulus of the j-th layer. Substitute equation 6.2 into 6.4, we obtain:

$$\sigma(x,t) = \left[A_+^{(j)}Q_{(j)}ie^{ik_{(j)}x} - A_-^{(j)}Q_{(j)}ie^{-ik_{(j)}x}\right]e^{-i\omega t}, \tag{6.6}$$

where

$$Q_{(j)} = E_{(j)}k_{(j)} = Z_{(j)}\omega, \tag{6.7}$$

$Z_{(j)} = \rho_{(j)}c_{(j)}$ is the impedance of the j-th layer. The displacement and stress in the j-th layer can be expressed in the matrix form as:

$$\begin{bmatrix} u(x) \\ \sigma(x) \end{bmatrix} = \boldsymbol{B}_{(j)} \begin{bmatrix} A_+^{(j)}e^{ik_{(j)}x} \\ A_-^{(j)}e^{-ik_{(j)}x} \end{bmatrix}, \tag{6.8}$$

where

$$\boldsymbol{B}_{(j)} = \begin{bmatrix} 1 & 1 \\ iQ_{(j)} & -iQ_{(j)} \end{bmatrix}. \tag{6.9}$$

Let $x_{(j)L}$ and $x_{(j)R}$ denote the left and right boundaries of j-th layer in the unit cell, respectively. $x_{(j)L}$ and $x_{(j)R}$ for each layer are related through:

$$x_{(j)R} = x_{(j)L} + d_{(j)}, \tag{6.10}$$

where $d_{(j)}$ is the thickness of the j-layer. Using equations 6.8 and 6.10, the displacement and stress on the left and the right boundaries of the j-layer are related by:

$$\begin{bmatrix} u\left(x_{(j)R}\right) \\ \sigma\left(x_{(j)R}\right) \end{bmatrix} = \boldsymbol{B}_{(j)}\boldsymbol{D}_{(j)}\left(d_{(j)}\right)\boldsymbol{B}_{(j)}^{-1}\begin{bmatrix} u\left(x_{(j)L}\right) \\ \sigma\left(x_{(j)L}\right) \end{bmatrix}, \tag{6.11}$$

where

$$\boldsymbol{D}_{(j)}\left(d_{(j)}\right) = \begin{bmatrix} e^{ik_{(j)}d_{(j)}} & 0 \\ 0 & e^{-ik_{(j)}d_{(j)}} \end{bmatrix}. \tag{6.12}$$

The product of $\boldsymbol{B}_{(j)}\boldsymbol{D}_{(j)}\left(d_{(j)}\right)\boldsymbol{B}_{(j)}^{-1}$ is a $2X2$ matrix which can be simplified as:

$$\boldsymbol{B}_{(j)}\boldsymbol{D}_{(j)}\left(d_{(j)}\right)\boldsymbol{B}_{(j)}^{-1} = \begin{bmatrix} \cos\left(k_{(j)}d_{(j)}\right) & \frac{\sin\left(k_{(j)}d_{(j)}\right)}{Q_{(j)}} \\ -Q_{(j)}\sin\left(k_{(j)}d_{(j)}\right) & \cos\left(k_{(j)}d_{(j)}\right) \end{bmatrix} = \boldsymbol{T}_{(j)}, \tag{6.13}$$

where $T_(j)$ is called the transfer matrix for j-th layer. Due to the continuity of displacement and stress between each two adjacent layers, the displacement and stress at the left boundary of the first layer (1) in the unit cell (shown in Figure 6.2) are

related to those at the right boundary of the (N)-th layer by:

$$\begin{bmatrix} u\left(x_{(N)R}\right) \\ \sigma\left(x_{(N)R}\right) \end{bmatrix} = \boldsymbol{T} \begin{bmatrix} u\left(x_{(1)L}\right) \\ \sigma\left(x_{(1)L}\right) \end{bmatrix}, \tag{6.14}$$

where

$$\boldsymbol{T} = \boldsymbol{T}_{(N)}\boldsymbol{T}_{(N-1)}...\boldsymbol{T}_{(1)}, \tag{6.15}$$

$\boldsymbol{T}$ is the cumulative transfer matrix of the unit cell. For Bloch type waves the displacement and stress at a given point of the unit cell are related to the corresponding point in the adjacent unit cell by:

$$\boldsymbol{y}\left(x+d\right) = e^{ikd}\boldsymbol{y}\left(x\right), \tag{6.16}$$

where

$$\boldsymbol{y}\left(x\right) = \begin{bmatrix} u\left(x\right) \\ \sigma\left(x\right) \end{bmatrix}, \tag{6.17}$$

k is the Bloch wavenumber and d is the length of the unit cell shown in Figure 6.2. Equations 6.14-6.17 lead to the following eigenvalue problem:

$$\boldsymbol{T}\left(\omega\right)\boldsymbol{y}\left(x_{(1)L}\right) = \lambda\boldsymbol{y}\left(x_{(1)L}\right), \tag{6.18}$$

where

$$\lambda = e^{ikd}, \tag{6.19}$$

λ is the eigenvalue and $\boldsymbol{y}\left(x_{(1)L}\right)$ is the eigenvector. The solutions of equation 6.18 yield the band structure for longitudinal wave propagation in an infinitely extended one-dimensional periodic layered composite.

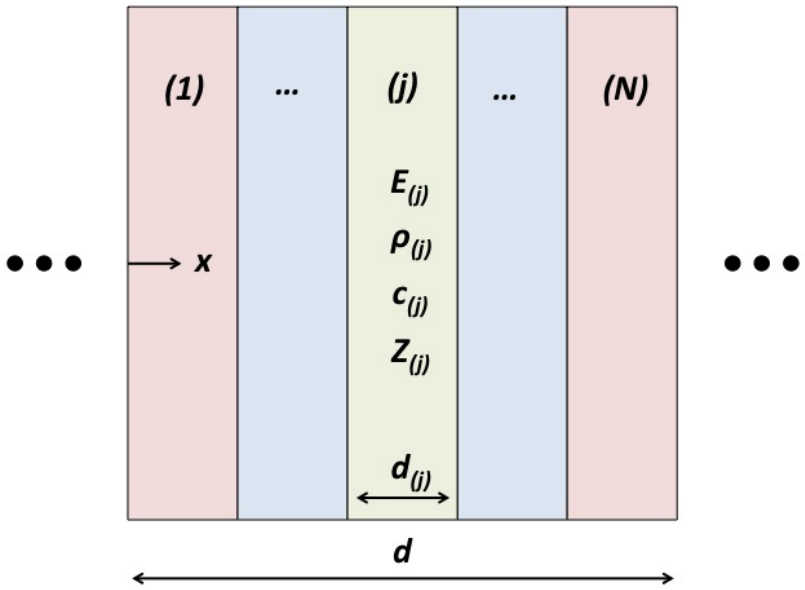

Figure 6.2: Unit cell of a one-dimensional periodic layered composite

6.2 Dynamic Homogenization for One-Dimensional Periodic Layer Composites

The effective dynamic properties of one-dimensional periodic layered composites can be calculated using dynamic homogenization. In this study, a method based

on integration of field variables will be discussed [132, 133]. Consider Bloch waves in an infinitely extended periodic layered composite consisting of identical repeated unit cells $\Omega = \{x : 0 \leq x \leq d\}$. The unit cell is shown in Figure 6.2 For harmonic waves traveling in the layered composite with wavenumber k and frequency ω, the field variables can be expressed as:

$$u\left(x,t\right) = U\left(x\right)e^{i(kx-\omega t)}, \tag{6.20}$$

$$\dot{u}\left(x,t\right) = \dot{U}\left(x\right)e^{i(kx-\omega t)}, \tag{6.21}$$

$$\epsilon\left(x,t\right) = E\left(x\right)e^{i(kx-\omega t)}, \tag{6.22}$$

$$\sigma\left(x,t\right) = \Sigma\left(x\right)e^{i(kx-\omega t)}, \tag{6.23}$$

$$p\left(x,t\right) = P\left(x\right)e^{i(kx-\omega t)}, \tag{6.24}$$

where u and $\dot{u}$ are the displacement and velocity fields, ϵ and σ are strain and stress fields, and p is the linear momentum filed, The capital variables, U, $\dot{U}$, E, Σ, and P represent the periodic parts of displacement, velocity, strain, stress, and linear momentum, respectively. The equation of motion and kinetic relation are given by:

$$\rho\left(x\right)\frac{\partial^2 u\left(x,t\right)}{\partial t^2} = \frac{\partial \sigma\left(x,t\right)}{\partial x}, \tag{6.25}$$

$$\epsilon\left(x,t\right)=\frac{\partial u\left(x,t\right)}{\partial x}. \tag{6.26}$$

Equation 6.25 can be written in term of linear mentum as:

$$\frac{\partial p\left(x,t\right)}{\partial t}=\frac{\partial\sigma\left(x,t\right)}{\partial x}, \tag{6.27}$$

where the linear momentum p is:

$$p\left(x,t\right)=\rho\left(x\right)\dot{u}\left(x,t\right). \tag{6.28}$$

Differentiate equation 6.26 with respect to time give the strain-rate/velocity relation as:

$$\frac{\partial\epsilon\left(x,t\right)}{\partial t}=\frac{\partial\dot{u}\left(x,t\right)}{\partial x}. \tag{6.29}$$

Substitute equations 6.23 and 6.24 into 6.27 and equations 6.21 and 6.22 into 6.29 and multiply them with e^{-kX}, we obtain:

$$\nabla\left(\Sigma\left(x\right)e^{ik(x-X)}\right)+i\omega P\left(x\right)e^{ik(x-X)}=0, \tag{6.30}$$

$$\nabla\left(\dot{U}\left(x\right)e^{ik(x-X)}\right)+i\omega E\left(x\right)e^{ik(x-X)}=0, \tag{6.31}$$

where $\nabla = \frac{\partial}{\partial x} + ik$. Introduce the change of variable $y = x - X$ in the equations 6.30 and 6.31 to obtain:

$$\nabla_y \left(\Sigma \left(X + y \right) e^{ik(y)} \right) + i\omega P \left(X + y \right) e^{ik(y)} = 0, \tag{6.32}$$

$$\nabla_y \left(\dot{U} \left(X + y \right) e^{ik(y)} \right) + i\omega E \left(X + y \right) e^{ik(y)} = 0. \tag{6.33}$$

Average the two equations above with respect to X over the unit cell to arrive at

$$\nabla_y \left(\bar{\Sigma} e^{ik(y)} \right) + i\omega \bar{P} e^{ik(y)} = 0, \tag{6.34}$$

$$\nabla_y \left(\bar{\dot{U}} e^{ik(y)} \right) + i\omega \bar{E} e^{ik(y)} = 0, \tag{6.35}$$

where any of the barred quantities are the averages of the unbarred and defined by:

$$\bar{G} = \frac{1}{d} \int_{x=0}^{x=d} G \left(x \right) dx. \tag{6.36}$$

It is worth pointing out that the overall field variables defined according to equation 6.36 satisfy the overall field equations 6.34 and 6.35, from which we have:

$$\bar{\Sigma} + \frac{\omega}{k} \bar{P} = 0, \tag{6.37}$$

$$\bar{\dot{U}} + \frac{\omega}{k} \bar{E} = 0. \tag{6.38}$$

The mean constitutive relations can be defined as:

$$\bar{\Sigma} = C_{eff}\bar{E}, \tag{6.39}$$

$$\bar{P} = \rho_{eff}\bar{\dot{U}}, \tag{6.40}$$

where C_{eff} and ρ_{eff} are the effective or overall dynamic stiffness and density, respectively. It is worth noting that for the four linear and homogeneous equations 6.37-6.40 to admit nontrivial solutions for the overall effective field quantities, $\bar{\Sigma}$, $\bar{P}$, $\bar{\dot{U}}$, and $\bar{E}$ we must have:

$$\frac{C_{eff}}{\rho_{eff}} = \left(\frac{\omega}{k}\right)^2. \tag{6.41}$$

Equation 6.41 gives the dispersion relations or the acoustic band structure as discussed previously. The effective acoustic impedance of the periodic layered composite, Z_{eff} can be calculated from:

$$Z_{eff} = \sqrt{\rho_{eff}C_{eff}}. \tag{6.42}$$

6.3 Transfer Matrix Approach For Analysis of Energy Reflection, Transmission, and Dissipation

In this section, transfer matrix method is discussed. It provides an exact solution for calculating the energy reflection, transmission, and dissipation coefficients at the interfaces of a one-dimensional finite periodic layered composite sandwiched by two homogenous half-spaces. Consider m unit cells of a one-dimensional periodic layered composite in which each of unit cell consists of N individual layers. The unit cell is shown in Figure 6.2. The periodic layered composite is sandwiched by two homogenous half-spaces, as shown in Figure 6.3. Consider an incoming harmonic wave with amplitude $A_+^{(0)}$ moving from the medium, $M_{(0)}$ toward the composite in positive x-direction, and a reflected wave with amplitude $A_-^{(0)}$, moving away from the composite to the incident medium, $M_{(0)}$. The displacement in the incident medium, can be expressed as

$$u\left(x,t\right)=\left[A_+^{(0)}e^{ik_{(0)}x}+A_-^{(0)}e^{-ik_{(0)}x}\right]e^{-i\omega t}, \tag{6.43}$$

where $k_{(0)}$ is wavenumber in the incident medium $M_{(0)}$. The displacement in each layer of the composite can be given by equation 6.2. In the transmission medium $M_{(mN+1)}$, there is a harmonic wave with amplitude $A_+^{(mN+1)}$ moving out from the composite in the positive x-direction. The displacement in the transmission medium

$M_{(mN+1)}$ can be given by:

$$u\left(x,t\right)=\left[A_{+}^{(mN+1)}e^{ik_{(mN+1)}x}\right]e^{-i\omega t}, \tag{6.44}$$

where $k_{(mN+1)}$ is wavenumber in the transmission medium $M_{(mN+1)}$. Similar to Section 6.1, the displacement and stress at the left boundary of the first layer in the first unit cell of the composite are related to those at the right boundary of the N-th layer in the m-th unit cell by:

$$\begin{bmatrix} u\left(x_{(N)R,m}\right) \\ \sigma\left(x_{(N)R,m}\right) \end{bmatrix}=\boldsymbol{T}^{m}\begin{bmatrix} u\left(x_{(1)L,1}\right) \\ \sigma\left(x_{(1)L,1}\right) \end{bmatrix}, \tag{6.45}$$

where $u\left(x_{(N)R,m}\right)$ and $\sigma\left(x_{(N)R,m}\right)$ are the displacement and stress, respectively, at the right boundary of the N-th layer in the m-th unit cell, while $u\left(x_{(1)L,1}\right)$ and $\sigma\left(x_{(1)L,1}\right)$ are the displacement and stress, at the left boundary of the first layer in the first unit cell, $\boldsymbol{T}$ is the cumulative transfer matrix of a unit cell (see equation 6.15). From equations 6.8 and 6.12 and the continuity of displacement and stress at the interfaces between the composite and the surrounding media, $M_{(0)}$ and $M_{(mN+1)}$, we can write:

$$\begin{bmatrix} u\left(x_{(N)R,m}\right) \\ \sigma\left(x_{(N)R,m}\right) \end{bmatrix}=\boldsymbol{B}_{(Nm+1)}\boldsymbol{D}_{(Nm+1)}\left(L\right)\begin{bmatrix} A_{+}^{(nM+1)} \\ 0 \end{bmatrix}, \tag{6.46}$$

$$\begin{bmatrix} u\left(x_{(1)L,1}\right) \\ \sigma\left(x_{(1)L,1}\right) \end{bmatrix}=\boldsymbol{B}_{(0)}\boldsymbol{D}_{(0)}\left(0\right)\begin{bmatrix} A_{+}^{(0)} \\ A_{-}^{(0)} \end{bmatrix}, \tag{6.47}$$

where L is the total length of the composite, Matrices $\boldsymbol{B}$ and $\boldsymbol{D}$ are defined in equations 6.9 and 6.12, respectively. Substitute equations 6.46 and 6.47 into equation 6.45, we obtain:

$$\begin{bmatrix} A_+^{(nM+1)} \\ 0 \end{bmatrix} = \boldsymbol{K} \begin{bmatrix} A_+^{(0)} \\ A_-^{(0)} \end{bmatrix}, \tag{6.48}$$

where

$$\boldsymbol{K} = \boldsymbol{D}_{(Nm+1)}^{-1}(L)\, \boldsymbol{B}_{(Nm+1)}^{-1} \boldsymbol{T}^m \boldsymbol{B}_{(0)} \boldsymbol{D}_{(0)}(0). \tag{6.49}$$

From equation 6.48, $A_-^{(0)}$ and $A_+^{(mN+1)}$ can be written in term of $A_+^{(0)}$ as:

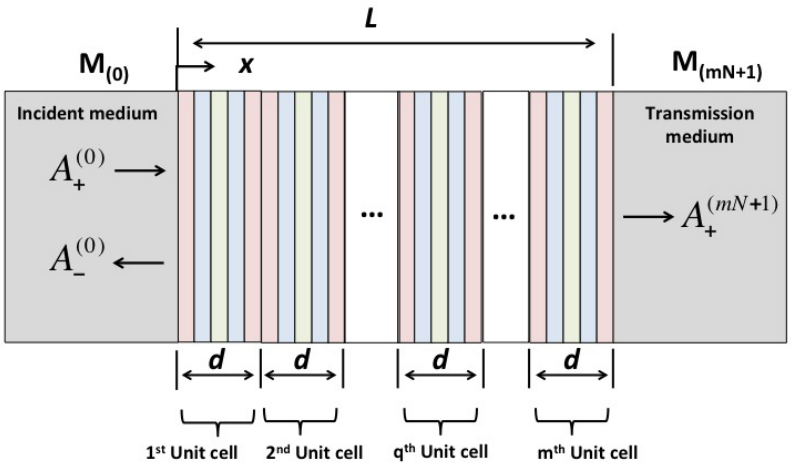

Figure 6.3: A finite one-dimensional periodic layered composite sandwiched by two homogenous half-spaces

$$A_-^{(0)} = -\frac{K_{21}}{K_{22}} A_+^{(0)}, \tag{6.50}$$

$$A_{+}^{(Nm+1)} = \left(K_{11} - \frac{K_{12}K_{21}}{K_{22}} \right) A_{+}^{(0)}, \tag{6.51}$$

where K_{ij} is component ij $(i, j = 1, 2)$ of the matrix $\boldsymbol{K}$. Since the energy of acoustic wave is proportional to the square of its amplitude, we then define energy reflection and transmission coefficients, RC and TC as:

$$RC = \left| \frac{A_{-}^{(0)}}{A_{+}^{(0)}} \right|^2 = \left| -\frac{K_{21}}{K_{22}} \right|^2, \tag{6.52}$$

$$TC = \left| \frac{Z_{(Nm+1)}}{Z_{(0)}} \left(\frac{A_{+}^{(Nm+1)}}{A_{+}^{(0)}} \right) \right|^2 = \left| \frac{Z_{(Nm+1)}}{Z_{(0)}} \left(K_{11} - \frac{K_{12}K_{21}}{K_{22}} \right) \right|^2. \tag{6.53}$$

The ratio, $\frac{Z_{(Nm+1)}}{Z_{(0)}}$ accounts for when the media $M_{(0)}$ is different from $M_{(Nm+1)}$. The energy dissipation coefficient is then defined as:

$$DC = 1 - RC - TC \tag{6.54}$$

If there is no energy dissipation in the composite, DC will be zero. In general, if the composite consists of layers of elastic materials, DC will be zero. However, this is not true when the composite has one or more viscoelastic layers.

6.4 Towards Active Acoustic Metamaterial

In this section, the calculation tools presented in Sections 6.1-6.3 will be used to design an active acoustic metamaterial. Due to the limitation in time, the experimental validation of the design will be future work. The definition of the so-called

active acoustic metamaterial (AAM) in this study is a one-dimensional periodic layered composite that can absorb, measure, dissipate, generate and transmit acoustic waves. For the sake of experimental validation in the future, the incident and transmission media in the design are chosen to be aluminum bars. The AAM is divided into two sequential sections (see Figure 6.4). The incident wave is coming from left to right. The wave will hit section A first. Section A is a periodic layered composite designed with the objective that it can absorb and measure or generate and transmit acoustic waves in the 1st acoustic branch (longitudinal vibration mode). Section B is another periodic layered composite designed with the objective that it can absorb and dissipate the acoustic waves.

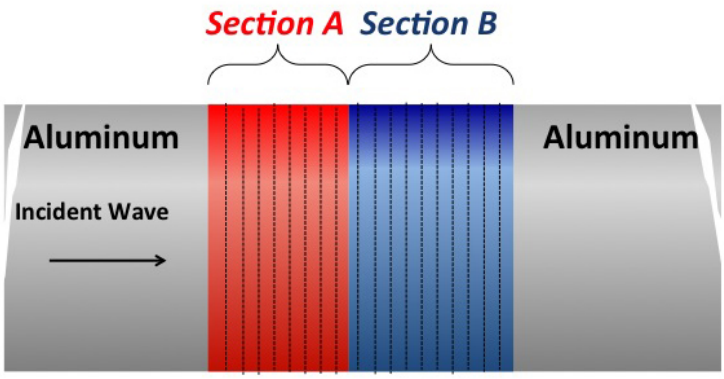

Figure 6.4: Two sequential sections in the active acoustic metamaterial

Table 6.1: Section A: material parameters

	Kapton	Copper	Piezoelectric Material
E (GPa)	2.5	120	84
ρ (kg m^{-3})	1420	8193	7900
Z (MPa s m^{-1})	1.88	31.36	25.76
Thickness (mm)	0.1	0.2	2

From the design objective of section A, it needs to have a layer in a unit cell

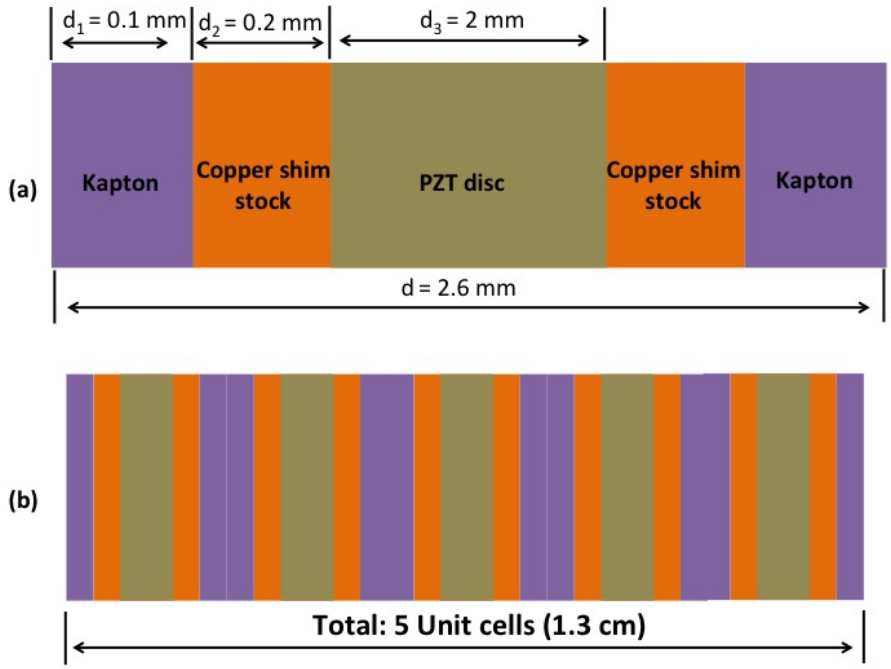

Figure 6.5: (a) Dimensions of a unit cell in the periodic layered composite section A (b) Total number of unit cells in section A

Table 6.2: Material parameters for aluminum

	Aluminum
E (GPa)	69
ρ (kg m^{-3})	2700
Z (MPa s m^{-1})	13.6

that can sense or measure the incident acoustic wave and later generate, if and when necessary, a wave similar to the measured incident wave. Therefore, a piezoelectric material, which can convert mechanical stress/strain to electrical voltage and vice versa, is chosen as one of the components in a unit cell. To drive the piezoelectric material, we need two electrical conductor layers: one at the front and another one at the back of the piezoelectric material. Therefore, two copper shim stocks are chosen as electric conductor layers. Two polyimide films (Kapton) are chosen to cover both front and back side of the unit cell. These two polyimide layers help electrically

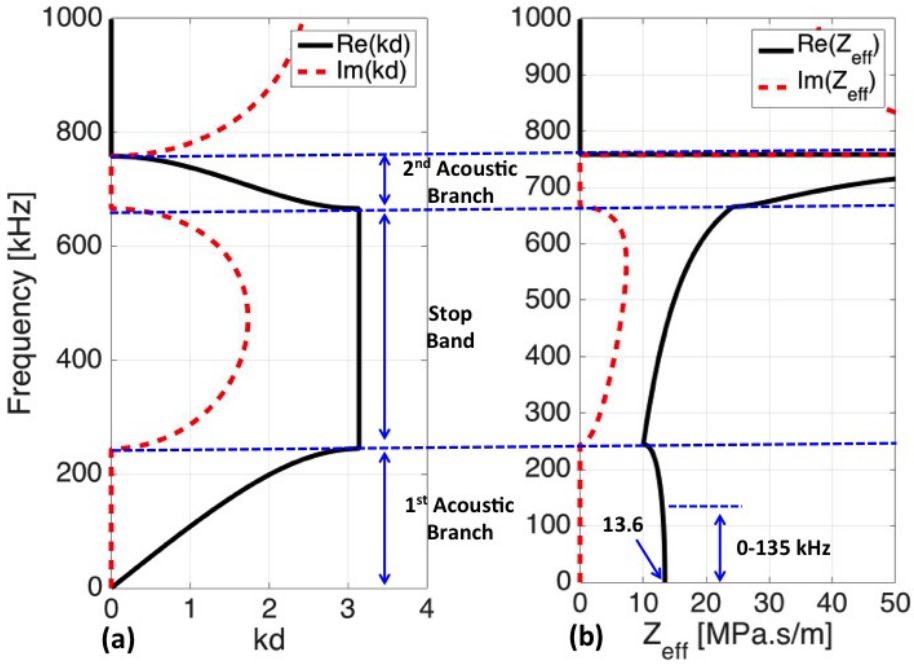

Figure 6.6: (a) Band structure of the periodic layered composite section A (b) Frequency versus effective impedance of the periodic layered composite section A

insulate the unit cell and prevent the unit cell from short circuit. Figure 6.5a shows a design of a unit cell in the section A that has the effective acoustic impedance, Z_{eff} matches with the impedance of the surrounding aluminum, Z_{Al}. Figure 6.5b shows the total number of unit cell in the composite. The materials parameters for the section A composite and aluminum are shown in Tables 6.1 and 6.2. Figure 6.6a shows the acoustic band structure of the section A composite. The vertical axis is frequency, while the horizontal axis is the normalized wavenumber kd. To be noted, k is the Bloch wavenumber and d is the length of the unit cell. The first acoustic branch is from 0 to 245 kHz, followed by stop band from 245 kHz to 666 kHz. In this stop band, there is no acoustic wave passing through the section A composite. From 666 to 759 kHz is the second acoustic branch. The band structure in Figure 6.6a was calculated using

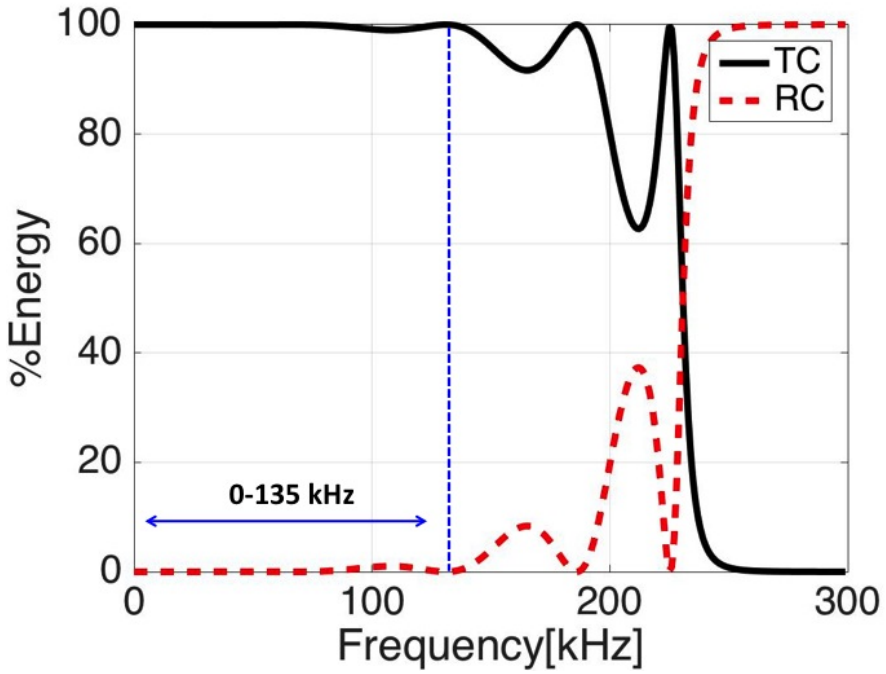

Figure 6.7: Composite section A: Energy reflection and transmission coefficients versus frequency

equation 6.18. Figure 6.6b shows the frequency versus effective acoustic impedance of the section A composite. As we can see, the effective impedance, Z_{eff} of the composite matches the impedance of aluminum ($13.6\,\mathrm{MPa\,s\,m^{-1}}$) from 0 up to 135 kHz within 5% difference. The effective impedance was calculated using equation 6.42. If Z_{eff} really matches Z_{Al}, there should not be acoustic waves reflected from the interface between the composite and the surrounding aluminum. To prove this, the energy reflection and transmission coefficients, RC and TC were calculated using equations 6.52 and 6.53, respectively. RC and TC of the section A composite as functions of frequency are shown in Figure 6.7. It can be seen that within 0 to 135 kHz RC is zero and TC is 100%, meaning that there is no reflection of the acoustic waves in this frequency range. Therefore, this confirms that the design of section A is reliable. Next step will be experimental proof. This will be future work.

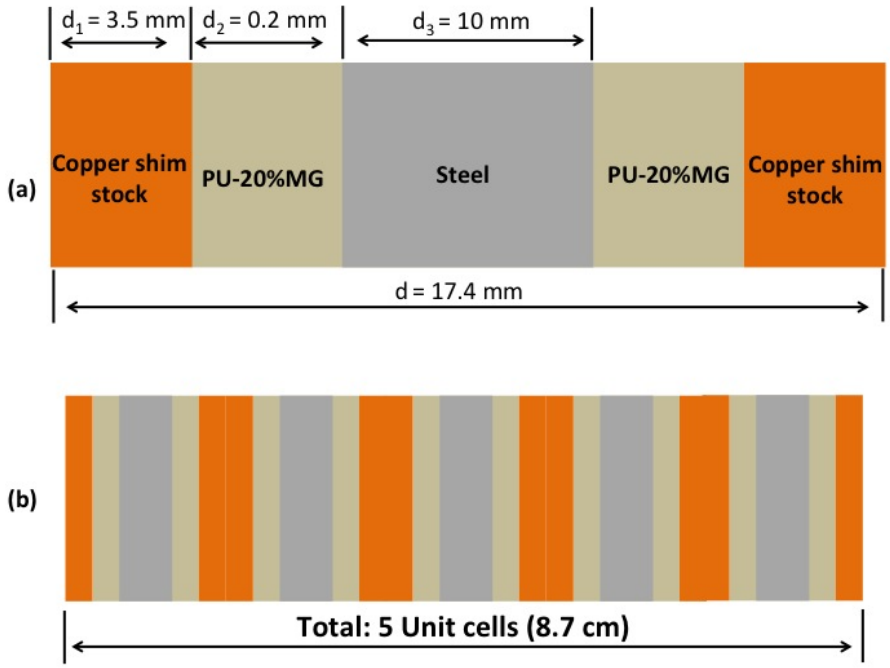

Figure 6.8: (a) Dimensions of a unit cell in the periodic layered composite section B (b) Total number of unit cells in section B

From the design objective of section B, it needs to have a layer in a unit cell that can dissipate the energy of the incident acoustic wave. Therefore, a viscoelastic material, which has high loss modulus, should be used as one of the components in a unit cell. In this work, PU-20%MG is chosen. Mechanical properties of PU-20%MG composite as functions of frequency are reported in Section 3.4, and micromechanical models for PUMG composites are shown in Section 5.4. Since PU-20%MG is a soft viscoelastic material, it has low E', E'', and density, leading to low impedance compared to aluminum (see Tables 6.2 and 6.3). Since we want to match the effective impedance of the composite to that of aluminum, two stiff materials with high densities are used for the two remaining components of the section B composite in order to compensate for the low impedance of the PU-20%MG layer. Therefore, steel and

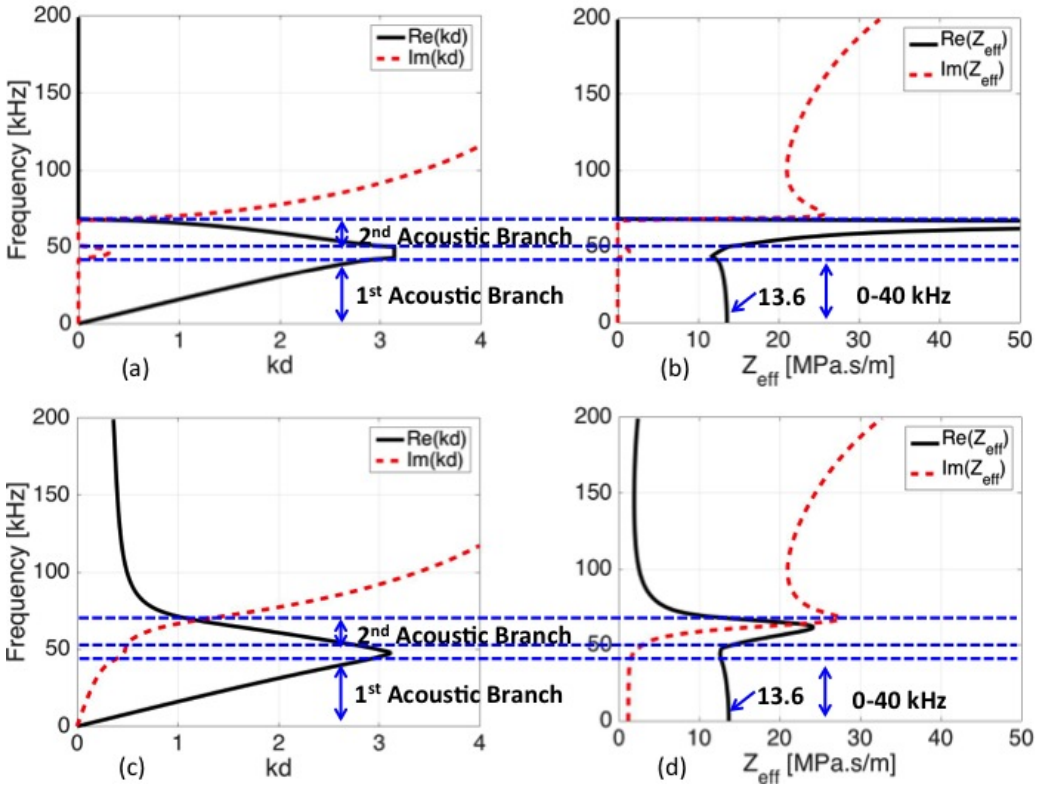

Figure 6.9: (a) Band structure of the periodic layered composite section B [Assume: E'' of PU-20%MG is 0] (b) Frequency versus effective impedance of the periodic layered composite section B [Assume: E'' of PU-20%MG is 0] (c) Band structure of the periodic layered composite section B (d) Frequency versus effective impedance of the periodic layered composite section B

copper are chosen. In this work, three phase periodic layered composite is preferred. However there is no restriction to use higher or lower number of phases. Further study is required in order to understand the benefits of the composites with higher or lower number of phases. For our design, the stiffest material (Steel) is placed at the center of the unit cell and sandwiched by the two soft viscoelastic layers (PU-20%MG). The second stiffest material (Copper) is placed at both ends of the unit cell. Figure 6.8a shows a design of a unit cell of the section B composite that has the effective acoustic impedance, Z_{eff} matches with the impedance of the surrounding aluminum, Z_{Al}. Fig-

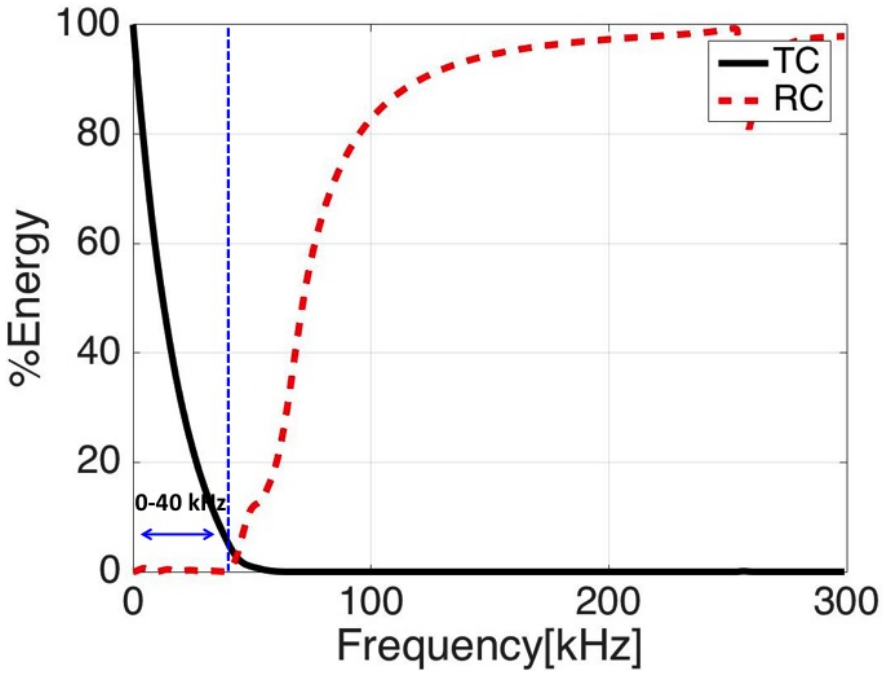

Figure 6.10: Composite section B: Energy reflection and transmission coefficients versus frequency

ure 6.8b shows the total number of unit cell in the composite. As we can see, the total length of the composite is quite long. This is due to the fact that the impedance of the surrounding medium (aluminum) is quite high. If the surrounding medium is a material with lower impedance (for example water), then the steel and copper phases can be redesigned with thinner thicknesses. Figure 6.9c shows the acoustic band structure of the section B composite. Due to the effect of the complex viscoelastic modulus of the PU-20%MG phase, the band structure of the section B becomes complicated. It is more difficult to locate the boundaries of first and second acoustic branches (see Figure 6.9c). To aid the separation of the two acoustic branches, another band structure of the section B composite was calculated with the assumption that E'' of the PU-20%MG is zero (see Figure 6.9a) and compared with the actual one in Figure 6.9c. From Figures 6.9a and 6.9c, the first acoustic branch is from 0 to 43 kHz, followed by

a very tiny stop band from 43 kHz to 50 kHz. The second acoustic branch is from 50 to 67 kHz. After that, there is a large stop band that goes beyond 200 kHz. The band structures in Figures 6.9a and 6.9c were calculated using equation 6.18. The materials parameters for the section B composite are shown in Table 6.3. To be noted, E' and E'' of PU-20%MG depend on frequency. Since the composite is designed for the first acoustic branch which covers low frequency range, we use E' and E'' of PU-20%MG obtained at 10 kHz and 20 °C using the acoustic ball impact measurement discussed in Section 3.5. The more appropriate E' and E'' would be the numbers at the mid frequency of the operating frequency range of the designed composite. Figure 6.9d shows the frequency versus effective acoustic impedance of the section B composite. As we can see, the real part of the effective impedance, $Re(Z_{eff})$ of the composite matches impedance of aluminum ($13.6\,\mathrm{MPa\,s\,m^{-1}}$) from 0 up to 40 kHz within 5% difference. To be noted, the imaginary part is small and negligible for this case. The effective impedance was calculated using equation 6.42. Clearly, the design of section B has effective impedance that matches with impedance of aluminum. If this is true, there should not be acoustic waves reflected from the interface between the composite and the surrounding aluminum. To prove this, the energy reflection and transmission coefficients, RC and TC were calculated using equations 6.52 and 6.53. RC and TC of the section B composite as functions of frequency are shown in Figure 6.10. It can be seen that within 0 to 40 kHz RC is zero and TC is less than 100%, meaning that there is no reflection of the acoustic waves in this frequency range while there is energy dissipation occurs in the composite. Interestingly, at 40 kHz, the energy dissipation coefficient, DC is as high as 90% (see equation 6.54).

The final step is to combine sections A and B to create the active acoustic

Table 6.3: Section B: material parameters

	Copper	PU-20%MG	Steel
E' (GPa)	120	0.636	200
E'' (GPa)	0	0.132	0
ρ (kg m^{-3})	8193	1445	7850
Z (MPa s m^{-1})	31.35	0.964+0.099i	39.62
Thickness (mm)	3.5	0.2	10

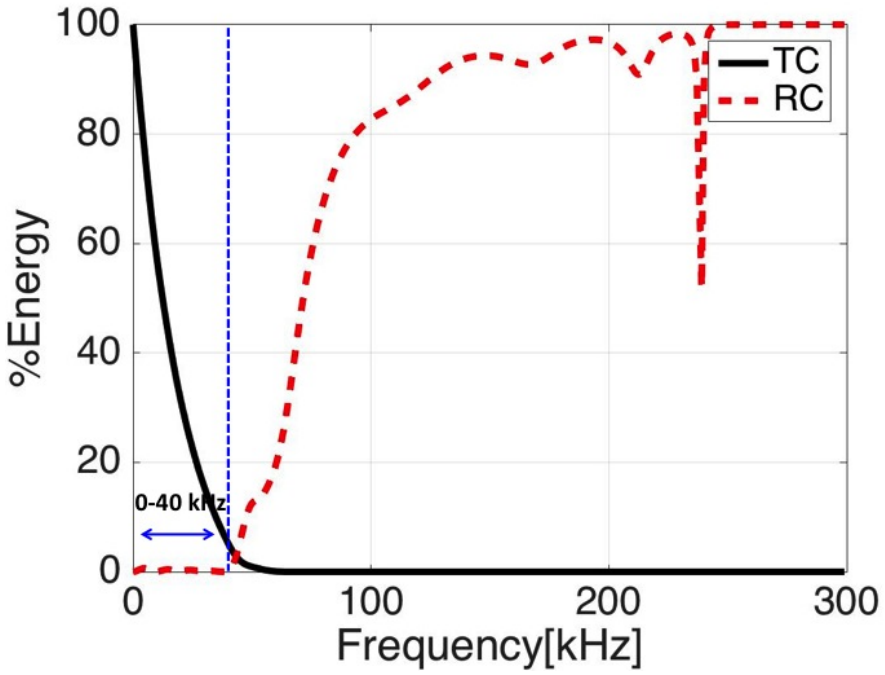

Figure 6.11: Section A and section B together: Energy reflection and transmission coefficients versus frequency

metamaterial (AAM). Figure 6.11 shows the energy reflection and transmission coefficients of AAM versus frequency. It is obvious that TC and RC of AAM are the combinations of TC and RC of sections A and B. At the current stage, the section A composite was already made. The composite has cylindrical shape. Each layer has 3/4 inch diameter (see Figure 6.12). This composite will be tested using the acoustic ball impact setup shown in Section 3.5. At this point, the Section B composite has not

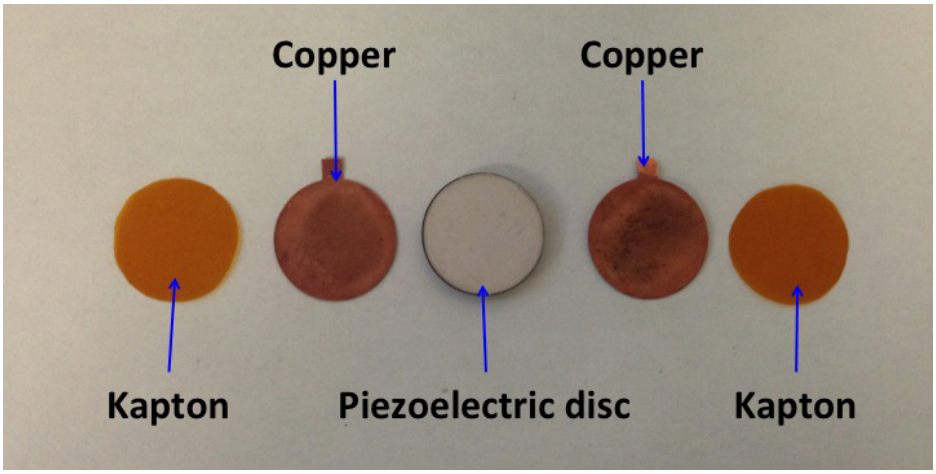

Figure 6.12: Components in a unit cell of section A composite

been made yet. If the experimental validation of this AAM shows promising result, further step will be to create an active acoustic metamaterial for applications under water, using the same design tools and method. One of the possible applications is a skin of a submarine which it can help hide the submarine from detection by SONAR (SOund Navigation And Ranging), imitate, and generate the sensed SONAR signal if and when necessary. In this case, the surrounding medium will be water which has lower impedance than aluminum, therefore the composite needs to be redesigned and the total length of the redesigned composite would be a lot shorter and more practical than the one discussed previously. It is worth noting that this is just preliminary study since it is one-dimensional problem. The real application concerns acoustic waves traveling in a three-dimensional space. The angle of the impact of acoustic waves on the surface of the composite must be considered. In this work, acoustic waves perpendicularly strike the surface of the composite.

Acknowledgements

This work has been conducted at the Center of Excellence for Advanced Materials (CEAM) at the University of California, San Diego, and has been supported through ONR Grant N00014-09-1-1126 and DARPA Grant RDECOM W91CRB-10-1-0006. The work is done in collaboration with Dr. Christian Nielsen. Section A composite was initially designed by Dr. Christina Nielsen. The author created the design tools presented in Sections 6.1 to 6.3, rechecked the design of the section A composite, and designed the section B composite.

Bibliography

[1] James C Gerdeen, Ronald AL Rorrer, et al. *Engineering design with polymers and composites*, volume 30. CRC Press, 2011.

[2] JA Pathak, JN Twigg, KE Nugent, DL Ho, EK Lin, PH Mott, CG Robertson, MK Vukmir, TH Epps Iii, and CM Roland. Structure evolution in a polyurea segmented block copolymer because of mechanical deformation. *Macromolecules*, 41(20):7543–7548, 2008.

[3] D Fragiadakis, R Gamache, RB Bogoslovov, and CM Roland. Segmental dynamics of polyurea: effect of stoichiometry. *Polymer*, 51(1):178–184, 2010.

[4] K Holzworth, Z Jia, AV Amirkhizi, J Qiao, and S Nemat-Nasser. Effect of isocyanate content on thermal and mechanical properties of polyurea. *Polymer*, 54(12):3079–3085, 2013.

[5] RG Rinaldi, AJ Hsieh, and MC Boyce. Tunable microstructures and mechanical deformation in transparent poly (urethane urea) s. *Journal of Polymer Science Part B: Polymer Physics*, 49(2):123–135, 2011.

[6] Inc. Air Products Chemicals. Polyurethane specialty products. 2003.

[7] JL Reddinger and KM Hillman. The international polyurethanes conference and exhibition for latin america. *London: Footwear and CASE Session*, 2001.

[8] George Odian. *Principles of polymerization*. John Wiley & Sons, 2004.

[9] AV Amirkhizi, J Isaacs, J McGee, and S Nemat-Nasser. An experimentally-based viscoelastic constitutive model for polyurea, including pressure and temperature effects. *Philosophical Magazine*, 86(36):5847–5866, 2006.

[10] CM Roland and R Casalini. Effect of hydrostatic pressure on the viscoelastic response of polyurea. *Polymer*, 48(19):5747–5752, 2007.

[11] J Yi, MC Boyce, GF Lee, and E Balizer. Large deformation rate-dependent stress–strain behavior of polyurea and polyurethanes. *Polymer*, 47(1):319–329, 2006.

[12] Joseph Brinson. *Ultra-violet radiation effect on the mechanical properties polyurea*. PhD thesis, California State University, Northridge, 2013.

[13] SW Guan. paper presented at the 2nd china international corrosion control conference, 2002.

[14] James S Davidson, Jeff W Fisher, Michael I Hammons, Jonathan R Porter, and Robert J Dinan. Failure mechanisms of polymer-reinforced concrete masonry walls subjected to blast. *Journal of Structural Engineering*, 131(8):1194–1205, 2005.

[15] Srinivasan Arjun Tekalur, Arun Shukla, and Kunigal Shivakumar. Blast resistance of polyurea based layered composite materials. *Composite Structures*, 84(3):271–281, 2008.

[16] MR Amini, JB Isaacs, and S Nemat-Nasser. Experimental investigation of response of monolithic and bilayer plates to impulsive loads. *International Journal of Impact Engineering*, 37(1):82–89, 2010.

[17] Damith Mohotti, Tuan Ngo, Priyan Mendis, and Sudharshan N Raman. Polyurea coated composite aluminium plates subjected to high velocity projectile impact. *Materials & Design*, 52:1–16, 2013.

[18] W Mock and E Balizer. Penetration protection of steel plates with polyurea layer. *polyurea properties and enhancement of structures under dynamic loads, Airlie, VA*, 2005.

[19] RB Bogoslovov, CM Roland, and RM Gamache. Impact-induced glass transition in elastomeric coatings. *Applied physics letters*, 90(22):221910–221910, 2007.

[20] Jing Qiao, Alireza V Amirkhizi, Kristin Schaaf, Sia Nemat-Nasser, and Gaohui Wu. Dynamic mechanical and ultrasonic properties of polyurea. *Mechanics of Materials*, 43(10):598–607, 2011.

[21] Jing Qiao, Wiroj Nantasetphong, Alireza V Amirkhizi, and Sia Nemat-Nasser. Ultrasonic properties of fly ash/polyurea composites. *Materials & Design*, 89:264–272, 2016.

[22] Natalia L Carey. *Discrete fiber-reinforced polyurea systems for infrastructure strengthening and blast mitigation*. 2012.

[23] Adriana M Mihut, Antoni Sánchez-Ferrer, Jérôme J Crassous, Liliane Ackermann Hirschi, Raffaele Mezzenga, and Hervé Dietsch. Enhanced properties of polyurea elastomeric nanocomposites with anisotropic functionalised nanofillers. *Polymer*, 54(16):4194–4203, 2013.

[24] Xiaodong Qian, Lei Song, Qilong Tai, Yuan Hu, and Richard KK Yuen. Graphite oxide/polyurea and graphene/polyurea nanocomposites: a comparative investigation on properties reinforcements and mechanism. *Composites Science and Technology*, 74:228–234, 2013.

[25] Dongyu Cai and Mo Song. High mechanical performance polyurea/organoclay nanocomposites. *Composites Science and Technology*, 103:44–48, 2014.

[26] The Dow Chemical Company. Isonate 143l; modified (mdi dow chemical, midland, mi; 2001).

[27] Marc Broekaert. Polyurea spray coatings. the technology and latest developments. *Paint & Coatings Industry*, 18(10):80–82, 2002.

[28] Louis Pilato. *Phenolic resins: a century of progress*. Springer, 2010.

[29] Michael F Ashby. *Materials and the environment: eco-informed material choice*. Elsevier, 2012.

[30] 3M. Glass bubbles k series s series.

[31] Zhanzhan Jia, Alireza V Amirkhizi, Wiroj Nantasetphong, and Sia Nemat-Nasser. Experimentally-based relaxation modulus of polyurea and its composites. *Mechanics of Time-Dependent Materials*, pages 1–20, 2016.

[32] 3M. 3m microspheres selection guide.

[33] Martin A Krenzke and Robert M Charles. The elastic buckling strength of spherical glass shells. Technical report, DTIC Document, 1963.

[34] PerkinElmer. Dynamic mechanical analysis (dma), a biginner's guide.

[35] TA Instrument. Dma 2980 dynamic mechanical analyser operator's manual.

[36] John D Ferry. *Viscoelastic properties of polymers*. John Wiley & Sons, 1980.

[37] AW Nolle. Acoustic determination of the physical constants of rubber-like materials. *The Journal of the Acoustical Society of America*, 19(1):194–201, 1947.

[38] Herbert Kolsky. *Stress waves in solids*, volume 1098. Courier Corporation, 1963.

[39] Wiroj Nantasetphong, Alireza V. Amirkhizi, Zhanzhan Jia, and Sia Nemat-Nasser. Dynamic properties of polyurea-milled glass composites part ii: Micromechanical modeling. *(in preparation)*, 2016.

[40] CM Roland, JN Twigg, Y Vu, and PH Mott. High strain rate mechanical behavior of polyurea. *Polymer*, 48(2):574–578, 2007.

[41] Wiroj Nantasetphong, Alireza V. Amirkhizi, and Sia Nemat-Nasser. Constitutive modeling and experimental calibration of pressure effect for polyurea based on free volume concept. *(in preparation)*, 2016.

[42] Jing Qiao, Alireza V Amirkhizi, Kristin Schaaf, and Sia Nemat-Nasser. Dynamic mechanical analysis of fly ash filled polyurea elastomer. *Journal of Engineering Materials and Technology*, 133(1):011016, 2011.

[43] AV Amirkhizi, J Qiao, K Schaaf, and S Nemat-Nasser. Properties of elastomer-based particulate composites. In *Dynamic Behavior of Materials, Volume 1*, pages 69–72. Springer, 2011.

[44] JI Velasco, D Arencon, M Sanchez-Soto, A Gordillo, and M Ll Maspoch. Milled glass fiber filled-poly (ethylene terephthalate-co-isophthalate) composites-thermal and mechanical properties. *Journal of Thermoplastic Composite Materials*, 16(4):365–380, 2003.

[45] PV Vasconcelos, FJ Lino, A Magalhaes, and RJL Neto. Impact fracture study of epoxy-based composites with aluminium particles and milled fibres. *Journal of Materials Processing Technology*, 170(1):277–283, 2005.

[46] Roshdy Barsoum. William Andrew Publishing, 2015.

[47] J Zhao, WG Knauss, and G Ravichandran. Applicability of the time–temperature superposition principle in modeling dynamic response of a polyurea. *Mechanics of Time-Dependent Materials*, 11(3-4):289–308, 2007.

[48] Vipin Agrawal, Kristin Holzworth, Wiroj Nantasetphong, Alireza V Amirkhizi, Jay Oswald, and Sia Nemat-Nasser. Prediction of viscoelastic properties with coarse-grained molecular dynamics and experimental validation for a benchmark polyurea system. *Journal of Polymer Science Part B: Polymer Physics*, 2016.

[49] M Baumgaertel and HH Winter. Determination of discrete relaxation and retardation time spectra from dynamic mechanical data. *Rheologica Acta*, 28(6):511–519, 1989.

[50] Wiroj Nantasetphong, Alireza V Amirkhizi, Zhanzhan Jia, and Sia Nemat-Nasser. Polyurea-based composites: Ultrasonic testing and dynamic mechanical properties modeling. In *Composite Materials and Joining Technologies for Composites, Volume 7*, pages 235–243. Springer, 2013.

[51] Malcolm L Williams, Robert F Landel, and John D Ferry. The temperature dependence of relaxation mechanisms in amorphous polymers and other glass-forming liquids. *Journal of the American Chemical society*, 77(14):3701–3707, 1955.

[52] Nicholas W Tschoegl, Wolfgang G Knauss, and Igor Emri. The effect of temperature and pressure on the mechanical properties of thermo-and/or piezorheologically simple polymeric materials in thermodynamic equilibrium–a critical review. *Mechanics of Time-Dependent Materials*, 6(1):53–99, 2002.

[53] VM Kamath and MR Mackley. The determination of polymer relaxation moduli and memory functions using integral transforms. *Journal of non-newtonian fluid mechanics*, 32(2):119–144, 1989.

[54] HM Laun. Description of the non-linear shear behaviour of a low density polyethylene melt by means of an experimentally determined strain dependent memory function. *Rheologica Acta*, 17(1):1–15, 1978.

[55] inc. ultran laboratories. Modern ultrasonic transducers including phenomenally high sensitivity and high frequency non-contact transducers.

[56] Rohn Truell, Charles Elbaum, and Bruce B Chick. *Ultrasonic methods in solid state physics*. Academic press, 2013.

[57] Josef Krautkrämer and Herbert Krautkrämer. *Ultrasonic testing of materials*. Springer Science & Business Media, 2013.

[58] Wolfgang Sachse and Yih-Hsing Pao. On the determination of phase and group velocities of dispersive waves in solids. *Journal of Applied Physics*, 49(8):4320–4327, 1978.

[59] Ronald A Kline. Measurement of attenuation and dispersion using an ultrasonic spectroscopy technique. *The Journal of the Acoustical Society of America*, 76(2):498–504, 1984.

[60] T Pialucha, CCH Guyott, and P Cawley. Amplitude spectrum method for the measurement of phase velocity. *Ultrasonics*, 27(5):270–279, 1989.

[61] Vikram K Kinra and Eric Ker. Effective elastic moduli of a thin-walled glass microsphere/pmma composite. *Journal of Composite Materials*, 16(2):117–138, 1982.

[62] S Nemat-Nasser, H Sadeghi, AV Amirkhizi, and A Srivastava. Phononic layered composites for stress-wave attenuation. *Mechanics Research Communications*, 68:65–69, 2015.

[63] Bertram Hopkinson. A method of measuring the pressure produced in the detonation of high explosives or by the impact of bullets. *Philosophical Transactions of the Royal Society of London. Series A, Containing Papers of a Mathematical or Physical Character*, 213:437–456, 1914.

[64] H Kolsky. An investigation of the mechanical properties of materials at very high rates of loading. *Proceedings of the Physical Society. Section B*, 62(11):676, 1949.

[65] J Harding, EO Wood, and JD Campbell. Tensile testing of materials at impact rates of strain. *Journal of Mechanical Engineering Science*, 2(2):88–96, 1960.

[66] J Duffy, JD Campbell, and RH Hawley. On the use of a torsional split hopkinson bar to study rate effects in 1100-0 aluminum. *Journal of Applied Mechanics*, 38(1):83–91, 1971.

[67] W Chen, B Zhang, and MJ Forrestal. A split hopkinson bar technique for low-impedance materials. *Experimental mechanics*, 39(2):81–85, 1999.

[68] Han Zhao and Gérard Gary. A three dimensional analytical solution of the longitudinal wave propagation in an infinite linear viscoelastic cylindrical bar. application to experimental techniques. *Journal of the Mechanics and Physics of Solids*, 43(8):1335–1348, 1995.

[69] H Zhao, G Gary, and JR Klepaczko. On the use of a viscoelastic split hopkinson pressure bar. *International Journal of Impact Engineering*, 19(4):319–330, 1997.

[70] Omar Sawas, N Singh Brar, and RA Brockman. Dynamic characterization of compliant materials using an all-polymeric split hopkinson bar. *Experimental Mechanics*, 38(3):204–210, 1998.

[71] C Bacon. An experimental method for considering dispersion and attenuation in a viscoelastic hopkinson bar. *Experimental Mechanics*, 38(4):242–249, 1998.

[72] Kulite Semiconductor Products Inc. Kulite strain gage manual.

[73] Wiroj Nantasetphong, Zhanzhan Jia, Alireza V. Amirkhizi, and Sia Nemat-Nasser. Dynamic properties of polyurea-milled glass composites part i: Experimental characterization. *(in preparation)*, 2016.

[74] Yuli Starosvetsky and Alexander F Vakakis. Primary wave transmission in systems of elastic rods with granular interfaces. *Wave Motion*, 48(7):568–585, 2011.

[75] KR Jayaprakash, Yuli Starosvetsky, Alexander F Vakakis, and Oleg V Gendelman. Nonlinear resonances leading to strong pulse attenuation in granular dimer chains. *Journal of nonlinear science*, 23(3):363–392, 2013.

[76] M Arif Hasan, Shinhu Cho, Kevin Remick, Alexander F Vakakis, D Michael McFarland, and Waltraud M Kriven. Primary pulse transmission in coupled steel granular chains embedded in pdms matrix: experiment and modeling. *International Journal of Solids and Structures*, 50(20):3207–3224, 2013.

[77] R Potekin, KR Jayaprakash, DM McFarland, K Remick, LA Bergman, and AF Vakakis. Experimental study of strongly nonlinear resonances and anti-resonances in granular dimer chains. *Experimental Mechanics*, 53(5):861–870, 2013.

[78] Vitali Nesterenko. *Dynamics of heterogeneous materials*. Springer Science & Business Media, 2013.

[79] Erheng Wang, Philippe Geubelle, and John Lambros. An experimental study of the dynamic elasto-plastic contact behavior of metallic granules. *Journal of Applied Mechanics*, 80(2):021009, 2013.

[80] EB Herbold and VF Nesterenko. Shock wave structure in a strongly nonlinear lattice with viscous dissipation. *Physical Review E*, 75(2):021304, 2007.

[81] JM Lifshitz and H Leber. Data processing in the split hopkinson pressure bar tests. *International Journal of Impact Engineering*, 15(6):723–733, 1994.

[82] D Randall and S Lee. The huntsman polyurethanes book, 2002.

[83] R Esquivel-Sirvent and GH Cocoletzi. Band structure for the propagation of elastic waves in superlattices. *The Journal of the Acoustical Society of America*, 95(1):86–90, 1994.

[84] C Cai, GR Liu, and KY Lam. A transfer matrix approach for acoustic analysis of a multilayered active acoustic coating. *Journal of sound and vibration*, 248(1):71–89, 2001.

[85] Montgomery T Shaw and William J MacKnight. *Introduction to polymer viscoelasticity*. John Wiley & Sons, 2005.

[86] Howard A Barnes, John Fletcher Hutton, and Kenneth Walters. *An introduction to rheology*, volume 3. Elsevier, 1989.

[87] Danton Gutierrez-Lemini. *Engineering viscoelasticity*. Springer, 2014.

[88] AB Bestul and SS Chang. Excess entropy at glass transformation. *The Journal of Chemical Physics*, 40(12):3731–3733, 1964.

[89] Gerold Adam and Julian H Gibbs. On the temperature dependence of cooperative relaxation properties in glass-forming liquids. *The journal of chemical physics*, 43(1):139–146, 1965.

[90] Martin Goldstein. Some thermodynamic aspects of the glass transition: Free volume, entropy, and enthalpy theories. *The Journal of Chemical Physics*, 39(12):3369–3374, 1963.

[91] Rongzhi Li. Time-temperature superposition method for glass transition temperature of plastic materials. *Materials Science and Engineering: A*, 278(1):36–45, 2000.

[92] Arthur K Doolittle and Dortha B Doolittle. Studies in newtonian flow. v. further verification of the free-space viscosity equation. *Journal of Applied Physics*, 28:901–905, 1957.

[93] F Schwarzl and AJ Staverman. Time-temperature dependence of linear viscoelastic behavior. *Journal of Applied Physics*, 23(8):838–843, 1952.

[94] Bernhard Gross. Time-temperature superposition principle in relaxation theory. *Journal of Applied Physics*, 40(8):3397–3397, 1969.

[95] Wolfgang Gustav Knauss and IJ Emri. Non-linear viscoelasticity based on free volume consideration. *Computers & Structures*, 13(1):123–128, 1981.

[96] Wolfgang Gustav Knauss and Igor Emri. Volume change and the nonlinearly thermo-viscoelastic constitution of polymers. *Polymer Engineering & Science*, 27(1):86–100, 1987.

[97] Carl Frank Popelar and KM Liechti. Multiaxial nonlinear viscoelastic characterization and modeling of a structural adhesive. *Journal of Engineering Materials and Technology*, 119(3):205–210, 1997.

[98] CF Popelar and KM Liechti. A distortion-modified free volume theory for nonlinear viscoelastic behavior. *Mechanics of Time-Dependent Materials*, 7(2):89–141, 2003.

[99] Giancarlo U Losi and Wolfgang G Knauss. Free volume theory and nonlinear thermoviscoelasticity. *Polymer Engineering & Science*, 32(8):542–557, 1992.

[100] John D Ferry and Robert A Stratton. The free volume interpretation of the dependence of viscosities and viscoelastic relaxation times on concentration, pressure, and tensile strain. *Kolloid-Zeitschrift*, 171(2):107–111, 1960.

[101] James M O'reilly. The effect of pressure on glass temperature and dielectric relaxation time of polyvinyl acetate. *Journal of Polymer science*, 57(165):429–444, 1962.

[102] RW Fillers and NW Tschoegl. The effect of pressure on the mechanical properties of polymers. *Transactions of The Society of Rheology (1957-1977)*, 21(1):51–100, 1977.

[103] G Chevellard, K Ravi-Chandar, and KM Liechti. Modeling the nonlinear viscoelastic behavior of polyurea using a distortion modified free volume approach. *Mechanics of Time-Dependent Materials*, 16(2):181–203, 2012.

[104] MS Paterson. Effect of pressure on young's modulus and the glass transition in rubbers. *Journal of Applied Physics*, 35(1):176–179, 1964.

[105] Paul J Blatz and William L Ko. Application of finite elastic theory to the deformation of rubbery materials. *Transactions of the Society of Rheology*, 6(1):223–251, 1962.

[106] Richard Christensen. *Theory of viscoelasticity: an introduction*. Elsevier, 2012.

[107] Inc ABAQUS. Abaqus, theory manual, version 6.5, 2005.

[108] Ellen M Arruda and Mary C Boyce. A three-dimensional constitutive model for the large stretch behavior of rubber elastic materials. *Journal of the Mechanics and Physics of Solids*, 41(2):389–412, 1993.

[109] Allen C Pipkin. *Lectures on viscoelasticity theory*, volume 7. Springer Science & Business Media, 2012.

[110] JC Simo and Thomas JR Hughes. Computational inelasticity, volume 7 of interdisciplinary applied mathematics, 1998.

[111] ZVI Hashin. Complex moduli of viscoelastic composites-i. general theory and application to particulate composites. *International Journal of Solids and Structures*, 6(5):539–552, 1970.

[112] Zvi Hashin. The elastic moduli of heterogeneous materials. *Journal of Applied Mechanics*, 29(1):143–150, 1962.

[113] KJ Lee and RA Westmann. Elastic properties of hollow-sphere-reinforced composites. *Journal of Composite Materials*, 4(2):242–252, 1970.

[114] John D Eshelby. The determination of the elastic field of an ellipsoidal inclusion, and related problems. In *Proceedings of the Royal Society of London A: Mathematical, Physical and Engineering Sciences*, volume 241, pages 376–396. The Royal Society, 1957.

[115] JD Eshelby. Elastic inclusions and inhomogeneities. *Progress in solid mechanics*, 2(1):89–140, 1961.

[116] Sia Nemat-Nasser and Muneo Hori. *Micromechanics: overall properties of heterogeneous materials*. Elsevier, 2013.

[117] Toshio Mura. *Micromechanics of defects in solids*. Springer Science & Business Media, 2013.

[118] Charles L Tucker III and Erwin Liang. Stiffness predictions for unidirectional short-fiber composites: review and evaluation. *Composites science and technology*, 59(5):655–671, 1999.

[119] Bruce Hartmann. Ultrasonic properties of phenolic and poly (phenylquinoxaline) polymers. *Journal of Applied Polymer Science*, 19(12):3241–3255, 1975.

[120] Rodney Hill. Elastic properties of reinforced solids: some theoretical principles. *Journal of the Mechanics and Physics of Solids*, 11(5):357–372, 1963.

[121] Tanaka Mori and K Tanaka. Average stress in matrix and average elastic energy of materials with misfitting inclusions. *Acta metallurgica*, 21(5):571–574, 1973.

[122] Y1 Benveniste. A new approach to the application of mori-tanaka's theory in composite materials. *Mechanics of materials*, 6(2):147–157, 1987.

[123] S Nemat-Nasser, T Iwakuma, and M Hejazi. On composites with periodic structure. *Mechanics of materials*, 1(3):239–267, 1982.

[124] T Iwakuma and S Nemat-Nasser. Composites with periodic microstructure. *Computers & Structures*, 16(1-4):13–19, 1983.

[125] HL Cox. The elasticity and strength of paper and other fibrous materials. *British journal of applied physics*, 3(3):72, 1952.

[126] TS Chow. Effect of particle shape at finite concentration on the elastic moduli of filled polymers. *Journal of Polymer Science: Polymer Physics Edition*, 16(6):959–965, 1978.

[127] M Taya and T Mura. On stiffness and strength of an aligned short-fiber reinforced composite containing fiber-end cracks under uniaxial applied stress. *Journal of Applied Mechanics*, 48(2):361–367, 1981.

[128] Tsu-Wei Chou, Seiichi Nomura, and Minoru Taya. A self-consistent approach to the elastic stiffness of short-fiber composites. *Journal of Composite Materials*, 14(3):178–188, 1980.

[129] N Laws and R McLaughlin. The effect of fibre length on the overall moduli of composite materials. *Journal of the Mechanics and Physics of Solids*, 27(1):1–13, 1979.

[130] Muneo Hori and Sia Nemat-Nasser. Double-inclusion model and overall moduli of multi-phase composites. *Mechanics of Materials*, 14(3):189–206, 1993.

[131] Lawrence J Broutman and Richard H Krock. *Modern composite materials*. Addison-Wesley Publishing Company, 1967.

[132] Sia Nemat-Nassera, John R Willis, Ankit Srivastavaa, and Alireza V Amirkhizia. Homogenization of periodic elastic compositesand locally resonant sonic materials. 2010.

[133] Sia Nemat-Nasser and Ankit Srivastava. Overall dynamic constitutive relations of layered elastic composites. *Journal of the Mechanics and Physics of Solids*, 59(10):1953–1965, 2011.